



HAL
open science

A sharpened close-up of R136 and NGC3603: unshrouding the nature of their stellar population

Zeinab Khorrami

► **To cite this version:**

Zeinab Khorrami. A sharpened close-up of R136 and NGC3603: unshrouding the nature of their stellar population. Other. Université Nice Sophia Antipolis, 2016. English. NNT : 2016NICE4030 . tel-01371583

HAL Id: tel-01371583

<https://theses.hal.science/tel-01371583v1>

Submitted on 26 Sep 2016

HAL is a multi-disciplinary open access archive for the deposit and dissemination of scientific research documents, whether they are published or not. The documents may come from teaching and research institutions in France or abroad, or from public or private research centers.

L'archive ouverte pluridisciplinaire **HAL**, est destinée au dépôt et à la diffusion de documents scientifiques de niveau recherche, publiés ou non, émanant des établissements d'enseignement et de recherche français ou étrangers, des laboratoires publics ou privés.

UNIVERSITÉ DE NICE-SOPHIA ANTIPOLIS
UFR Sciences
Ecole Doctorale des Sciences Fondamentales et Appliquées

T H È S E

pour obtenir le titre de
Docteur en Sciences
de l'UNIVERSITE de Nice-Sophia Antipolis

Spécialité: Astrophysique Relativiste

présentée et soutenue par
Zeinab KHORRAMI

Laboratoire Lagrange - UMR7293, Observatoire de la Côte d'Azur

T I T R E

**A sharpened close-up of R136 and NGC3603:
unshrouding the nature of their stellar population**

Soutenue le 22 Juin 2016 à l'Observatoire de la Côte d'Azur
Membres du jury :

M.	Farrokh Vakili	Directeur de thèse
M.	Thierry Lanz	Co-directeur de thèse
M.	Mathias SCHULTHEIS	Président du jury
M.	Fabrice MARTINS	Rapporteur
M.	David MOUILLET	Rapporteur
Mme	Caroline SOUBIRAN	Examineur
M.	Richard WUNSCH	Examineur
M.	Pascal CHARDONNET	Examineur

In memory of

Olivier

Abstract

The aim of this thesis is to understand the different aspects of the dynamical and stellar evolution of very massive clusters. These newly formed massive clusters are the most important link between the formation of the massive star clusters and their evolution. We chose two young massive clusters, located in the most massive Galactic/extra-Galactic HII regions, NGC3603 and R136 which hosts the most massive stars in the local universe.

This thesis contains the photometric analysis of the core of R136 and NGC3603 using the Hubble Space Telescope (HST) data in the visible and the Very Large Telescope (VLT/SPHERE) in the infrared. Thanks to SPHERE extreme AO system, I detected many faint low-mass stars for the first time in the core of both clusters in the vicinity of massive bright objects. Comparing the results of the HST and SPHERE photometry analysis, NGC3603 shows no signature of mass segregation in its core for two main reasons: First, the MF slope in the very core is not flatter than the next radial bin. Second, both slopes are similar to the MF values found in previous works for the outer regions. R136 is partially resolved in SPHERE/IRDIS data. The majority (above 90%) of massive stars (brighter than 17 mag in K and 16 mag in J) have visual companions closer than $0.2''$. Among them, R136a1 and R136c have visual companions detected for the first time. R136a3 is resolved as two stars (PSF fitting). Considering the spectroscopic and photometric errors on the extinction ($A_J = 1.3 \pm 0.5$ and $A_K = 0.4 \pm 0.5$) and the age ($1.8^{+1.2}_{-0.8}$ Myr) of the cluster members, we estimate a mass range for each detected star. The generalized histogram of stellar masses (MF) was plotted at different ages with given errors on each stellar mass. We created series of simulated images of R136 from the output of Nbody6 code, to be compared with the HST/WFPC2 data of R136. These numerical simulations are done in order to check the effect of initial binarities, mass segregation and stellar evolution on the dynamical evolution of R136-like clusters at the early stages of their life (4 Myr).

The analysis of the bright stellar population (spectroscopic and photometry), shows that we need more resolution to go further on studying R136 which is 7-8 times further than NGC3603. The spectroscopic analysis find very massive stars in the core of R136 where, for some of them SPHERE data has resolved them visually.

Future instruments with higher angular resolution (milliarcsec) like E-ELT (MICADO), JWST and VLTI/GRAVITY can resolve the compact core of R136 and similar objects at further distances. The kinematics of the core of these compact clusters can be studied by using astrometric analysis with $\mu arcsec$ accuracy with GRAVITY in near future.

Keywords: Star clusters: individual (R136, NGC3603)- Stars: imaging- Stars: luminosity function, mass function- Stars: massive- Stars: pre-main sequence- Instrumentation: high angular resolution- Methods: numerical- Methods: observational

Résumé

Cette thèse a pour objectif de comprendre les différents aspects de l'évolution des amas d'étoiles massives NGC3603 et R136 qui possèdent les étoiles les plus massives connues de l'univers local. L'analyse photométrique des noyaux de R136 et NGC3603 utilisant l'imagerie infrarouge de l'instrument SPHERE sur VLT et son système d'optique adaptative extrême de SPHERE, m'a permis de détecter pour la première fois un grand nombre d'étoiles de faible masse et luminosité au coeur de ces amas et pour la plupart au voisinage des étoiles les plus lumineuses et massives. La comparaison des données de SPHERE de NGC3603 à celles du HST montre l'absence de ségrégation de masse dans le noyau de cet amas. De plus la pente de la fonction de masse de cette région est la même que celle de la région suivante et similaire aux valeurs de la MF correspondant aux régions extérieures de l'amas connues jusqu'ici. L'amas R136 est partiellement résolu par SPHERE/IRDIS dans l'IR. La majorité de ses étoiles massives ont des compagnons visuels. En prenant compte des mesures spectroscopiques et photométriques et leurs erreurs sur l'extinction et l'âge des membres de l'amas, j'ai estimé une gamme de masses pour chaque étoile identifiée. La MF a été calculée pour différents âges ainsi que les erreurs sur les masses stellaires. J'ai simulé des séries d'images de R136 grâce au code Nbody6, et les ai comparées aux observations du HST/WFPC2. Ces simulations permettent de vérifier l'effet de la binarité initiale des étoiles de l'amas, la ségrégation de masse et l'évolution des étoiles sur l'évolution dynamique propre à R136. Ces analyses démontrent l'importance d'une résolution angulaire encore plus fine pour mieux comprendre la nature physique de R136, qui se trouve à une distance 7-8 fois plus loin que NGC3603. Les études spectroscopiques ont trouvé des étoiles super massives dans le noyau de R136, alors que notre présent travail avec SPHERE résoud clairement certaines d'entre elles comme multiples visuelles.

Mots-clés: Les amas stellaires: individuel (R136, NGC3603) - Etoiles: étoiles massives - Imagerie: fonction de masse-luminosité, fonction de masse - Etoiles : préséquence principale Etoiles : séquence principale - Instrumentation: haute résolution angulaire Méthodes: numérique Méthodes : observationnelle

ACKNOWLEDGMENTS

It is my great pleasure to write the acknowledgements after all the hard work writing my thesis.

Firstly, I would like to express my sincere gratitude to my supervisor, Farrokh Vakili, for his continuous support during my Ph.D study, with his patience, motivation and considerable freedom for developing my ideas. I would like to cordially thank Thierry Lanz, who has been a tremendous mentor for me. I am really grateful to Thierry for encouraging my research and for allowing me to grow as a research scientist. I am glad that I started my doctoral journey under the supervision of Olivier Chesneau. He was a prolific scientist, full of energy, who helped me taking the first steps on my project. His untimely departure was a tragic loss and we all miss Olivier at OCA.

Besides my supervisors, I would like to thank the rest of my thesis committee: Dr. Mathias Schultheis, Dr. Fabrice Martins, Prof. David Mouillet, Dr. Richard Wunsch, Prof. Caroline Soubiran and Prof. Pascal Chardonnet, for their insightful comments.

I am also grateful to many collaborators for their contributions to this thesis. I would like to thank Djamel Mekarnia for his help on using IDL photometric packages and Marcel Carbillet for teaching me how to work with CAOS. I am grateful to Armando Domiciano De Souza and Florentin Millour for teaching me how to handle interferometric data (AMBER and MATISSE) and create OBs. I am really thankful to Martin Vannier, who was a great officemate and friend, for numerous discussions on scientific matters.

My deepest gratitude goes to Richard Wunsch and Jan Palous for the joyful collaboration on cluster's formation and evolution, and all their support during my visits to Prague. I am really thankful to Andreas Kuepper, Pavel Kroupa and Sambaran Banerjee for the helpful discussions and comments on Nbody6 simulations. I also want to thank Maud Langlois and Hans-Martin Schmid for their help on IRDIS and ZIMPOL data reduction. I thank Michael Meyer for his helpful comments and discussions on R136 and his support during my visit to ETH-Zurich.

I thank Chris Evans for providing MAD catalog and reduced data on R136, and Aaron Dotter for useful discussions on the bolometric-corrections and zero-points.

In particular, I would like to thank Wolfgang Brandner for his useful comments on NGC3603 SPHERE results and also arranging my first observational trip to Paranal to achieve an exceptional experience of five nights observations with NACO.

I thank Antti Tamm and Jaan Einasto for their warm hospitality on Tartu Observatory during my mobility.

I want to express my deep acknowledgement to all my colleagues, officemates and friends at OCA for their supports.

I would have difficulty to complete all the administrative work without the help of Pascal Chardonnet, Pina Barbaro, Emmanuel Losero, Gildas Tchibozo from IRAP and all the secretaries in Lagrange. I appreciate the help of directors of OCA and Lagrange during my PhD: Farrokh Vakili, Thierry Lanz and Philippe Stee, and also people in the computational center especially Arielle Willm and Alain Miniussi.

A special thanks to my dear family, my mother and father, my amazing sister Zahra, Amir, Sama, Human and my parents-in-law. Words cannot express how grateful I am to my family, for all of the sacrifices that they have made on my behalf.

At the end I would like to express appreciation to my beloved Samir for his constant love, support and faith in me through all those hard times together.

Contents

Table of Contents	vii
1 Introduction	1
1.1 Formation of Star Clusters	1
1.2 Evolution of Star Clusters	3
1.3 Massive stars within clusters	5
1.3.1 Formation of massive stars	7
1.3.2 Evolution and Fate	9
1.4 Mass estimation	12
1.5 Binary systems	14
1.6 Case of R136 and NGC3603	16
1.7 Observation	18
1.7.1 Adaptive Optics	24
1.7.2 SPHERE	26
1.7.3 Telescopes comparison	28
1.8 This thesis	29
2 HST Photometry (R136, NGC3603)	35
2.1 Introduction	36
2.2 Data and photometry	37
2.3 Method	38
2.3.1 Bolometric Corrections for HST filters	40
2.3.2 Correcting the extinction	42
2.3.3 Estimating stellar masses	44
2.4 Extinction and CMDs of the two clusters	45
2.5 Mass Functions	51
2.6 Comparison with earlier analyses	56
2.7 Summary	58
3 Simulations	67
3.1 Modeling a young massive star cluster	68
3.1.1 Physical conditions and Mechanisms	69

3.1.2	Initial conditions	69
3.2	Results of the simulations	73
3.2.1	Expansion of the cluster	73
3.2.2	Escapers and cluster's mass loss	73
3.2.3	Binary fraction	75
3.2.4	Periods and eccentricities	80
3.3	Comparison with observations	81
3.3.1	SBP of R136	87
3.3.2	MF slopes	88
3.3.3	Half-light radius	99
3.3.4	Neighbor radius	103
3.4	Discussion of the results	104
3.5	Summary	109
4	VLT/SPHERE Photometry on NGC3603	113
4.1	Introduction	114
4.2	Data and photometry	115
4.3	Extinction and CMD	118
4.4	Mass Functions	120
4.5	Discussion	127
5	VLT/SPHERE Photometry on R136	133
5.1	Observations	134
5.2	Photometry of R136's compact core	139
5.2.1	Strehl ratio	141
5.3	Age and extinction	144
5.4	Visual companions	149
5.5	Density and Surface Brightness Profile	151
5.6	Discussion and conclusion	152
6	Summary and prospects	175
6.1	Main results	175
6.1.1	NGC3603	175
6.1.2	R136	176
6.2	Prospects	178
6.3	Look into the future	178
A	SPHERE/IRDIS catalog of NGC3603	181
B	SPHERE/IRDIS catalog of R136	191
C	Papers	221

List of Figures

- 1.1 Feitzinger+1980 observation in Visible (630-880nm) using ESO 3.6m telescope. R136a was recognized as a single object covering 0.7pc^2 or $2.8''^2$ with T_{eff} about 50 to 55 kK and mass of 250 to 1000 M_{\odot} 18
- 1.2 Top: CCD image of R136 taken by 4m CTIA telescope in 470nm with FoV of 3' x 5'. Moffat+1985 using spectrophotometry on the core of R136, deduced R136a contains 4-5 WN stars. Bottom: Resolving core of R136 and R136a's members using speckle-interferometry. Right: Weigelt+1985 for the first time, R136a resolved as 8 stars (R136a1 to R136a8). Left: Pehlemann+1992 used the same method with more frames, found more than 40 objects in the core of R136 ($4''.9 \times 4''.9$). Both observations were done using 1.54m Danish/ESO telescope. 19
- 1.3 TOP: A region of $50 \times 50\text{pc}^2$ ($3.3' \times 3.3'$) around the cluster R136 in the 30 Doradus region of the LMC, at the distance of 50 kpc taken by HST/WFC3. Left: in the visible; Right: in the Infrared (1.1, 1.6 μm) Bottom: VLT/MAD image of R136 in Ks band covering $12'' \times 12''$ [Campbell et al. (2010)] together with a $4'' \times 4''$ central view of the core. Image courtesy of Crowther et al. 2010 where he analyzed spectroscopic data on the 5 WR stars in the core of r136 using HST/HRS, HST/FOS and VLT/SINFONI. They found the initial mass of $320_{-40}^{+100} M_{\odot}$ for R136a1 with T_{eff} of 53 ± 3 kK. 20

1.4	Right: Central part of NGC3603 with 4 minutes exposure, taken by 74-inch (1.88m) reflector plate in Mount Stromlo observatory by Sher 1964. Left: CCD image of NGC3603 taken by 4m CTIA telescope in 470nm. Circle has a diameter of 59". Moffat+1985 using spectrophotometry on the core of NGC3603, found this cluster contains 2-3 WN stars.	21
1.5	Top: Image of NGC3603 taken by HST/WFC3 in visible and infrared. Illustration Credit: NASA, ESA, and Z. Levay (STScI). Bottom: Left: HST/HRC image of the core of NGC3603, three WR stars has been shown. Middle: Average spectra (VLT/SINFONI in K-band) of the three WR stars. Right: Same as middle but just for A1 almost at quadrature phase. Primary and secondary are shown with upward and downward arrows respectively. Spectra in middle and right are taken from Schnurr et al. 2008.	22
1.6	Diffraction limited resolution of telescopes with different diameter in four different wavelengths (300, 500, 1000 and 2000 nm).	23
1.7	Left: Atmosphere turbulence and its effect on the wavefront is shown schematically. Right: AO system. <i>Source: http://slittlefair.staff.shef.ac.uk/teaching/phy217/lectures/telescopes/L</i>	24
1.8	Right: Image of the core of R136 (12"×12") using SPHERE AO in K band. The resolution is about 49 mas. Left: Same image without AO so the resolution is limited by seeing (0.8").	25
1.9	SPHERE instruments (courtesy of ESO). <i>source: https://www.eso.org/sci/facilities/paranal/instruments/</i>	
1.10	Inside view of IRDIS instrument (courtesy of ESO). The common path beam enters the common filter wheel and Lyot stop wheel, then it splits into two beams and passes through dual filter wheel and at the end lands on the detector. <i>source: https://www.eso.org/sci/facilities/paranal/instruments/sphere/inst.html</i>	28

2.1	WFPC2/F814W image of R136 with the 26 selected O stars shown by circles The color-bar represents the range of extinction values and the selected stars are marked with blue or red circles depending on the estimated extinction. We divided the cluster in three different concentric regions with annulus of 4".5 (corresponding to about 1 pc at a distance of 48.5 kpc).	41
2.2	WFPC2/F814W image of NGC 3603 with the 21 selected O stars. Three concentric regions are also shown (at 5", 10" and 15"). At the cluster distance, 5" corresponds to about 0.17 pc.	43
2.3	Histogram of extinction of 26 O-type stars with known spectral types in R136 in two HST/WFPC2 filters (F555W and F814W) using three different isochrones: 1 Myr (top), 1.5 Myr (middle) and 2 Myr (bottom). Red and pink histograms represents extinction in the F814W and F555W filters and the filled blue histogram shown to the color excess distribution.	45
2.4	Top: Extinction toward 21 O-stars in NGC 3603 in three different HST/WFPC2 filters. Bottom: Same in seven different HST/HRC filters.	46
2.5	Color-Magnitude Diagrams of R136. Panels from left to right show the CMD for the whole cluster, and in the three regions (core and annuli shown in Fig. 2.1. The 10 Wolf-Rayet stars in the FoV are shown with black crosses. Solid lines are the 1.0, 1.5 and 2.0 Myr Geneva isochrones.	49
2.6	Color-Magnitude Diagrams of the core of NGC 3603 from WFPC2 (top) and HRC (bottom) data. Panels from left to right show the CMD for the whole cluster, and in the three regions (core and annuli shown in Fig. 2.2. The solid line is the 1.0 Myr Geneva isochrone.	50

2.7	Mass function derived independently in two filters (F555W in the left and F814W in the right) assuming 1.0 Myr isochrone to derive stellar luminosities. The MF is plotted for the whole cluster (red dots) and in the three different regions (core and two annuli from top to bottom).	53
2.8	Mass function derived independently in two filters (F555W in the left and F814W in the right) assuming 1.5 Myr isochrone to derive stellar luminosities. The MF is plotted for the whole cluster (red dots) and in the three different regions (core and two annuli from top to bottom).	54
2.9	Mass function derived independently in two filters (F555W in the left and F814W in the right) assuming 2.0 Myr isochrone to derive stellar luminosities. The MF is plotted for the whole cluster (red dots) and in the three different regions (core and two annuli from top to bottom).	55
2.10	Mass function of NGC 3603 derived for the whole cluster (red dots) and in three different regions (from top to bottom). Top: Data from three WFPC2 filters (F547M, F675W, F814W). Bottom: Data from three ACS/HRC filters (F550M, F658N, F850LP)	61
2.11	Mass function slopes of NGC 3603 derived in three WFPC2 filters (F547M, F675W, F814W from top to bottom) for the whole cluster and in three spatial regions (HRC data - dashed blue) and 5 spatial regions (WFPC2 data - solid red).	62
2.12	Mass function slopes of R136 derived in F555W (red) and F814W (blue) for the whole cluster and in three different regions using three different isochrones: 2, 1.5 and 1 Myr from top to bottom. Left plot is for the standard mass loss (c-models from Geneva stellar evolution models) and right plot for enhanced mass loss (e-models from Geneva stellar evolution models)	63

2.13	Mass function slopes of NGC 3603 derived in three WFPC2 filters (F547M, F675W, F814W from top to bottom) for the whole cluster and in three different regions. Red and blue represents standard and high mass loss from Geneva stellar evolution models (c020 and e020 models).	64
4.1	SPHERE/IRDIS image of NGC3603-F0 in J (left) and K (right)	116
4.2	SPHERE/IRDIS image of NGC3603-F1 in J (left) and K (right)	116
4.3	SPHERE/IRDIS image of NGC3603-F2 in J (left) and K (right)	117
4.4	Incompleteness test on three fields in NGC3603 of SPHERE data in J (left) and K (right). Each point represent the 500 artificial star test. Up: F0; middle: F1 and F2; bottom: shows the final results with fitted line in F0 (left) and F1-F2 (right). . .	119
4.5	HST/WFPC2-PC/F814W core of NGC 3603: blue squares depict the three fields observed with SPHERE-IRDIS. Green circles refer to the known O-type stars from [Harayama et al. (2008)]. Red circles show the stars in [Harayama et al. (2008)] catalog, which we used for calibrating zero-points in different fields. There are 113, 45, and 51 stars common between [Harayama et al. (2008)] in the SPHERE F0, F1, and F2 fields.	121
4.6	CMD of the core of NGC 3603 in IRDIS J and K band for the whole FoV (left) followed to the right for the three fields F0, F1, and F2. Black circles show the K-excess stars. Three black crosses represent stellar models with initial masses of 100, 120, and 150 M_{\odot} . The black arrow signifies the effect of extinction, $A_V = 4.5$. 122	
4.7	CMD from VLT/NACO (from [Harayama et al. (2008)]) overplotted with SPHERE data (red circles) to set the zeropoints of SPHERE/IRDIS detectors. The stars are shown in Figure 4.5 (Red circles in three fields)	123
4.8	The sources with $E(J - K) > 1.8$ in F0, F1 and F2 shown in red circles. The image is a combination of all three fields in IRDIS/B-J.	124

4.9	Mass functions derived for IRDIS data in BB-J (right) and BB-K (left) in F0 (shown in Figure 4.5 Top). Last three red bins represent the MF considering the A1 and C as a binaries and B as a single source. The last three black stars represent the MF if the WR stars are considered single objects, which is the case for the photometry analysis.	127
4.10	Mass functions derived for IRDIS data in BB-J (right) and BB-K (left) in F1 and F2 together. F1 and F2 are shown in Figure 4.5 Top.	128
5.1	SPHERE/IRDIS images of the core of R136 in K-band.	135
5.2	SPHERE/IRDIS images of the core of R136 in J-band.	136
5.3	Top: HST images in V-band (F555W) from the core of R136, same FoV of SPHERE/IRDIS data. Left: WFPC2, Right:WFC3. Bottom: VLT images of the core of R136 in K band. Left: MAD, Right: SPHERE.	137
5.4	Zoom to the WR stars in the core of R136 in K-band (left) and J-band (right). Each frame covers about 2". In the top R136a1, R136a2 and R136a3 can be seen and in Bottom, R136b and R136c with its new companion.	138
5.5	Map of the correlation coefficients calculated by starfinder along the FoV in J (left) and in K (right).	140
5.6	Top: Background images in J (left) and in K (right) after removing the detected sources using Starfinder. Bottom: Residual images in J (left) and K (right) after filtering out the AO halo in the background image at Fourier space.	142
5.7	PSF fitting errors (red pluses) and residual errors (blue crosses) in J (bottom) and K (top). PSF fitting error is the outcome of the Starfinder. Residual errors is the outcome of the background analysis after removing the stellar sources signals from the image.	143
5.8	Position errors in J (bottom) and K (top), estimated from the photometry.	144

5.9	Top: map of the PSF fitting errors (outcome of the SExtractor photometry) along the IRDIS FoV. Middle: map of the residual errors, outcome of the background analysis after removing the stellar sources signals from the image. Bottom: map of the total error, combination of the PSF-fitting errors and the residuals background errors. Left: J; Right: K	156
5.10	Top: r136 in K (left) and J (right) with the circle of 3" radii. Bottom: Incompleteness test in J (red pluses) and K (blue crosses) for two regions: Very core of R136 ($r < 3''$) in the left and outside of the core ($r > 3''$) in the right.	157
5.11	Theoretical diffraction pattern PSF (Airy disc) is shown in Red (left) and the simulation of the observed PSF with $S_r = 0.3$ is presented in Blue. The green Gaussian profile indicates the AO halo.	158
5.12	The Strehl ratio as a function of minimum correlation coefficient between the input PSF and detected stellar source, in K-band (left) and J-band (right) data of SPHERE/IRDIS from the core of R136.	158
5.13	The top image corresponds to the IRDIS/Ks on which the 54 spectroscopically known stars from [Crowther et al. (2016)] have been added as red circles. The bottom plot depicts the T_{eff} , $\log L/L_{\odot}$ and corresponding error-bars on these 54 sources taken from Crowther et al. 2016 in blue. The solid red lines indicate the PARSEC isochrones covering ages from 0.1 to 8 Myr.	159
5.14	generalized histogram of the age of 55 known stars from Crowther et al. 2016. . . .	160
5.15	Generalized histogram of the extinction of 55 spectroscopically known stars from Crowther et al. 2016.	161

5.16	isochrones at the ages of 1, 2 and 3 Myr (corrected for distance modulus of 18.45 and central values of extinctions, $A_J = 1.3 \text{ mag}$ and $A_K = 0.4 \text{ mag}$). The CMD is plotted for the whole FoV (818 sources), in the very core of the cluster ($r < 3''$) and outside ($r > 3''$), from left to right respectively. The error-bars on each point is the combination of the PSF-fitting errors and the residual errors from the background image after removing the stellar sources signals from the images.	162
5.17	Generalized histogram of the MF at 1, 2 and 3 Myr.	163
5.18	Top: Histogram of the separation of the close detected sources. For each star which is detected in both J and K data, we determined a distance between the star and its closest neighbor. Bottom: Separation of the visual close detected sources versus their distance from the core of R136.	164
5.19	Left: Surface brightness profile (mag/pixel) of R136 in IRDIS FoV centered on R136a1. Right: same as Left, but the differences in the Kmag/pixel and Jmag/pixel is shown.	165
5.20	Projected density profile of R136 in IRDIS FoV centered on R136a1. Up: number density [stars/pc ²]. Number of stars is taken from the catalog of common stars between IRDIS, J and Ks data. Bottom: mass density [M_{\odot} /pc ²]. The stellar masses are estimated at the age of 2 Myr with extinction values of $A_J = 1.3 \pm 0.5$ and $A_K = 0.4 \pm 0.5$ in J and Ks band. Eq. 5.1 and Eq. 5.2 are used to fit the blue solid line to the data in upper and bottom plots, respectively.	166
5.21	Cumulative total mass of R136 using extrapolation in 2D.	167
5.22	The 3D mass density profiles for different values of $R_{cluster}$. I used Eq. 5.1 for fitting. The fitting parameters, γ and a , are given in Table 5.4.	168

5.23	Comparison of NGC3603 and R136 images from VLT/SPHERE. Left: Core of R136 (1.56"×1.56") at its real distance. Right: Core of NGC3603 (12.5"×12.5") at its real distance. Middle: NGC3603 as it would appear at the same distance as R136. Upper and bottom panels are in IRDIS Ks and J brand bands images, respectively.	169
5.24	Top: SBP of NGC3603 in SPHERE/IRDIS J and K band data. Bottom: the difference of Kmag/pixel-Jmag/pixel. Left: NGC3603 real images. Right: NGC3603 in the distance of R136.	170
5.25	Reconstructed image of the R136 taken by IRDIS/Ks. The position and flux of stellar sources is estimated by Starfinder.	171
5.26	FoV: 1.225"×1.225" of the core of R136 taken by HST in V-band at the top (Left:WFPC2 and Right: WFC3). At Bottom is the reconstructed images of IRDIS/Ks (left) and E-ELT/MICADO/Ks (right), with the same FoV as top images.	172

List of Tables

1.1	Categorization of star clusters according to their fundamental parameters (Table 1 in Portegies Zwart et al. 2010).	5
1.2	Comparison different telescopes resolving powers	29
1.3	SPHERE imaging modes compared to E-ELT/MICADO	29
2.1	Exposure log of HST/WFPC2 observations	39
2.2	Exposure log of HST/ACS observations of NGC 3603	39
2.3	Maximum-weighted values of Extinction and color excess of R136 in different HST/WFPC2 filters at the ages of 1, 1.5 and 2 Myr and distance of 48.5 kp, using models with standard (c008) and high (e008) mass-loss rates.	47
2.4	Median values of Extinction and color excess of NGC3603 in different HST filters at the age of 1 Myr and distance of 7 Kpc. The Galactic extinction law values by Rieke & Lebofsky (1985) are shown in the fourth column (R&L) to be compared with the extinction values we estimated for different HST filters shown in third column.	48
2.5	Slopes of the mass function of the R136 cluster.	52
2.6	Slopes of the mass function of NGC 3603 cluster (1 Myr isochrone).	56
2.7	Mass function slopes for R136 and NGC 3603 from previous analyses.	57

3.1	Different simulated clusters grouped by minimum mass. Total mass of the clusters is $10^5 M_{\odot}$. Summary of naming convention for these simulated clusters is explained hereafter:	72
3.2	χ^2 of SBP of simulated scenes at 2 Myr in XZ plane in three different regions and for the whole cluster. The smallest value is the closest one to SBP of R136.	97
3.3	χ^2 of SBP of simulated scenes at 2 Myr in XY plane in three different regions and for the whole cluster. The smallest value is the closest one to SBP of R136.	98
3.4	MF's slopes from simulated scenes at 2 Myr in XZ plane in three different regions and also for the the whole cluster.	100
3.5	MF's slopes from simulated scenes at 2 Myr in XY plane in three different regions and also for the the whole cluster.	101
3.6	R_{hl} calculated for different simulated scenes at 2Myr in XY and XZ plane.	103
4.1	Exposure time log and faintest stars (SNR > 4.2) of VLT/SPHERE observations. Δ_J and Δ_K are the differences between the maximum and minimum magnitudes in F0, F1 and F2 fields.	118
4.2	Number of detected stars (N_J and N_K in J and K bands) and MF slopes (Γ_J and Γ_K in J and K bands) using Equation 4.2, at 1.5 Myr in three F0, F1, and F2 fields of NGC 3603 from SPHERE/IRDIS.	128
4.3	Slopes of the mass function derived for NGC3603 in earlier works.	131
5.1	Exposure time log of VLT/SPHERE observations on R136.	139

5.2	Information on 54 spectroscopically known stars with T_{eff} and $\log L/L_{\odot}$ estimated by Crowther et al. 2016 (second and third columns). Using PARSEC evolutionary isochrones (0.1 to 8 Myr), the age, color excess, extinctions and initial masses are estimated (columns five to eight). N2 and N1 are the number of visual companions for each source in a radius of 0.2" and 0.1" respectively. The identifications (ID) of the sources are from Hunter et al. 1995.	146
5.3	List of 20 stars which have a companion closer than 0.08". These stars detected in both J- and Ks- band data.	150
5.4	Estimation of central density of R136 in three-dimension considering different $R_{cluster}$. First column gives the hypothetical radius of the cluster. The second column is the three-dimensional central mass density. Third and fourth columns are the fitting parameters, γ and a , in the Eq. 5.1. Finally the last column is the ratio of observed mass which is limited by $r < 1.4pc$, to the total mass estimated of the cluster, within a given radius. $M_{obs} = (1.06_{0.16}^{0.20}) \times 10^4 M_{\odot}$	153

Chapter 1

Introduction

1.1 Formation of Star Clusters

Interstellar medium (ISM) is a space between the stars, filled by gas, dust and cosmic rays. According to the temperature and density of the ISM, it can have different phases. It can be very hot ($T > 10^6$ K) ionized gas with very low density (10^4 atoms/m³) or very cold (~ 10 K) and dense (10^{12} atoms/m³). The latter case is known as molecular clouds. The giant molecular clouds (GMCs) can reach to a total mass of a few million solar-masses, extending a few parsecs. If the molecular cloud becomes gravitationally unstable, when its internal pressure is insufficient to support gravity, it collapses and forms stars [Ward-Thompson & Whitworth (2011)]. This gravitational instability in the cloud happens 1) due to a random statistical fluctuation in the medium, leading to produce some dense self-gravity cores (Jeans instability) or 2) due to any external mechanisms that compress a molecular cloud and initiate its gravitational collapse, like collision of the molecular clouds or the external pressure of the nearby supernova explosion.

Newly-formed hot stars ionize the gas embedded within the cluster and make the whole HII region being observable in visible wavelengths (H_α emission).

Most stars form embedded in clusters [Lada & Lada (2003)]. Observations of the galactic embedded clusters show the signature of infant mortality as the formation rate of star clusters is much less than the formation rate of embedded star clusters [Lada & Lada (2003)]. Only about 10% of galactic embedded clusters survive longer than 10 Myr [Lada & Lada (2003)]. Destructive feedbacks from massive star formation, gas removal phase or high degree of initial mass segregation are some of the scenarios which are proposed to explain the high galactic infant mortality of star clusters.

On one side, one tries to understand the evolution of the newly formed stellar clusters and their survival from infant mortality. On the other hand, one needs to know the star formation process (specially of massive stars) within the clusters and its feedback on the evolution of the cluster. Young stellar clusters are unique objects to provide a clue on the formation and evolution of the clusters at the very early stages of their lives. In this thesis we focus on two young massive star clusters: R136 in the Large Magellanic Cloud (LMC) and NGC3603 in the Carina arm of our Galaxy. These two clusters are located in the largest HII regions in LMC and in Milky Way (MW), hosting very massive stars (VMSs). They provide a rare opportunity to study the formation of massive stars and their feedback on the cluster formation and evolution. The young age of the clusters opens another door to the astronomers to check the stellar masses produced by molecular clouds and their initial distribution. One can check if the Initial Mass Function (IMF) has a universal shape in MW and LMC.

It is also possible to check if massive stars tend to be formed deeper in the center of the cloud (primordial mass segregation). Mass segregation is observed in most of the globular clusters which can be explained by the dynamical evolution of gravitationally bound systems. During the close encounters, the energy and momentum are exchanged between the stellar members. According to the principle of equipartition of kinetic energy, there is an statistical tendency for stars to equalize their kinetic energies during encounters. So after a given time, called relaxation time, the kinetic

energy of the stars is roughly equalized. The kinetic energy is proportional to the mass and the square velocity. Therefore the low-mass-stars will have higher velocities and go further from the center of the cluster and the high-mass-stars will have lower velocities and sink into orbits closer to the center of the cluster (dynamical mass segregation).

In the case of young massive clusters (YMCs), if segregation exists, its origin is most likely primordial as the cluster is younger than the time needed for dynamical segregation. Primordial segregation provides additional information on the formation of the stellar clusters and massive stars.

Objects, such as R136 and NGC303, enable us to investigate these questions. But the main problem remains in the interpretation of observations and the models that we need to use for understanding the whole process. How much can we improve our telescopes and their tools to have better angular resolution to get a clear and sharp image/spectra of these clusters? How much additional physics can we put in our models to get closer to the explanation of the mechanisms that govern the nature of these clusters and their stellar populations?

1.2 Evolution of Star Clusters

After the formation of stars within the cluster, dynamical evolution begins. The dynamical evolution can be characterized by two important time-scales:

1) Dynamical timescale (T_{dyn}) which is the time required for a typical star to cross the system. The dynamic (crossing) time may be defined as the characteristic radius of the cluster divided by the mean velocity of stars with respect to the cluster center (Eq. 1.1).

$$T_{dyn}[Myr] = \frac{r_h [pc]}{\bar{v} [km/s]} \quad (1.1)$$

If the cluster is in Virial equilibrium, then:

$$\begin{aligned}\bar{v}^2 &= \frac{1}{2} \frac{GM}{r_h} \\ T_{dyn}[Myr] &= 21 \times \frac{(r_h [pc])^{3/2}}{(M[M_\odot])^{1/2}}\end{aligned}\tag{1.2}$$

2) Two-body relaxation timescale (T_{rh}) which is the timescale on which two-body encounters transfer energy between individual stars and cause the system to establish thermal equilibrium [Portegies Zwart et al. (2010)]. If a stellar system consist of N stars of average mass m per star, the local T_{rh} is (Spitzer 1987):

$$\begin{aligned}T_{rh} &= 0.138 \frac{N^{1/2} r_h^{3/2}}{G^{1/2} m^{1/2} \ln \Lambda} \\ T_{rh} &\approx \frac{N}{7 \ln \Lambda} T_{dyn}\end{aligned}\tag{1.3}$$

For systems where all stars have the same mass $\Lambda \sim 0.11 N$ [Giersz & Heggie (1994)].

In the dense collisional stellar systems, like globular star clusters, T_{rh} is comparable to the cluster's lifetime. In more dilute systems the relaxation could take longer than the age of the universe. These are called collisionless stellar systems.

The star cluster lifetime is proportional to their T_{rh} and T_{dyn} . Also speed of the star cluster's evolution has a relation with the inverse T_{rh} .

For any stellar system, knowing its fundamental parameters (Age, total mass and characteristic radius), one can estimate these two important time-scales (T_{rh} and T_{dyn}), in order to better understand the evolution and survival of the system. If the T_{dyn} is shorter than the age of stellar system, then the system is gravitationally bound.

Table 1.1 compares the fundamental parameters and two dynamical time-scales of clusters in three different classes. These clusters are categorized according to their age, density and total mass. Globular clusters (GC) are old (age > 10 Gyr), massive ($M > 10^5 M_\odot$) and dense aggregate of stars.

Table 1.1 Categorization of star clusters according to their fundamental parameters (Table 1 in Portegies Zwart et al. 2010).

Cluster	Age [Gyr]	M [M_{\odot}]	ρ_c [M_{\odot}/pc^{-3}]	T_{dyn} [Myr]	T_{rh} [Myr]
OC	$\lesssim 0.3$	$\lesssim 10^3$	$\lesssim 10^3$	~ 1	$\lesssim 100$
GC	$\gtrsim 10$	$\gtrsim 10^5$	$\gtrsim 10^3$	$\gtrsim 1$	$\gtrsim 1000$
YMC	$\lesssim 0.1$	$\gtrsim 10^4$	$\gtrsim 10^3$	$\lesssim 1$	$\lesssim 100$

In contrast, Open clusters (OC) are young (age < 0.3 Gyr) with lower total mass ($M < 10^3 M_{\odot}$) and less density. YMCs, are younger than Open clusters but with comparable total mass and density of Globular clusters.

The evolution and survival of these stellar systems depends on several internal and external parameters: Dynamical interaction between the stellar masses and also between the star cluster itself with its host galaxy (tidal force); Distribution of stellar masses and its variation within time and space; Stellar evolution of stars and mass-loss from evolving stars; Formation and evolution of binary stars; Embedded gas potential and the interaction between stars and the gas within the cluster.

Note that the potential energy of YMCs is dominated by gas (embedded). The gas is removed within a few Myr by the feedback from massive stars (e.g. stellar winds and supernovae). Consequently, the cluster expands as the cluster's potential changes significantly. This expansion depends on how fast is the gas removal phase. R136 and NGC3603, host many massive stars which affects the evolution of these clusters in the early phases of their life.

1.3 Massive stars within clusters

Usually stars with masses higher than $8M_{\odot}$ during their main sequence lifetime, are considered as massive stars. They have short main sequence phase, go beyond carbon-burning phase and

produce elements heavier than Oxygen. They can end up as a blue (O,B and A-type), yellow (F and G type) or red (K and M-type) supergiant or as a Wolf-Rayet (WR) stars and luminous blue variables (LBV) with gigantic outbursts.

Massive stars have a fundamental influence on the ISM and galactic evolution for three main reasons:

- 1) They enrich their environment by producing heavy elements in their core and ejecting them in their surroundings via strong winds and when they explode as core collapse supernovae (CC-SNe).

- 2) Their powerful stellar winds inject mechanical energy into the ISM.

- 3) Because of their high effective temperature ($T_{eff} > 25000K$ on the main sequence), they are the principal source of ionizing flux which creates HII regions.

An important question is what is the upper-mass limit for the stars? The clue to tackle this question relies on young massive clusters!

Studying massive stars is not easy due to two main reasons:

- 1) Observationally, we are limited to the angular resolution of the telescopes. During the last decades the observational techniques developed using space telescopes, adaptive optics (AO) for the large ground-based telescopes (see section 1.7.1), interferometry and image analysis methods (like deconvolution). As the angular resolution improved, several very massive stars were found to be in fact multiple objects.

For example, HDE 268743 was listed as a blue supergiant in LMC, more massive than $100M_{\odot}$ [Humphreys (1983)] but later using deconvolution method, it was decomposed into 6 components [Heydari-Malayeri et al. (1988)] and later using AO observation this system revealed to be 12 stars, where the most massive one was about $50M_{\odot}$.

The mass of the brightest component of the most massive young star cluster in SMC, NGC346-1, was estimated to be about $113M_{\odot}$ [Kudritzki et al. (1989)]. But later, using deconvolution

method this object was found to be a $58M_{\odot}$ star with two other components [Heydari-Malayeri & Hutsemekers (1991)].

R136a, the brightest component of the massive cluster in LMC was claimed to be a $1000M_{\odot}$ star [Feitzinger et al. (1980)]. In 1985 Weigelt & Baier, could resolve it to eight components (R136a1 to a8) using speckle interferometry with a $0.09''$ resolution. Later on, the new data from Hubble space telescope (HST) and ground observations using AO on very large telescopes (VLT), more stars could be detected in the core of R136 [Hunter et al. (1995), Campbell et al. (2010)].

2) The other uncertainty relies on the models (stellar interiors and atmosphere) to estimate the stellar mass. Pistol is a late type massive star (probably an LBV). Using IR spectroscopy, its T_{eff} was estimated to be about $14 - 20kK$ leading to have $L \sim (0.4 - 1.5) 10^7 L_{\odot}$ and $M \sim 200 - 250M_{\odot}$ [Figer et al. (1998)]. But later, in 2009, using modern atmosphere models $T_{eff} \sim 11.8kK$ and $L \sim 1.6 10^6 L_{\odot}$ leading to $M \sim 100M_{\odot}$ [Najarro et al. (2009)].¹

1.3.1 Formation of massive stars

Very massive stars can be formed via direct gas accretion and by collision between the lower-mass stars. Krumholz (2015) presents in detail the formation of very massive stars which is not basically different from the common massive-star-formation. It seems that the formation of very massive stars can be treated in a context of the formation of upper end of the IMF. Fragmentation and radiation pressure are the main classical mechanisms that put a limit on the mass of the massive-forming star.

A collapsing cloud is unstable till it reaches the Jeans mass. Jean mass is a function of temperature and inverse of the density (Eq. 1.4). It can be calculated by balancing the gravitational energy ($\frac{3}{5} \frac{GM^2}{R}$) and the kinetic (thermal) energy ($\frac{3}{2}NKT$) of the collapsing cloud².

¹For more information on the empirical properties of massive stars see Chapter 2 of "Very massive stars in the local universe" by F. Martins

²M: total mass of the cloud; R: radius of the cloud; ρ : density; T: temperature; K: Boltzmann constant; N: number

$$M_J = \left(\frac{5KT}{Gm}\right)^{3/2} \left(\frac{3}{4\pi\rho}\right)^{1/2} \quad (1.4)$$

The fragmentation (instability) continues until stellar cores reach the Jean mass (stability). For example the Jeans-mass of a cloud with $T = 20K$ and $\rho = 10^{11} \text{molecules}/m^3$ is about $3M_\odot$. So if this cloud contains $5M_\odot$ of matter, it is Jeans-unstable and will collapse to form a star. In the simulations, if one considers just the hydrodynamics and gravity, a massive star (with the mass much higher than Jeans mass) should not form in principle. But recent simulations (radiation-hydrodynamics) considering more physical processes, like radiation feedback and magnetic fields, reduce significantly the fragmentation process by heating the surrounding gas, increasing the Pressure and thus the Jeans mass [Krumholz et al. (2007), Krumholz et al. (2010), Krumholz et al. (2011), Bate (2009), Bate (2012), Offner et al. (2009)]. Magnetic fields by removing angular momentum (magnetic braking) and providing extra pressure can prevent collapse [Hennebelle et al. (2011)]. The combination of both radiation feedback and magnetic field, which are locally complementary, shows almost no fragmentation [Commerçon et al. (2011), Myers et al. (2013)].

$$F_{grav} = \frac{GMm}{r^2} \quad (1.5)$$

$$F_{rad} = \frac{L}{c} \frac{\kappa m}{4\pi r^2} \quad (1.6)$$

The radiation pressure force is proportional to opacity (Eq. 1.6). So the radiation force of stars more massive than $20 M_\odot$ overcomes its gravitational force³ [Wolfire & Cassinelli (1987), Krumholz et al. (2009)]. The answer to the question of why stars more massive than $20 M_\odot$ (for MW dust abundances) cannot form from accretion, lies on considering the opacity source (dust mixed with gas) varying locally. One should consider non-spherically symmetric 2 (or 3) dimensional radiation-hydrodynamic simulations. In this way absorption and re-emission of photons as passing

of particles; m: average mass of the particles

³L: luminosity; κ : opacity

through dust is reprocessed within the simulation. Krumholz et al. (2009) showed the non-limiting mass accretion using three dimensional radiation-hydrodynamic simulations.

Very massive stars can also form via collision in a very dense (higher than $10^4 \text{star}/\text{pc}^3$) young stellar cluster. The Nbody simulations from Moeckel & Clarke (2011) and Baumgardt & Klessen (2011) show that the collisionally-formation of very massive stars is significant in an extremely high densities (higher than $10^7 \text{star}/\text{pc}^3$) with surface densities of $10^5 \text{star}/\text{pc}^2$. Although no observed cluster provides such a condition for collisional formation of VMS, it does not mean that none of the observed clusters never experienced such a condition to produce collisionally-formed massive stars.

New models/simulations introduce mechanisms which overcome the stellar mass limitations in previous models. But it does not mean no mechanism can limit stellar mass.

To distinguish the original route of the VMS formation (accretion or collision), one can follow the observable consequences and predictions of these models (for more details see [Krumholz (2015)]).

1.3.2 Evolution and Fate

Evolution of the structure of stars can be described with a series of differential equations involving mass, pressure, temperature, and density. The basic equations are conservation of mass (Eq.1.7), momentum (Eq.1.8), energy (Eq.1.9) and energy transport equation (Eq.1.10), to study the thermal structure of the star⁴. The evolution of chemical elements abundances⁵ (schematically shown

⁴**m**: Lagrangian mass coordinate; **r**: Radius of the shell enclosing mass m; **G**: Gravitational constant; **L**: Luminosity; **P**: Pressure; **T**: Temperature; **t**: Time; ϵ : Energy generation rate per unit mass for nuclear reactions (ϵ_n) or neutrinos (ϵ_ν); c_p : Specific heat at constant pressure; κ : Total opacity; σ : Stefan-Boltzmann constant; ρ : Density; $\delta = \partial \ln \rho / \partial \ln T$

⁵ X_i : the composition variable; r_{ji} is the rate at which species i is created from species j, and r_{ik} the rate at which i is destroyed to create k.

in Eq.1.11) should be added to the equations of the stellar structure as these equations are supplemented by some physical inputs (like opacity and nuclear reaction rate) influenced by local chemical elements.

$$\frac{\partial r}{\partial m} = \frac{1}{4\pi r^2 \rho} \quad (1.7)$$

$$\frac{\partial P}{\partial m} = -\frac{Gm}{4\pi r^4} - \frac{1}{4\pi r^2} \frac{\partial^2 r}{\partial t^2} \quad (1.8)$$

$$\frac{\partial L_r}{\partial m} = \epsilon_n - \epsilon_v - c_p \frac{\partial T}{\partial t} + \frac{\delta}{\rho} \frac{\partial P}{\partial t} \quad (1.9)$$

$$\frac{\partial T}{\partial t} = -\frac{GmT}{4\pi r^4 P} \nabla \quad (1.10)$$

$$\nabla = \nabla_{rad} = \frac{3}{16\pi\sigma G} \frac{\kappa L_r P}{mT^4}$$

$$\nabla = \nabla_{con} (\approx \nabla_{ad}) = \frac{P\delta}{T\rho c_p}$$

$$\frac{\partial X_i}{\partial t} = \frac{m_i}{\rho} \left(\sum_j r_{ji} - \sum_k r_{jk} \right) \quad (1.11)$$

Depend on how energy is transported from the core to stellar surface, there will be convective (by gas) or radiation zones (photon diffusion). Low-mass stars have radiative cores as photons carry energy away, but convective envelope as high-energy-photons are absorbed by neutral hydrogen near the surface (opacity is high). Massive stars have a steep temperature gradient (very hot core) and radiation is not sufficient to transfer the energy of the high-photon-flux in a very dense core. So they have convective cores, but a radiative envelope as photons can carry energy without being absorbed by the ionized hydrogen in the outer layers.

The evolution of massive stars is different from low mass stars because they have large convective cores during the MS phase leading to evolve quasi-chemically homogeneously (internal

mixing). For example, stars massive than $150 M_{\odot}$ have a convective core larger than 75% of the total stellar mass (Figure 1 in Yusof et al. 2013). Very massive stars, due to their high mass-loss and strong internal mixing (convection), evolve vertically in the HRD. They cover a small range of T_{eff} and a very large range of L . It is different from low-mass stars that show this behavior only at high rotation rate.

Rotation and mass-loss affect the evolution and life-time of massive stars significantly. Stars in regions with lower metallicity have smaller mass-loss, larger convective core (total mass decreases slower than the convective core mass) and they enter to the WR-phase at an older age. Evolutionary tracks of the lower metallicities are shifted to higher L and T_{eff} . Rotation increases the mass-loss and the size of a convective core. Stars without rotation have less chemical-mixing so transition between H-He burning phase happens earlier (shorter MS life) and they end up with higher L (Figure 2 in Yusof et al. 2013).

More massive stars have shorter MS life. They live longer in lower metallicity regions. Fate of the VMS can be determined with the Carbon-Oxygen core mass (part of the core's mass in which fraction of C+O is more than 75%) or Helium core mass, regardless of their prior evolutions (Figure 18 in Yusof et al. 2013). Rotation and mass-loss affect the fate of massive stars significantly. For example, rotation by introducing additional mixing elements, produce larger He-core mass. Rotation also increases the MS life of the VMSs avoiding them to go to the supergiant phase. VMSs have high luminosities and a strong mass-loss in radiation zones, leading instabilities mostly in the stellar envelope and in some conditions in the interiors. According to the mass of the star and the different element-layers, they can end up in PreSupernova (with or without remnants), forming a Black-Hole, pulsational pair instability supernova or pair instability supernova.

1.4 Mass estimation

Depending on the kind of observational data and the nature of the object itself, different estimates of stellar masses can be derived. For example, it can be evolutionary (photometric), spectroscopic mass for imaging or spectroscopic data or direct dynamical mass estimation for the binary systems (spectroscopic or visual with high angular resolution instruments). Usually, effective temperature (T_{eff}) and Luminosity (L) are estimated using the spectral energy distribution (SED) fitting from the atmospheric models. Evolutionary mass is determined using evolutionary models which provide a direct relation between L and initial mass in HR diagram. In the spectroscopic mass, we need to estimate surface gravity ($\log g$) in addition to T_{eff} and L to estimate the mass directly from Eq. 1.12

$$M = \frac{g}{G} \frac{L}{4\pi\sigma T_{eff}^4} \quad (1.12)$$

$\log g$ is obtained from the fit of Balmer, Paschen or Brackett lines in the visible and infrared as the line wings are sensitive to pressure broadening, especially Stark broadening. As Stark broadening is created by neighboring charged particles, the broadening is stronger in denser environment. The best indicator lines are $H\beta$ and $H\gamma$ in the visible and $Br\gamma$ and $Br10$ in the infrared. Usually an accuracy of 0.1 dex in $\log g$ is achieved which corresponds to 25% uncertainty in mass, itself [Martins (2015)].

T_{eff} is a most important parameter to constrain since the derived luminosity scales as T_{eff}^4 . Atmosphere models are the tools to derive T_{eff} by providing the emitted flux by a star and its SED. For low and intermediate mass stars, SED peak is in visible wavelengths so their T_{eff} can be obtained from optical photometry. For (very) massive stars the SED peak is in (extreme) UV and the spectra is affected by line opacity (far UV). In the visible, the Rayleigh-Jeans tail of SED is located where the slope depends weakly on T_{eff} . So ionization balance method is usually used to estimate T_{eff} for massive stars. Synthetic spectra from the atmosphere models, shows that the

ionization increases as T_{eff} increases. The ratio of the different ionization states of a specific element is sensitive to the T_{eff} .

For hot stars (30 - 45 kK), the ratio of HeI and HeII is considered. In this range of temperature, as the T_{eff} increases, the ratio of HeII lines to HeI lines increases. For the higher temperatures ($T_{eff} > 45$ kK), HeI lines disappear and nitrogen lines (NIV/NV) can be used instead of helium lines. For lower temperatures ($T_{eff} < 30$ kK), as HeII lines disappear Si lines (SiII/SiIII, SiIII/SiIV) can be taken into account.

So the determination of effective temperature of a massive star requires an atmosphere model which predicts the flux emitted at the top of the atmosphere so that it can be compared with the observed spectrum. The current atmosphere models for massive stars are far from the ideal 3D and time-dependent models. Still some of them have the main three characteristics which are necessary for the massive stars: 1) They have to be calculated in non-LTE (non Local Thermodynamic Equilibrium); 2) The assumption of thin atmosphere (plane-parallel) cannot be applied as these stars emit strong stellar winds with sizes much larger than the stellar radius; 3) They have to include as many elements as possible heavier than hydrogen and helium (Line-Blanketing effects).

CMFGEN (Hillier & Miller 1998), FASTWIND (Puls et al. 2005) and POWR (Hamann & Grafener) are the model atmospheres which account for three key ingredients. In this thesis, We used TLUSTY⁶ model atmospheres [Hubeny & Lanz (1995)], as comprehensive grids of non-LTE, metal line-blanketed, plane-parallel, hydrostatic model atmospheres cover the parameter space of O and B-type stars [Lanz & Hubeny (2003), Lanz & Hubeny (2007)]. Despite neglecting the stellar wind, these model atmospheres provide very good predictions of the continuum flux (especially in the visible and near-IR), as demonstrated by Hillier & Lanz (2001) for the case of the WC5 Wolf-Rayet star HD 165763. A fortiori, in most O and B stars, the continuum flux is formed in a quasi-static photosphere with limited extension and, hence, the TLUSTY model assumptions

⁶Model atmospheres and source codes are available at <http://nova.astro.umd.edu>

are not a limitation for our application. We note furthermore that there are no comparable grids of model atmospheres with winds. For cooler stars, we use Kurucz [Castelli et al. (1997)] LTE line-blanketed model atmospheres.

1.5 Binary systems

Binary systems are important in astrophysics since knowing their orbital parameters leads to estimate the component's stellar masses directly. Moreover, stellar parameters of the stars can be estimated indirectly from their mass and the mass-luminosity relation can be tested on these systems.

According to the detection method of binary systems, they are classified in four main groups: Visual, Spectroscopic, Eclipsing and Astrometric binaries.

In visual binaries, two components can be individually resolved in imaging surveys. Relative positions of the components can be derived in long-term observations. Then the orbital parameters (period and separation) can be estimated after some epochs. Usually visual binaries have long periods, widely separated and need to be relatively close to us to be resolved visually (observational bias).

If the components are physically very close to each other or the whole system is very far from us, then they can be detected by Doppler shifts in their spectral lines. These systems are called spectroscopic binaries. In observation of spectroscopic binaries, the spectrum of two components are collected but the spectral signature of one (SB1) or both stars (SB2) can be separated. The Doppler shift in the lines can be measured using Gaussian profile fitting to several observed lines, or cross-correlation techniques that are more efficient with many lines. Then according to the Doppler shift in the lines, Radial Velocities (RV) can be calculated from Eq. 1.13. Final RV is an

average of the RVs of several lines.

$$\frac{\Delta\lambda}{\lambda_0} = \frac{RV}{C} \quad (1.13)$$

The spectroscopic binaries should be close enough to each other, to produce significant variation of RVs. That is why most of the detected spectroscopic binaries have short periods between 1day up to few years (observational bias).

Semi-amplitude of RV variations (K) is related to orbital elements (Eq. 1.14)

$$\begin{aligned} K_1 &= \left(\frac{2\pi G}{P}\right)^{1/3} M_1^{1/3} \frac{q}{(1+q)^{2/3}} \frac{\sin i}{\sqrt{(1-e^2)}} \\ K_2 &= \left(\frac{2\pi G}{P}\right)^{1/3} M_1^{1/3} \frac{1}{(1+q)^{2/3}} \frac{\sin i}{\sqrt{(1-e^2)}} \end{aligned} \quad (1.14)$$

Where $q = \frac{M_2}{M_1}$

So the mass ratio M_2/M_1 is the inverse of the RV amplitude ratio (K_1/K_2)

$$\frac{K_1}{K_2} = q = \frac{M_2}{M_1}$$

Using Radial Velocity (RV) curves, one can estimate the lower limits of the binary components masses (Dynamical mass), $M_1 \sin i$ and $M_2 \sin i$.

If there is a periodic change in the apparent magnitude of a star, it can be due to:

1) A change in the intrinsic luminosity of a single star (pulsating variables) or 2) An edge-on binary system which periodically eclipse one another (eclipsing binary).

If the binary system is eclipsing, we can obtain the inclination of the system ($\sin i \simeq 1$) leading to estimate the dynamical mass instead of the lower limit.

The last group of binaries is the Astrometric binaries which can be detected by the wave-like (wobble) in the proper motion of one or two components. Sirius system is an example of astrometric binary [Bessel (1844)]. Astrometric binaries are hard to detect due to the need for long-term observations and also the uncertainty in position and proper motion measurements.

By improving angular resolution (single telescope or interferometry), one can push further the limits of the visual binaries observations, so that the combination of visual binaries determined

parameters added to spectroscopic binaries equations (Eq. 1.14), completely solves the unknown parameters.

Note that all suspected very massive stars in multiple systems discovered so far, are in spectroscopic systems. For example, multi-epoch spectroscopic analysis of 360 O-type stars in the VLT-FLAMES Tarantula Survey of massive stars, shows that more than 50% of observed O-type stars are in binary systems [Sana et al. (2013)].

Massive stars can be born in a binary system as they have high accretion rate and possibility of disk fragmentation leading to produce a very massive companion [Kratte & Matzner (2006), Kratter et al. (2008), Kratter et al. (2010)]. Massive stars born in a crowded core of the young clusters have a chance to have massive companions within close encounters (expelling the low-mass companions).

1.6 Case of R136 and NGC3603

R136 is a very young massive star cluster in the heart of 30 Doradus in LMC. This dense cluster by hosting many massive stars (most observed massive stars in the Local Universe) provides a unique opportunity to study the formation of massive stars and clusters and the evolution in their early stages.

NGC3603 is located in the most massive Galactic HII region. This cluster hosts many massive O-type stars (up to 50) and three WR stars similar to those found in the core of R136. This cluster also is very young (few Myr) and massive (about $10^4 M_{\odot}$).

Lack of high angular resolution brought two main hypothesis for the nature of the fuzzy object in the core of R136: a super-massive star with a mass $> 1000 M_{\odot}$ [Feitzinger et al. (1980), Cassinelli et al. (1981), Savage et al. (1983)] or a dense cluster core that contains normal-mass O stars [Walborn (1973), Melnick (1982), Melnick (1983), Moffat & Seggewiss (1983), Huchra et al. (1983), Moffat et al. (1985)]. Figure 1.1 shows the observation by Feitzinger et al. 1980 in the

visible. They could not resolve the core so R136a was thought to be a single $1000 M_{\odot}$ object at that time.

Observational difficulties to resolve the core of NGC3603 was less than R136 as this cluster is about 7-8 times closer than R136 but still, studying this cluster is not straightforward as it is located in a high-extinction region ($A_V = 4.5$). Figure 1.4 shows an example of images of NGC3603 taken in the visible in 1964 and 1985. Later on, when HST and AO-assisted ground telescopes came, NGC3603 was studied better in several wavelengths both imaging and spectroscopically (Figure 1.5).

Observations improved using different methods in order to find the nature of R136a: Photometry and Spectroscopy from UV to IR, Speckle-interferometry, Optical surface photometry. Figure 1.2 shows the later observations by Moffat et al. (1985) and Weigelt et al. (1985) where they could resolve R136a from Spectrophotometry and Speckle-Interferometry.

Thinking to have data from space to overcome the atmosphere turbulence problem opened a new era in astronomy. HST brought a new images and spectroscopic data with higher resolution on R136a revealing many sources within the core of R136. Figure1.3 shows the observation on R136 with HST in visible and infrared. Combination of photometry and spectroscopy analysis from HST data put more constrains on the nature of R136 and its member stars.

In parallel to the improvements on space telescopes, larger telescopes were built on the ground that could overcome atmospheric turbulence problems using Adaptive Optics technique. Figure 1.3 (Bottom) shows one of the images from the core of R136 in Ks band taken by VLT/MAD in K band. Atmosphere effects were corrected by AO facilities in ESO. This image is the best and most recent one from the core of R136. Then the ESO/VLT telescope second generation instruments came which have better AO systems like SPHERE. R136 was observed in the GTO time of SPHERE in K and J bands. Thousands stars can be detected in a compact core of R136 ($r < 6''$). This thesis describes these observations to improve our knowledge on the nature of R136.

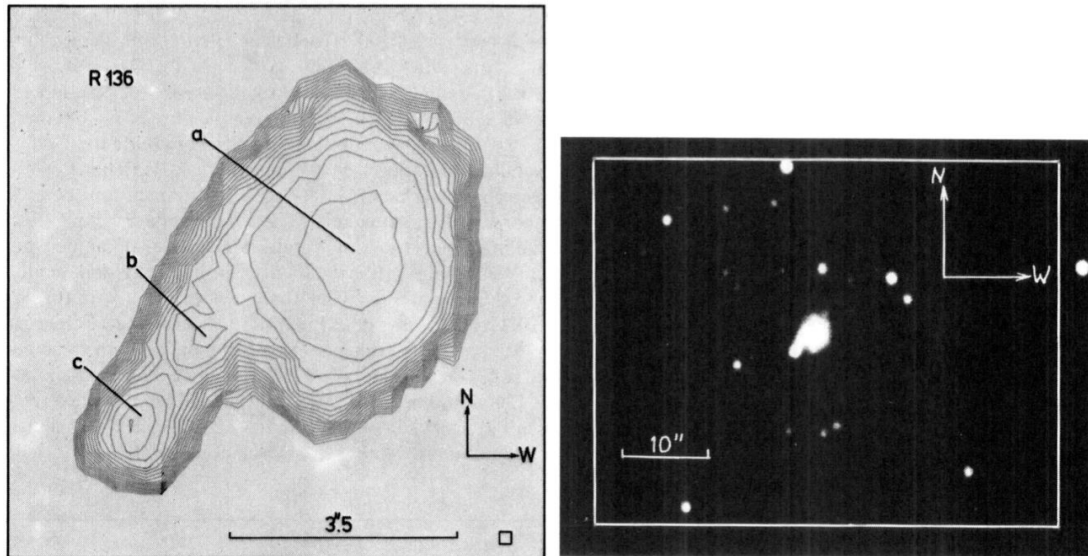


Figure 1.1 Feitzinger+1980 observation in Visible (630-880nm) using ESO 3.6m telescope. R136a was recognized as a single object covering 0.7pc^2 or $2.8''^2$ with T_{eff} about 50 to 55 kK and mass of 250 to 1000 M_{\odot}

As usual, theoretical models improved step by step with the improvement of telescopes and new observational data from better angular resolutions.

1.7 Observation

An astronomical object can be observed by several methods: Spectroscopy, imaging, interferometry and their combinations.

In order to better resolve the object, the angular resolution should be improved. The angular resolution of a telescope is limited by the aberration and diffraction. The origin of aberration comes from the instrument optics so it can be fixed by improving the optic quality of the instrument. Diffraction comes from the wave nature of the light as it interferes with itself while passing through the telescope aperture (Airy pattern). Diffraction is related to the wavelength (λ) of the light

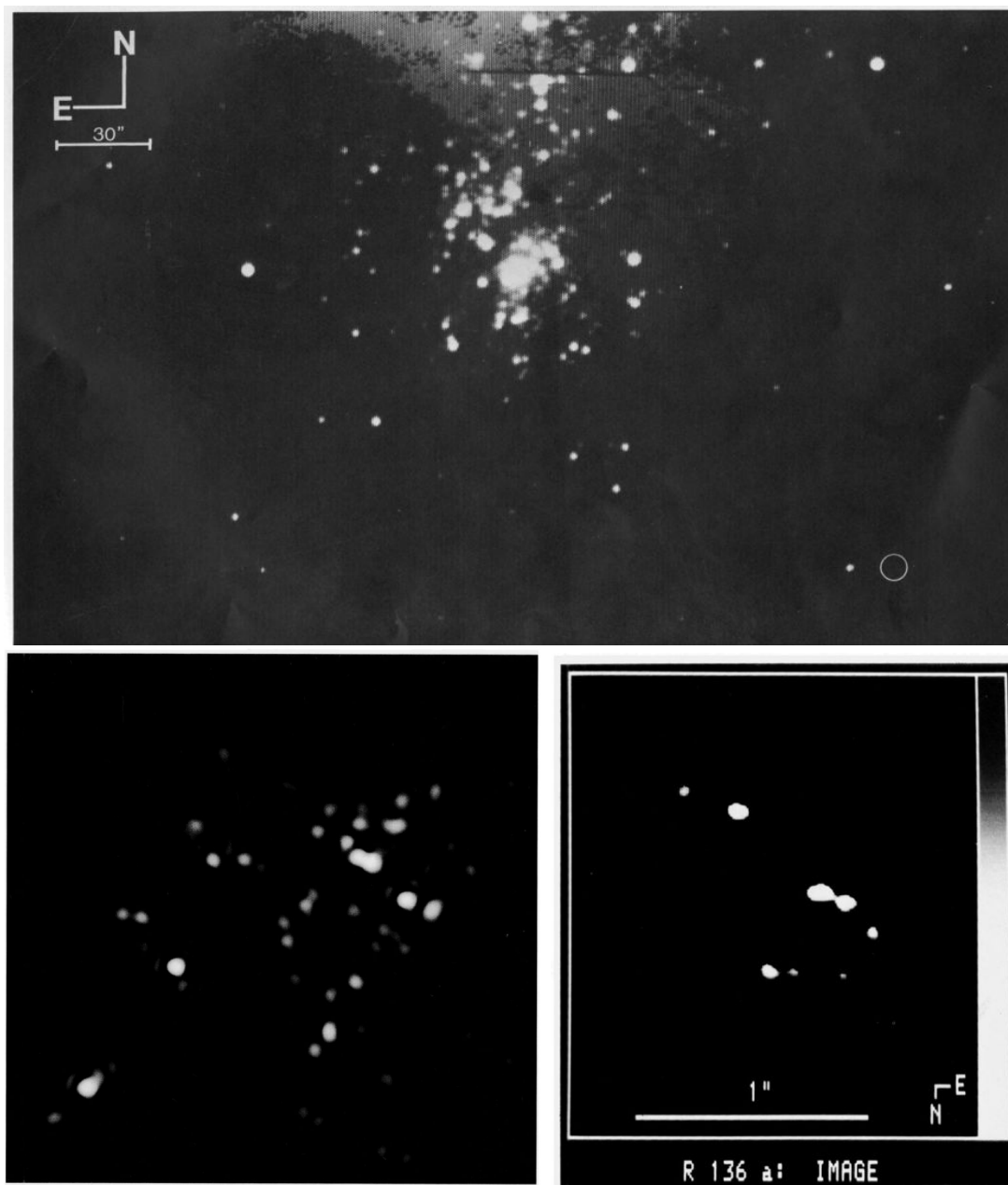


Figure 1.2 Top: CCD image of R136 taken by 4m CTIA telescope in 470nm with FoV of 3' x 5'. Moffat+1985 using spectrophotometry on the core of R136, deduced R136a contains 4-5 WN stars.

Bottom: Resolving core of R136 and R136a's members using speckle-interferometry. Right: Weigelt+1985 for the first time, R136a resolved as 8 stars (R136a1 to R136a8). Left: Pehlemann+1992 used the same method with more frames, found more than 40 objects in the core of R136 (4".9 x 4".9). Both observations were done using 1.54m Danish/ESO telescope.

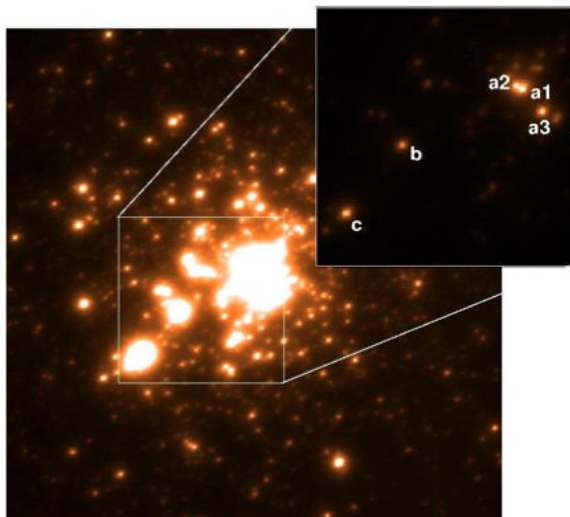
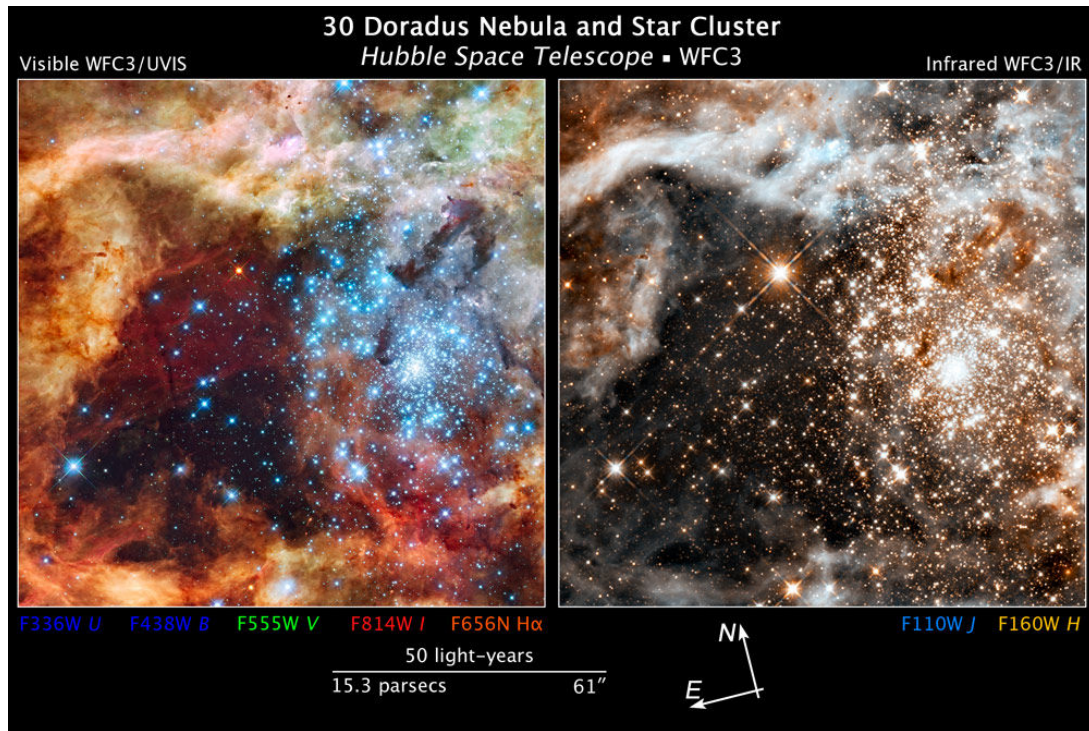


Figure 1.3 TOP: A region of $50 \times 50 \text{ pc}^2$ ($3.3' \times 3.3'$) around the cluster R136 in the 30 Doradus region of the LMC, at the distance of 50 kpc taken by HST/WFC3. Left: in the visible; Right: in the Infrared (1.1, 1.6 μm)
 Bottom: VLT/MAD image of R136 in Ks band covering $12'' \times 12''$ [Campbell et al. (2010)] together with a $4'' \times 4''$ central view of the core. Image courtesy of Crowther et al. 2010 where he analyzed spectroscopic data on the 5 WR stars in the core of r136 using HST/HRS, HST/FOS and VLT/SINFONI. They found the initial mass of $320_{-40}^{+100} M_{\odot}$ for R136a1 with T_{eff} of $53 \pm 3 \text{ kK}$.

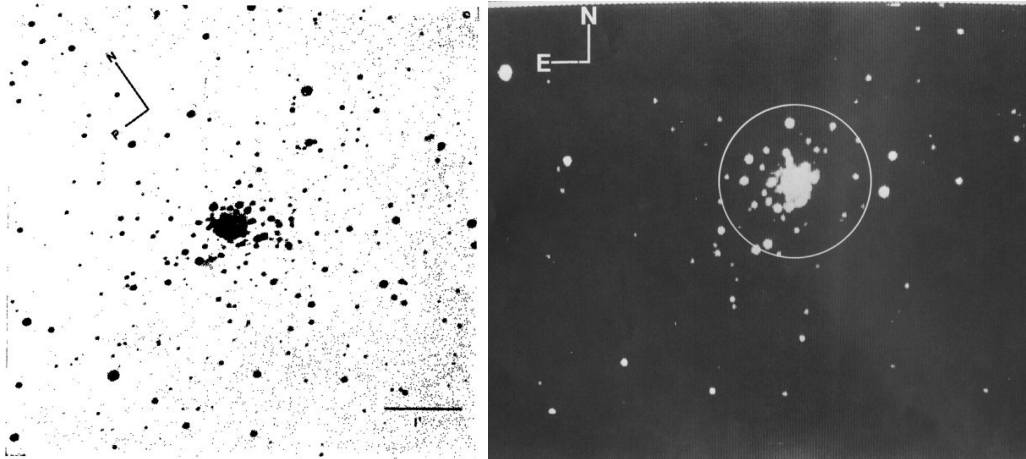


Figure 1.4 Right: Central part of NGC3603 with 4 minutes exposure, taken by 74-inch (1.88m) reflector plate in Mount Stromlo observatory by Sher 1964. Left: CCD image of NGC3603 taken by 4m CTIA telescope in 470nm. Circle has a diameter of 59". Mof-fat+1985 using spectrophotometry on the core of NGC3603, found this cluster contains 2-3 WN stars.

and the diameter of the aperture (D). The angular resolution of an ideal telescope (diffraction limited) scales as λ/D . So larger telescopes have better angular resolution in principle, specially in shorter wavelengths. But for the ground telescope, the atmosphere brings another limitation to the resolution. The images from large telescopes are blurred and distorted by the atmospheric turbulence. The full width at half maximum (FWHM) of the blurred image is called seeing which is usually around 1".

If λ/D is larger than FWHM of the seeing disk, then there is no need to correct the atmosphere turbulence. But for λ/D smaller than the FWHM of the seeing disk, the resolution will be limited to the seeing (regardless to the diameter of the telescope).

Figure 1.6 shows the diffraction-limited resolution (λ/D) of telescopes with different diameters at four different wavelengths (300, 500, 1000 and 2000 nm). For example, a 10cm telescope in 500nm has a resolution of about 1" so for larger telescopes in the same wavelength, one should correct the atmosphere-effects to reach to the resolution better than seeing (1"). The same telescope

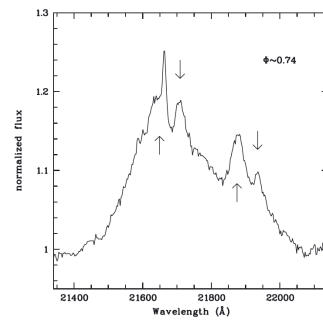
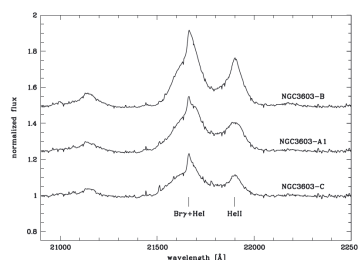
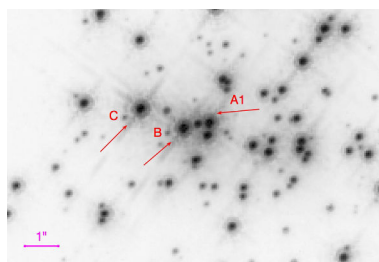
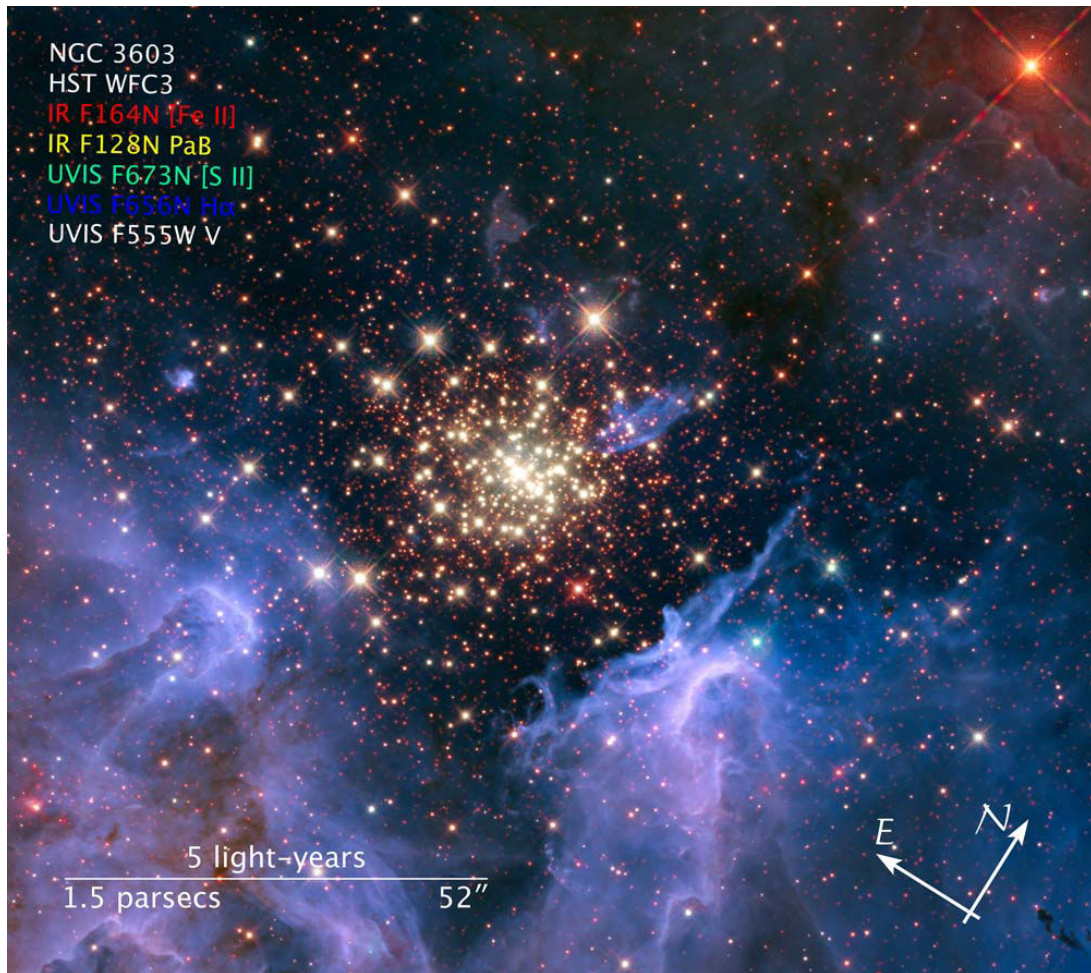


Figure 1.5 Top: Image of NGC3603 taken by HST/WFC3 in visible and infrared. Illustration Credit: NASA, ESA, and Z. Levay (STScI).

Bottom: Left: HST/HRC image of the core of NGC3603, three WR stars has been shown. Middle: Average spectra (VLT/SINFONI in K-band) of the three WR stars. Right: Same as middle but just for A1 almost at quadrature phase. Primary and secondary are shown viwh upward and downward arrows respectively. Spectra in middle and right are taken from Schnurr et al. 2008.

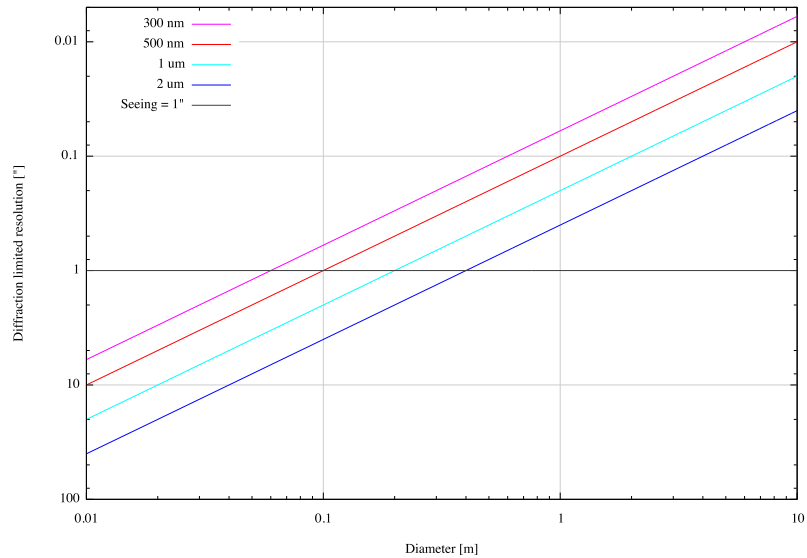


Figure 1.6 Diffraction limited resolution of telescopes with different diameter in four different wavelengths (300, 500, 1000 and 2000 nm).

(10cm) at larger wavelengths (like 2 μm) does not need AO correction as its resolution (4") is already worse than the seeing!

The instrumentation to correct the atmosphere-turbulence-effects, is called Adaptive Optics (AO). So to reach to the diffraction limited resolution of large telescopes ($D \geq 1\text{m}$) one should use AO systems. But still, some part of the electromagnetic spectrum is totally blocked by the atmosphere (Gamma-rays, X-ray, UV and most of the IR). Using the space telescopes is a solution proposed to overcome the atmosphere effect on the blocked spectrum and also on the degraded resolution by the atmosphere turbulence.

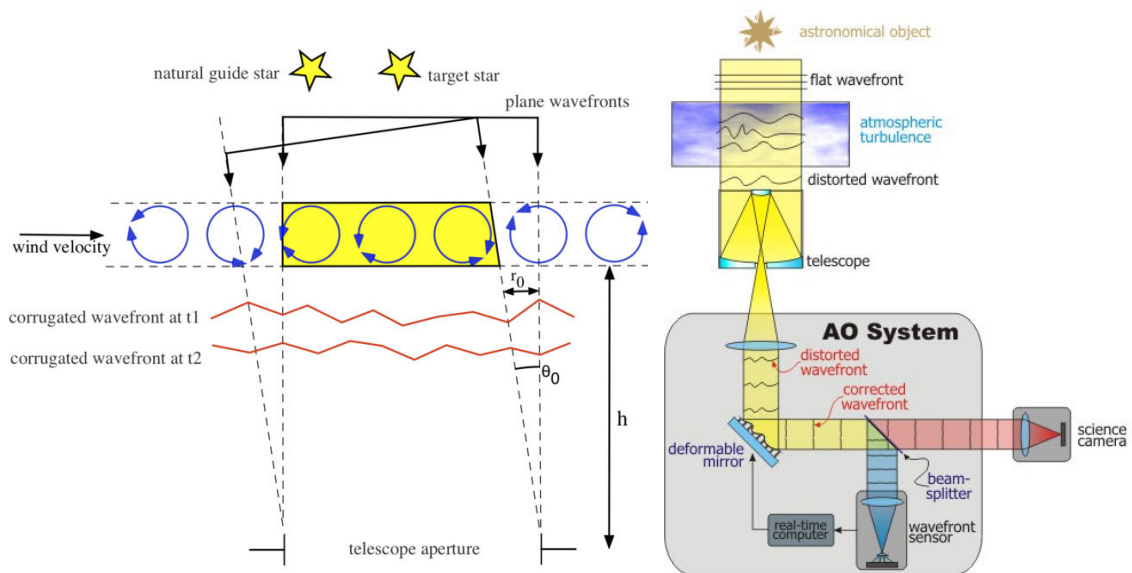


Figure 1.7 Left: Atmosphere turbulence and its effect on the wavefront is shown schematically. Right: AO system.

Source: <http://slittlefair.staff.shef.ac.uk/teaching/phy217/lectures/telescopes/L10/index.html>

1.7.1 Adaptive Optics

The effects of turbulence in Earth's atmosphere on a wavefront can be quantified with three parameters⁷:

1) Fried parameter (r_0), is a length over which the wavefront can be considered as planar. It is approximately equal to the size of the turbulent cells. Figure 1.7 (left) schematically shows the Fried parameter. Theoretically, $r_0 \propto \lambda^{6/5}$. Typically r_0 is about 10 cm in the visible ($\lambda = 500\text{nm}$) and 70 cm in the infrared ($\lambda = 2.5\mu\text{m}$).

2) Coherence Time (t_0), is a time that the wavefront changes according to the turbulence cells movement by wind across the aperture of the telescope. Figure 1.7 (left) shows two wavefronts at time t_1 and t_2 . Then, the coherence time is $t_0 = t_2 - t_1 = \frac{r_0}{V}$ where V is a wind velocity. If the wind

⁷On-line lectures of Stuart Littlefair on observational astronomy at the University of Sheffield:

<http://slittlefair.staff.shef.ac.uk/teaching/phy217/lectures/telescopes/L10/index.html>

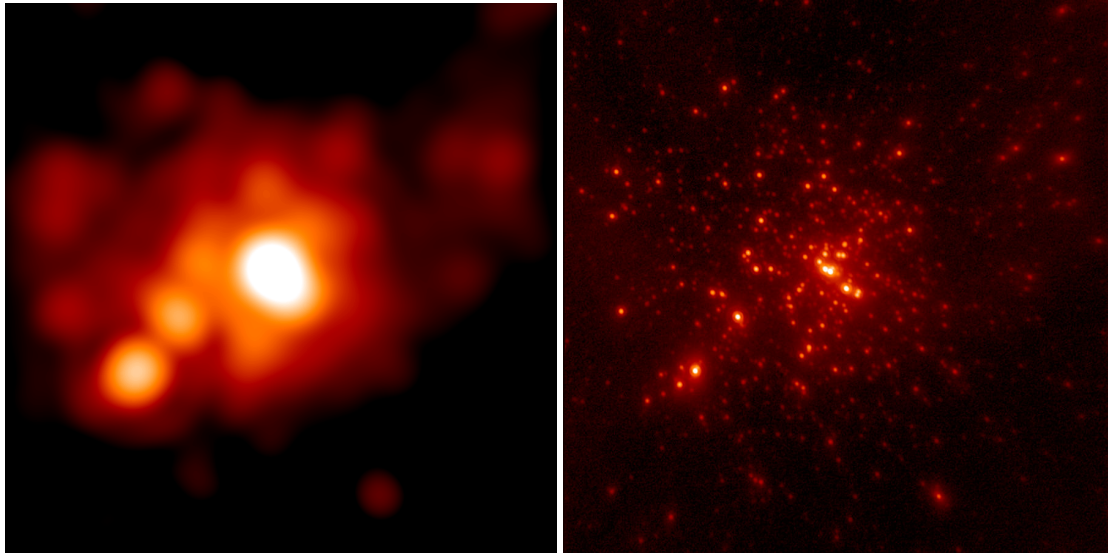


Figure 1.8 Right: Image of the core of R136 ($12'' \times 12''$) using SPHERE AO in K band. The resolution is about 49 mas. Left: Same image without AO so the resolution is limited by seeing ($0.8''$).

velocity is about 10 m/s, then the coherence time would be about 10 ms in the visible and 70 ms in the infrared.

3) Isoplanatic angle (θ_0), is the largest separation of the stars to have their light passes through the same turbulence region. If the height of the turbulent layer is h , the $\theta_0 = r_0/h$. In a good seeing condition, isoplanatic angle is about $2''$ in visible and $14''$ in infrared.

Figure 1.7 (right) shows the schematics of an AO system. The atmosphere aberrations are measured by a device called the Wave Front Sensor (WFS). Then, the aberrations are corrected by a deformable mirror (DM). Figure 1.8 shows an example of AO correction using VLT/SPHERE extreme AO system in K band. In the left, the resolution of the image is limited by the seeing (about $0.8''$). After correcting the atmosphere distortions (right image) with AO system, the resolution of the image approaches to the diffraction limited resolution (49mas) of the VLT/Melipal telescope (UT3).

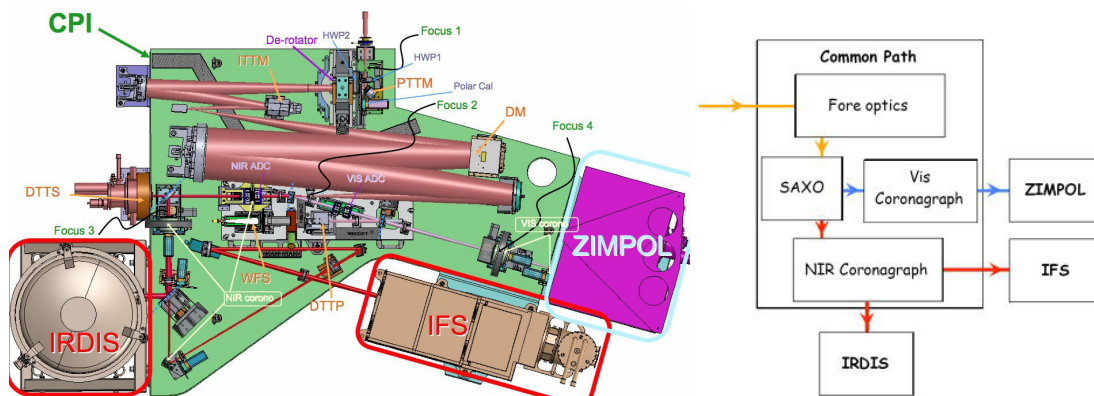


Figure 1.9 SPHERE instruments (courtesy of ESO).

source: <https://www.eso.org/sci/facilities/paranal/instruments/sphere/inst.html>

1.7.2 SPHERE

For the purpose of this thesis we used the data taken for the first time by a second generation VLT instrument, The Spectro-Polarimetric High-contrast Exoplanet Research (SPHERE)⁸ [Beuzit et al. (2008)]. The first aim of this instrument is to detect new extra-solar giant planets orbiting nearby stars by direct imaging of their circumstellar environment. The instrument has been designed in a way to detect planets with the flux ratio higher than 12.5 magnitudes (or 10^5 in flux ratio) with their host stars at very small angular separations, typically a fraction of the seeing halo. I used SPHERE's high contrast and angular resolution to resolve the crowded core of the young massive clusters, R136 and NGC3603.

SPHERE is located at the Nasmyth focus of UT3 in VLT. The instrument as shown in Figure 1.9 is composed of 4 major subsystems: the common path including the powerful AO system and the three science instruments Infra-Red Dual-beam Imager and Spectrograph (IRDIS), Infrared Integral Field Spectrograph (IFS) and Zurich Imaging Polarimeter (ZIMPOL) each fed by a sophisticated pupil apodized Lyot, Lyot, or phase-mask coronagraphs.

⁸<https://www.eso.org/sci/facilities/paranal/instruments/sphere.html>

An eXtreme AO system (SAXO) uses a 1600 actuators DM, thus correcting up to 1200 modes at loop frequencies up to 1.2kHz. The system also provides a stabilized pupil for the coronographic system and extra-stable PSFs during calibration procedures.

ZIMPOL, an innovative and state-of the art differential polarimeter working at visual to very near infra-red wavelengths. It provides diffraction limited classical imaging (CI) and differential polarimetric imaging (DPI).

IRDIS, a dual-band imager providing simultaneous imaging in two channels throughout the near-IR bands. It provides classical imaging (CI), dual-band imaging (DBI), dual-polarization imaging (DPI), and also long slit spectroscopy (LSS) with low and medium resolution (LRS and MRS).

IFS, an integral field spectrograph working in near-IR bands, the concept of which will allow to exceed the contrast limits of conventional differential imaging by a factor of 3-10. It provides a data cube of 30 monochromatic images in Y-J (0.95-1.35 μm) with spectral resolution of $R\sim 50$ or in Y-H (0.95-1.65 μm) with $R\sim 30$.

The Adaptive Optic System of SPHERE is based on the Shack-Hartmann WFS, with an array of 40×40 sub-apertures. It has a Single Conjugate Adaptive Optics (SCAO) Controlling System and Stacked Actuator Mirror (SAM) with a grid of 41×41 .

For R136 and NGC3603 observations, we used imaging mode of IRDIS which has a FOV of $11''\times 12.5''$ with a pixel scale of 12.25 mas. Figure 1.10 shows the layout of IRDIS instrument. The common path beam passes through two main wheels, 1) common filter wheel which contains 18 broad and narrow band filters and 2) Lyot stop wheel which contains 14 sections for different coronagraphs of the CPI, LRS prism and MRS grism. Then two parallel beams are produced using a beam-splitter combined with a mirror. These parallel beams passes through the third wheel which contains several dual-band filters. For our observations, we used classical imaging mode of IRDIS using just J and Ks broad-band filters.

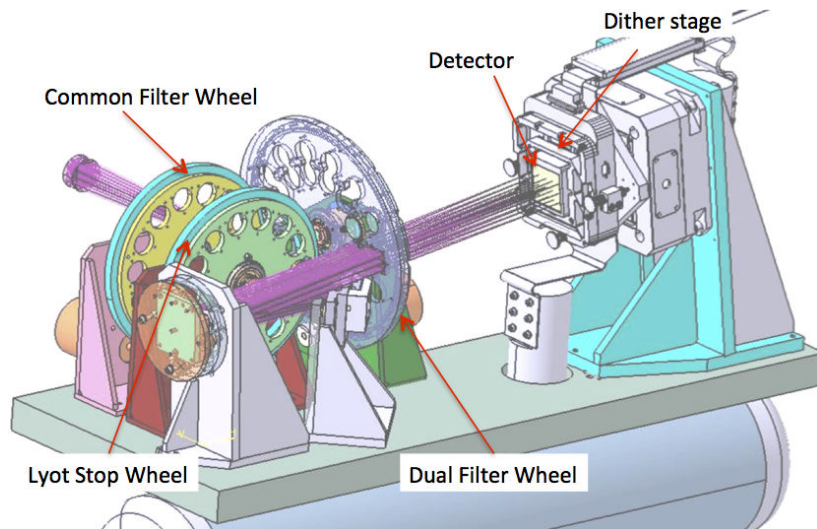


Figure 1.10 Inside view of IRDIS instrument (courtesy of ESO). The common path beam enters the common filter wheel and Lyot stop wheel, then it splits into two beams and passes through dual filter wheel and at the end lands on the detector.

source: <https://www.eso.org/sci/facilities/paranal/instruments/sphere/inst.html>

1.7.3 Telescopes comparison

Table 1.2 compares the capabilities of four telescopes (instruments): in space we already have HST and in future there will be James Webb Space Telescope (JWST). The resolution of these telescopes is limited by their diameters and the wavelength. There are also larger ground telescopes like the VLT (8.2m), with a resolution depending not only by the diameter and wavelength but also by the AO system. The better the AO system, the closer we get to the diffraction limited resolution (λ/D). SPHERE has already the best AO system at the VLT which can reach to the diffraction limited resolution specially in longer wavelengths. European Extremely Large Telescope (E-ELT) is a future ground instrument which can reach to the best resolution among the mention telescopes. Multi-AO Imaging Camera for Deep Observations (MICADO) is one of the first-light instruments for the E-ELT. Table 1.3 compares the VLT/SPHERE's different imaging modes with E-ELT/MICADO ⁹

⁹<https://www.eso.org/public/teles-instr/e-elt/e-elt-instr/micado/>

Table 1.2 Comparison different telescopes resolving powers

Telescope	Type	Diameter [m]	λ_{cen} [μm]	optimum resolution [mas]	Pixel scale [mas/pix]
HST/WFPC2,WFC3	space	2.4	0.3 - 1.6	30 - 160	40-90
JWST/NIRCam	space	6.5	0.6 - 5.0	22 - 145	23-65
VLT/SPHERE/IRDIS	ground	8.2	1.0 - 2.3	25 - 50	12.25
E-ELT/MICADO	ground	39	0.8 - 2.4	6 - 12	2-3

Table 1.3 SPHERE imaging modes compared to E-ELT/MICADO

Main Characteristics	IRDIS	ZIMPOL	MICADO
wavelength range[um]	0.9-2.3	0.6-0.9	(0.6)-0.8-2.5
FoV [arcs]	13.5x13.5	3x3	53 x 53
Pixel scale [mas]	12.25	7.5	2-3
FWHM [mas]	31(J),55(K)	15(V)	6(J), 10(K)
observing modes	On axis guide star - Dual-band Imaging - Dual-Polarimetric Imaging - Long-slit Spectroscopy	- Differetial Imaging - Polarimetric Imaging	Off axis AO loop

instrument, as an example.

1.8 This thesis

The aim of this thesis is to understand the different aspects of the dynamical and stellar evolution of very massive clusters. These newly formed massive clusters are the most important link between the formation of the massive star clusters and their evolution. The YMCs fill the gap between two

main types of the stellar clusters (globular and open) in terms of mass and density [Portegies Zwart et al. (2010)]. By accepting the clustered formation of the stars, one should consider a possibility that YMCs are the progenitors of the globular clusters.

We chose two YMCs, located in the most massive Galactic/extra-Galactic HII regions NGC3603 and R136 which hosts the most massive stars in the local universe. The works on this thesis have two different eras, before and after SPHERE!

In the first era, we started to study these clusters using HST data with improved atmosphere models. To know more on the dynamics of such compact clusters with many massive stars, we used N-body simulations with different initial conditions.

In the second era, the same clusters were analyzed, this time with SPHERE data, taken by the largest available telescope at ESO Paranal using the most efficient AO instrument. These challenging observations showed the capabilities of SPHERE for imaging distant clusters. Moreover, its higher angular resolution and high dynamic imaging capabilities, open discovery windows to resolve objects which have remained unresolved to date by any other instrument.

In Chapter 2 we present the results on the HST analysis on both clusters. We used WFPC2-PC data for R136 and ACS/HRC data on NGC3603 in addition to WFPC2. We created the isochrones using Geneva evolutionary models and TLUSTY atmosphere models (for O and B type stars) and KURUCZ (for other spectral types). After correcting the extinction in each HST data independently, we estimated the stellar masses and MF for each cluster in different filters, locally.

For R136, we used the NBODY6 code to initiate a new method to study R136-like clusters. Chapter 3 shows the results of these simulations. The effect of stellar evolution, initial binaries and mass segregation on the evolution of the cluster till 4 Myr are discussed in this chapter. The new method, compares the direct results of the simulations with observational data (HST/WFPC2/F814W). We used stellar atmosphere models to estimate the flux of each star and create a synthetic scene that we compare to HST data. Four different method are used to find the

closest synthetic image to HST data on R136.

Chapter 4 shows the results of SPHERE data on NGC3603 cluster. The IRDIS data covers three fields of the core of NGC3603. After correcting the extinction in IRDIS J and K band data for 31 spectroscopically known O stars, we estimated the stellar masses in the range $0.6 - 120M_{\odot}$. We detected 286 and 406 stars in K and J band, respectively, in the very core of the cluster (F0). In the next radial bin (F1 and F2) we detected 1003 and 561 stars in K and J band respectively. This study shows no signature of mass segregation in the core of NGC3603 for two main reasons: First, MF slope in the very core (F0) is not flatter than the next radial bin (F1 and F2). Second, both slopes are similar to the MF values found in the previous works for the outer regions.

Using the same method to analyze NGC3603, the results on the HST (Chapter 2) and SPHERE (Chapter 4) data are different. This leads to understand the effect of observational confusion on the astrophysical analysis. In Chapter 3 we precisely added this confusion on the Nbody simulations of R136.

In Chapter 5 we discuss the results of SPHERE data on the core of R136. The SPHERE/IRDIS data covers $10.9'' \times 12.3''$ of the core of R136 in J and K band. Using Starfinder, we detected 1110 and 1059 sources in J and K band data and 818 common sources between two bands. More than 70% of the detected sources have companions closer than $0.2''$ in both J and K band data. The majority (above 90%) of massive stars (brighter than 17 mag in K and 16 mag in J) have visual companions closer than $0.2''$. Among them, R136a1 and R136c have visual companions which are detected for the first time. R136a3 was resolved as two stars (PSF fitting) separated by $0.06''$ which is larger than the FWHM of the PSF. Thanks to SPHERE high resolution data, we detected many stars in the compact crowded core of this unique cluster. To correct the extinction we used 55 spectroscopically known bright stars in the core of R136 from [Crowther et al. (2016)]. Knowing the T_{eff} and $\log g$ of these sources, we could estimate the extinction in J and K using the grid of evolutionary models at different ages. The age of $1.8_{-0.8}^{+1.2}$ Myr is the most probable age for these

sample of stars. The extinction in J and K are $A_J = 1.3 \pm 0.5$ and $A_K = 0.4 \pm 0.5$ respectively. Considering the spectroscopic and photometric errors on the extinction and the age of the cluster members, we estimate a mass range for each detected stellar source. The generalized histogram of stellar masses (MF) was plotted at different ages with a given error on each stellar mass.

In the last Chapter, the summary of the results will be explained for both NGC3603 and R136. I will compare the results of the HST analysis in visible (Chapter 2) with SPHERE in near-IR (Chapter 4 and 5). The results of the Nbody6 simulations on R136-like clusters will be summarized regarding to the HST data. At the end I will explain the future projects and prospects.



Top: Vincent Willem van Gogh's *Starry Night*, without adaptive optics!

Bottom: With adaptive optics (*ref: <http://thescinder.com/tag/atmospheric-turbulence>*)

Chapter 2

HST Photometry (R136, NGC3603)

Abstract In this chapter, we present a new analysis of archival HST WFPC2 and ACS images of two young massive star clusters, R136 and NGC 3603. Combining HST multi-color photometry with new bolometric correction tables set in the native HST photometric system, model stellar spectra and Geneva evolutionary models assuming cluster ages between 1Myr and 2Myr, we derived stellar masses and constructed mass functions (MF) of the two clusters. We found consistent MF derived in the different colors, supporting that the constant extinction correction over the cluster fields is a reasonable approximation. The derived MF of the two clusters is top-heavy compared to the standard Salpeter law, with a slope that is steeper in outer annuli than in the cluster cores. Mass segregation is well supported in NGC 3603, but uncertainties remain in the case of R136 because of the limited resolution and interstellar extinction. The difference between the two clusters then suggest that NGC 3603 had a single formation burst 1Myr ago, while R136 underwent sequential star formation from 1 to 2Myr ago.

2.1 Introduction

Massive stars shape their environment at the various stages of their evolution, from their formation in dense clusters to their demise as core-collapse supernovae. Locally two young massive clusters, NGC 3603 in the Carina spiral arm of the Milky Way and R136 in the heart of the 30 Doradus star forming region in the LMC, are remarkable concentrations of massive stars that can guide us for understanding the formation of massive stars and their influence on their environment.

R136 is a very massive ($10^5 M_{\odot}$) young star cluster (less than 2 Myr in the core, [de Koter et al. (1998), Massey & Hunter (1998), Crowther et al. (2010)]) containing a large number of massive stars that have been formed in a relatively small space [Hunter et al. (1995)]. The total number of O3 stars (at least 41) in this one cluster exceeds the total number known elsewhere in the Milky Way or Magellanic Clouds [Massey & Hunter (1998)]. The WN stars in R136 have individual luminosities that are a factor of 10 higher than normal for WN stars of similar types, showing that they are actually very massive hydrogen-core burning stars whose spectrum mimic Wolf-Rayet (WR) stars because of their thick stellar wind. Their spectrum closely resembles these of WN stars in the Galactic cluster NGC 3603 [Massey & Hunter (1998)].

Among the Galactic spiral arm clusters, the NGC 3603 young cluster, located in its namesake giant H II region NGC 3603 [Kennicutt (1984)], is the most compact and youngest cluster with an age of about 1 Myr [Kudryavtseva et al. (2012), Stolte et al. (2004), Sung & Bessell (2004), Brandl et al. (1999)] and a central density of $6 \times 10^4 M_{\odot} pc^3$ [Harayama et al. (2008)]. The cluster contains three WR stars and up to 50 O-type stars [Drissen et al. (1995)]. Its total mass is estimated to be $10^4 M_{\odot}$ [Harayama et al. (2008)] with an upper dynamical mass limit of $17600 \pm 3800 M_{\odot}$ [Rochau et al. (2010)]. The WR stars show characteristics of WN6 stars, but also have Balmer absorption lines [Drissen et al. (1995)], indicating that these stars are actually hydrogen-core burning rather than stars that have evolved off the main sequence [Conti et al. (1995), de Koter et al. (1997)].

Both clusters provide a rare opportunity to study the formation and early stages of evolution of

massive stars and star clusters as they are very massive, young and close to be spatially resolved.

These clusters are the relevant objects for studying the formation and evolution of massive stars and star clusters, and for addressing questions such as the determination of the top end of the initial mass function and to establish whether or not the massive stars tend to be formed in the core of the cluster and show mass segregation.

The initial step is therefore the accurate determination of stellar masses. Except the case of eclipsing binary systems, this determination relies on spectroscopic and evolutionary models to tie the mass to the stellar luminosity. For this latter quantity, a correction to interstellar extinction plays a crucial role.

This work is based on HST WFPC2 and HRC/ACS multi-color photometry described in Section 4.2, and our methodology is discussed in Section 2.3. Correction to interstellar extinction is presented in Section 2.4 Our results on the mass functions of the two clusters are discussed in Section 2.5, and are compared to earlier results in Section 2.6. Our main results are summarized in Section 2.7.

2.2 Data and photometry

Deep imaging data of R 136 and NGC 3603 obtained by the NASA/ESA Hubble Space Telescope have been extracted from the STScI MAST archive, focusing on data with the highest resolution and longest exposure times.

HST/WFPC2 observations of R 136 were carried out on 1994-09-25 (PI: Westphal), from which we use a combination of shallow, intermediate and long exposures ranging from 3–5 s to 80–120 s with the planetary camera (PC) and the F555W and F814W filters. We use also similar HST/WFPC2 PC data of NGC 3603 obtained on 1997-07-30 (PI: Drissen), with shallow, intermediate and long exposures ranging from 0.4–1 s to 20–30 s, but with the F547M, F675W and F814W

filters. Details of the exposures are given in Table 2.1. HST observations of NGC 3603 with the High Resolution Channel (HRC) of the Advanced Camera for Surveys (ACS) have also been conducted on 2005-12-29 (PI: Maiz Apellaniz). Details of the exposure times and filters are given in Table 2.2. After applying a mask for the border noise, the FoV of the WFPC2/PC images is about $32.5'' \times 32.5''$ and about $24.8'' \times 25.7''$ for the NGC 3603 ACS/HRC images.

We performed Point Spread Function (PSF) photometry for the detection of stellar objects and the derivation of instrumental magnitudes using the STARFINDER package implemented in IDL [Diolaiti et al. (2000)]. We assumed precomputed PSFs based on analytical models with a detector-dependent FWHM instead of choosing empirical PSFs extracted from sources in the image itself that is more suitable for AO-assisted imaging. We adopted threshold values in such a way that the second peak of the Airy pattern of the very bright stellar sources is not detected. In the R 136 data, we found respectively 2509 and 2660 sources in the F555W and F814W images. In the NGC 3603 WFPC2 images, we found 1333, 2063 and 1493 sources in the F547M, F675W and F814W images, respectively, while we detected 282, 376 and 562 sources in the ACS/HRC F550M, F658N and F850LP images.

2.3 Method

We aim at deriving stellar masses by combining the HST photometry with stellar evolution and stellar atmosphere models. We use photometric data in each filter for independent estimates of the stellar mass. The basic output of stellar structure models the luminosity L and the effective temperature T_{eff} must be first converted into observable photometric quantities, i.e. magnitudes and colors. This conversion is performed by means of bolometric corrections BC and T_{eff} -color relations, and later by considering the proper distance, absorption and reddening of the observed population, and the photometric errors [Girardi et al. (2002)].

Table 2.1 Exposure log of HST/WFPC2 observations

Shallow ¹ / N ²	Middle ¹ / N ²	Deep ¹ / N ²	Filter	Pixel Scale [arcsec/pix]	Spatial Resolution [arcsec]	Observation Date
R 136						
3.0 / 1	23.0 / 16	120.0 / 7	F555W	0.050	0.110	1994-09-25
5.0 / 1	40.0 / 16	80.0 / 7	F814W	0.050	0.121	1994-09-25
NGC 3603						
1.0 / 3	10.0 / 12	30.0 / 8	F547M	0.050	0.110	1997-07-30
0.4 / 15	...	20.0 / 8	F675W	0.050	0.115	1997-07-30
0.4 / 3	5.0 / 12	20.0 / 8	F814W	0.050	0.121	1997-07-31

¹ Exposure time of each frame in seconds² Number of frames**Table 2.2** Exposure log of HST/ACS observations of NGC 3603

Exp. Time[s]	Frames	Detector	Filter	Pixel Scale	Spatial Resolution	Observation Date
44.0	4	HRC	F250W	0.025	0.049	2005-12-29
10.0	4	HRC	F330W	0.025	0.052	2005-12-29
2.0	4	HRC	F435W	0.025	0.057	2005-12-29
2.0	4	HRC	F550M	0.025	0.065	2005-12-29
10.0	4	HRC	F658N	0.025	0.071	2005-12-29
1.5	4	HRC	F850LP	0.025	0.088	2005-12-29

Our work proceeds in three steps. First, we have constructed *BC* tables for the HST filters listed in Tables 2.1 and 2.2. Second, we need to correct the observed photometric magnitudes for extinction. For each cluster, we have obtained an averaged extinction based on a sample of spectroscopically known O-type stars. Finally, for each filter, we combine the photometric data, the extinction correction, the proper *BC* table, and stellar evolution models to derive the stellar masses.

2.3.1 Bolometric Corrections for HST filters

We start from extended libraries of stellar model spectra F_λ , as calculated from stellar model atmospheres for a grid of effective temperatures T_{eff} , surface gravities $\log g$, and metallicities $[M/H]$. We aim at deriving absolute magnitudes M_{S_λ} for each star of known stellar parameters (T_{eff} , $\log g$, $[M/H]$) and hence known F_λ for the model library. These magnitudes M_{S_λ} can be obtained by means of Eq. 2.1:

$$M_{S_\lambda} = M_{bol} - BC_{S_\lambda} \quad (2.1)$$

Eq. 2.2 (taken from Eq. 7 in Girardi et al. 2002) is used to calculate BC_{S_λ} :

$$BC_{S_\lambda} = M_{bol\odot} - 2.5 \log[4\pi(10\text{pc})^2 \sigma T_{\text{eff}}^4 / L_\odot] + 2.5 \log\left(\frac{\int_{\lambda_1}^{\lambda_2} \lambda F_\lambda S_\lambda d\lambda}{\int_{\lambda_1}^{\lambda_2} f_\lambda^0 S_\lambda d\lambda}\right) - m_{S_\lambda}^0 \quad (2.2)$$

We adopt $M_{bol\odot} = 4.77$, and $L_\odot = 3.844 \times 10^{33} \text{ erg s}^{-1}$ [Bahcall et al. (1995)]. $f_{ST,\lambda}^0$ and $m_{ST,\lambda}^0$ are the zero-points in the HST STmag system and are defined as follows:

$$f_{ST,\lambda}^0 = 3.631 \times 10^{-9} \text{ erg s}^{-1} \text{ cm}^{-2} \text{ \AA}^{-1}$$

$$m_{ST,\lambda}^0 = 0 \text{ at all wavelengths.}$$

F_λ is the flux at the stellar surface (from the model atmosphere library) in a given passband with transmission curve S_λ in the interval $[\lambda_1, \lambda_2]$.

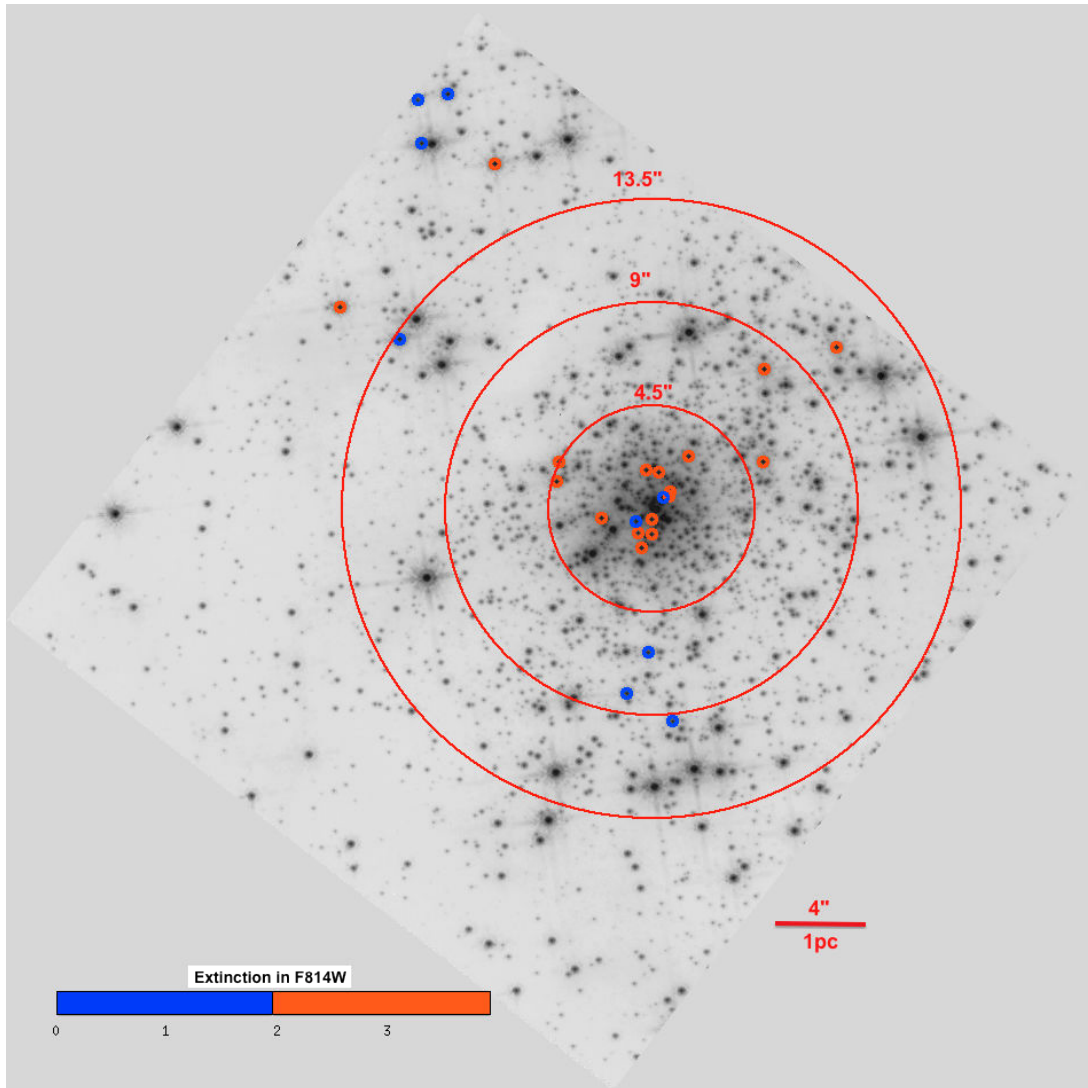


Figure 2.1 WFPC2/F814W image of R136 with the 26 selected O stars shown by circles. The color-bar represents the range of extinction values and the selected stars are marked with blue or red circles depending on the estimated extinction. We divided the cluster in three different concentric regions with annulus of $4''.5$ (corresponding to about 1 pc at a distance of 48.5 kpc).

We used TLUSTY¹ model atmospheres [Hubeny & Lanz (1995)], as comprehensive grids of non-LTE, metal line-blanketed, plane-parallel, hydrostatic model atmospheres cover the parameter space of O and B-type stars [Lanz & Hubeny (2003), Lanz & Hubeny (2007)]. Despite neglecting the stellar wind, these model atmospheres provide very good predictions of the continuum flux (especially in the visible and near-IR) as demonstrated by [Hillier & Lanz (2001)] for the case of the WC5 Wolf-Rayet star HD 165763. A fortiori, in most O and B stars, the continuum flux is formed in a quasi-static photosphere with limited extension and, hence, the TLUSTY model assumptions are not a limitation for our application. We note furthermore that there are no comparable grids of model atmospheres with winds. For cooler stars, we use Kurucz [Castelli et al. (1997)] LTE line-blanketed model atmospheres. We apply Eq. 2.2 to tabulate BC_{S_λ} for all spectra in our model spectral libraries, and for several different photometric filters in the HST system. For any intermediate (T_{eff} , $\log g$, [M/H]) values, BC_{S_λ} can then be derived by interpolations (we used cubic interpolations). In the following, these tables will be referred as the Atmosphere-BC tables.

2.3.2 Correcting the extinction

Knowledge of the intrinsic properties and colors is required in order to derive the extinction in each filter toward the star clusters. Only limited information is available for these two clusters, mostly about their hottest and brightest stars. We had then to start from the known spectral types of some O stars from which we could assign stellar parameters and intrinsic colors.

In R136, we selected 26 O-type stars classified by [Massey & Hunter (1998)]. The selected stars are shown in Fig. 2.1. We then adopted effective temperatures from the spectral type– T_{eff} relation in Table 1 of [Simon-Diaz et al. (2014)]. Surface gravities, $\log g$, (and hence luminosities) are assigned using isochrones (1.0, 1.5 and 2 Myr) in the Geneva stellar evolution models. Bolometric corrections are then interpolated from the Atmosphere-BC tables constructed from model atmo-

¹Model atmospheres and source codes are available at <http://nova.astro.umd.edu>

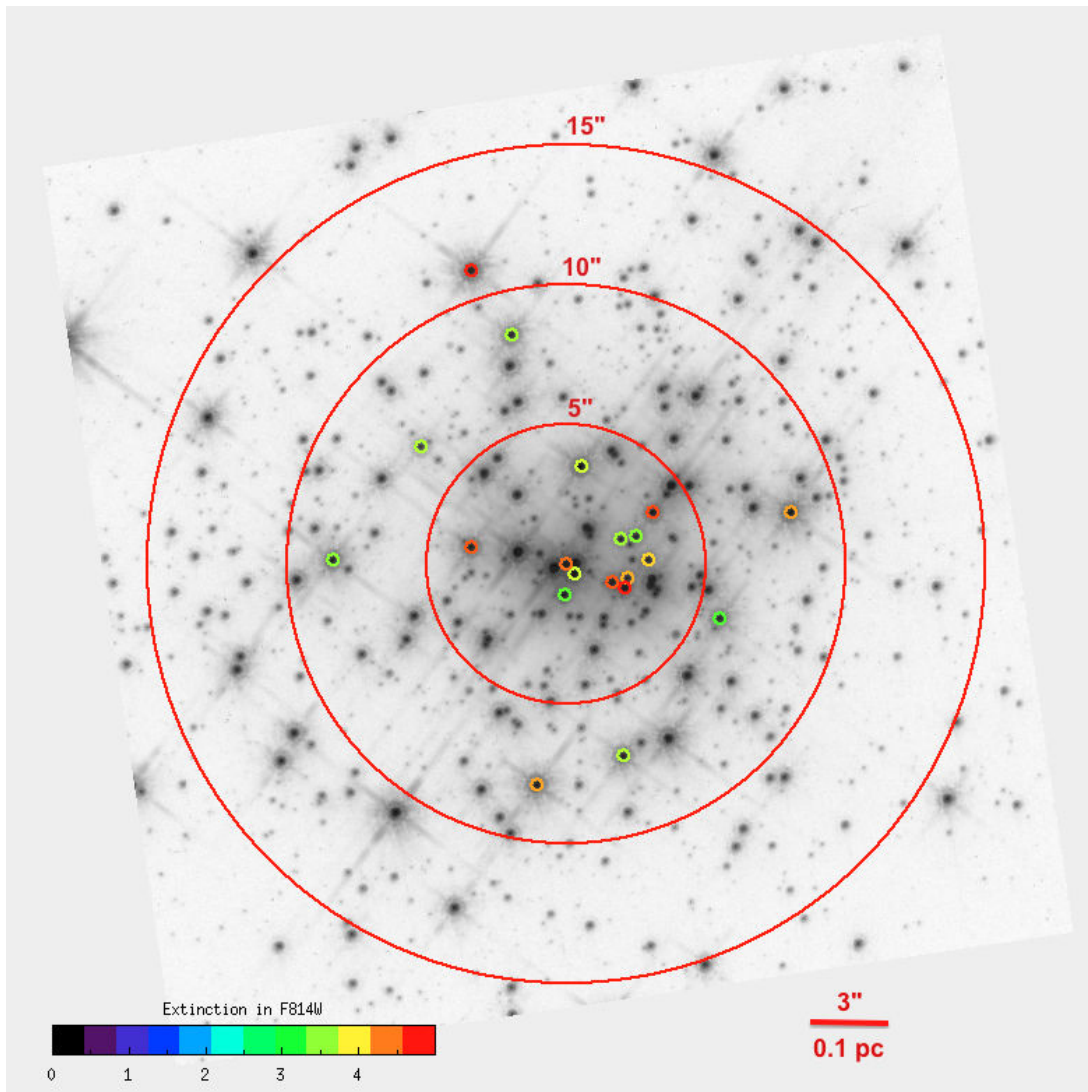


Figure 2.2 WFPC2/F814W image of NGC 3603 with the 21 selected O stars. Three concentric regions are also shown (at 5", 10" and 15"). At the cluster distance, 5" corresponds to about 0.17 pc.

spheres with a half-solar metallicity appropriate for LMC stars. Intrinsic magnitudes, and then the extinction, in the F814W and F555W filters follow from Eq. 2.1 and the measured magnitudes.

For NGC 3603, we proceeded in a similar way selecting 21 O-type stars (15 class V stars and 7 class III stars) from [Melena et al. (2008)], as shown in Fig. 2.2. The stellar parameters of these stars are derived from Table 4 or Table 5 of [Martins et al. (2005)] depending on their luminosity class. We obtained the extinction and color excesses for the three WFPC2 filters and the seven ACS/HRC filters, similarly to R136 but for using the Atmosphere-BC tables calculated for model atmospheres with solar metallicity and the 1 Myr isochrone. The results are discussed in Section 2.4.

2.3.3 Estimating stellar masses

We finally built sets of evolutionary tables that are a combination of stellar evolution models and Atmosphere-BC tables. Hereafter, we call these sets of tables Evolutionary-BC tables. These tables gives the mass of stars and their T_{eff} , $\log g$ and $\log L$ according to their BC calculated in different HST WFPC2 and ACS/HRC filters. It is the reverse relation built on the common entries, metallicity, T_{eff} and $\log g$, between the Atmosphere-BC tables and the stellar evolution models.

To create the Evolutionary-BC tables, we used the Geneva stellar evolution models² [Lejeune & Schaerer (2001)], and in particular the 1.0, 1.5 and 2 Myr isochrones at half-solar metallicity for R136 and the 1 Myr isochrone at solar metallicity for NGC 3603. To derive luminosities, we assumed that stars were on the main sequence given the young age of the two clusters and we adopted the following distances to the clusters: 48.5 kpc for R136 [Selman et al.1999, Gieren et al. (1998)] and 7 kpc for NGC 3603 [Moffat (1983), Sagar et al. (2001), Sung & Bessell (2004), van den Bergh (1978), De Pree et al. (1999)].

²<http://webast.ast.obs-mip.fr/equipe/stellar/>

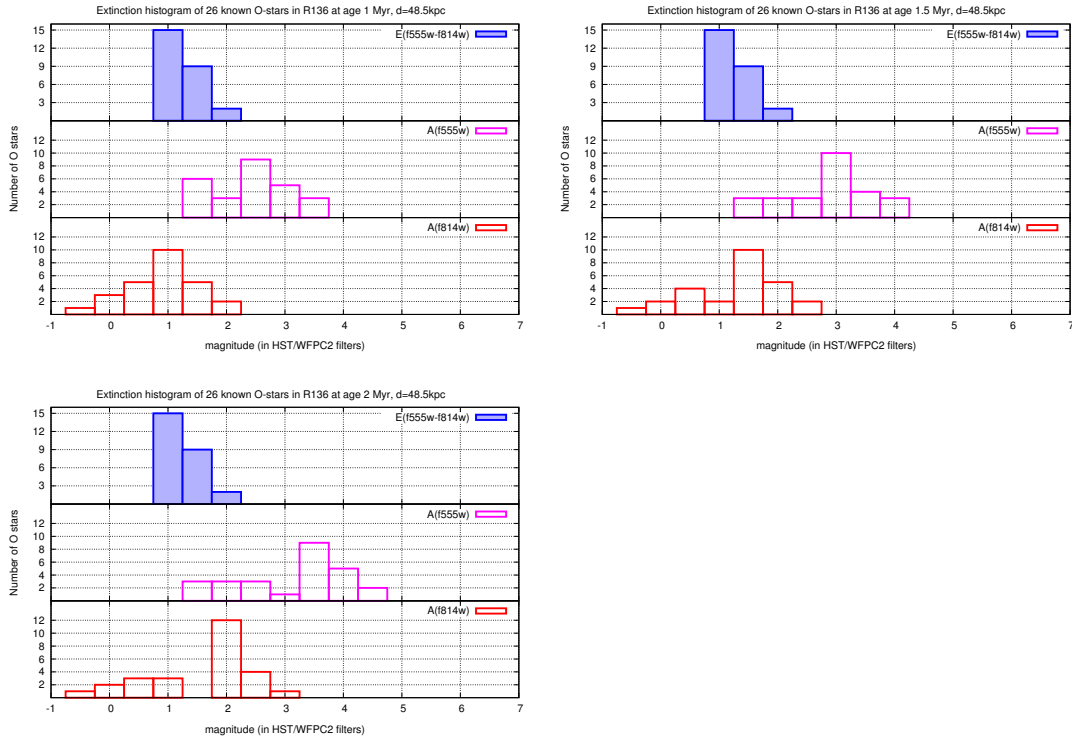


Figure 2.3 Histogram of extinction of 26 O-type stars with known spectral types in R136 in two HST/WFPC2 filters (F555W and F814W) using three different isochrones: 1 Myr (top), 1.5 Myr (middle) and 2 Myr (bottom). Red and pink histograms represents extinction in the F814W and F555W filters and the filled blue histogram shown to the color excess distribution.

2.4 Extinction and CMDs of the two clusters

Figure 2.3 shows the histogram of the extinction of the 26 O-type stars in R136 in two filters (F814W and F555W) as well as the (F555W-F814W) color excess, obtained using in turn the 1.0, 1.5 and 2.0 Myr isochrones (from top to bottom). The distribution of extinction values become bimodal when using the 2 Myr isochrone with O3 stars showing the larger extinction and the later O stars being distributed in the first peak. The reason of this behavior remains unclear.

The histogram of the extinction toward the 21 O stars in NGC 3603 is similarly displayed in

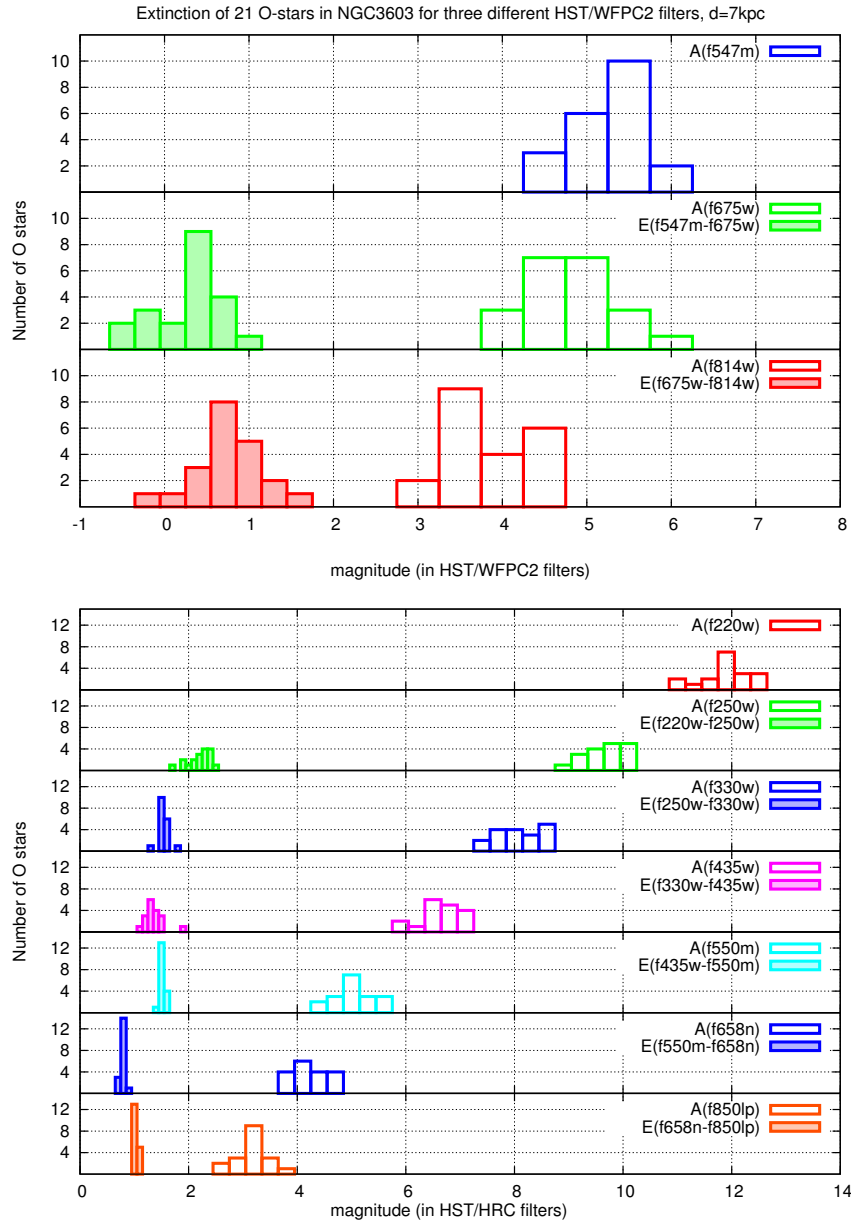


Figure 2.4 Top: Extinction toward 21 O-stars in NGC 3603 in three different HST/WFPC2 filters. Bottom: Same in seven different HST/HRC filters.

Table 2.3 Maximum-weighted values of Extinction and color excess of R136 in different HST/WFPC2 filters at the ages of 1, 1.5 and 2 Myr and distance of 48.5 kp, using models with standard (c008) and high (e008) mass-loss rates.

Models	c008			e008		
	1 Myr	1.5 Myr	2 Myr	1 Myr	1.5 Myr	2 Myr
A(F555W)	2.56	3.03	3.63	2.56	3.63	4.47
A(F814W)	1.00	1.59	2.12	1.38	2.10	3.06
E(F555W-F814W)	1.19	1.19	1.19	1.19	1.19	1.19

Fig. 2.4 that shows extinction in the three WFPC2 filters (upper panel) and in seven ACS/HRC filters (lower panel). The filled histograms pertain to the labeled color excesses. The uncertainty on the cluster distance cancels out when examining color excesses. We point at the general trend of increased extinction at shorter wavelengths that can be seen clearly for NGC 3603 in both the WFPC2 and HRC filter sets. Both, in the WFPC2 data and in the HRC data, the RI color excess ($E(F675W-F814W)$) is larger than the VR color excess ($E(F547M-F675W)$). The calculated extinction and color excess are derived independently with the two instruments. The same general trend therefore provides confidence with the adopted methodology.

We examine the spatial distribution of the extinction over the cluster fields. As no trend seems obvious, we decided to apply the same extinction correction to all the cluster stars adopting the median value for O stars derived in each filter for each cluster. For R136, we have thus determined a VI color excess, $E(F555W - F814W) = 1.19$. The extinctions and color excesses adopted for NGC 3603 are listed in Table 2.4. In this Table, the Galactic extinction law values by Rieke & Lebofsky (1985) are shown in the fourth column (R&L) to be compared with the extinction values we estimated for different HST filters shown in third column. For the ACS/HRC data, the extinction law is consistent with the Galactic extinction law. Note that the HST filter transparency is different from the filters which Rieke & Lebofsky (1985) estimated the extinction law, especially

Table 2.4 Median values of Extinction and color excess of NGC3603 in different HST filters at the age of 1 Myr and distance of 7 Kpc. The Galactic extinction law values by Rieke & Lebofsky (1985) are shown in the fourth column (R&L) to be compared with the extinction values we estimated for different HST filters shown in third column.

λ	A_λ	A_λ/A_{F547M}	R&L		
WFPC2/F547M	5.46	1.0	1.0	E(F547M-F675W):	0.54
WFPC2/F675W	5.05	0.92	0.75	E(F675W-F814W):	0.93
WFPC2/F814W	4.16	0.76	0.48		
λ	A_λ	A_λ/A_{F550M}	R&L		
ACS/HRC/F220W	12.09	2.19	-	E(F220W-F250W):	2.33
ACS/HRC/F250W	9.83	1.78	-	E(F250W-F330W):	1.55
ACS/HRC/F330W	8.24	1.49	1.53	E(F330W-F435W):	1.39
ACS/HRC/F435W	6.80	1.23	1.32	E(F435W-F550M):	1.58
ACS/HRC/F550M	5.23	1.0	1.0	E(F550M-F658N):	0.85
ACS/HRC/F658N	4.37	0.79	0.75	E(F658N-F850LP):	1.08
ACS/HRC/F850LP	3.30	0.59	0.48		

for WFPC2 broad-band filters. A_{F547M} is narrower than standard V-filter used to extract extinction law, this can explain the larger A_λ/A_{F547M} values compared to Rieke & Lebofsky (1985).

The R136 CMD is constructed from the F555W and F814W magnitudes. We identified 1674 stars in common between the WFPC2 frames obtained with these two filters. The selection threshold was set as to avoid assigning the Airy pattern second peak of very bright stars as (spurious) single stars. We found 420 common stars in the core ($r < 4''.5$) region, 558 stars in the first annulus region ($4''.5 < r < 9''$) and 696 stars in the outer annulus ($4''.5 < r < 9''$) – see Fig. 2.1. The CMDs are displayed in Fig. 2.5 for the whole cluster and the three different sub-fields. The solid lines are the Geneva isochrones (using Evolutionary-BC tables) with LMC metallicity at age 1.0

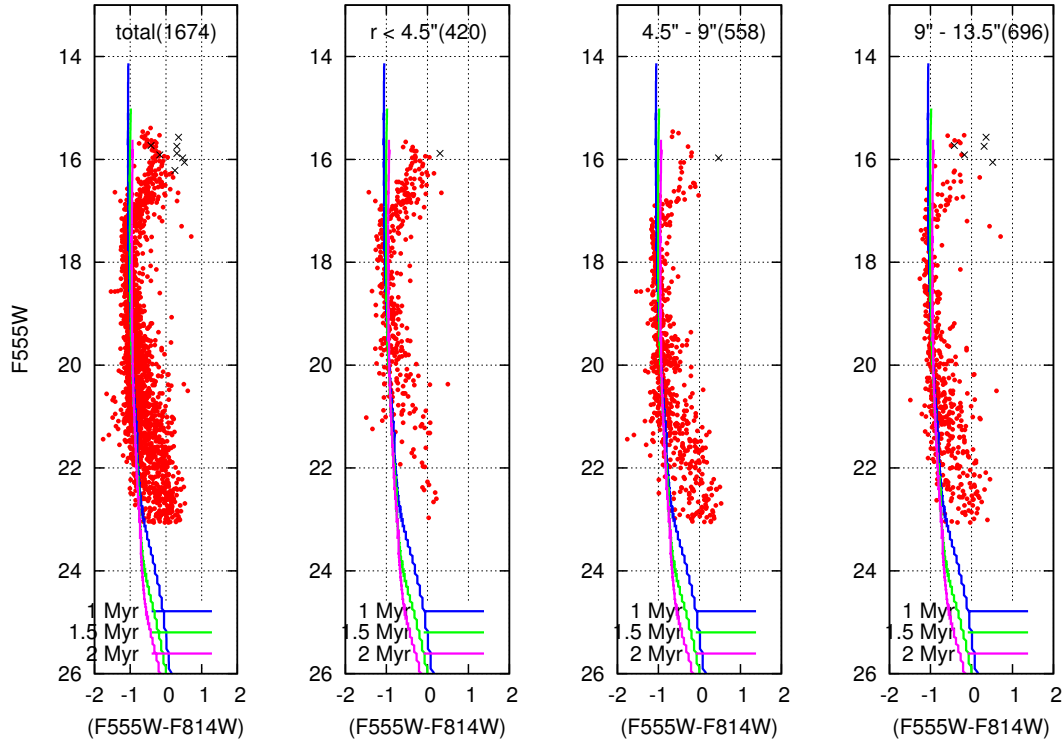


Figure 2.5 Color-Magnitude Diagrams of R136. Panels from left to right show the CMD for the whole cluster, and in the three regions (core and annuli shown in Fig. 2.1). The 10 Wolf-Rayet stars in the FoV are shown with black crosses. Solid lines are the 1.0, 1.5 and 2.0 Myr Geneva isochrones.

(blue), 1.5 (green) and 2 (pink) Myr, assuming a distance of 48.5 kpc, and corrected by the median extinction values and the adopted VI color excess. The brightest stars in the CMD favor a cluster age of about 2 Myr (a younger cluster might have even brighter stars). We point out to the top of R136 main sequence (MS). As expected the brightest O stars are leaving the MS, evolving to the red as expected from classical stellar evolution. However, the top of the MS turns back to the blue: this is a telltale sign of fast rotation leading to homogeneous evolution of the most massive stars [Meynet & Maeder (2000), Kohler et al. (2015)].

For NGC 3603, we built separate CMDs from WFPC2 and ACS/HRC data. We identified 609

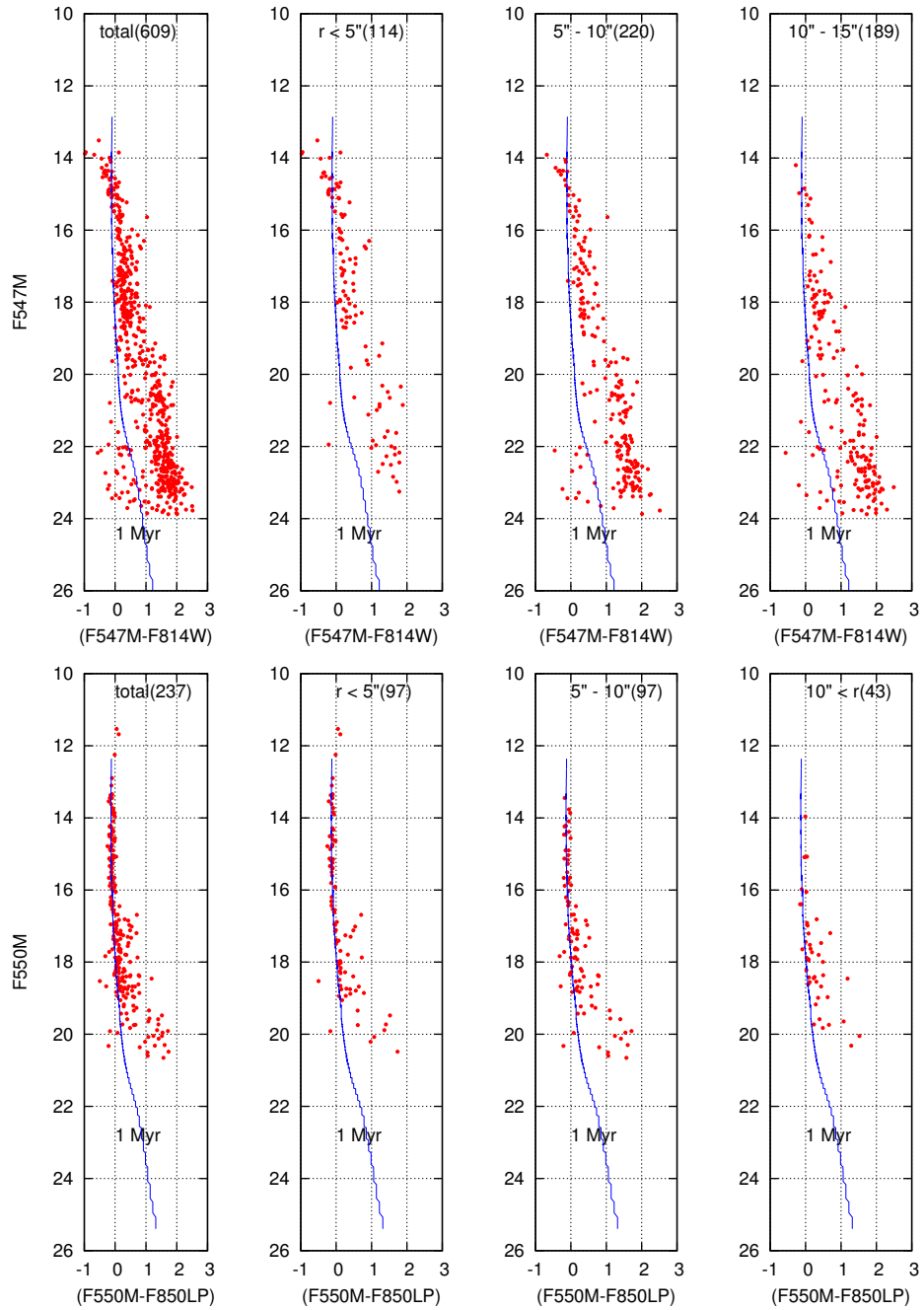


Figure 2.6 Color-Magnitude Diagrams of the core of NGC 3603 from WFPC2 (top) and HRC (bottom) data. Panels from left to right show the CMD for the whole cluster, and in the three regions (core and annuli shown in Fig. 2.2). The solid line is the 1.0 Myr Geneva isochrone.

common stars in WFPC2/F547M and WFPC2/F814W frames. Among them, 192 stars are in the cluster core region ($r < 5''$), 156 stars in the annulus ($5'' < r < 10''$) and 139 stars in the outer region ($10'' < r < 15''$). The CMDs are displayed in upper panel of Fig. 2.6. The solid blue line shows the 1 Myr Geneva isochrone (using Evolutionary-BC tables) with solar metallicity assuming a cluster distance of 7 kpc, and the median values of extinction and color excess as before. In the HRC data, we found 237 common stars in the HRC/F550M and HRC/F850LP frames (121, 69 and 47 common stars in three different regions). The CMDs are shown in the lower panel of Fig. 2.6. The top part of the CMD does not reveal any star that is evolving off the MS, suggesting a very young age for NGC 3603 and, therefore, we have adopted an age of 1 Myr.

2.5 Mass Functions

Following Sect. 2.3.3, we derived the stellar masses from photometric data of R136 in two filters (WFPC2/F555W and WFPC2/F814W) independently, combining them with stellar atmospheres and stellar evolution models. As explained above, we have used in turn the 1.0, 1.5 and 2 Myr isochrones to estimate the stellar masses. The mass functions (MF) is displayed in Fig. 2.7 (at 1 Myr), Fig. 2.8 (at 1.5 Myr) and Fig. 2.9 (at 2 Myr) in the whole cluster (red dots and lines) and in three pre-defined regions (core and annuli - blue dots and lines). In both photometric colors, the MF turns down indicating that our photometry is incomplete at the lowest mass end ($\log(\frac{M}{M_{\odot}}) < 0.8$). The MF is commonly modeled by a log-log relation:

$$\log(N) = \Gamma \log\left(\frac{M}{M_{\odot}}\right) + b \quad (2.3)$$

For NGC3603, WFPC2 data we considered all mass bins for deriving the slopes while for the ACS/HRC data we excluded the first mass bin to calculate the MF slopes. For R136, in outer regions, we excluded the first mass bin and in the core, 2 (at 1, 1.5 Myr) and 3 (at 2 Myr) mass bins are excluded.

Table 2.5 Slopes of the mass function of the R136 cluster.

WFPC2	F555W	F814W
1 Myr isochrone		
Whole cluster	-0.98 ± 0.19	-1.04 ± 0.12
$r < 4''.5$	-0.15 ± 0.20	-0.74 ± 0.23
$4''.5 < r < 9''$	-1.17 ± 0.19	-1.33 ± 0.15
$9'' < r < 13''.5$	-1.03 ± 0.12	-1.07 ± 0.07
1.5 Myr isochrone		
Whole cluster	-0.73 ± 0.14	-0.77 ± 0.07
$r < 4''.5$	-0.34 ± 0.28	-0.25 ± 0.16
$4''.5 < r < 9''$	-1.03 ± 0.20	-0.98 ± 0.12
$9'' < r < 13''.5$	-0.83 ± 0.09	-0.93 ± 0.10
2 Myr isochrone		
Whole cluster	-0.48 ± 0.11	-0.59 ± 0.08
$r < 4''.5$	-0.12 ± 0.18	-0.27 ± 0.09
$4''.5 < r < 9''$	-0.72 ± 0.17	-0.77 ± 0.13
$9'' < r < 13''.5$	-0.65 ± 0.11	-0.79 ± 0.10

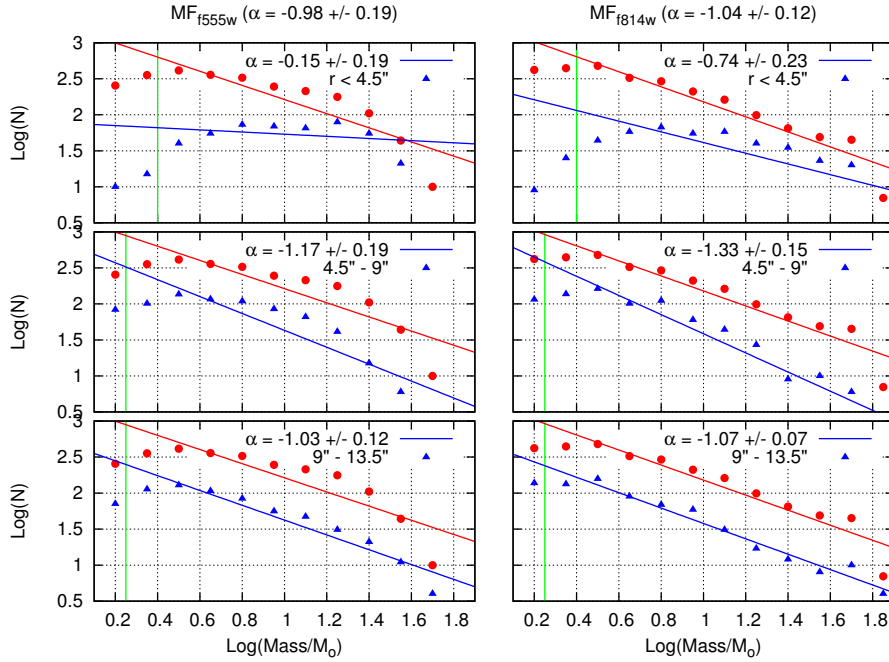


Figure 2.7 Mass function derived independently in two filters (F555W in the left and F814W in the right) assuming 1.0 Myr isochrone to derive stellar luminosities. The MF is plotted for the whole cluster (red dots) and in the three different regions (core and two annuli from top to bottom).

Table 2.5 gives the MF slopes Γ for the different spatial regions, filters and assumed isochrones. The MF slopes derived from F555W and F814W photometry are consistent, with the exception of the cluster core assuming the 1 Myr isochrone. The MF slope in the core of R136 is much flatter than in the two outer annuli, in both colors and for all the assumed isochrones. The steeper slope at 1 Myr for the F814W data thus appears as an outlier that might be ignored. The flatter slope in the core may either reveal the mass segregation of the cluster or may be explained by a confusion effect in a way that massive bright objects in the dense core mask fainter low-mass stars. Between the two outer regions, however, the MF slope does not decrease from the inner to the outer annulus. Hence, either the most massive stars are concentrated in the inner core, or the confusion effect is not as acute as in the core.

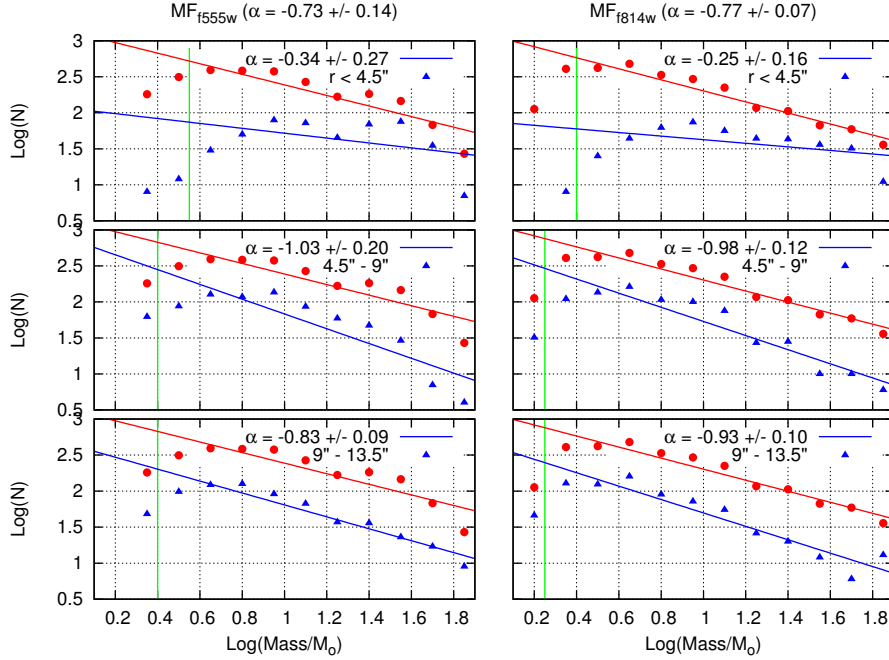


Figure 2.8 Mass function derived independently in two filters (F555W in the left and F814W in the right) assuming 1.5 Myr isochrone to derive stellar luminosities. The MF is plotted for the whole cluster (red dots) and in the three different regions (core and two annuli from top to bottom).

For NGC 3603, we calculated the stellar masses starting from six different photometric datasets, three WFPC2 images with F547M, F675W, and F814W filters and three ACS/HRC images (F550M, F658N, F850LP). The derived MFs are shown in Fig. 2.10. The upper panels relate to WFPC2 data and the lower panels to HRC data. As for R136, we show the MF for the whole cluster and for three spatial regions and we fitted log-log relations with derived slopes listed in Table 2.6. While the MF slopes derived from different sets of filters and detectors are mostly consistent, a close examination suggests that the MF slope derived from WFPC2 data is somewhat steeper than the MF slope from HRC data. We may identify two competing effects that are responsible of this difference: WFPC2 data reach deeper with more low-mass stars identified in the images; on the other hand, the higher resolution of HRC (25 mas/pix) allows to resolve better close stars than on

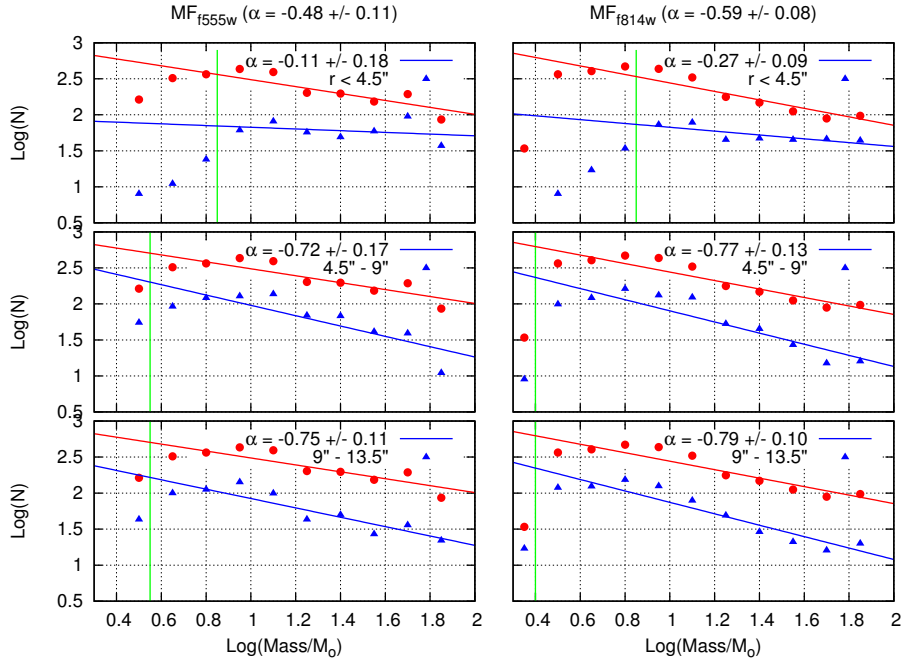


Figure 2.9 Mass function derived independently in two filters (F555W in the left and F814W in the right) assuming 2.0 Myr isochrone to derive stellar luminosities. The MF is plotted for the whole cluster (red dots) and in the three different regions (core and two annuli from top to bottom).

WFPC2 images (50 mas/pix). Despite these differences, we point out that the general trend of MF slopes is decreasing in both datasets revealing the fingerprints of mass segregation in NGC 3603. This is illustrated more particularly in Fig. 2.11 that shows the values of MF slopes for both HRC (blue) and WFPC2 (red) data. In the inner three regions (common in both detectors), slopes trend similarly. In the outer two regions, the MF slopes in WFPC2 are even steeper.

Finally, we check the sensitivity of our derived MF with the two classes of Geneva evolutionary models, with standard (c008 and c020 models) and with enhanced mass loss rates (e008 and e020 models) for massive stars. We do not find any substantial changes in our results as illustrated in Fig. 2.12 for R136. MF slopes derived from the two colors are closer for models with enhanced mass loss and larger ages (1.5 and 2 Myr). Similar comparison for NGC 3603 is shown in Fig. 2.13

Table 2.6 Slopes of the mass function of NGC 3603 cluster (1 Myr isochrone).

WFPC2	F547M	F675W	F814W
Whole cluster	-0.86 ± 0.12	-0.89 ± 0.14	-0.90 ± 0.15
$r < 5''$	-0.37 ± 0.09	-0.42 ± 0.12	-0.30 ± 0.14
$5'' < r < 10''$	-0.83 ± 0.16	-0.80 ± 0.12	-0.77 ± 0.10
$10'' < r < 15''$	-1.11 ± 0.17	-1.14 ± 0.14	-1.08 ± 0.14
ACS/HRC	F550M	F658N	F850LP
Whole cluster	-0.58 ± 0.08	-0.60 ± 0.07	-0.73 ± 0.04
$r < 5''$	-0.40 ± 0.08	-0.47 ± 0.08	-0.49 ± 0.04
$5'' < r < 10''$	-0.73 ± 0.17	-0.74 ± 0.13	-0.74 ± 0.07
$10'' < r < 15''$	-0.78 ± 0.20	-0.71 ± 0.15	-1.01 ± 0.14

with the same kind of agreement.

2.6 Comparison with earlier analyses

Table 4.3 summarizes the results from previous determinations of the mass functions of these two young massive star clusters.

The MF slope that we derived for R136 is generally flatter than earlier published values. There is marginal consistency with the MF slope in R136 core from [Malumuth & Heap (1994)] and our value in the red F814W filter and a 1 Myr isochrone. We note however that this steeper slope in the core was considered an outlier compared to the other flatter values derived in the core. In the outer annuli, [Selman et al. 1999] slope is consistent with our slopes derived in both colors and with the younger isochrones. We note in both cases that the MF slopes obtained using the 2 Myr isochrone – the age favored by the CMD, see Sect. 4 – are flatter than the earlier results. A direct comparison

Table 2.7 Mass function slopes for R136 and NGC 3603 from previous analyses.

R136		
MF slope	condition	Reference
-0.90	$r < 3''.3$	[Malumuth & Heap (1994)]
-1.89	$r > 3''.3$	[Malumuth & Heap (1994)]
$(-1.3) - (-1.4)$		[Massey & Hunter (1998)]
-1.17 ± 0.05	$4''.6 - 19''.2$	[Selman et al. 1999]
-1.37 ± 0.08	$15'' - 75''$	[Selman et al. 1999]
-1.59	$r < 1''.6$	[Brandl et al. (1996)]
-1.33	$1''.6 - 3''.2$	[Brandl et al. (1996)]
-1.63	$3''.2 < r$	[Brandl et al. (1996)]
NGC 3603		
MF slope	condition	Reference
-0.73	$(1 - 30) M_{\odot}$	[Eisenhauer et al. (1998)]
-0.9	$(2.5 - 100) M_{\odot}$	[Sung & Bessell (2004)]
-0.5 ± 0.1	$r < 6''$	[Sung & Bessell (2004)]
-0.8 ± 0.2	$6'' - 12''$	[Sung & Bessell (2004)]
-1.2 ± 0.2	$r > 12''$	[Sung & Bessell (2004)]
-0.91 ± 0.15	$(0.4 - 20) M_{\odot}$	[Stolte et al. (2006)]
-0.31	$0 - 5''$	[Harayama et al. (2008)]
-0.55	$5'' - 10''$	[Harayama et al. (2008)]
-0.72	$10'' - 13''$	[Harayama et al. (2008)]
-0.75	$13'' - 30''$	[Harayama et al. (2008)]
-0.26	$0 - 5''$	[Pang et al. (2013)]
-0.55	$5'' - 10''$	[Pang et al. (2013)]
-0.76	$10'' - 15''$	[Pang et al. (2013)]

to explain this difference is however hindered by two main issues. First, the resolution and depth of the images are different: [Malumuth & Heap (1994)] used early (1992) WFPC observations that were not corrected for the spherical aberration of HST primary mirror, while the other studies are based on early AO observations with ground-based 4m telescopes. Second, extinction correction is difficult and possibly variable across the cluster. Our consistent results from V and I photometry increases confidence in our approach to correct extinction, although there is no clear explanation to the bimodal distribution of extinction (at 2 Myr) that we found for the 26 O-type stars with known spectral types. In all cases, however, the results show a flatter MF in the cluster core and steeper in the outer regions. [Malumuth & Heap (1994)] interpreted this result as the first indication of mass segregation in young massive clusters. We have argued that confusion from limited resolution and extinction remains major issues. These issues may hopefully be in good part solved with upcoming VLT/SPHERE observations of R136 with HST-like resolution and lower extinction in the K band.

Deriving the median of the six values tabulated in Table 2.6 for NGC 3603, we obtain $\Gamma = -0.41 \pm 0.07$ in the core region ($r < 5''$), $\Gamma = -0.76 \pm 0.04$ in the inner annulus ($5'' < r < 10''$), and $\Gamma = -1.05 \pm 0.18$ in the outer annulus ($10'' < r < 15''$). These values agree with earlier studies [Sung & Bessell (2004), Harayama et al. (2008), Pang et al. (2013)] within error bars, though we obtained consistently slightly steeper MF slopes. [Sung & Bessell (2004)] and [Pang et al. (2013)] used the same WFPC2 data in their analyses, demonstrating the sensitivity of the results to the instrumental resolution as discussed above for R136.

2.7 Summary

We have analyzed archival HST images of two young massive clusters obtained with WFPC2 and ACS/HRC with broad filters covering the visual and red spectral regions. From native multi-color HST photometry, model stellar atmospheres and stellar evolution models, we have derived the

extinction, age, the mass function and its radial dependency of the two clusters. We apply the same methodology for the two clusters, to assess our method and to compare the two clusters.

Extinction was determined for a set of over 20 O stars in both clusters. In NGC 3603, we can examine the behavior of extinction with wavelength thanks to available images in 7 different HRC filters. The extinction decreases smoothly with increasing wavelength, from the UV (220 nm) to the red (814 nm), as expected. For R136, such wavelength coverage is not available. However, the extinction shows an unexpected bimodal distribution that cannot be assigned to a spatial variation of the extinction. VLT/SPHERE data in the near-IR will be most helpful to enlighten this issue. As there is no obvious distribution of extinction over the two clusters, we assigned a unique extinction value: the median extinction for each filter of the O star samples. Based in this extinction correction, we built CMDs for both clusters and fitted Geneva isochrones. The favored ages for NGC 3603 and R136 are 1 Myr and 2 Myr, respectively, in agreement with earlier studies [Pang et al. (2013), Crowther et al. (2010)].

In both clusters, we found a more top-heavy MF than the Salpeter standard MF in agreement with earlier studies (see Sect. 6). The combined analysis of WFPC2 and higher-resolution HRC/ACS data confirm the mass segregation in NGC 3603 found in previous studies based on the WFPC2 data alone [Sung & Bessell (2004), Pang et al. (2013)]: NGC 3603 cluster core contains all massive stars with the most top-heavy MF, while the MF is steeper in outer annuli. This agreement provides good support to our method combining multi-color photometric data to derive the MF. The results for R136 are also possibly suggestive of mass segregation, though the evidence is not as strong because of uncertainties due to lower resolution from the larger distance and due to extinction.

A comparison between the two clusters is not straightforward because the larger distance of R136 means that the selected spatial regions in R136 are actually 7 times larger than the NGC 3603 regions. The mass segregation evidenced in NGC 3603 would therefore fit within the central 2" core

of R136. Nevertheless, the fact that the younger (1 Myr) and less massive ($10^4 M_{\odot}$) cluster is segregated while the older (up to 2 Myr) and more massive ($10^5 M_{\odot}$) is possibly not segregated may seem surprising. A possible scenario would be that NGC 3603 was formed during a unique burst about 1 Myr ago, while R136 might have undergone sequential star formation up to 1 Myr ago when star formation was quenched by the most massive stars ($M > 80 M_{\odot}$). If star formation was propagating spatially in the R136 and 30 Dor region, then this might explain the lack of similar evidence of mass segregation in R136. Such sequential star formation was also suggested to have taken place in the SMC young cluster NGC 346, with the most massive star MPG 355 formed less than 1 Myr ago and the late O stars formed 4 to 7 Myr ago [Bouret et al. (2003), Bouret et al. (2013)].

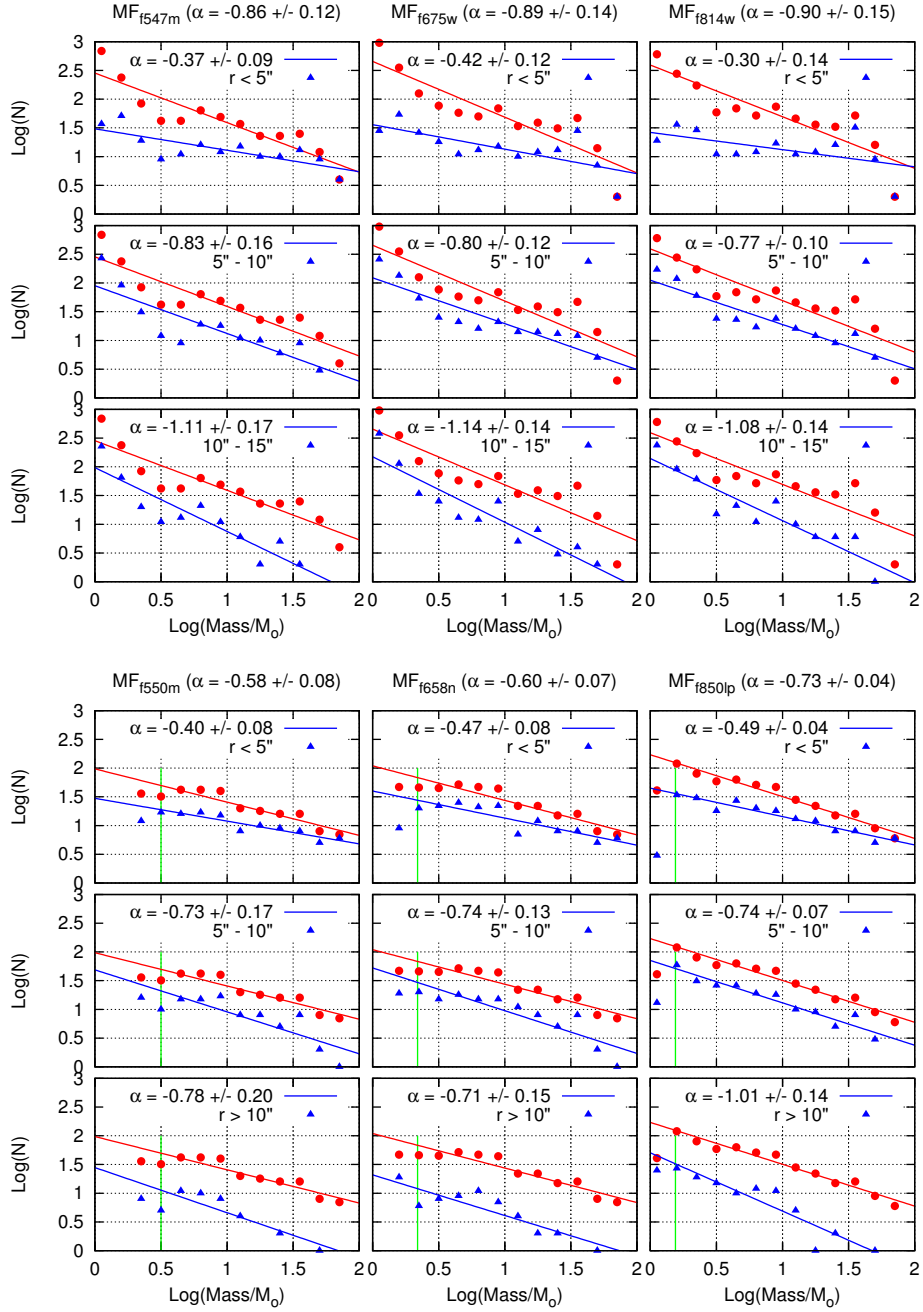


Figure 2.10 Mass function of NGC 3603 derived for the whole cluster (red dots) and in three different regions (from top to bottom). Top: Data from three WFPC2 filters (F547M, F675W, F814W). Bottom: Data from three ACS/HRC filters (F550M, F658N, F850LP)

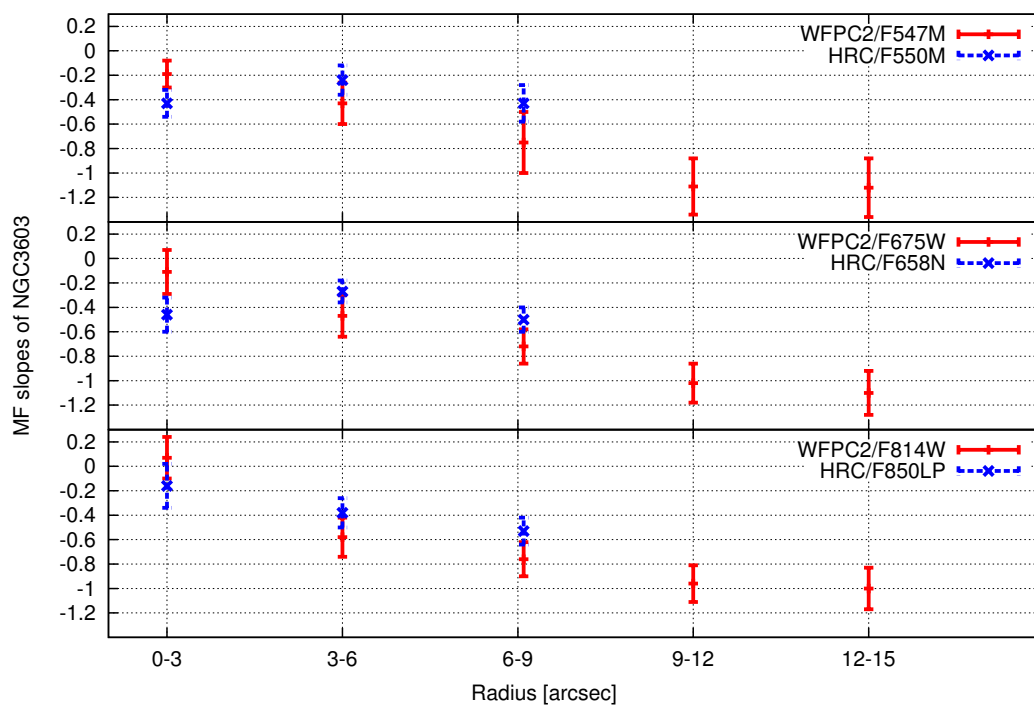


Figure 2.11 Mass function slopes of NGC 3603 derived in three WFPC2 filters (F547M, F675W, F814W from top to bottom) for the whole cluster and in three spatial regions (HRC data - dashed blue) and 5 spatial regions (WFPC2 data - solid red).

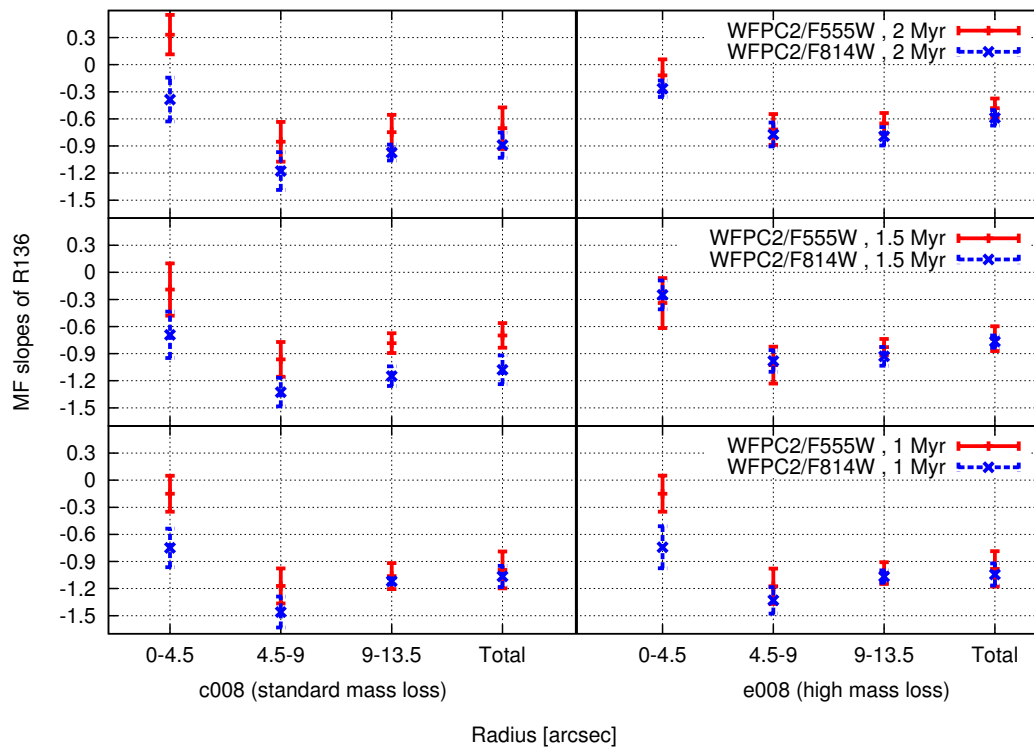


Figure 2.12 Mass function slopes of R136 derived in F555W (red) and F814W (blue) for the whole cluster and in three different regions using three different isochrones: 2, 1.5 and 1 Myr from top to bottom. Left plot is for the standard mass loss (c-models from Geneva stellar evolution models) and right plot for enhanced mass loss (e-models from Geneva stellar evolution models)

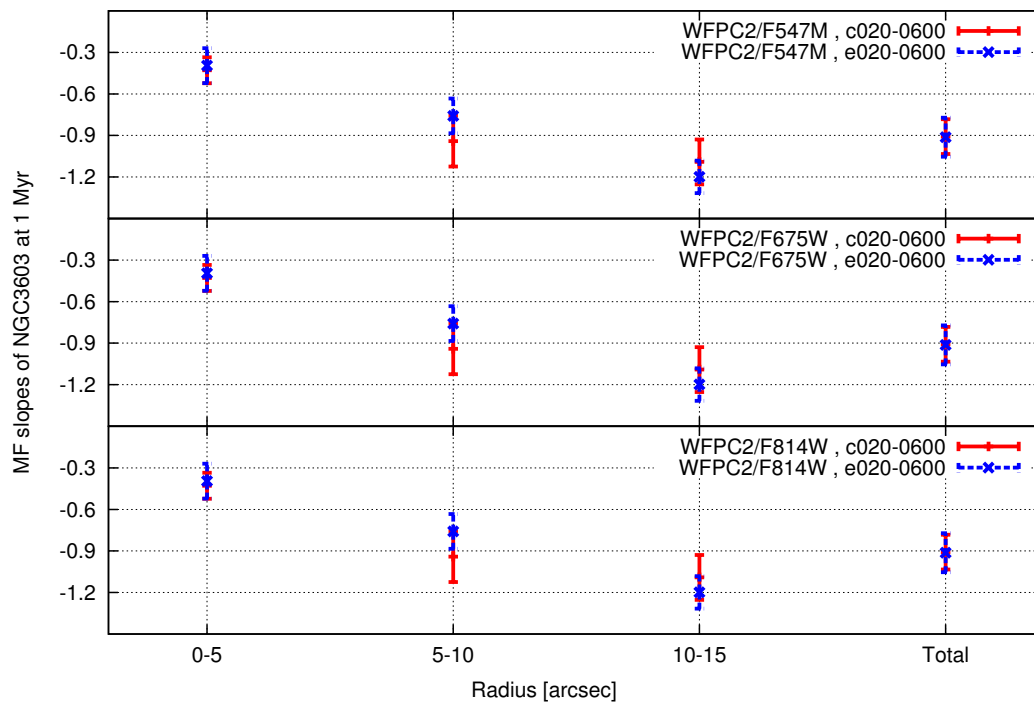


Figure 2.13 Mass function slopes of NGC 3603 derived in three WFPC2 filters (F547M, F675W, F814W from top to bottom) for the whole cluster and in three different regions. Red and blue represents standard and high mass loss from Geneva stellar evolution models (c020 and e020 models).



Top: HR 5171, a yellow hypergiant, a very rare type of stars with only a dozen known in our galaxy, discovered by Olivier Chesneau. Bottom: The artistic impression of this system.

Credit:ESO

Chapter 3

Simulations

Abstract: In the present study, we have adopted a new approach to unveil the different facets of R136. Our approach is primarily motivated by the fact that presently operated 8-10m class optical telescopes and foreseen extremely large telescopes like E-ELT should deliver diffraction limited visible and IR images of crowded field clusters such as R136.

Having this in mind we created a series of simulated images of R136 from the output of the numerical dynamical model (NBODY6 code, [Aarseth et al. (2003)]). In this work, we present the results from the comparison of the HST/WFPC2 imaging data with synthesized images from the output of the NBODY6 simulations at the age of 2 Myr. For this we used Geneva stellar evolution models [Lejeune & Schaerer (2001)] and TLUSTY [Lanz & Hubeny (2003)] or KURUCZ ([Castelli et al. (1997)] model atmospheres depending on the spectral type of stars to calculate their flux in WFPC2/F814W filter at the age of 2 Myr.

The present chapter is organized as followings. In Section 3.1 we shortly describe the NBODY6 code with special emphasis on the options and parameters that are relevant to the present work. We outline the initial conditions from which the evolution of R136 can be simulated and recorded following different tracks. Section 3.2 describes the results of these simulations, including their

observational aspects. These results are compared to the HST observations ¹ in Section 3.3. We introduce our method to create the synthetic images from the output of the NBODY6 code. For this comparison we define a number of criteria applied to simulated scenes from HST versus observed scenes. The relevance of the comparisons is then discussed in the Section 3.4. While we derive some general and preliminary results in perspective of high dynamic, high dynamic and spatially resolved images of R136 to become soon available with SPHERE and GPI in the coming years in Section 3.5 .

3.1 Modeling a young massive star cluster

We used NBODY6² code which includes the individual stellar equations of motion for all members of the cluster without any simplifying assumption and approximation ([Aarseth et al. (2003)]). We remind that NBODY6 integrates the particle orbits using the highly accurate fourth-order Hermite scheme and deals with the diverging gravitational forces in close encounters through regularizations. In addition, this code can track the evolution of the individual stars since it employs the well-tested Single Star Evolution (SSE) and Binary Star Evolution (BSE) recipes [Hurley et al. (2000), Hurley et al. (2002)].

The whole modeling intends to better understand the nature of R136 as it can be imaged nowadays, by taking into account the parameters and different mechanisms that drive the evolution of the cluster such as the degree of initial mass segregation, initial binary fraction, lower/upper stellar masses and stellar evolution. The initial parameters for R136 have been set to the values that represent the best this cluster according to its general properties.

¹Based on observations made with the NASA/ESA Hubble Space Telescope, obtained from the data archive at the Space Telescope Institute. STScI is operated by the association of Universities for Research in Astronomy, Inc. under the NASA contract NAS 5-26555.

²<http://www.ast.cam.ac.uk/sverre/web/pages/nbody.htm>

3.1.1 Physical conditions and Mechanisms

Stellar clusters are born embedded in giant molecular clouds, with a few percent of them surviving and becoming bound clusters [Lada & Lada (2003)]. It is generally admitted that the fate of the clusters must occur during the early stages of their evolution. In massive star-burst clusters, such as R136, dynamical evolution of the cluster can be affected by their significant number of massive stars. The initial distribution of these massive stars (mass segregation) in space, specially if they form in binary systems, plays an important role on the evolution of the cluster.

In order to include such effects, we simulated full segregated clusters (in which most massive stars are located deeper in the core) versus non-segregated clusters (in which the massive stars are randomly distributed in space). The result of these simulations can tell us if R136 is more similar to an initially segregated cluster or not. A result that should put important constraints on theories of massive star formation and the cluster consequent evolution as a whole.

Following clusters without initial binaries, we also considered clusters with 30 and 60 % initial binaries which is not far from the observation as lower-limit of the spectroscopic binaries detected in the clusters of 30 Dor is found to be 45% [Bosch et al. (2009)].

Finally, by comparing the results from clusters with and without stellar evolution, one can check for the effect of stellar evolution on the binaries and the dynamical effect of the binaries themselves on the evolution of the cluster.

3.1.2 Initial conditions

Initial setup of the clusters made by MCLUSTER³ [Kupper et al. (2011)]. The simulation time is limited to an age of 4 Myr with 0.1Myr time-steps. The total mass of the cluster is estimated by Selman & Melnick (2013) to be in the range of:

$$4.6 \times 10^4 M_{\odot} < M_{\odot} < 1.3 \times 10^5 M_{\odot}$$

³<https://ahwkuepper.wordpress.com/mcluster/>

Therefore we adopt the total mass of the cluster to be $1.0 \times 10^5 M_{\odot}$. Kroupa IMF with mass ranging between $0.2M_{\odot}$ or $0.5M_{\odot}$ to $150M_{\odot}$. For the density profile we adopted Plummer model [Aarseth et al. (1974)]. Simulated clusters are assumed isolated and not impacted by tidal fields (tf=0). The initial half mass radius of the clusters is 0.8 pc. And finally the metallicity of LMC (R136) is taken as half of the solar metallicity. All the clusters are in virial equilibrium as [Henault-Brunet et al. (2012)] find that R136 is in virial equilibrium.

The set-up of the numerical experimentations is as follows: half of the clusters are segregated (s=1.0) and the others are non-segregated (s=0.0). We adopted 60%, 30% and 0% percent of initial binary for the simulated clusters. There will be two groups of clusters. These groups are totally similar to each other (even the initial position and velocity of stars) but for one group stellar evolution is ON and for other group stellar evolution is OFF to see the effect of stellar evolution Table 3.1.

Table 3.1 depicts the main characteristics of simulated clusters ⁴. The first column is the name

⁴Explanation on the naming of the clusters:

$$\underbrace{S}_1 \underbrace{10 \text{ seg}}_2 \underbrace{03 \text{ bin}}_3 \underbrace{01 \text{ m } 100}_4$$

- 1 : **S** means Stellar evolution is ON and **D** means Stellar evolution is OFF (Pure Dynamically evolution).
- 2 : Number before **seg** shows the degree of mass segregation. **10 seg** means fully segregated and **00 seg** means non-segregated.
- 3 : Number before **bin** shows the initial binary fraction. **03 bin** means 0.3 binary fraction (30 percent of binaries) and **00 bin** means no initial binaries.
- 4 : The numbers before and after **m** shows the mass range. The first number before **m** can be **01** which means the low mass cutoff is $0.1M_{\odot}$ or it can be **10** which means the low mass cutoff is $1.0M_{\odot}$ and the second number after **m** can be **100** which means the maximum mass of the particles is $100M_{\odot}$ or it can be **300** which mean the maximum mass is $300M_{\odot}$.

So name **S10seg03bin01m100** stand for a cluster with stellar evolution is ON and it is fully segregated with 0.3 binary fraction and mass range between $0.1M_{\odot}$ to $100M_{\odot}$. Also **D00seg00bin10m300** means this cluster evolves just

of the cluster. The second column says if stellar evolution is ON or OFF. Column 3 corresponds to the degree of mass segregation, 0.0 means non-segregation and 1.0 means the cluster is fully segregated. The fourth column corresponds to the binary fraction. The fifth column defines the number of initial binaries. M_{min} and M_{max} are the lower and upper mass cutoff respectively of initial mass function (The canonical Kroupa, [Kroupa (2001)]) and N is the initial number of stars.

For the initial number of binaries we used random pairing but separate pairing for components with $m > m_{sort}$. In this way, pairing of primary and secondary components of binary stars above m_{sort} are randomly paired among each other. The motivation for this lies in extensive observational data showing that massive O, B stars are more likely to be found in an equal mass binary system [Sana & Evans (2011)]. m_{sort} is equal to $5M_{\odot}$ in agreement with [Kobulnicky& Fryer (2007)]. More detail about semi-major axis and period distribution of binaries can be found in section 3.2.3.

The period distribution was taken from the [Kroupa (1995)] period distribution since it unifies the observed Galactic field and pre-main sequence populations (see also [Kroupa (2008)]). But for massive binaries with $M_{primary} > m_{sort}$ we used the period distribution from Sana&Evans 2011 since the period distribution of massive O,B spectroscopic binaries has been found to be significantly different from what is observed for low-mass binaries [Sana & Evans (2011)]. Massive binaries are found to have short periods in the range from 2 days to 10 years with a peak at 10 days.

Eccentricities are assumed to have a thermal distribution i.e. $f(e)=2e$ [Kroupa (2008)] and for the eccentricities of high mass binaries the distribution is taken according to [Sana & Evans (2011)], leading to the computation of the semi-major axis (a) of each binary.

Dynamically without stellar evolution and it is not initially segregated without any initial binaries and mass range between $1.0M_{\odot}$ to $300M_{\odot}$.

Model	SE	Seg	BF	N_{bin}	M_{min}	M_{max}	N
S00seg00bin05m150	ON	0.0	0.0	0	0.5	150	55992
D00seg00bin05m150	OFF	0.0	0.0	0	0.5	150	55992
S10seg00bin05m150	ON	1.0	0.0	0	0.5	150	55815
D10seg00bin05m150	OFF	1.0	0.0	0	0.5	150	55815
S00seg03bin05m150	ON	0.0	0.3	8404	0.5	150	56032
D00seg03bin05m150	OFF	0.0	0.3	8404	0.5	150	56032
S10seg03bin05m150	ON	1.0	0.3	8536	0.5	150	56908
D10seg03bin05m150	OFF	1.0	0.3	8536	0.5	150	56908
S00seg06bin05m150	ON	0.0	0.6	17000	0.5	150	56669
D00seg06bin05m150	OFF	0.0	0.6	17000	0.5	150	56669
S10seg06bin05m150	ON	1.0	0.6	16686	0.5	150	55622
D10seg06bin05m150	OFF	1.0	0.6	16686	0.5	150	55622
S00seg00bin02m150	ON	0.0	0.0	0	0.2	150	105666
D00seg00bin02m150	OFF	0.0	0.0	0	0.2	150	105666
S10seg00bin02m150	ON	1.0	0.0	0	0.2	150	107722
D10seg00bin02m150	OFF	1.0	0.0	0	0.2	150	107722
S00seg03bin02m150	ON	0.0	0.3	16134	0.2	150	107565
D00seg03bin02m150	OFF	0.0	0.3	16134	0.2	150	107565
S10seg03bin02m150	ON	1.0	0.3	16084	0.2	150	107230
D10seg03bin02m150	OFF	1.0	0.3	16084	0.2	150	107230
S00seg06bin02m150	ON	0.0	0.6	32225	0.2	150	107419
D00seg06bin02m150	OFF	0.0	0.6	32225	0.2	150	107419
S10seg06bin02m150	ON	1.0	0.6	32309	0.2	150	107698
D10seg06bin02m150	OFF	1.0	0.6	32309	0.2	150	107698

Table 3.1 Different simulated clusters grouped by minimum mass. Total mass of the clusters is $10^5 M_{\odot}$. Summary of naming convention for these simulated clusters is explained hereafter:

3.2 Results of the simulations

3.2.1 Expansion of the cluster

Figure 3.1 shows the evolution of half mass radii of 24 simulated clusters in 4 Myr. The upper plots correspond to clusters with a mass distribution in the range of $0.5M_{\odot} - 150M_{\odot}$ and bottom plots correspond to clusters with mass distribution in the range of $0.2M_{\odot} - 150M_{\odot}$. From left to right the plots depict clusters with 0%, 30% and 60% initial binaries. It can be seen in all plots that segregated clusters expand more than non-segregated ones due to dynamical interactions. Stellar evolution plays also an important role in the expansion of the cluster, especially around 3-3.5 Myr on the evolution of massive stars and their high mass-loss. The expansion due to the stellar evolution (mass-loss) is larger than the expansion due to initial segregation, unless there are binary systems. Dynamical interaction for the clusters with binaries is very significant. So segregated clusters which contains binaries expand remarkably even if the stellar evolution is OFF for them (red-dashed lines in the middle and left plots in Figure 3.1).

Clusters which contain more massive stars, present a larger expansion. This can be checked by comparing the half-mass radius evolution of clusters with pure dynamical evolution (D-clusters). At the same time, changing the binary fraction does not affect the expansion of the clusters in a significant way.

3.2.2 Escapers and cluster's mass loss

Clusters lose mass due to escaping stars and also if stellar evolution is ON, which drives the mass-loss of massive stars. Figure 3.2 to 3.4 show the total mass loss of each cluster per time-step. In these figures, top plot correspond to 4 clusters in the mass range of $0.5M_{\odot} - 150M_{\odot}$ and bottom plot for 4 clusters with the mass range of $0.2M_{\odot} - 150M_{\odot}$. The numbers at the top of each bin correspond to the number of escapers. In each plot, all 4 clusters have similar initial total mass,

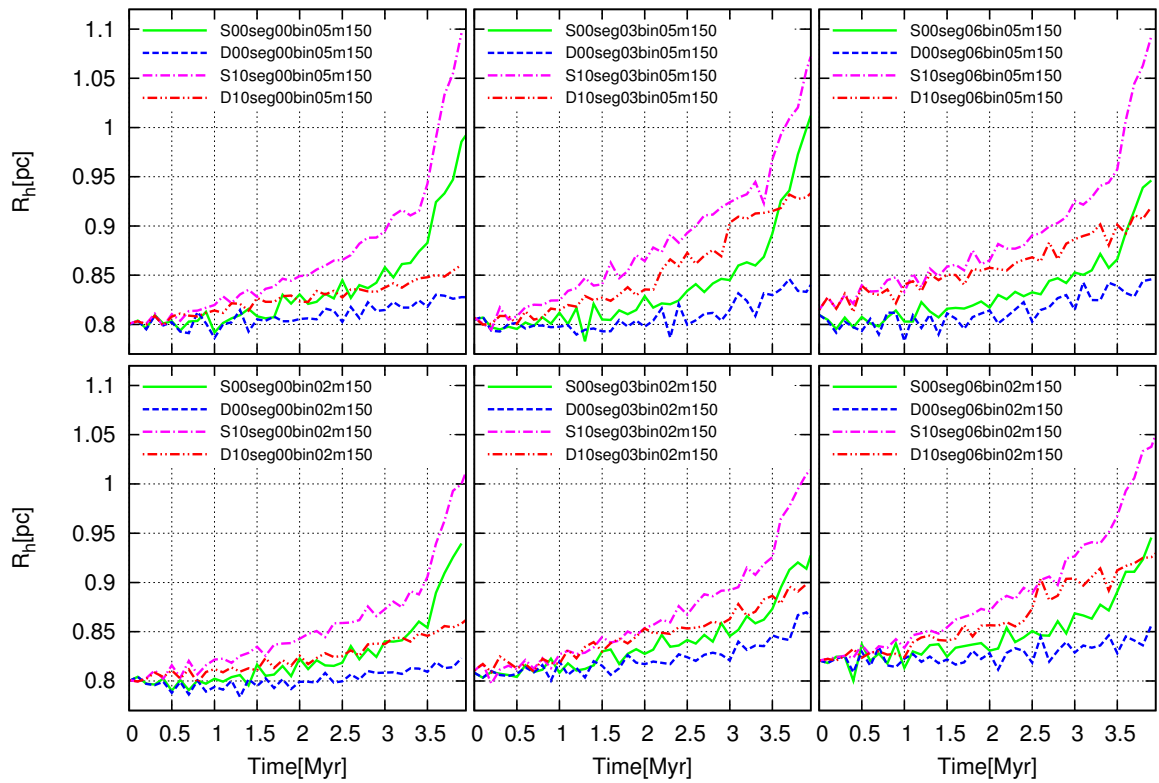


Figure 3.1 Half-mass radius evolution of different clusters within 4 Myr. Up: mass range of $0.5M_{\odot} - 150M_{\odot}$. Down: $0.2M_{\odot} - 150M_{\odot}$. Left: No initial binaries, Middle: 30% initial binaries, Right: 60% initial binaries. Green and Blue: Non-segregated; Pink and Red: Segregated.

mass-range and binary fraction. But they differ in initial segregation and stellar evolution. In each plot, from top to bottom, 4 clusters stand for initially: 1) Non-segregated with stellar evolution (Green), 2) Segregated with stellar evolution (Pink), 3) Non-segregated without stellar evolution (Blue) and 4) Segregated without stellar evolution (Red).

Figure 3.2, 3.3 and 3.4 represent clusters with 0%, 30% and 60% initial binaries.

The mass-loss of the clusters with stellar evolution (hereafter call S-clusters) is much larger than the clusters without stellar evolution (here after call D-clusters) especially around time 3.5 Myr which is a time when massive stars ($M > 60M_{\odot}$) turn out to supernova events. Clusters on the left with $M_{min} = 0.5M_{\odot}$ contain indeed more massive stars than clusters at the right (with $M_{min} = 0.2M_{\odot}$), so for these clusters mass loss is more than for clusters with $M_{min} = 0.2M_{\odot}$. that for D-clusters the number of escapers increases with the increasing binary fraction.

3.2.3 Binary fraction

Figure 3.5 shows the fraction of bound binary systems for different clusters versus time. Segregated clusters lose less binaries than non-segregated clusters. It seems that the segregated clusters are safer places for binaries to be survive. It can be explain by two main reasons: Location of the binaries and their neighbors.

In segregated clusters binaries are located deeper in the cluster and they interact mostly with the same-mass neighbors so the chance to be disrupted by single massive star and massive binaries decreases in segregated clusters. Also when a binary is disrupted in the segregated cluster, If it is going to be ejected/evaporated from cluster, It has to pass from a outer layer of the cluster which is contaminated by single stars. This star still has a chance to interact with single stars and remain in the cluster which decreases the evaporation probability. This is not a case for Non-segregated clusters.

For clusters with 30% binaries it can be seen that if they contain more low mass stars and less

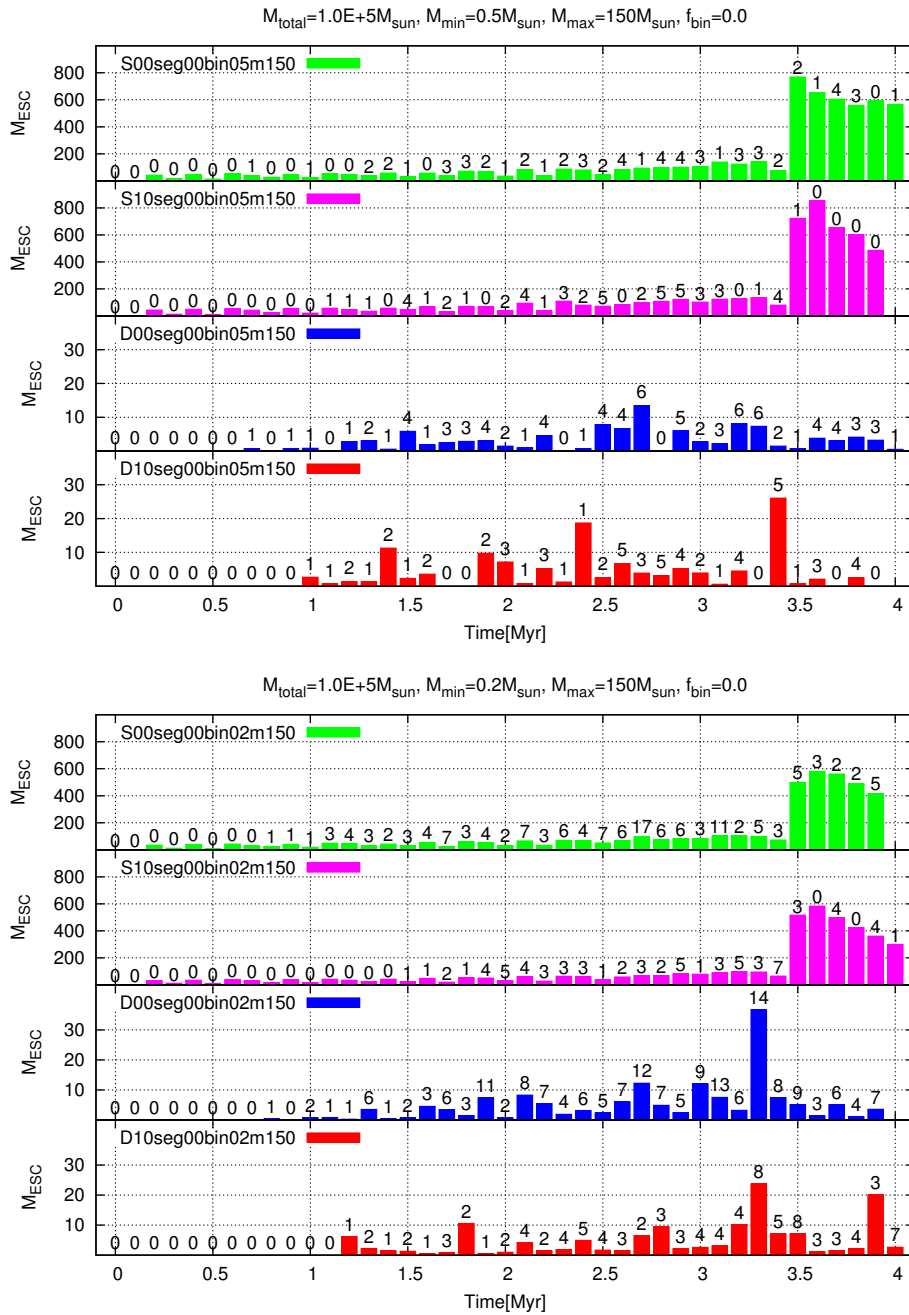


Figure 3.2 Total mass loss of the clusters (with 0% initial binaries) per time-step. Top: mass range of $0.5M_{\odot} - 150M_{\odot}$. Bottom: mass range of $0.2M_{\odot} - 150M_{\odot}$. The numbers at the top of each bin correspond to the number of escapers. Green and Blue: non-segregated; Pink and Red: Segregated. Stellar evolution is ON for Green and Red, and OFF for blue and Red.

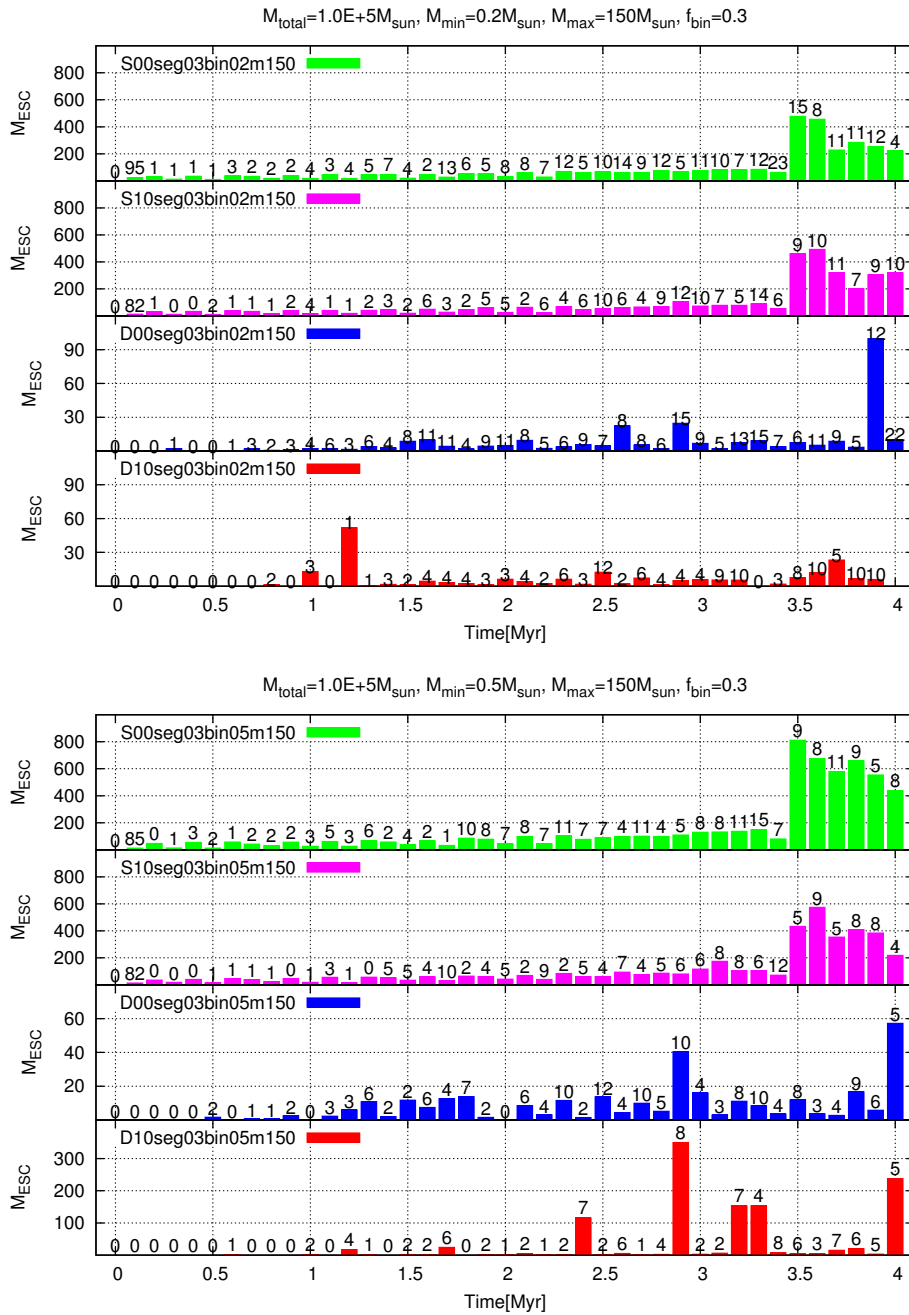


Figure 3.3 Total mass loss of the clusters (with 30% initial binaries) per time-step. Top: mass range of $0.5M_{\odot} - 150M_{\odot}$. Bottom: mass range of $0.2M_{\odot} - 150M_{\odot}$. The numbers at the top of each bin correspond to the number of escapers. Green and Blue: non-segregated; Pink and Red: Segregated. Stellar evolution is ON for Green and Red, and OFF for blue and Red.

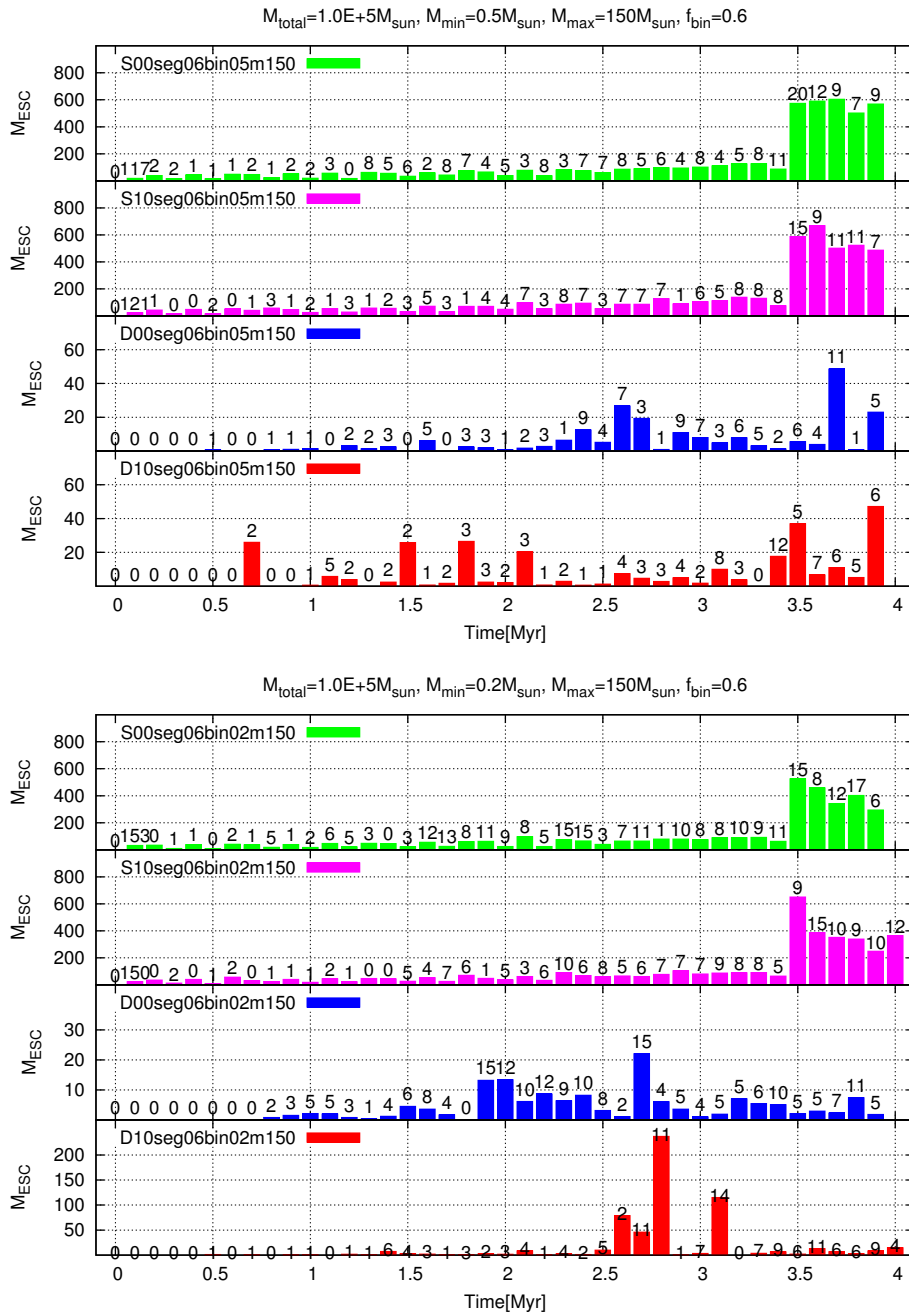


Figure 3.4 Total mass loss of the clusters (with 60% initial binaries) per time-step. Top: mass range of $0.5M_{\odot} - 150M_{\odot}$. Bottom: mass range of $0.2M_{\odot} - 150M_{\odot}$. The numbers at the top of each bin correspond to the number of escapers. Green and Blue: non-segregated; Pink and Red: Segregated. Stellar evolution is ON for Green and Red, and OFF for blue and Red.

massive binaries (the case of clusters with $M_{min} = 0.2M_{\odot}$), they lose more binaries than clusters with $M_{min} = 0.5M_{\odot}$.

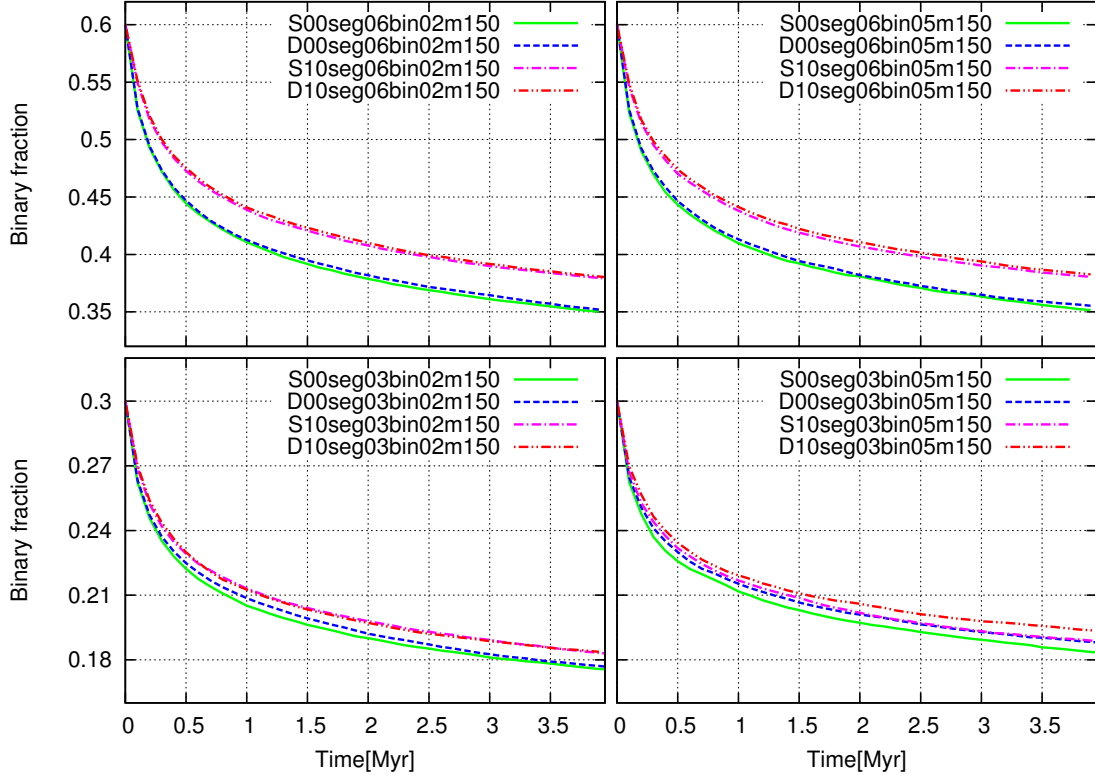


Figure 3.5 Fraction of bound binary systems for different clusters in each time-steps. Left, Up: clusters with mass range of $1.0M_{\odot} - 100M_{\odot}$ and 30% Initial binaries. Right, Up: clusters with mass range of $1.0M_{\odot} - 300M_{\odot}$ and 30% Initial binaries. Left, Down: clusters with mass range of $0.5M_{\odot} - 150M_{\odot}$ and 30% Initial binaries. Right, Down: clusters with mass range of $0.5M_{\odot} - 150M_{\odot}$ and 60% Initial binaries. Green and Blue: non-segregated; Pink and Red: Segregated. Stellar evolution is ON for Green and Red, and OFF for blue and Red.

3.2.4 Periods and eccentricities

Figures 3.6 to 3.9 shows the histogram of periods in units of days (logarithmic) in six time-steps for 16 clusters. These clusters have similar initial total mass but they differ in the number of initial binaries and mass-range. 1) Figure 3.6 belongs to 4 clusters with 30% initial binaries and mass-range of $0.5M_{\odot} - 150M_{\odot}$. Figure 3.8 is similar to Figure 3.6 but with the mass-range of $0.2M_{\odot} - 150M_{\odot}$. Finally Figure 3.7 and 3.9 are similar to previous plots but with 60% initial binaries.

Different colors represent different times. For example red plot is at the time of 0.0 Myr which is the initial distribution of periods that we have chosen according to observations reported in literature (see Section 3.1.2). It is a bimodal distribution, for low mass binaries it is Kroupa distribution and for massive O, B binaries it is Sana&Evans 2011 which exhibits in its a first part a peak around 10 days.

Evolution of the first part is according to stellar evolution, that is why it is not visible in D-clusters. Evolution of second part is according to the dynamics of the cluster, that is why we see this for both S-clusters and D-clusters.

Almost half of the low-mass binaries dissolve within 1 Myr.

Figures 3.10 to 3.13 show the evolution of eccentricity distributions in 6 time-steps for the same 16 clusters that the histogram of periods were plotted (Figures 3.6 to 3.9). Initial distribution ($T = 0.0$ Myr) is the red plot. Like the period distribution, eccentricities also have a bimodal distributions, for low-mass and massive binaries (with a peak close to $e=0.0$). Stellar evolution, affects the evolution of the first peak (for massive binaries) that is why for D-clusters the peak does not evolve. For low-mass binaries, during the evolution (in different time-steps) the distribution keeps the memory of the initial distribution for different eccentricities.

For period distribution, after 2-3 Myr the new distribution could keep the memory of initial distribution of massive binaries not for low-mass binaries. But for eccentricity distribution, cluster

keeps the memory of initial distribution of eccentricities.

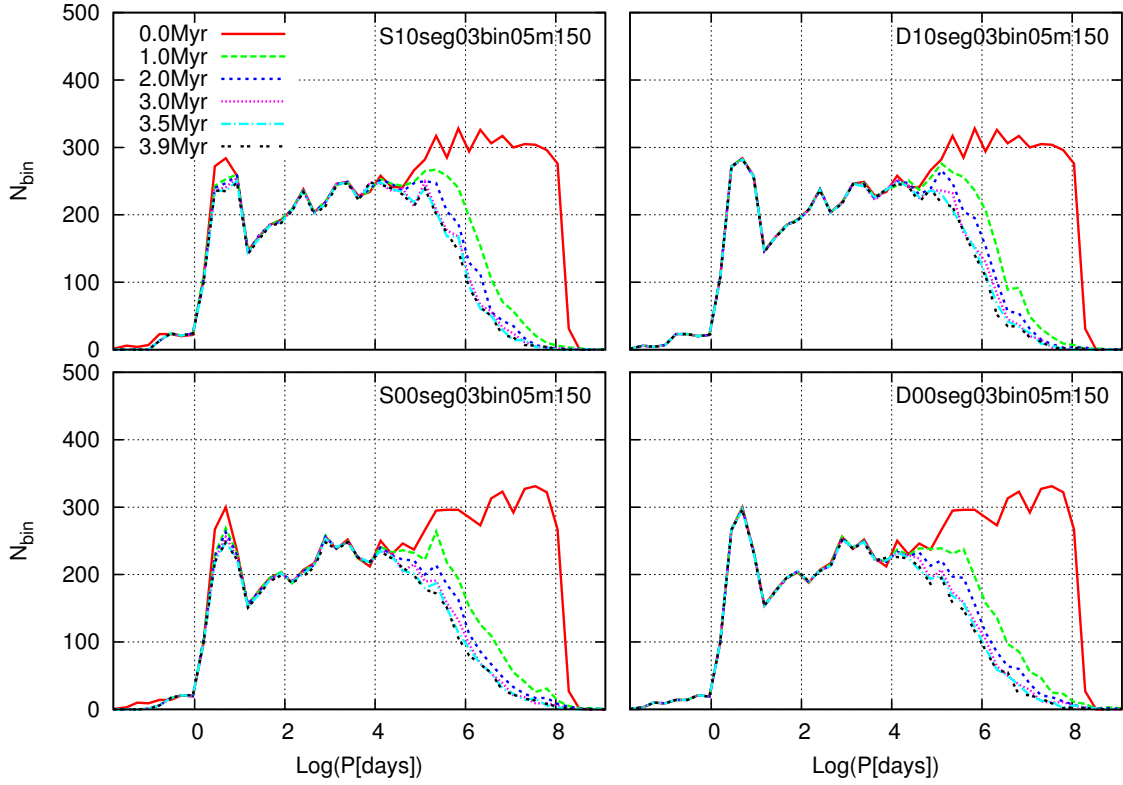


Figure 3.6 Histogram of the Log(period [days]) of bound binary systems in 6 time-steps (0.0, 1.0, 2.0, 3.0, 3.5 and 3.9 Myr) for 4 clusters with mass range of $0.5M_{\odot} - 150M_{\odot}$ and 30% Initial binaries.

3.3 Comparison with observations

For R136, the main observational data result from imaging in different filters. From these data, one can estimate the mass of stars and compare the density profile with simulations. In such an approach errors can dramatically increase from converting magnitudes to mass as the theoretical evolutionary models may not provide enough information for very massive and Wolf-Rayet stars

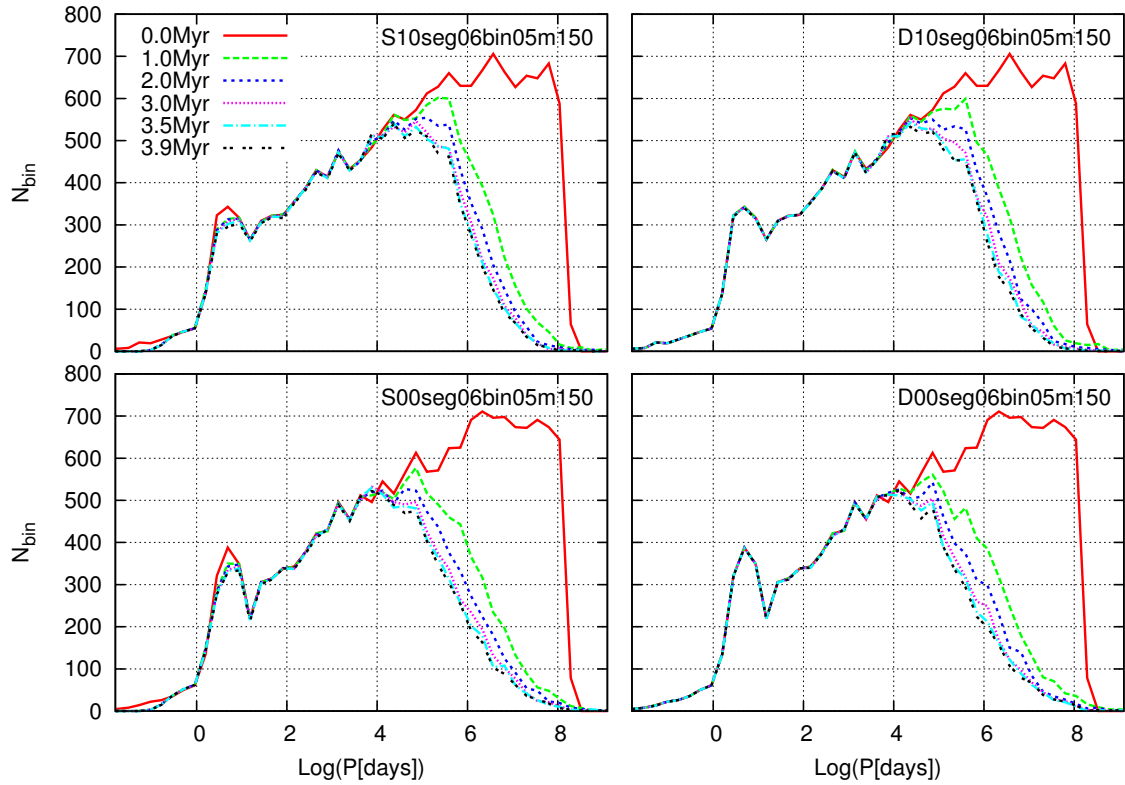


Figure 3.7 Histogram of the Log(period [days]) of bound binary systems in 6 time-steps (0.0, 1.0, 2.0, 3.0, 3.5 and 3.9 Myr) for 4 clusters with mass range of $0.5M_{\odot} - 150M_{\odot}$ and 60% Initial binaries.

specially. On the other hand, we probably cannot detect many low mass stars during the photometry. Moreover, if the detected object is a binary then estimated mass is biased.

At this point of our study we prefer to produce the imaging data from the simulations with the spatial resolution of HST/WFPC2 data from R136. HST/WFPC2 observations of R136 were carried out on 1994-09-25 (PI: Westphal), from which we use a combination of shallow, intermediate and long exposures ranging from 3–5 s to 80–120 s with the planetary camera (PC) and the F814W filter. So we wrote a code which reads the information of stars from the NBODY6 simulations as an input and creates the synthetic scenes that mimic HST/WFPC2 resolution in different HST

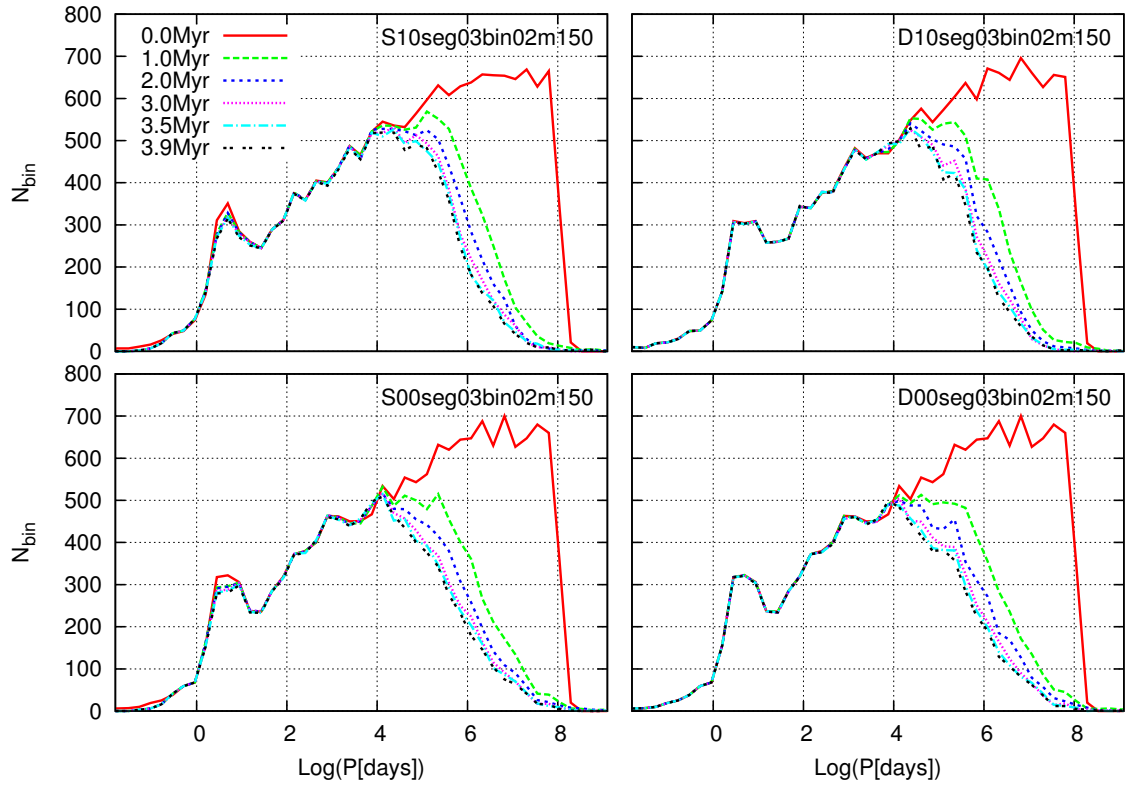


Figure 3.8 Histogram of the Log(period [days]) of bound binary systems in 6 time-steps (0.0, 1.0, 2.0, 3.0, 3.5 and 3.9 Myr) for 4 clusters with mass range of $0.2M_{\odot} - 150M_{\odot}$ and 30% Initial binaries.

filters. During this simulation we also need proper stellar evolution models and atmospheric models for calculating Bolometric Correction (BC) of different HST/WFPC2 filters. We created sets of BC tables (see Chapter 2) at the age of 2 Myr using Geneva stellar evolution models⁵ [Lejeune & Schaerer (2001)]. For calculating BCs we used SEDs from TLUSTY atmosphere models for O and B stars⁶ [Hubeny & Lanz (1995), Lanz & Hubeny (2003), Lanz & Hubeny (2007)] and KURUCZ⁷ [Castelli et al. (1997)] for the rest of the stellar types with a half-solar metallicity ap-

⁵<http://webast.ast.obs-mip.fr/equipe/stellar/>

⁶Model atmospheres and source codes are available at <http://nova.astro.umd.edu>

⁷ATLAS9 Kurucz ODFNEW /NOVER models

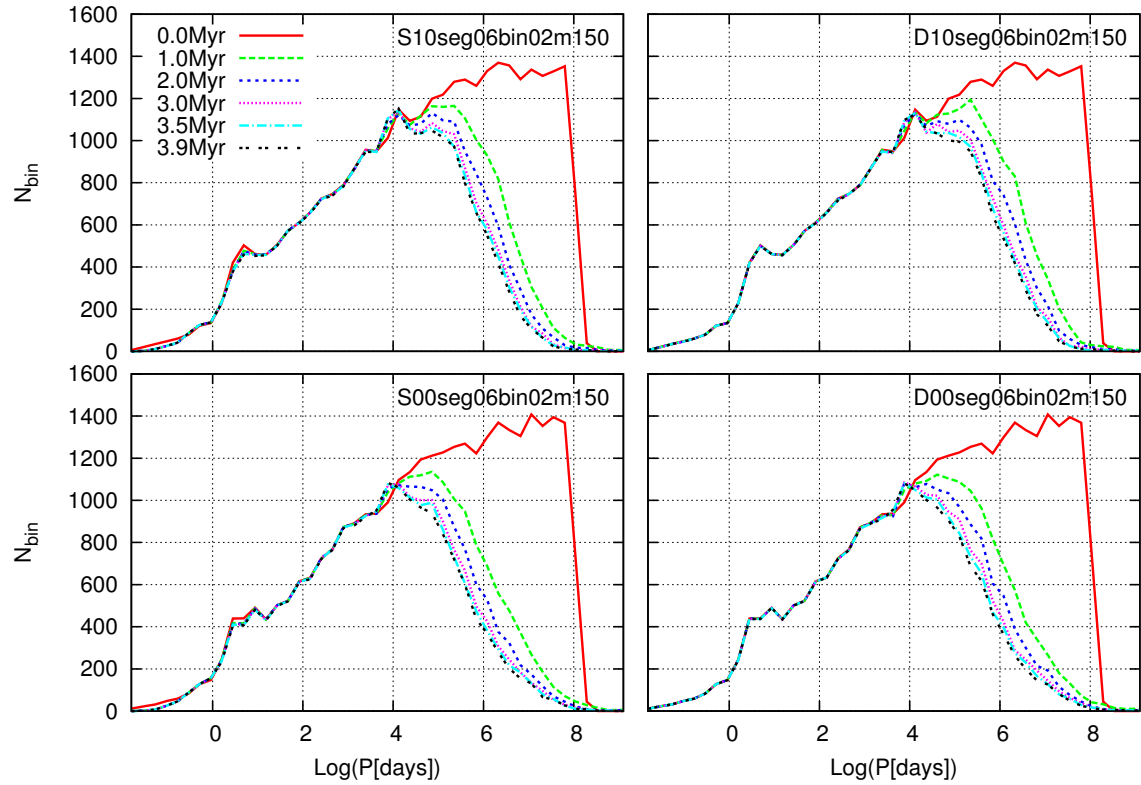


Figure 3.9 Histogram of the $\text{Log}(\text{period} [\text{days}])$ of bound binary systems in 6 time-steps (0.0, 1.0, 2.0, 3.0, 3.5 and 3.9 Myr) for 4 clusters with mass range of $0.2M_{\odot} - 150M_{\odot}$ and 60% Initial binaries.

appropriate for LMC stars. TLUSTY provides grids of non-LTE, metal line-blanketed, plane-parallel, hydrostatic model atmospheres which is well suited for the very massive stars specially in visible and near-IR.

At a given time (2 Myr) it is possible to calculate the flux (in different HST filters) for each star in the simulation using computed BC tables. We simulated a 800×800 pixels scene corresponding to a field of $32.5'' \times 32.5''$ on the detector where a star with a given flux falls on the detector with a Gaussian distribution as the PSF profile.

Figure 3.15-3.18 show synthetic scenes of 12 simulated clusters at time 2 Myr both in XY and

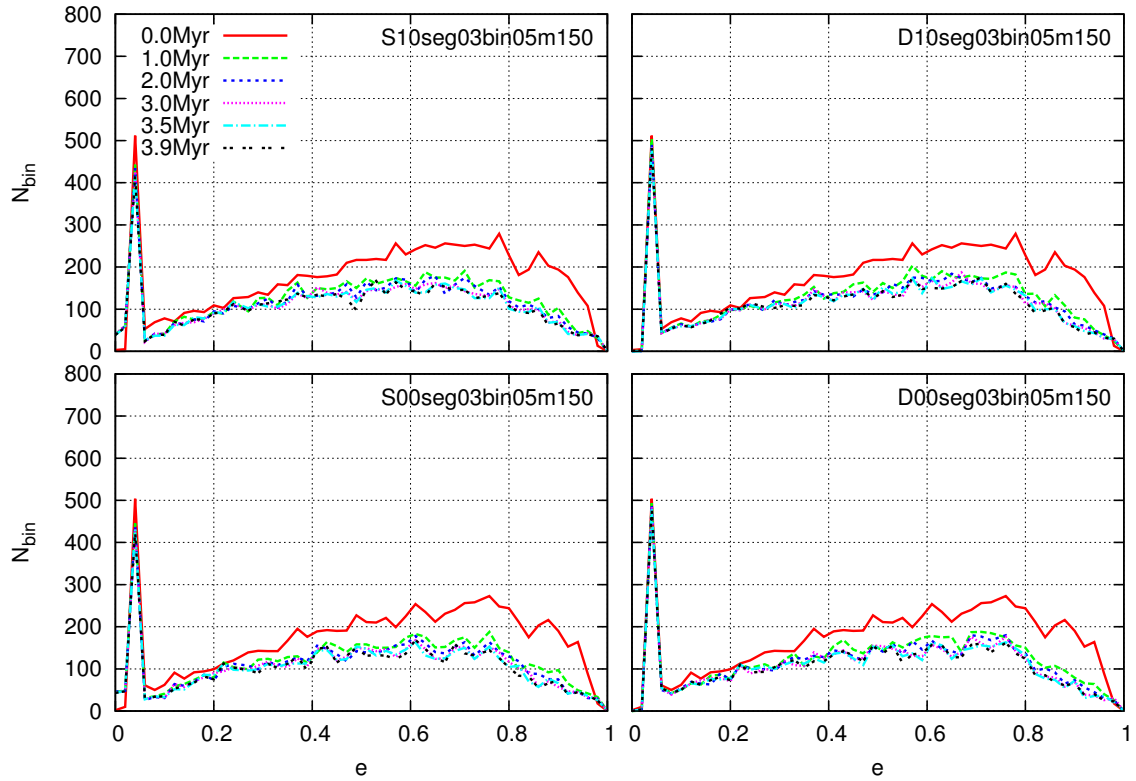


Figure 3.10 Histogram of the eccentricity of bound binary systems in 6 time-steps (0.0, 1.0, 2.0, 3.0, 3.5 and 3.9 Myr) for 4 clusters with mass range of $0.5M_{\odot} - 150M_{\odot}$ and 30% Initial binaries.

XZ plane. One can compare the synthetic images with real HST/WFPC2 data on R136 shown in Figure 3.14. Both images are in F814W filters.

However the question is at what degree a simulated cluster with thousands of stars within a given volume projected once on the sky to reproduce HST image of R136. What is the best criterion to select the closest simulated cluster to R136?

One useful way is to compare the Surface Brightness Profile (SBP) of R136 to those of synthetic scenes (Section 5.5). It is also possible to compare the Half-Light radius (R_{hl}) of R136 and synthetic scenes (Section 3.3.3). In Section 3.3.2 we compared the Mass Function (MF) slopes of

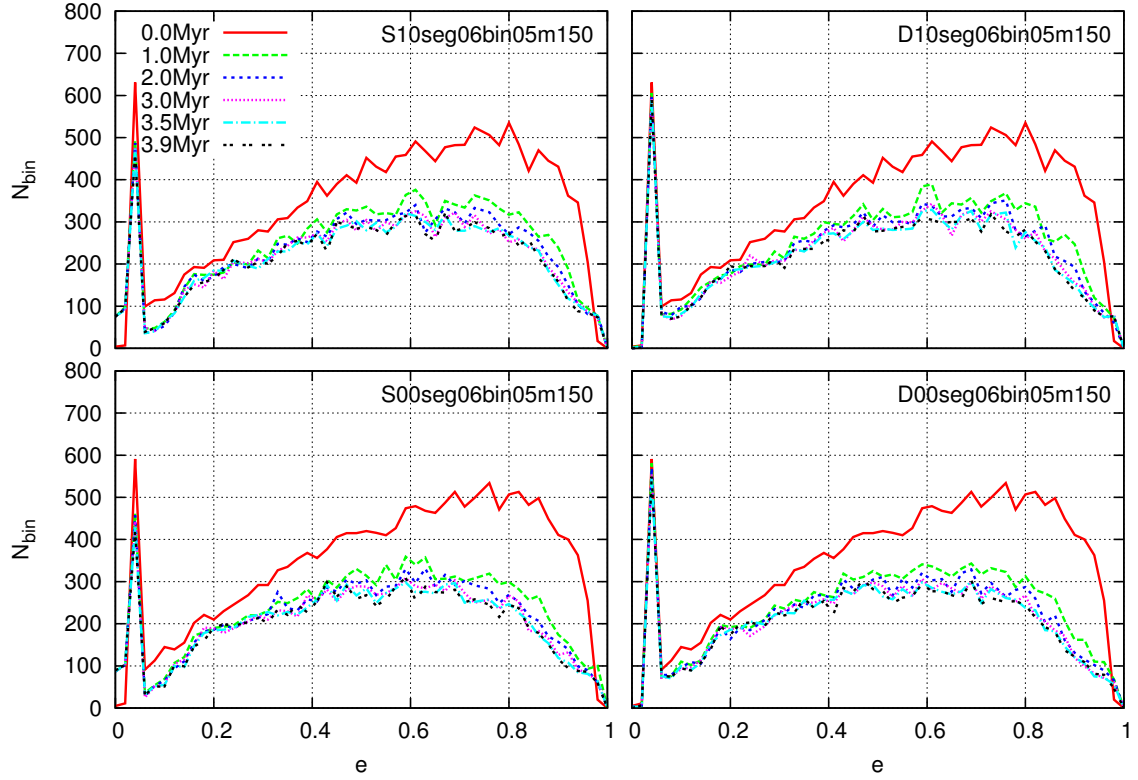


Figure 3.11 Histogram of the eccentricity of bound binary systems in 6 time-steps (0.0, 1.0, 2.0, 3.0, 3.5 and 3.9 Myr) for 4 clusters with mass range of $0.5M_{\odot} - 150M_{\odot}$ and 60% Initial binaries.

R136 with the MF slopes from simulations. The MF is not directly derived from simulation. The mass of stars in the FoV is estimated by the photometry on the synthetic scenes and we used the BC-tables for finding the mass of each detected star in a given field. In Section 3.3.4 we introduce a new definition for double checking. In this section we calculate a neighbor radius ($R_{neighbor}$) of each star in each cluster which is a radius containing for example, 100 neighbor stars. In a crowded regions (in the core) this radius is very short for each star while in outer regions it can be larger.

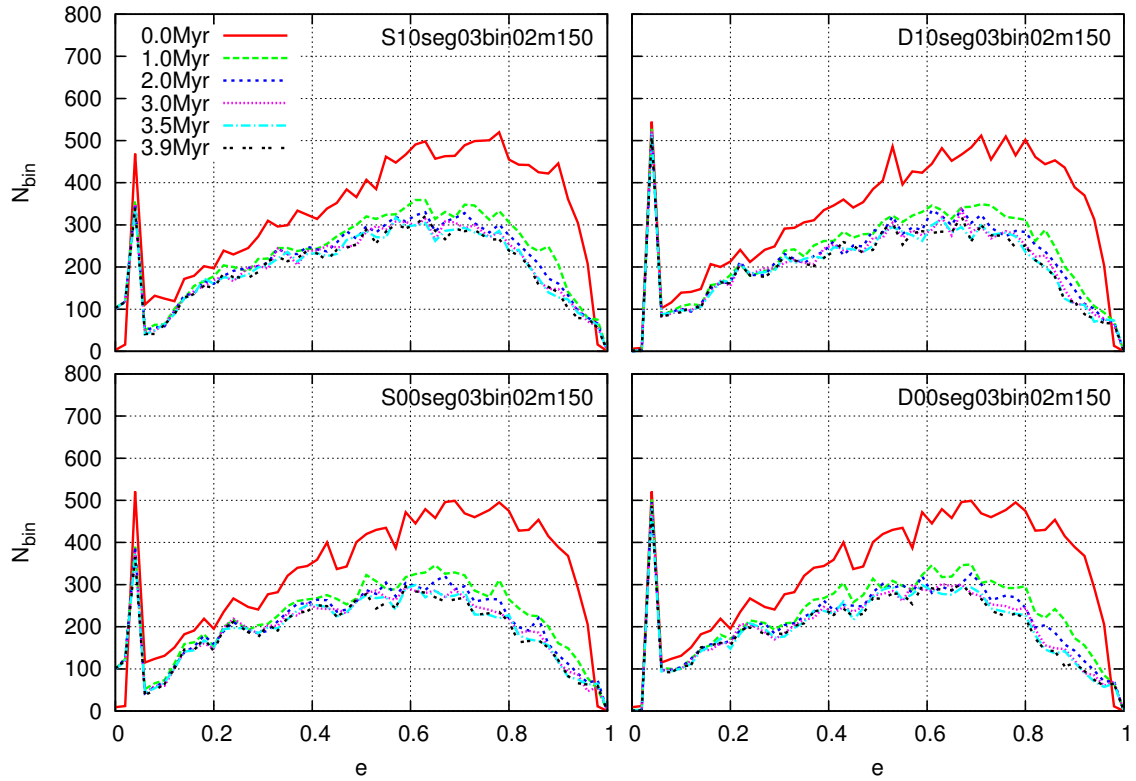


Figure 3.12 Histogram of the eccentricity of bound binary systems in 6 time-steps (0.0, 1.0, 2.0, 3.0, 3.5 and 3.9 Myr) for 4 clusters with mass range of $0.2M_{\odot} - 150M_{\odot}$ and 30% Initial binaries.

3.3.1 SBP of R136

Figure 3.19 shows the SBP of R136. It can be seen that at some radial distances from the core of the cluster the SBP suddenly increases with a significant deviation from the general trend. We checked for the distribution of the spectral type of R136 stars in the FoV of HST/WFPC2-PC imaging data and we found 9 WR stars. Figure 3.19 shows the radii at which a given WR is detected.

For synthetic scenes we have calculated the SBPs in the same regions as R136. Figure 3.20 and 3.21 shows the SBPs of the simulated R136 versus its simulated twin (pink stars).

To determine the closest SBP value of the simulated to the observed R136 we calculated the

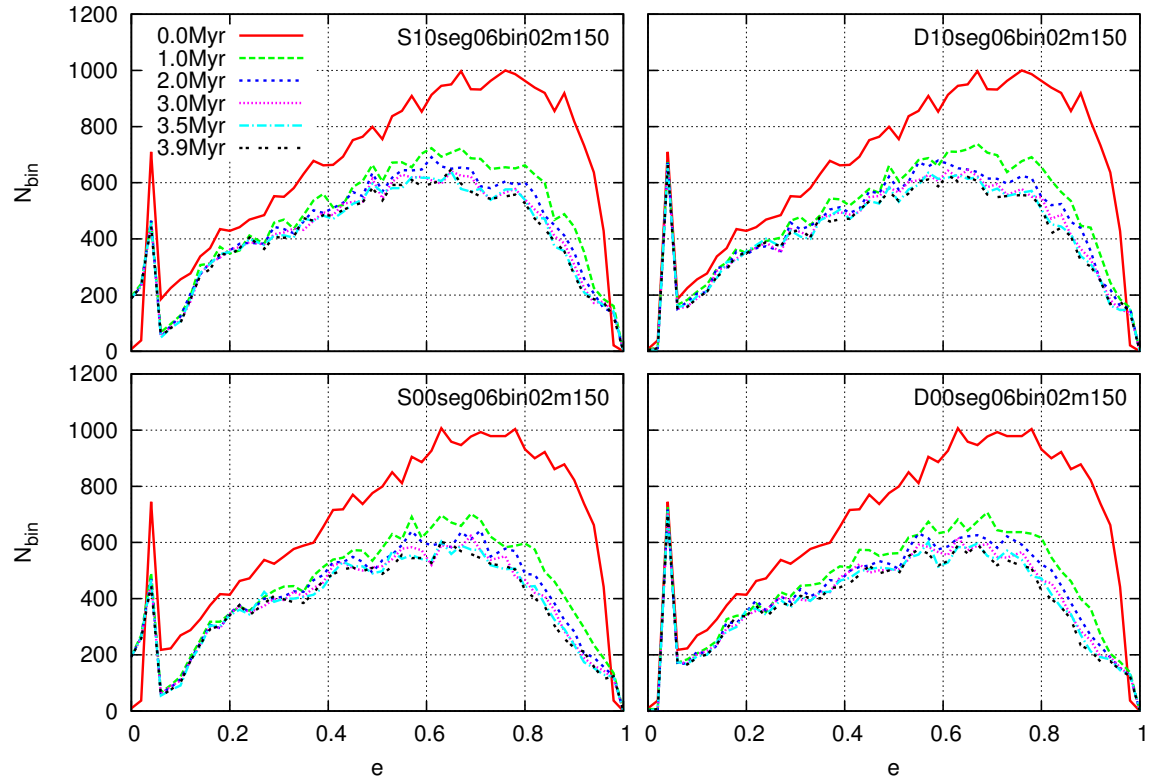


Figure 3.13 Histogram of the eccentricity of bound binary systems in 6 time-steps (0.0, 1.0, 2.0, 3.0, 3.5 and 3.9 Myr) for 4 clusters with mass range of $0.2M_{\odot} - 150M_{\odot}$ and 60% Initial binaries.

χ^2 for each cluster in three regions in addition to the whole cluster. Table 3.2 (simulated scenes in XZ plane) and Table 3.3 (simulated scenes in XY plane) depict the χ^2 values. Clusters with the smallest value have an SBP more closer to that of R136. Thus the non-segregated clusters match better R136 in all regions.

3.3.2 MF slopes

After having created series of synthetic scenes, in the first step photometry on each image have to be done. For the photometry on HST/WFPC2 data and also on the synthetic images we used

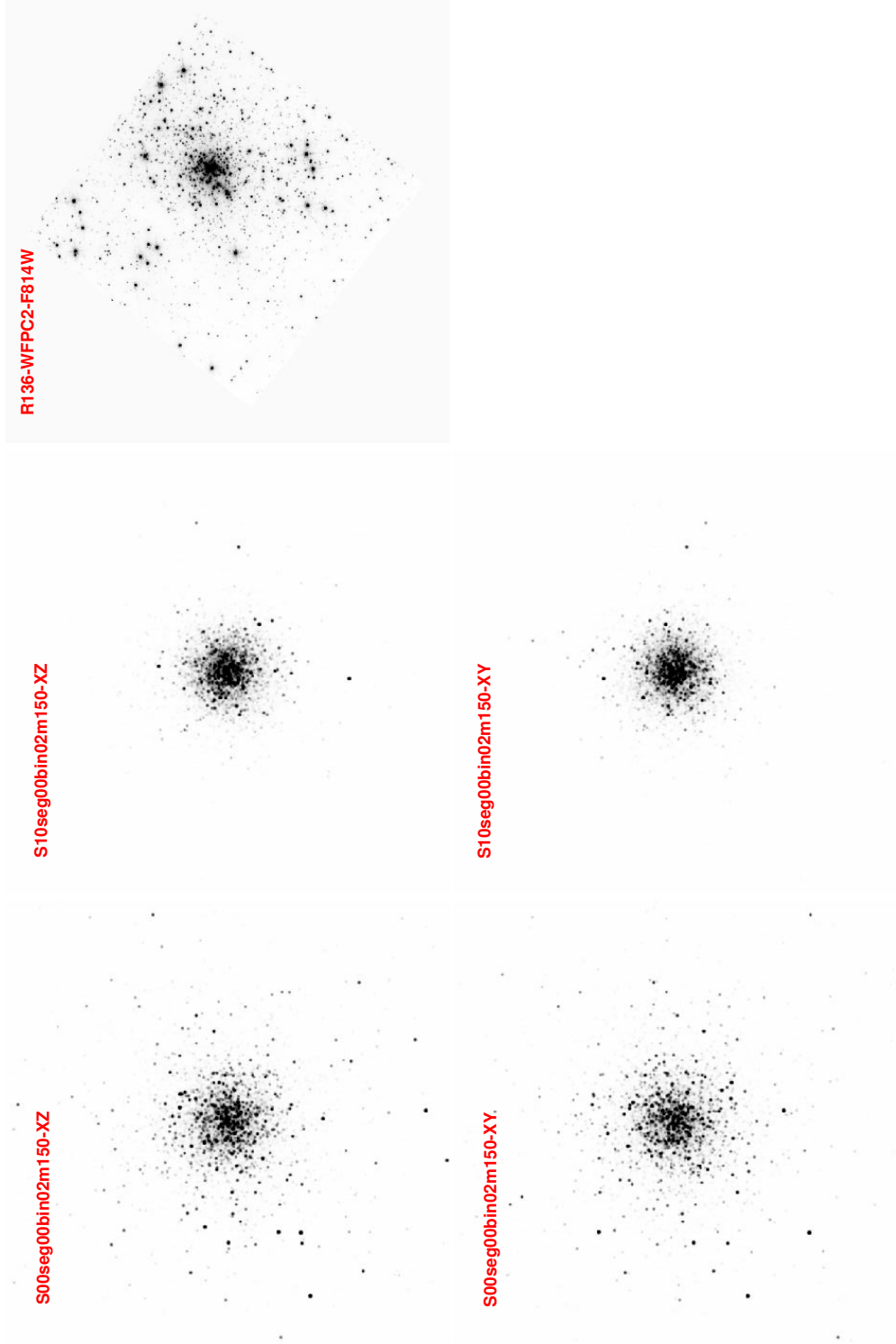


Figure 3.14 Synthetic scenes from simulation of S-clusters with the mass range of $(0.2 - 150)M_{\odot}$ and 0% initial binaries at time 2 Myr. Not segregated: Left images; Segregated clusters: Middle images; Top is in XZ plane and bottom is in XY plane. R136 image taken by HST/WFPC2-PC in F814W filter is in the Right top.

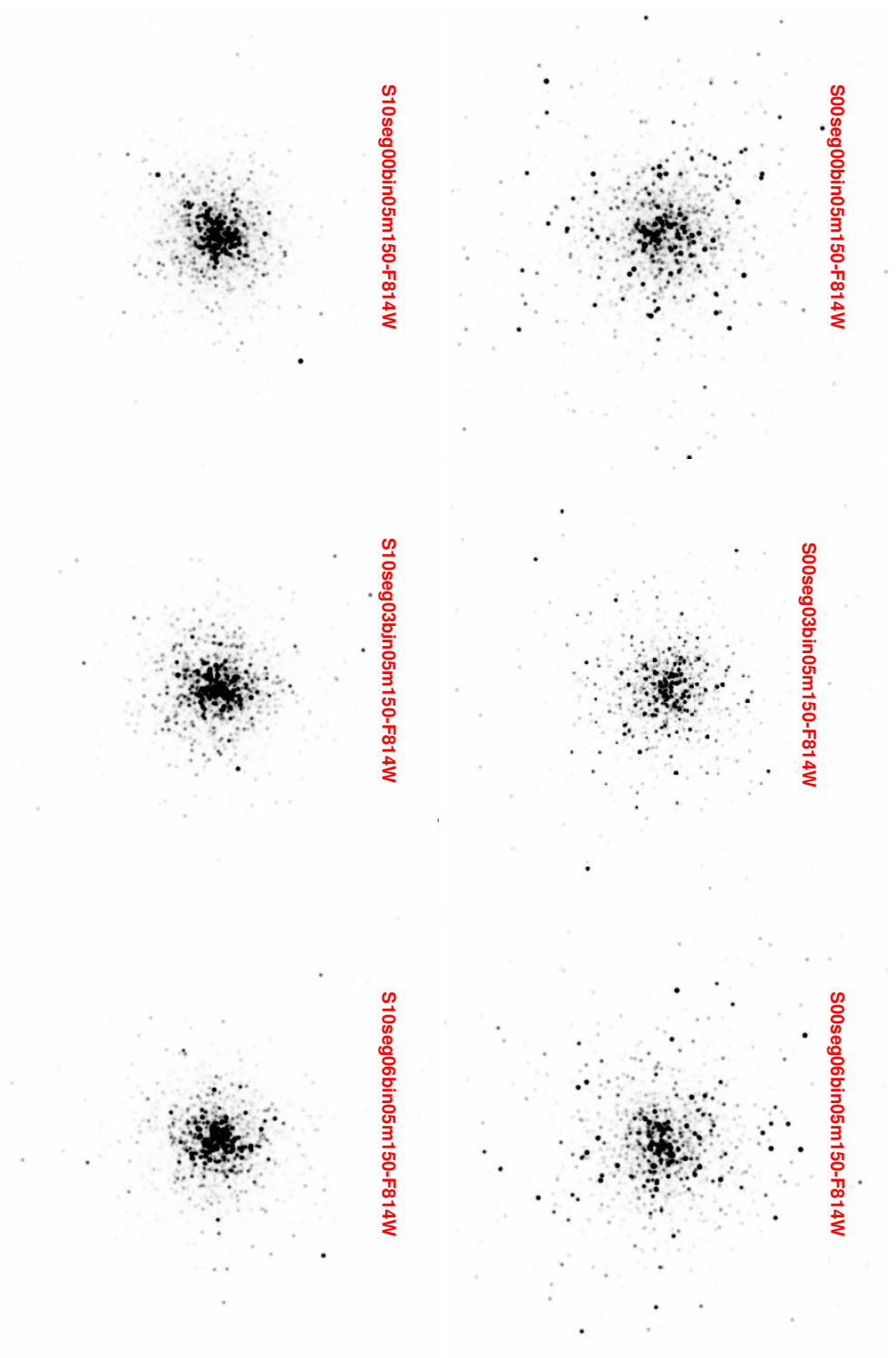


Figure 3.15 Synthetic scenes from simulation of S-clusters with the mass range of $(0.5 - 150)M_{\odot}$ at time 2 Myr in XZ plane. Not segregated: Upper images; Segregated clusters: Bottom images; 0% initial binaries: left; 30% initial binaries: middle; 60% initial binaries: right

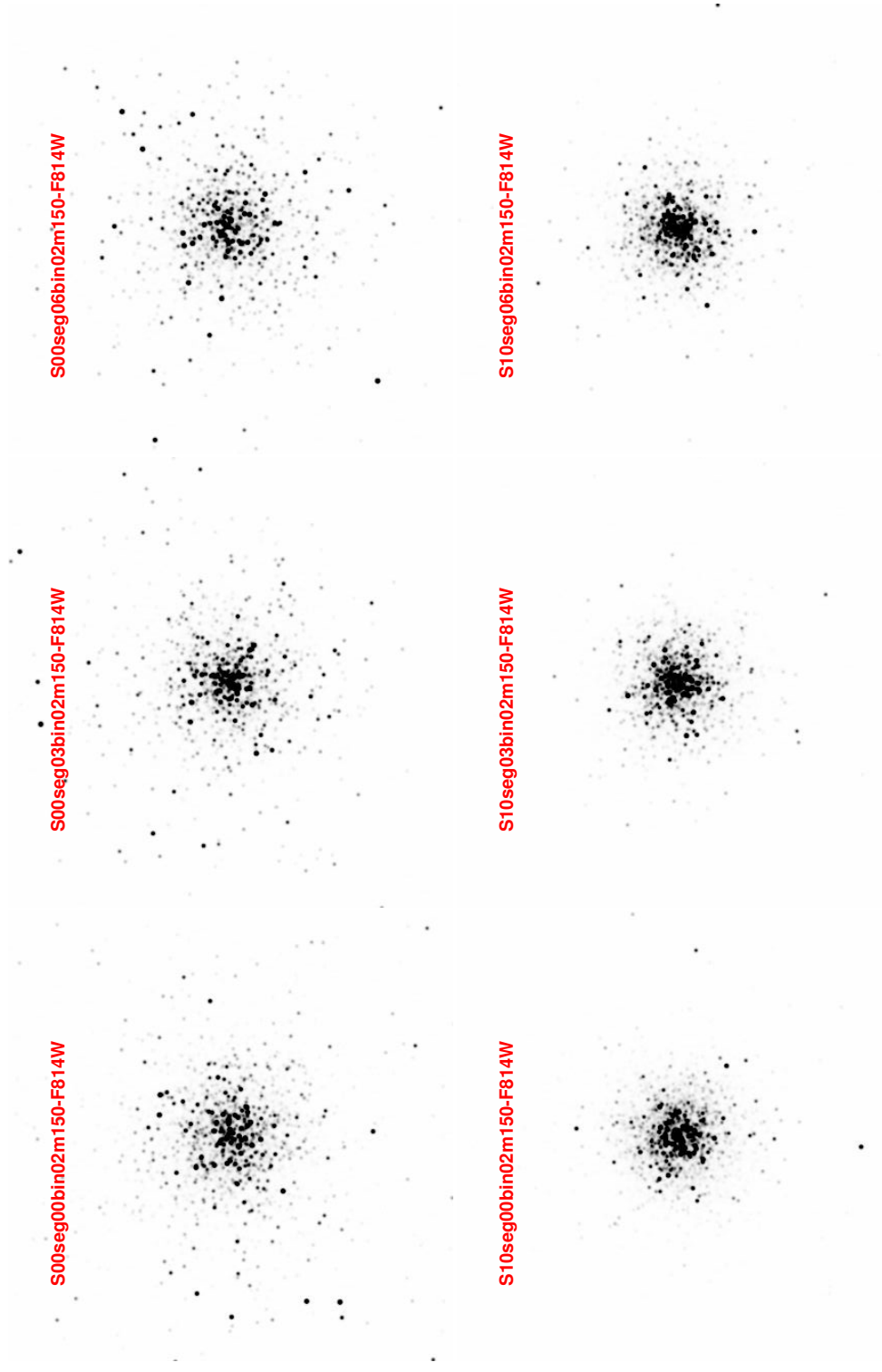


Figure 3.16 Synthetic scenes from simulation of S-clusters with the mass range of $(0.2 - 150)M_{\odot}$ at time 2 Myr in XZ plane. Not segregated: Upper images; Segregated clusters: Bottom images; 0% initial binaries: left; 30% initial binaries: middle; 60% initial binaries: right

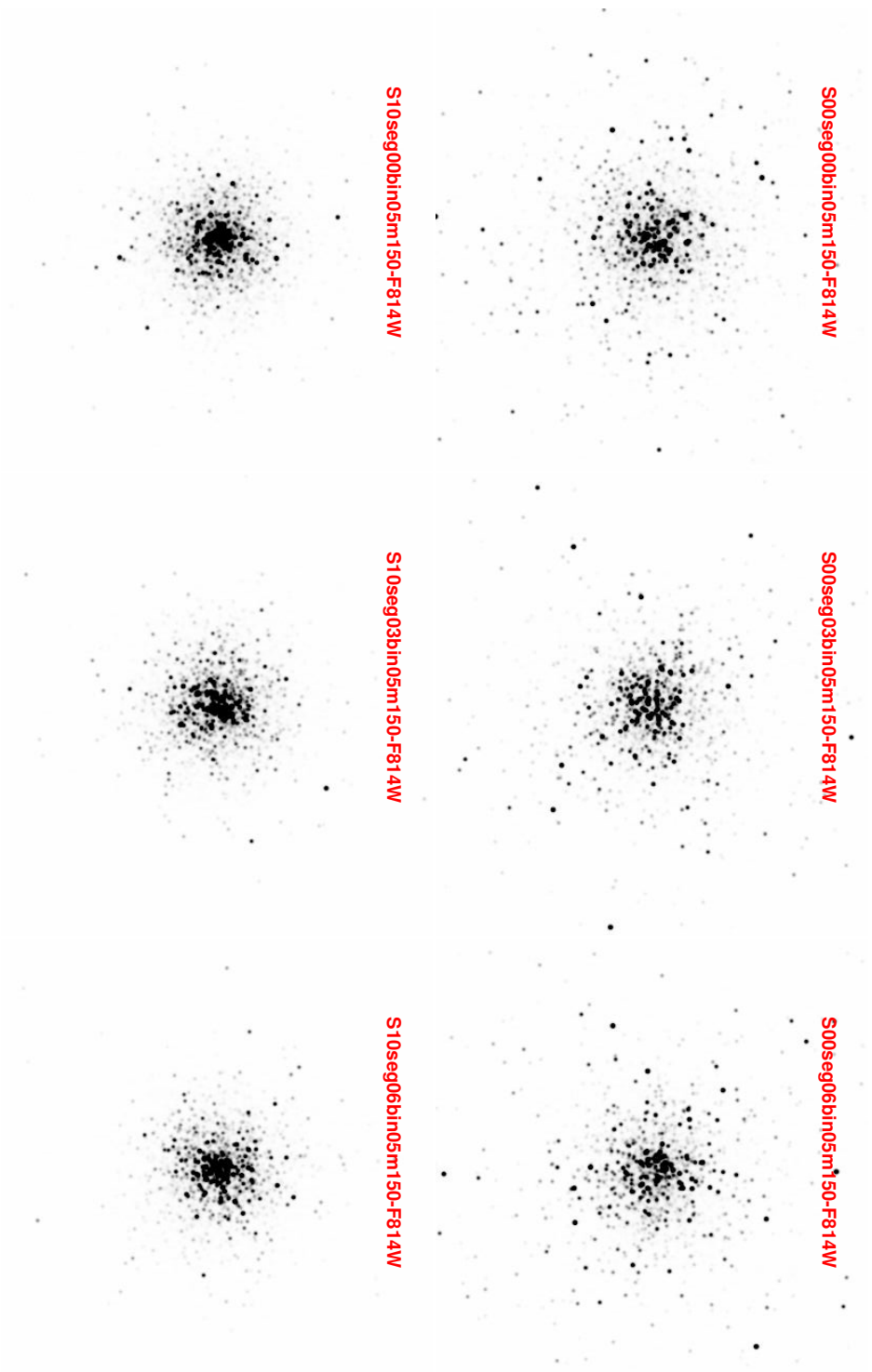


Figure 3.17 Same as Figure 3.15 but in XY plane.

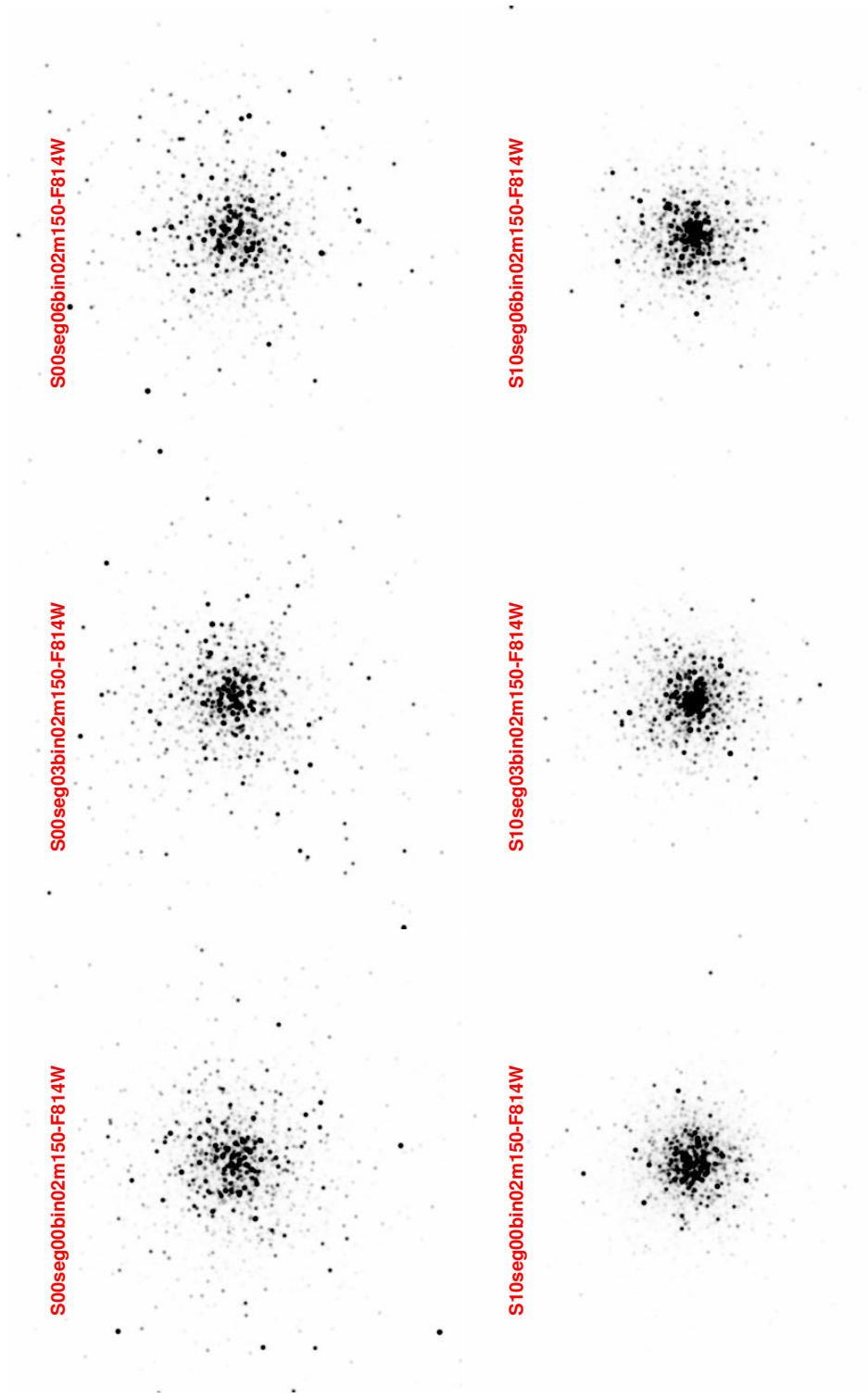


Figure 3.18 Same as Figure 3.16 but in XY plane.

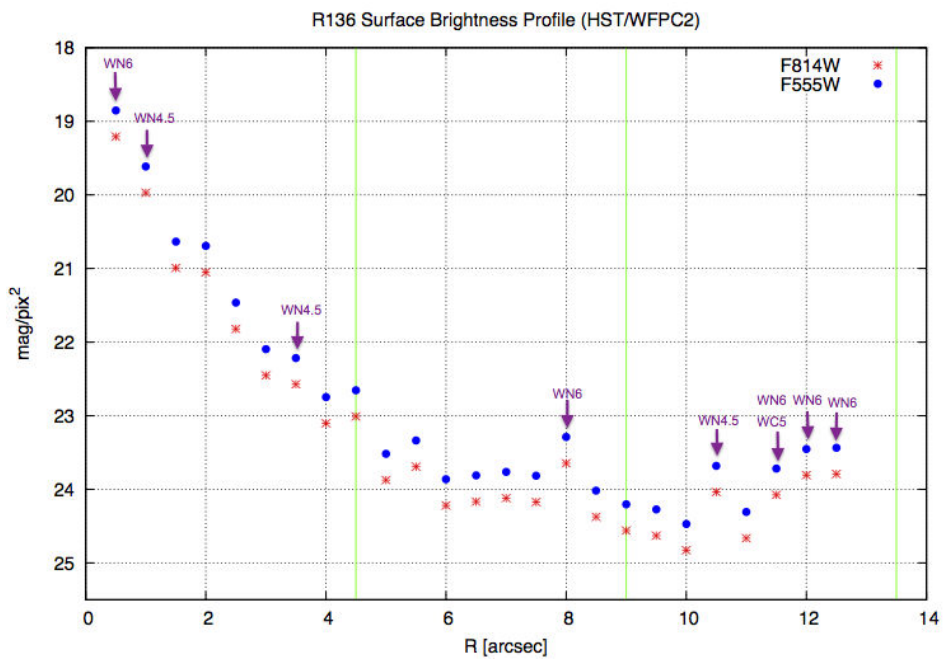


Figure 3.19 SBP of R136 in two filters F814W and F555W. 9 WR stars are shown in the plot.

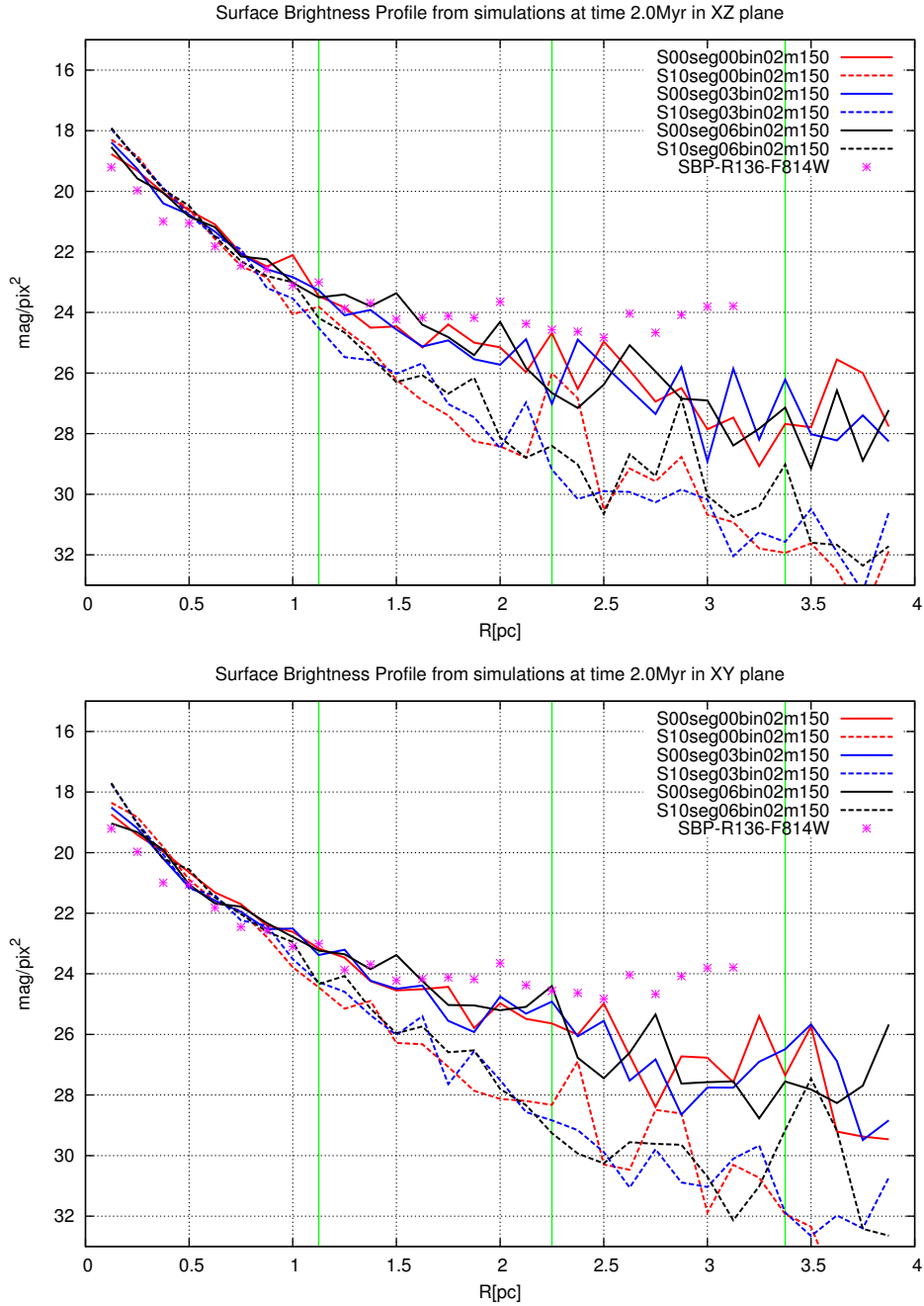


Figure 3.20 SBP from simulations at time 2 Myr for different sets of clusters in a mass range of $(0.2 - 150)M_{\odot}$. Top is the synthetic scenes created in XZ plan and Bottom belongs to XY plan. Solid lines belong to initial non-segregated clusters and dashed lines represent initial segregated clusters. Pink stars shows the SBP of R136 from WFPC2-PC data. Reddening is corrected for the HST data.

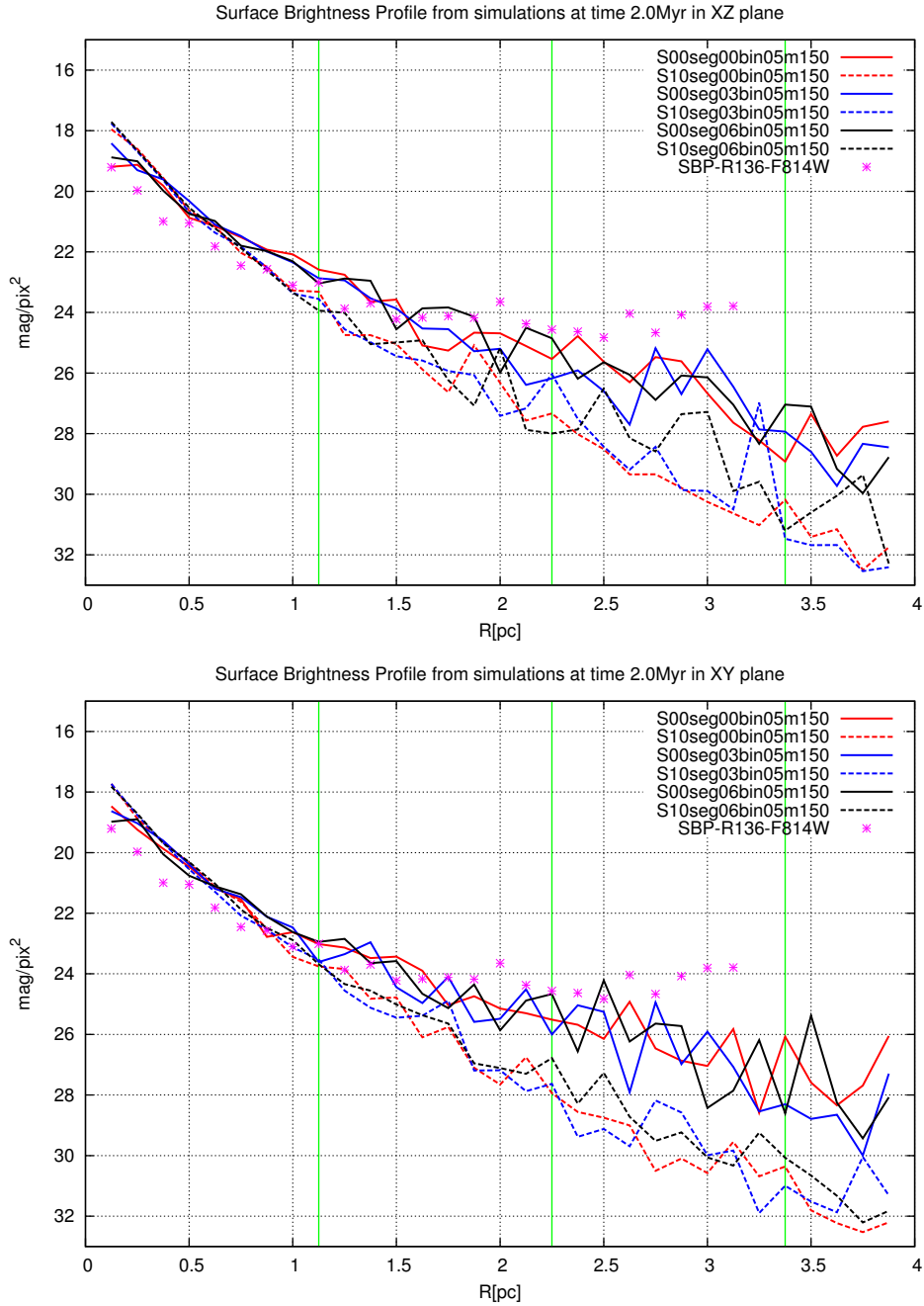


Figure 3.21 SBP from simulations at time 2 Myr for different sets of clusters in a mass range of $(0.5 - 150)M_{\odot}$. Top is the synthetic scenes created in XZ plan and Bottom belongs to XY plan. Solid lines belong to initial non-segregated clusters and dashed lines represent initial segregated clusters. Pink stars shows the SBP of R136 from WFPC2-PC data. Reddening is corrected for the HST data.

0.2 – 150 M_{\odot}						
Non segregated			Segregated			
Binary:	0%	30%	60%	0%	30%	60%
reg1:	0.165	0.105	0.114	0.244	0.339	0.275
reg2:	0.311	0.592	0.420	3.600	3.514	3.232
reg3:	2.002	2.233	2.258	8.679	11.800	8.542
total:	2.469	2.682	2.602	12.412	14.685	11.389
0.5 – 150 M_{\odot}						
Non segregated			Segregated			
Binary:	0%	30%	60%	0%	30%	60%
reg1:	0.234	0.279	0.200	0.315	0.327	0.379
reg2:	0.283	0.481	0.311	1.562	1.538	1.776
reg3:	1.368	1.533	1.339	8.448	7.462	4.861
total:	1.839	2.186	1.846	10.008	9.226	6.498

Table 3.2 χ^2 of SBP of simulated scenes at 2 Myr in XZ plane in three different regions and for the whole cluster. The smallest value is the closest one to SBP of R136.

0.2 – 150 M_{\odot}						
Non segregated			Segregated			
Binary:	0%	30%	60%	0%	30%	60%
reg1:	0.134	0.121	0.109	0.297	0.288	0.292
reg2:	0.314	0.346	0.233	3.535	3.247	3.147
reg3:	2.246	2.988	2.469	9.672	11.517	11.688
total:	2.646	3.444	2.808	12.837	14.238	14.153
0.5 – 150 M_{\odot}						
Non segregated			Segregated			
Binary:	0%	30%	60%	0%	30%	60%
reg1:	0.199	0.277	0.201	0.364	0.312	0.352
reg2:	0.268	0.388	0.334	2.085	2.056	1.620
reg3:	1.250	1.712	2.109	8.941	7.852	7.393
total:	1.680	2.278	2.644	10.902	9.824	9.145

Table 3.3 χ^2 of SBP of simulated scenes at 2 Myr in XY plane in three different regions and for the whole cluster. The smallest value is the closest one to SBP of R136.

STARFINDER ([Diolaiti et al. (2000)]) to extract the sources using analytical prepared Point Spread Function (PSF) related to the F814W filter. For HST/WFPC2-F814W we extracted 2660 stars and for the synthetic images, we extracted from 1759 up to 3193 sources depending on the scene. Using BC tables (explained in Section 3.3), we estimated the photometric mass of detected stars in each imaging data for different clusters. Furthermore we computed the MF for each simulated cluster at the evolution time of 2 Myr as following:

$$\log(N) = a \log\left(\frac{M}{M_{\odot}}\right) + b$$

Table 3.4 and 3.5, for the scenes in XZ and XY planes respectively, show the MF slopes for three regions ($r < 4''.5$, $4''.5 < r < 9''$, $9'' < r < 13.5''$) and also for the whole cluster at time of 2 Myr. MF slope of R136 in the same filter is as follow (see Figure 2.12 at 2 Myr with standard mass loss models.):

$$r < 4''.5 : a = -0.39 \pm 0.24$$

$$4''.5 < r < 9'' : a = -1.18 \pm 0.21$$

$$9'' < r < 13.5'' : a = -0.97 \pm 0.09$$

$$\text{For the whole FoV: } a = -0.89 \pm 0.14$$

To better compare the slopes Figure 3.22 on can compare them MF between simulations and R136 (Black solid line). In region 2 and 3 non-segregated simulated clusters exhibit closer values to the observed MF of R136.

3.3.3 Half-light radius

In a next step, we estimated the half-light radius (R_{hl}) of R136 versus those of synthetic scenes from the simulations at time 2 Myr.

In order to compare the simulated scenes to the observed R136 we computed R_{hl} in the same FoV as to HST imaging data (32.5"x32.5" in terms of PC). Corresponding results are outlined in Table 3.6. It can be seen that, unlike what $R_{half-mass}$ shows in the simulations, non-segregated

0.2 – 150 M_{\odot}						
Not segregated			Segregated			
Binary:	0%	30%	60%	0%	30%	60%
reg1:	0.06 ± 0.67	-0.06 ± 0.32	-0.03 ± 0.35	-0.23 ± 0.26	-0.31 ± 0.15	-0.19 ± 0.24
reg2:	-1.43 ± 0.15	-1.14 ± 0.17	-1.16 ± 0.28	-1.65 ± 0.02	-1.64 ± 0.13	-1.68 ± 0.15
reg3:	-1.32 ± 0.14	-1.06 ± 0.23	-1.31 ± 0.20	-1.44 ± 0.02	-1.58 ± 0.05	-1.47 ± 0.58
total:	-0.77 ± 0.09	-0.69 ± 0.15	-0.68 ± 0.19	-0.64 ± 0.06	-0.67 ± 0.16	-0.67 ± 0.67
0.5 – 150 M_{\odot}						
Non-segregated			Segregated			
Binary:	0%	30%	60%	0%	30%	60%
reg1:	0.13 ± 0.60	0.31 ± 0.54	0.11 ± 0.49	-0.04 ± 0.59	-0.08 ± 0.36	-0.09 ± 0.24
reg2:	-1.18 ± 0.11	-1.26 ± 0.40	-1.01 ± 0.14	-1.89 ± 0.24	-1.64 ± 0.26	-1.69 ± 0.29
reg3:	-1.17 ± 0.06	-1.33 ± 0.22	-1.22 ± 0.13	-1.79 ± 0.01	-2.54 ± 0.17	-1.20 ± 0.69
total:	-0.72 ± 0.04	-0.61 ± 0.22	-0.65 ± 0.10	-0.70 ± 0.04	-0.71 ± 0.15	-0.70 ± 0.12

Table 3.4 MF's slopes from simulated scenes at 2 Myr in XZ plane in three different regions and also for the the whole cluster.

0.2 – 150 M_{\odot}						
Non-segregated			Segregated			
Binary:	0%	30%	60%	0%	30%	60%
reg1:	0.01 ± 0.43	-0.05 ± 0.37	0.00 ± 0.54	-0.24 ± 0.23	-0.28 ± 0.29	-0.21 ± 0.21
reg2:	-1.42 ± 0.26	-1.18 ± 0.29	-1.26 ± 0.84	-2.03 ± 0.49	-1.64 ± 0.47	-1.61 ± 0.30
reg3:	-1.28 ± 0.01	-1.29 ± 0.29	-1.38 ± 0.43	-1.60 ± 0.44	-1.78 ± 0.28	-1.37 ± 0.29
total:	-0.75 ± 0.03	-0.70 ± 0.17	-0.73 ± 0.19	-0.66 ± 0.08	-0.68 ± 0.17	-0.65 ± 0.07
0.5 – 150 M_{\odot}						
Non-segregated			Segregated			
Binary:	0%	30%	60%	0%	30%	60%
reg1:	0.12 ± 0.62	0.11 ± 0.29	0.17 ± 0.46	-0.10 ± 0.41	-0.10 ± 0.35	0.01 ± 0.40
reg2:	-1.22 ± 0.11	-1.23 ± 0.15	-1.12 ± 0.20	-1.69 ± 0.10	-1.80 ± 0.28	-1.73 ± 0.35
reg3:	-1.32 ± 0.12	-1.29 ± 0.27	-1.06 ± 0.42	-1.99 ± 0.02	-1.49 ± 1.11	-1.93 ± 0.65
total:	-0.75 ± 0.05	-0.66 ± 0.12	-0.62 ± 0.13	-0.71 ± 0.07	-0.72 ± 0.14	-0.68 ± 0.13

Table 3.5 MF's slopes from simulated scenes at 2 Myr in XY plane in three different regions and also for the the whole cluster.

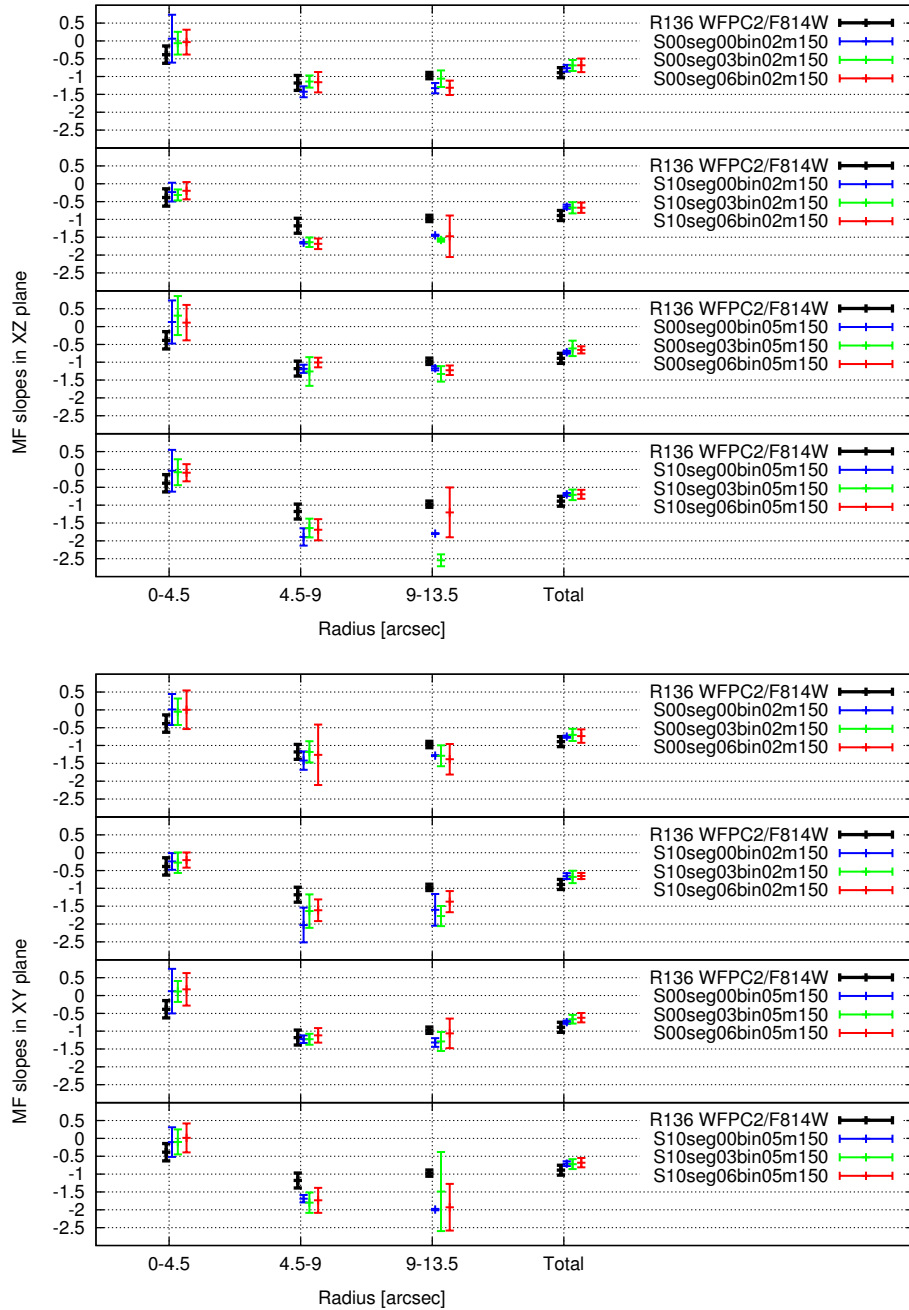


Figure 3.22 MF Slopes from simulated synthetic scenes at 2 Myrs in XZ (Top plots) and XY (Bottom plots) plane. Black solid lines belong to R136 from HST/WFPC2 data taken in F814W filter. Blue, Green and Red represents clusters with 0%, 30% and 60% initial binaries.

Model	Seg	BF	M_{min}	M_{max}	R_{hl} (XY)	R_{hl} (XZ)
			$[M_{\odot}]$	$[M_{\odot}]$	[pc]	[pc]
S00seg00bin05m150	0.0	0.0	0.5	150	0.43	0.50
S10seg00bin05m150	1.0	0.0	0.5	150	0.30	0.28
S00seg03bin05m150	0.0	0.3	0.5	150	0.40	0.43
S10seg03bin05m150	1.0	0.3	0.5	150	0.26	0.26
S00seg06bin05m150	0.0	0.6	0.5	150	0.46	0.48
S10seg06bin05m150	1.0	0.6	0.5	150	0.29	0.26
S00seg00bin02m150	0.0	0.0	0.2	150	0.42	0.43
S10seg00bin02m150	1.0	0.0	0.2	150	0.27	0.27
S00seg03bin02m150	0.0	0.3	0.2	150	0.36	0.38
S10seg03bin02m150	1.0	0.3	0.2	150	0.23	0.25
S00seg06bin02m150	0.0	0.6	0.2	150	0.42	0.43
S10seg06bin02m150	1.0	0.6	0.2	150	0.25	0.27

Table 3.6 R_{hl} calculated for different simulated scenes at 2Myr in XY and XZ plane.

clusters have larger half light radii than segregated ones.

At time 2Myr, clusters with $M_{min} = 0.5M_{\odot}$ have larger R_{hl} than clusters with $M_{min} = 0.2M_{\odot}$. It means that clusters with larger number of low-mass (high-mass) stars have smaller (larger) half-light radius. Also R_{hl} of the clusters with 0% and 60% initial binaries are more close together and both are larger than clusters with 30% initial binaries.

3.3.4 Neighbor radius

Neighbor radius ($R_{neighbor}$) is an arbitrary distance to find 100 neighbor stars from a given star. In the core of the cluster that has a higher stellar density, this radius is smaller than in the outer

regions of the cluster. For R136 we calculated this radius for all the sources that have been detected in the HST image. We carried the same procedure on every simulated scene, with different characteristics, i.e. segregated or not, different binary fractions, etc... both in XY and XZ planes. Figure 3.23 and 3.24 depict the corresponding results. Red dots in each plot correspond to R136, Green and Blue dots correspond to not-segregated and segregated clusters. One can conclude that for all the simulated scenes, non-segregated clusters better fit to the R136 by HST considering the general trend of the slope.

3.4 Discussion of the results

We carried out a study of R136 in two steps. In a first and as exhaustive as possible step based on the NBODY6 code, we simulated a grid of synthetic young starburst compact clusters similar to R136, starting from its state-of-the-art basic parameters: i.e. age, distance, luminosity of individual member stars. In a second step we selected the likeliest synthesized images of R136 that match the observed visible wavelengths data from HST. The choice of this image provides a set of physical properties that explain best the expansion, the mass loss of the stellar populations in R136 as well as their binary fraction for instance.

Regarding the expansion of the cluster we found that in all cases segregated clusters expand more than non-segregated clusters, and that the former have larger R_h than the latter. Clusters with stellar evolution (S-clusters) expand significantly around 3 Myr because of the evolution of very massive stars, that possess for some of them extreme winds of $10^{-8} - 10^{-5} [M_{\odot}/\text{yr}]$ [Lamers& Cassinelli (1999)]. Clusters with dynamical evolution (D-clusters) alone expand more due to the presence of more massive stars.

Regarding the mass loss of the cluster and escapers: the total mass loss of S-clusters is larger than for D-clusters. This is due to the evolution of massive stars themselves whilst D-clusters

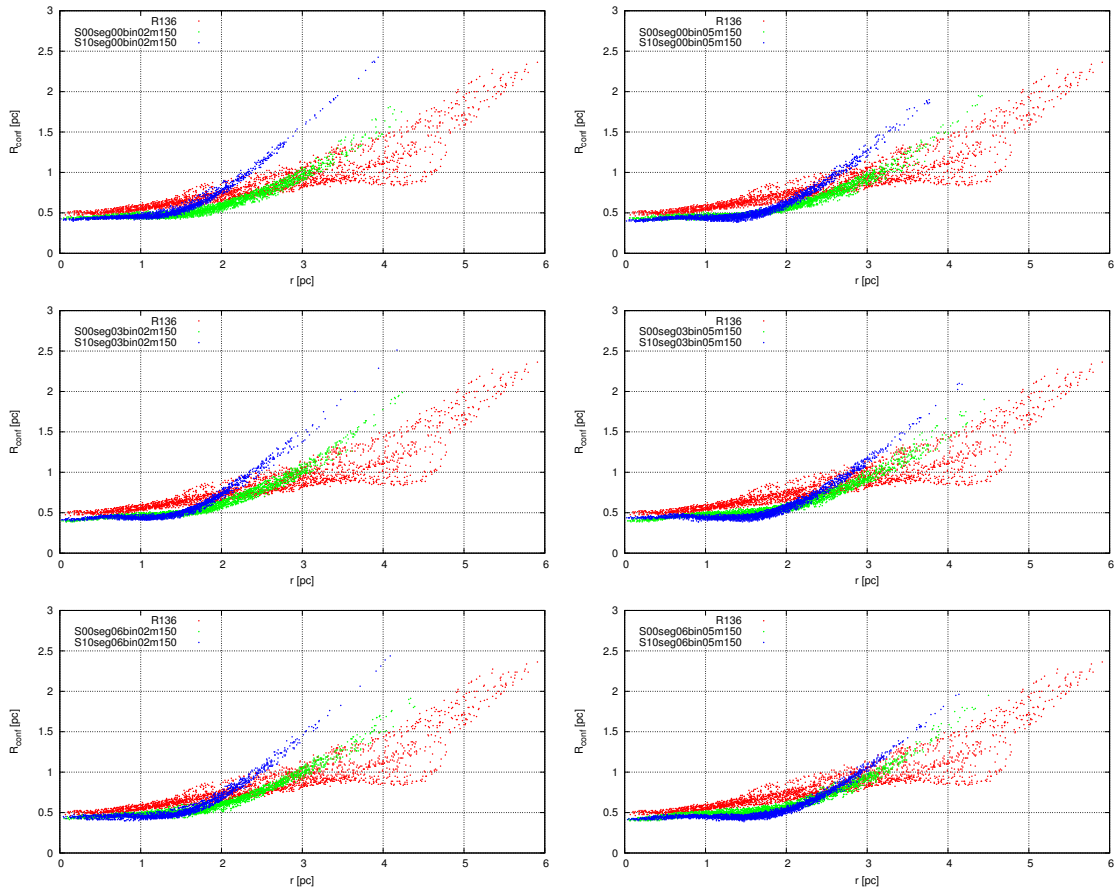


Figure 3.23 $R_{neighbor}$ of simulated scenes in XZ-plane compare to R136 (Red dots). Blue and Green dots belong to the Segregated and Non-Segregated clusters. Left: clusters with the mass range of $(0.2 - 150)M_{\odot}$ and Right plots are for $(0.5 - 150)M_{\odot}$. Upper, middle and bottom plot represents clusters with 0%, 30% and 60% initial binaries.

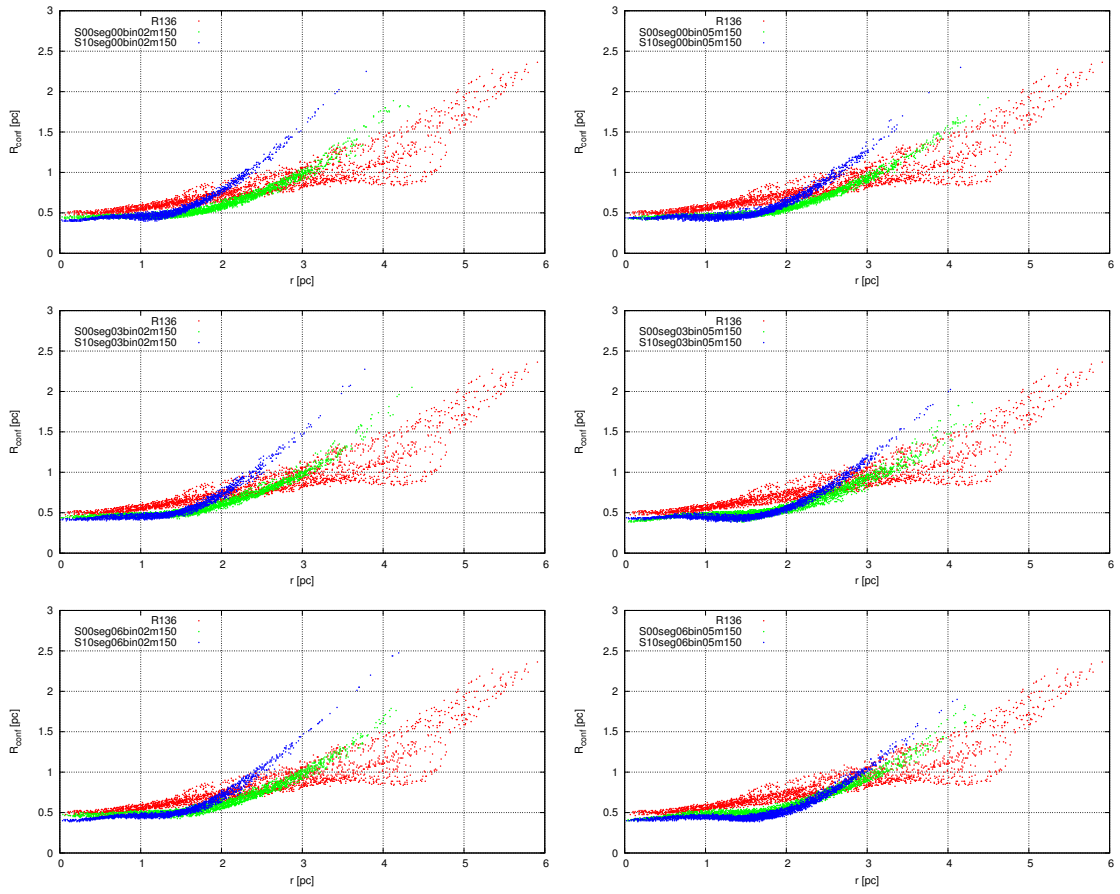


Figure 3.24 $R_{neighbor}$ of simulated scenes in XY-plane compare to R136 (Red dots). Blue and Green dots belong to the Segregated and Non-Segregated clusters. Left: clusters with the mass range of $(0.2 - 150)M_{\odot}$ and Right plots are for $(0.5 - 150)M_{\odot}$. Upper, middle and bottom plot represents clusters with 0%, 30% and 60% initial binaries.

undergo escapers loss only. S-clusters containing more massive stars, present a larger mass loss in their early stages of evolution. D-clusters lose more escapers as the binary fraction increases.

On the other hand segregated clusters lose less binaries than non-segregated ones and in the special case of clusters with 30% initial binaries made of low-mass stars, the binary loss is significantly larger.

Concerning periods and eccentricities: almost half of the low-mass binaries dissolve within 1 Myr. Clusters with stellar evolution lose their massive binaries according to the evolution of massive stars themselves. In all cases binaries keep the memory of initial eccentricities distribution during the first 4 Myr. For this period, only the massive binaries keep the memory of initial period distribution.

Having these general properties in mind we used synthetic scenes with the same observational resolution as HST/WFPC2-PC/F814W. For this purpose we computed a grid of bolometric correction tables which provide the flux of different stars in F814W filter using Geneva stellar evolution models and model atmosphere (TLUSTY for O,B stars and Kurucz for other spectral types). These synthetic images have the same pixel scale, spatial resolution and FoV of WFPC2 data on R136.

To conclude on the best R136 from its synthesized images we used 4 different criteria based on: SBP, MF's slopes, R_{hl} and R_{conf} .

We calculated the surface brightness profiles (SBP) of R136 and the synthetic scenes (in both XY and XZ planes). A χ^2 criterion on the SBP permits to chose can the most probable synthesized R136 in three different regions and also for the whole cluster. SBP, R_{hl} can easily be driven for each scene. Thus, using the photometry on each synthesized R136 image, we derived the mass of detected sources and plotted the mass function (MF) and $R_{neighbor}$.

Using the 4 criteria all together, even though they are not completely independent, we conclude that R136 is best represented by a non-segregated cluster (in $r < 4pc$).

This result can explain the dominant mechanism for the formation of very massive stars among

two main formation scenarios of gas accretion and collision between less massive stars that are explained in details by [Krumholz (2015)]. Initially a non-segregated cluster cannot provide sufficient dense conditions and a higher mean stellar mass in the core, for collisions to occur before the final stages of massive stars evolution. Presently, no convincing evidence exists such as fragmentation, radiation pressure, photoionization and stellar winds to stop the growth of stars by accretion [Krumholz (2015)]. So initially non-segregated clusters may better explain the formation of massive stars by accretion.

Effectively, accretion based models predict the low-mass companions, in addition to their massive companions, at separation of 100-1000 AU [Kratter & Matzner (2006), Kratter et al. (2008), Kratter et al. (2010), Krumholz et al. (2012)] while the collisionally-formed stars will lack low-mass companions. These companions can be observationally detected by using high angular resolution and high contrast instruments like VLT/SPHERE [Zurlo et al. (2014)], the future E-ELT where R136 would be resolved as NGC3603 by the VLT and NGC3603 resolved by the VLT as the Trapezium cluster in Orion by a 1-2m class telescope.

Note that for the comparison of synthesized versus observed images of R136, we considered the median value of the extinction (in F814W filter) derived from 26 known O-type stars in the FoV of the HST data (Khorrami et al. in prep). If the spatial distribution of dust were taken into account according to the real position of massive stars in the cluster, the effect of confusion would even be worse. Since massive stars are expected to clear out dust from their neighborhood, the extinction would affect the low mass stars specially. This would make them undetectable in the visible wavelengths, that introduces an additional bias on the HST images reinforcing the segregation scenario for R136 [Ascenso et al. (2009)].

3.5 Summary

In this work we proposed a new approach to compare the results of the NBODY6 code with data from high contrast imaging observations obtained on large optical telescopes at their diffraction limit. In previous studies, the direct output of the code is compared with observational material where one compares for example the density profile of hundred thousands of stars with the density of a few thousands of them extracted from observations in practice. Our method is rather based on synthesizing the observations directly from NBODY6 itself. These synthesized images are matched to real observations in a final step for their likeliness.

We based our study on data taken from HST/WFPC2 archives. For this we produced simulated scenes at the resolution of HST/WFPC2-pc/F814W images) and created BC tables which provide the flux of different stars in F814W filter using Geneva stellar evolution models and TLUSTY atmosphere model for O,B stars and Kurucz model for other spectral types. These synthetic images have the same pixel scale, spatial resolution and FoV as the WFPC2 data of R136 from HST. Note that our modeling of stellar members atmospheres could be improved by considering more appropriate atmosphere codes for the WR components of R136, for example using grids of model atmosphere like TLUSTY but including winds [Neugent et al. (2015)]. On the other hand our synthesized R136 clusters could be improved for their evolution by adding time-space depending gas potential to the model. This could ideally be included in NBODY6 code itself (private communication R. Wunsch).

In summary our study is in favor of the R136 to be a non-segregated cluster: a result contradicting the generally accepted picture. A result that deserves more exhaustive and systematic observations of R136 to be conclusive. Such observations should be carried out in as many spectral bands as possible: from the visible to optical and thermal IR wavelengths to overcome the confusion effect specially. This becomes possible using the VLT and high contrast AO imaging in the optical, future observations from space (JWST) or the E-ELT [Zinnecker (2006)]. Ultimately

long baseline imaging interferometry from the ground should enable us to resolve the stellar binary components of R136 or similar compact clusters.



ESO's Paranal Observatory. The first photograph from the ESO Ultra HD Expedition. The four Unit Telescopes, Antu, Kueyen, Melipal and Yepun, one of the Auxiliary Telescopes of the Very Large Telescope (VLT) and the VLT Survey Telescope (VST), are captured from an unusual perspective in this image. Taken by a fish-eye lens, this photography technique produces a 360 degree view of the location, creating an immersive Paranal world with the swirling Milky Way at the centre of it.

Credit: ESO/B.Tafreshi (twanight.org)

Chapter 4

VLT/SPHERE Photometry on NGC3603

Abstract: In this chapter we present new near-infrared photometric measurements of the core of the young massive cluster NGC 3603 obtained with extreme adaptive optics. The data were obtained with the SPHERE instrument mounted on ESO's Very Large Telescope, and cover three fields in the core of this cluster. We applied a correction for the effect of extinction to our data obtained in the J and K broadband filters and estimated the mass of detected sources inside the field of view of SPHERE/IRDIS, which is $13.5'' \times 13.5''$. We derived the mass function (MF) slope for each spectral band and field. The MF slope in the core is unusual compared to previous results based on Hubble space telescope (HST) and very large telescope (VLT) observations. The average slope in the core is estimated as -1.06 ± 0.26 for the main sequence stars with $3.5 M_{\odot} < M < 120 M_{\odot}$. Thanks to the SPHERE extreme adaptive optics, 814 low-mass stars were detected to estimate the MF slope for the pre-main sequence stars with $0.6 M_{\odot} < M < 3.5 M_{\odot}$, $\Gamma = -0.54 \pm 0.11$ in the K-band images in two fields in the core of the cluster. For the first time, we derive the mass function of the very core of the NGC 3603 young cluster for masses in the range 0.6 - 120 M_{\odot} . Previous studies were either limited by crowding, lack of dynamic range, or a combination of both.

4.1 Introduction

Among Galactic spiral arm clusters, the NGC 3603 young cluster, located in its namesake giant HII region [Kennicutt (1984)], is the most compact and youngest cluster with an age of 1 Myr [Brandl et al. (1999), Stolte et al. (2004), Sung & Bessell (2004)] and a central density of $6 \times 10^4 \text{ M}_\odot \text{ pc}^{-3}$ [Harayama et al. (2008)]. The cluster is known to contain three massive and luminous central stars with spectral types as early as O2V [Walborn et al. (2002), Moffat et al. (2004)], and up to 50 O-type stars in total [Drissen et al. (1995)]. The most massive stars exhibit both characteristics of WN6 stars and Balmer absorption lines [Drissen et al. (1995)], suggesting that they are actually core hydrogen burning rather than evolved stars [Conti et al. (1995), de Koter et al. (1997)]. Two of these three Wolf-Rayet (WR) stars are very close binaries [Schnurr et al. (2008)]. The total mass of the cluster is estimated as 10^4 M_\odot [Harayama et al. (2008)], with an upper limit to the dynamical mass of $17600 \pm 3800 \text{ M}_\odot$ [Rochau et al. (2010)]. NGC 3603 provides a unique opportunity to study the formation of massive stars embedded in clusters at their early stages. Studying such clusters is not generally straightforward owing to the limited angular resolution of telescopes in addition to uncertainties from existing models [Ascenso et al. (2009)]. Besides, extinction from the Galactic plane and the birth place of massive stars, which is immersed in dust and gas, play an important role.

All these combined effects can introduce an observational bias that hampers differentiating models of massive star and cluster formation: i.e., singular collapse of a rotating molecular cloud core with subsequent fragmentation in a flattened disk or competitive accretion, or, for example, external triggering by cloud-cloud collision (ref., e.g., Johnston et al. 2014). To test these models, high angular resolution observation in the infrared are the best strategy as they minimize the effects of source confusion and spatial extinction variations.

In this context, the extreme adaptive optics (XAO) of the new instrument SPHERE [Beuzit et al. (2008)] on the VLT, enabled us to observe deeper in the core of NGC 3603 in the near-infrared

J and K bands to better probe the massive star cluster at a high resolution in the range of 20-40 mas resolution, which is comparable to the HST in the visible.

4.2 Data and photometry

We obtained data via Guaranteed Time Observation (GTO) runs to image NGC 3603 using the dual mode of IRDIS [Langlois et al. (2014)], enabling simultaneous observations in two spectral bands on the VLT. The observations were performed in two epochs in 2015 (March and June), with high dynamic and spatial resolution imaging of three regions, each with a field of view (FoV) of $13.5'' \times 13.5''$, one centered on the core of the cluster (F0 shown in Figure 4.1) and two regions (F1 and F2 shown in Figure 4.2 and 4.3) to cover the radial extent of the cluster (Figure 4.5 Top). To facilitate homogeneous photometric calibrations, F1 and F2 partially overlap with F0. The data consist of 400, 300, and 320 frames of 0.8s exposures in the IRDIS broadband K filter (IRDIS/BB-K) for F0, F1, and F2, respectively, and 400, 150, and 160 frames of 4.0, 2.0, and 2.0s exposures in IRDIS broadband J (IRDIS/BB-J), respectively, during the two observing epochs. Neutral density (ND) filters were used for the IRDIS/BB-J data to avoid saturating the brightest stars. The average airmass during these observations was 1.25-1.26. A log of the observations is presented in Table 4.1.

We used the SPHERE pipeline package¹, for correcting dark, flat, distortion, and bad pixels. As SPHERE filters in BB-J and BB-K are similar to ESO's Nasmyth Adaptive Optics System Near-Infrared Imager and Spectrograph (NACO), we corrected the photometric zero-points of SPHERE by comparing them to the magnitudes of spectroscopically known stars (preferentially isolated sources) in NACO [Harayama et al. (2008)] J and K filters.

For the photometry, we used the STARFINDER package implemented in IDL [Diolaiti et al.

¹http://www.mpia.de/SPHERE/sphere-web/nightly_builds-page.html

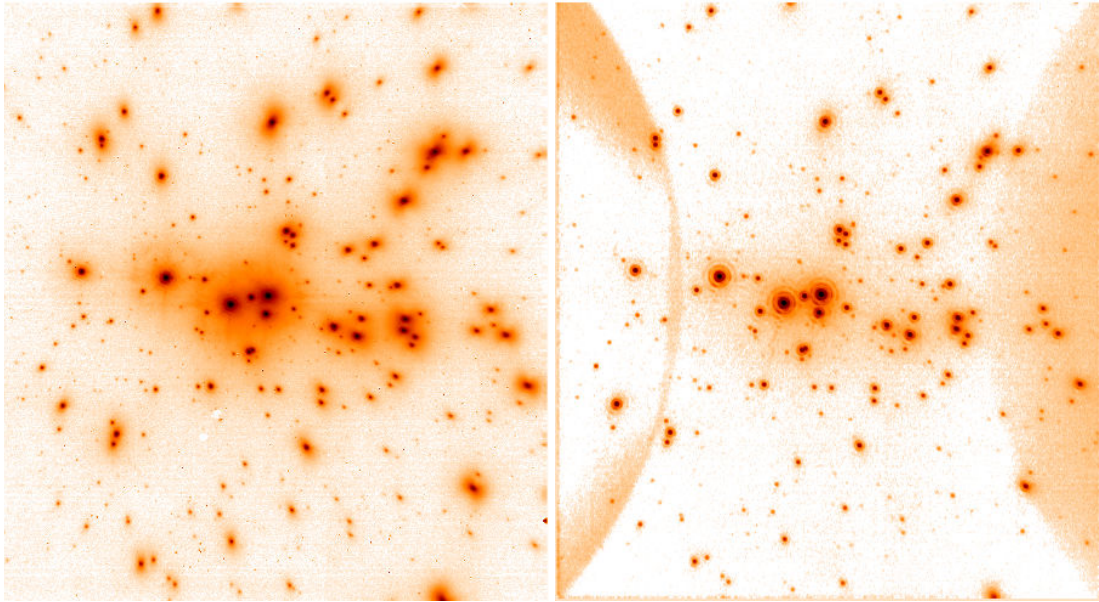


Figure 4.1 SPHERE/IRDIS image of NGC3603-F0 in J (left) and K (right)

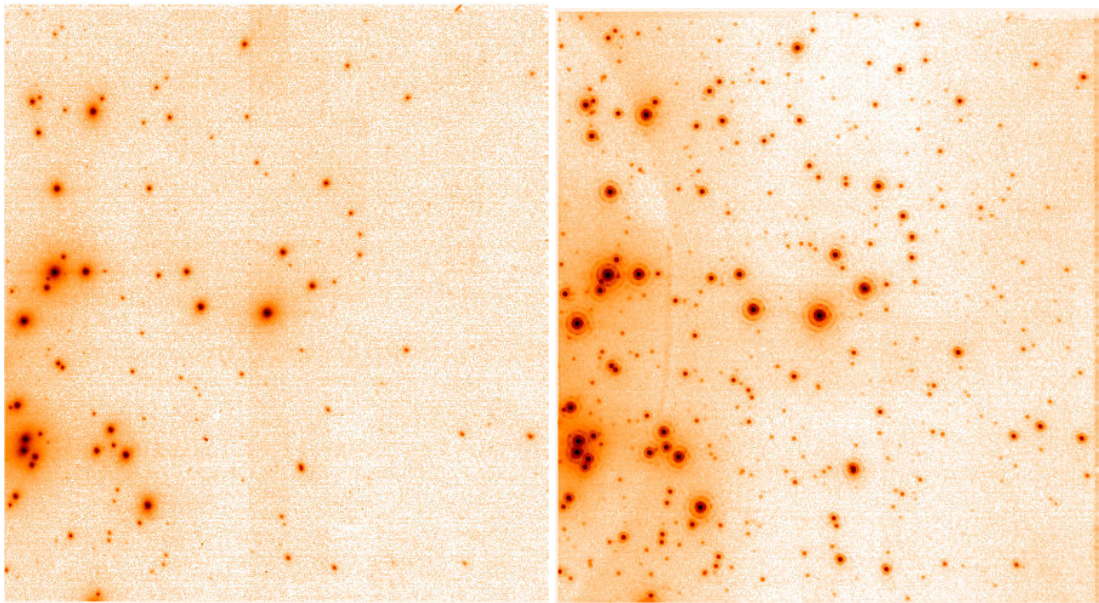


Figure 4.2 SPHERE/IRDIS image of NGC3603-F1 in J (left) and K (right)

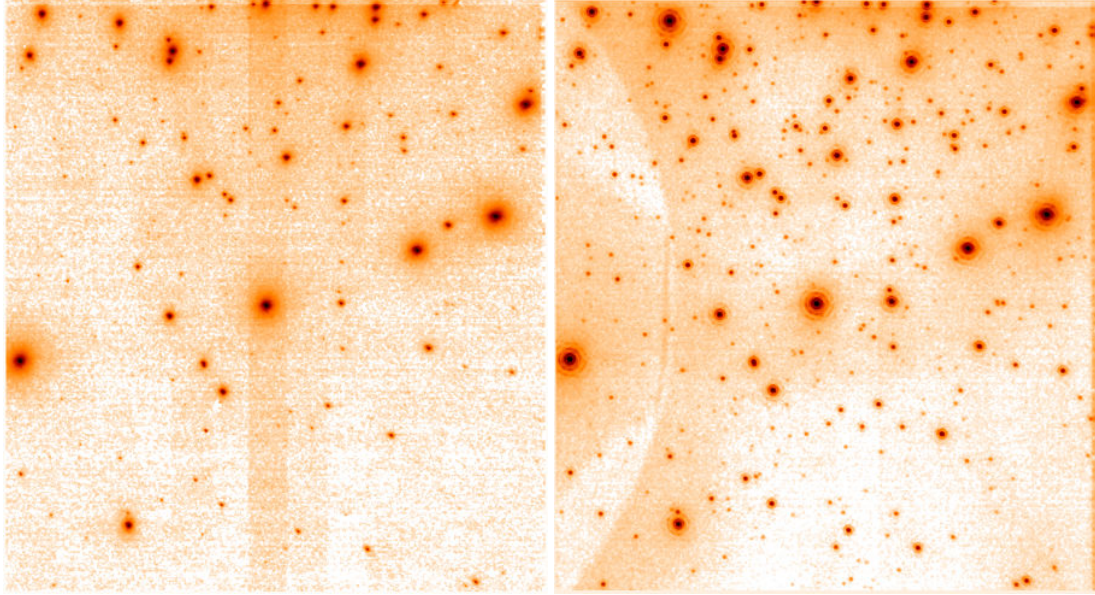


Figure 4.3 SPHERE/IRDIS image of NGC3603-F2 in J (left) and K (right)

(2000)] to derive the local point spread function (PSF) to detect stellar objects, while estimating instrumental magnitudes, i.e., before the photometric zero-point corrections. For this, each field is divided into subregions to extract the empirical local PSFs from isolated sources in the image itself. Local PSFs are then used to extract the flux of the sources to compensate for the local distortion effect. This is particularly suitable for AO-assisted imaging data where one can face locally distorted PSFs that hamper photometric measurements along different parts of the IRDIS FoV.

Consequently, 410 (290), 149 (364), and 445 (682) sources were detected in the J and K bands in F0, F1, and F2, respectively, by limiting them to a minimum correlation of 0.8 with the PSF. We also put a threshold limit of one standard deviation of sky brightness. Table 4.2 gives the details of the total number of detected sources in each field for a given filter.

The high Strehl ratio, and the resulting high dynamic range close to bright stars, enabled us to detect stellar sources that are 10.6 and 9.8 magnitudes fainter than the brightest sources in J and K

Table 4.1 Exposure time log and faintest stars (SNR > 4.2) of VLT/SPHERE observations. Δ_J and Δ_K are the differences between the maximum and minimum magnitudes in F0, F1 and F2 fields.

Field (Obs. date)	Filter	Single/Total Exposure[s]	λ_{cen} [nm]	Δ_λ [nm]	mag_{max}	mass [M_\odot]	Δ_{mag}
F0 (2015-03-31)	B-J	4.0/1600	1245	240	18.7	0.43	10.6
F0 (2015-03-31)	B-K	0.83/335.0	2182	300	16.4	0.63	9.5
F1 (2015-06-07)	B-J	2.0/300.0	1245	240	18.9	0.35	9.0
F1 (2015-06-07)	B-K	0.83/251.3	2182	300	18.1	0.16	9.8
F2 (2015-06-07)	B-J	2.0/320.0	1245	240	18.9	0.35	9.3
F2 (2015-06-07)	B-K	0.83/269.0	2182	300	18.8	0.11	9.6

bands, respectively. Sources with K magnitude of 18.8 and J magnitude of 18.9 could be detected in the core of NGC 3603.

Our test experiments (shown in 4.4) for completeness correction (500 artificial-star per flux) suggest that we should reach a completeness level $\geq 80\%$ for stars brighter than 17.5 mag in F1 and F2 (0.22 M_\odot in K-band and 0.94 M_\odot in J-band). The quality (Signal to Noise Ratio) of data in F0 in K-band (in March 2015) was not as good as in F1 and F2 in the second run (June 2015) thus the dynamic range is smaller. In F0, stars brighter than 15.3 in K-band (1.57 M_\odot) and 16.5 in J-band (1.8 M_\odot) have completeness level $\geq 80\%$. Table 4.1 gives the faintest magnitudes obtained in the different fields F0, F1 and F2 by SPHERE within the exposure time limits of the run.

4.3 Extinction and CMD

In order to correct for extinction, 31 O stars on or close to the main sequence (class V) were selected from [Harayama et al. (2008)]. These stars are encircled in green in the top panel of Figure 4.5.

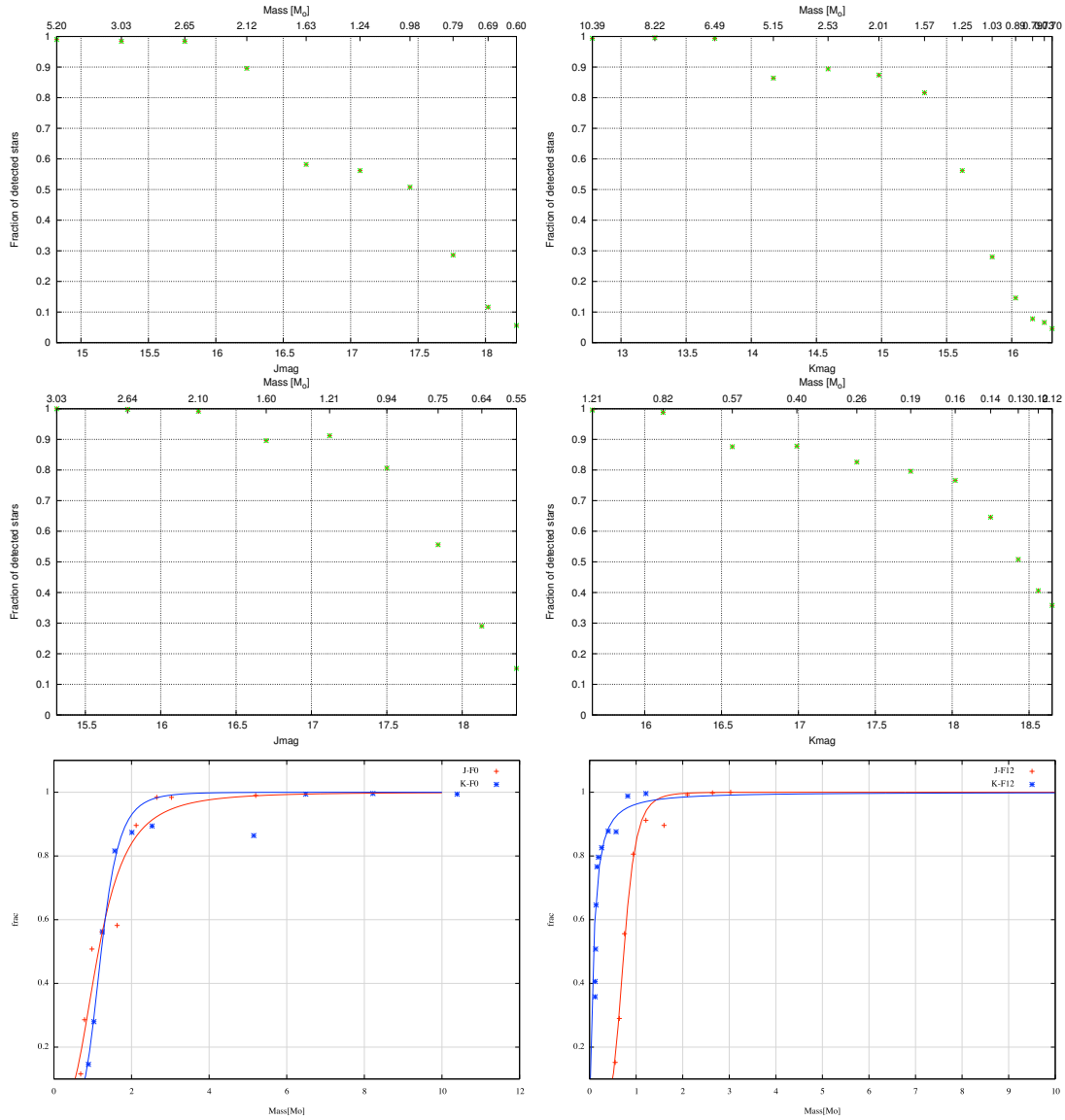


Figure 4.4 Incompleteness test on three fields in NGC3603 of SPHERE data in J (left) and K (right). Each point represent the 500 artificial star test. Up: F0; middle: F1 and F2; bottom: shows the final results with fitted line in F0 (left) and F1-F2 (right).

To estimate their intrinsic magnitude, their T_{eff} were estimated from Table 4 of [Martins et al. (2005)] and their $\log g$ as a function of age (1.5 Myr) according to the PARSEC² stellar evolution models [Bressan et al. (2012)], adopting Galactic metallicity. We assumed a distance of 6 kpc (Section 4.4) for these O stars.

We derived the color excess for selected O stars in the two IRDIS-BB J and K filters at the distance of 6 kpc. We adopted the maximum weighted value for $E(J-K)$, which is 0.76 ($A_V = 4.5$). This value results in A_J and A_K as 1.269 and 0.504, respectively, (from [Rieke & Lebofsky (1985)]).

We found 239, 118, and 191 sources detected in both J and K data in F0, F1, and F2, respectively. The color magnitude diagrams (CMDs) for these different fields are shown in Figure 4.6.

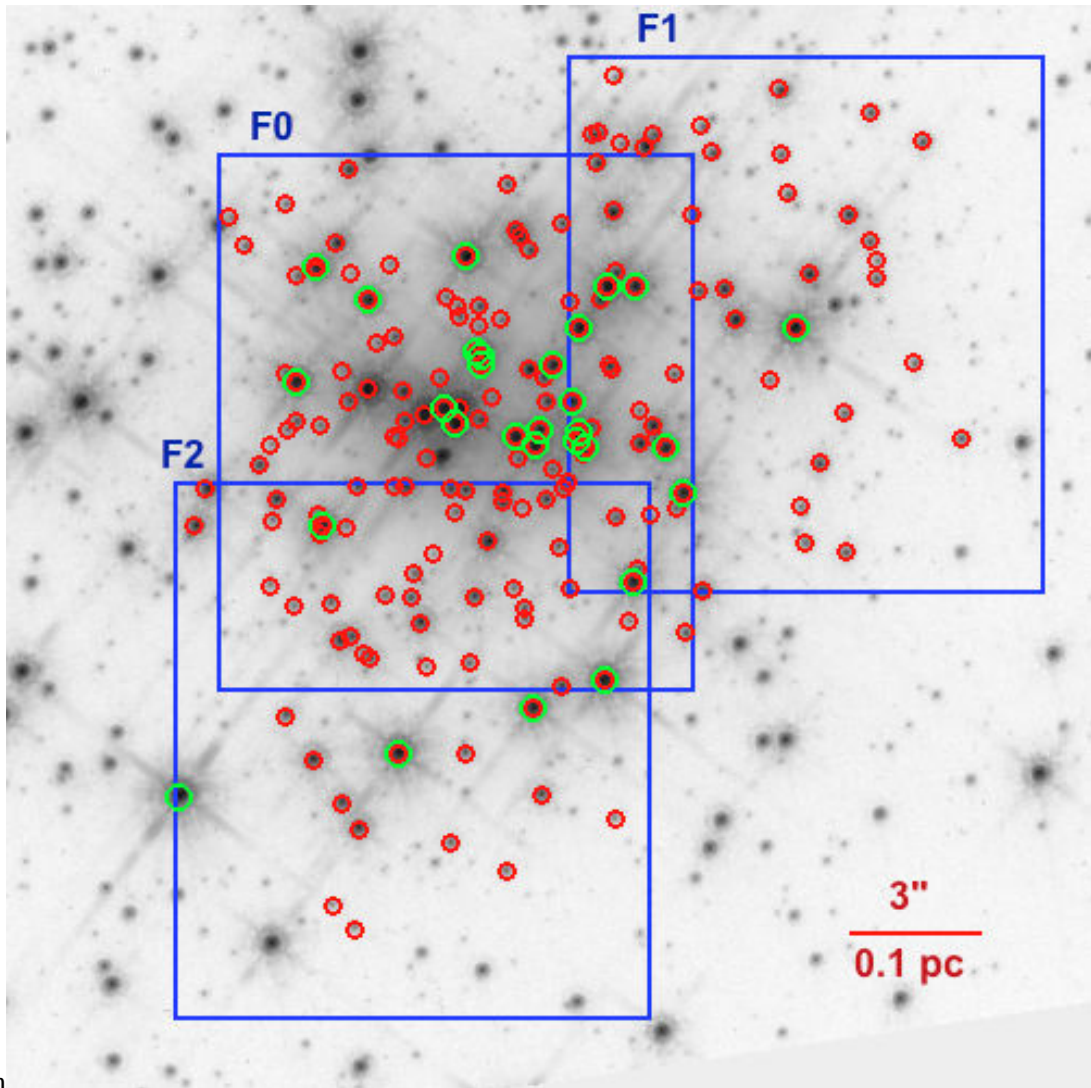
4.4 Mass Functions

We used the stellar evolution tracks from PARSEC mentioned above to estimate stellar masses at the age of 1 Myr. The distance of the cluster was taken as 6 kpc which fits well with the observed CMD, isochrone and extinction, and is also in good agreement with [Stolte et al. (2004)], [?] and [Harayama et al. (2008)].

Using grids of stellar evolutionary tracks and extinction for each filter we can estimate the stellar masses separately from the photometry in each filter.

The slope of the mass function Γ can be estimated from Eq. 4.2 where M is stellar mass and N is number of stars in the logarithmic mass interval $\log_{10}(M)$ to $\log_{10}(M) + 0.2\log_{10}(M)$. We used an implementation of the nonlinear least-squares (NLLS) Marquardt-Levenberg algorithm to

²<http://stev.oapd.inaf.it/cgi-bin/cmd>



mm

Figure 4.5 HST/WFPC2-PC/F814W core of NGC 3603: blue squares depict the three fields observed with SPHERE-IRDIS. Green circles refer to the known O-type stars from [Harayama et al. (2008)]. Red circles show the stars in [Harayama et al. (2008)] catalog, which we used for calibrating zero-points in different fields. There are 113, 45, and 51 stars common between [Harayama et al. (2008)] in the SPHERE F0, F1, and F2 fields.

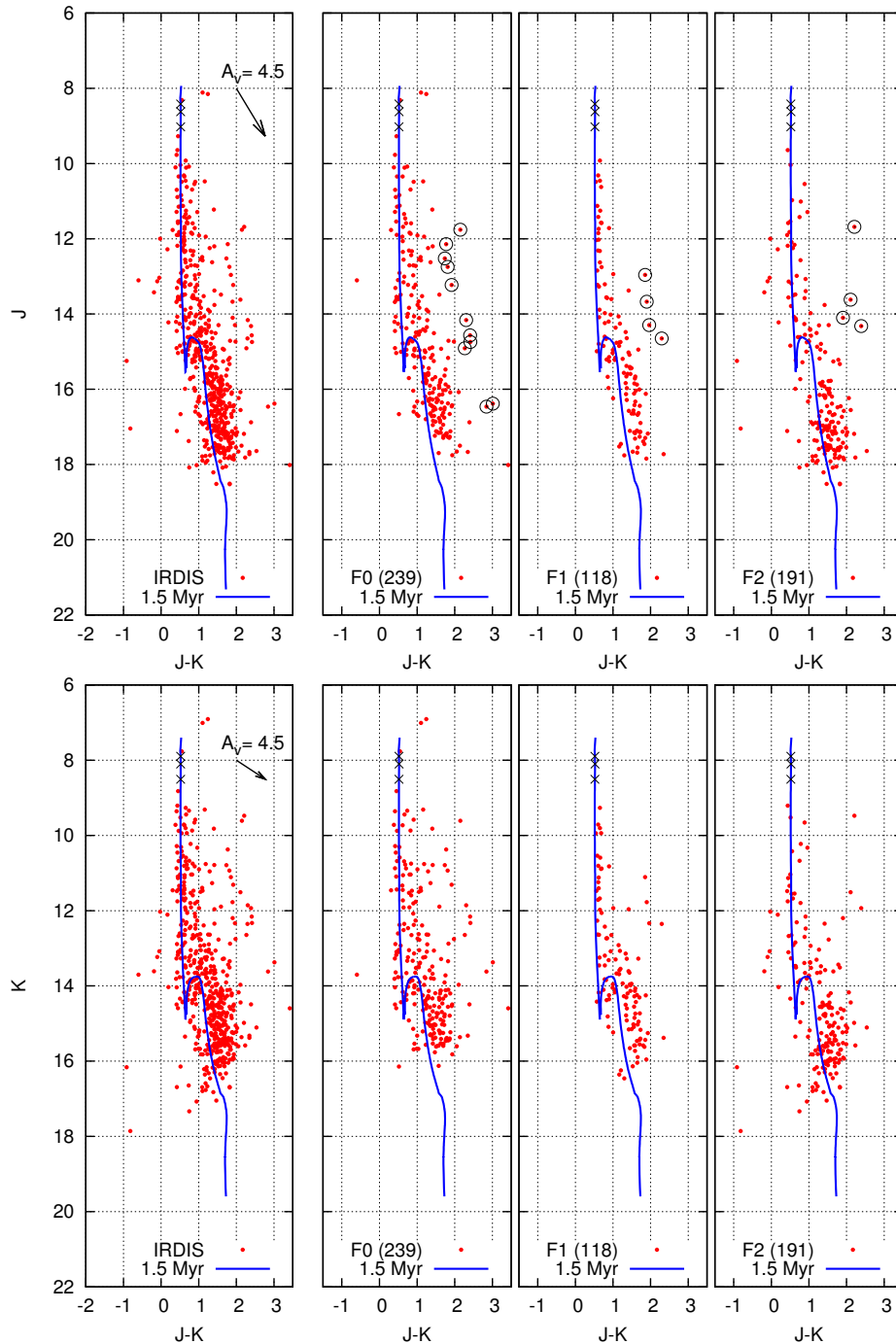


Figure 4.6 CMD of the core of NGC 3603 in IRDIS J and K band for the whole FoV (left) followed to the right for the three fields F0, F1, and F2. Black circles show the K-excess stars. Three black crosses represent stellar models with initial masses of 100, 120, and 150 M_{\odot} . The black arrow signifies the effect of extinction, $A_V = 4.5$.

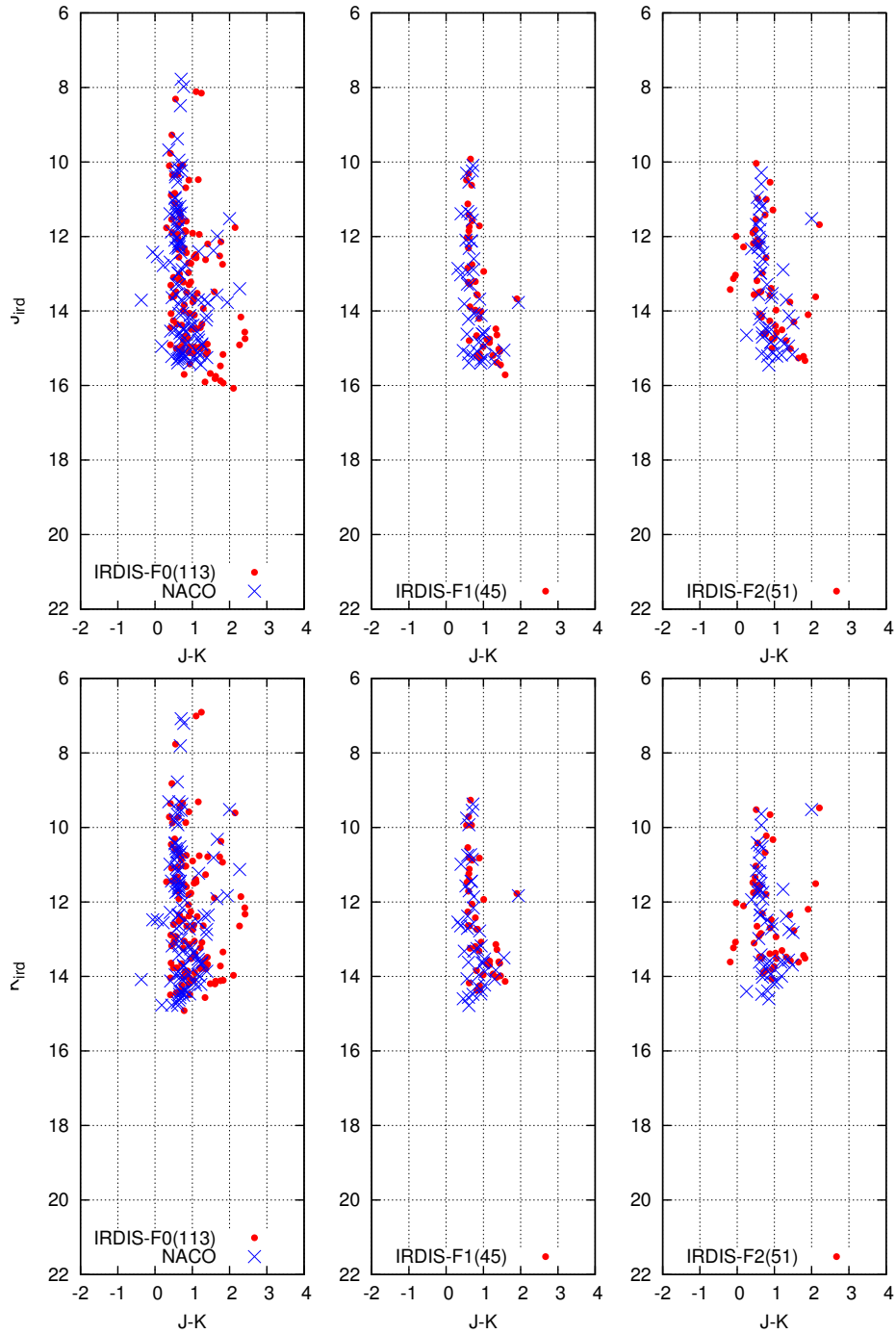


Figure 4.7 CMD from VLT/NACO (from [Harayama et al. (2008)]) overplotted with SPHERE data (red circles) to set the zeropoints of SPHERE/IRDIS detectors. The stars are shown in Figure 4.5 (Red circles in three fields)

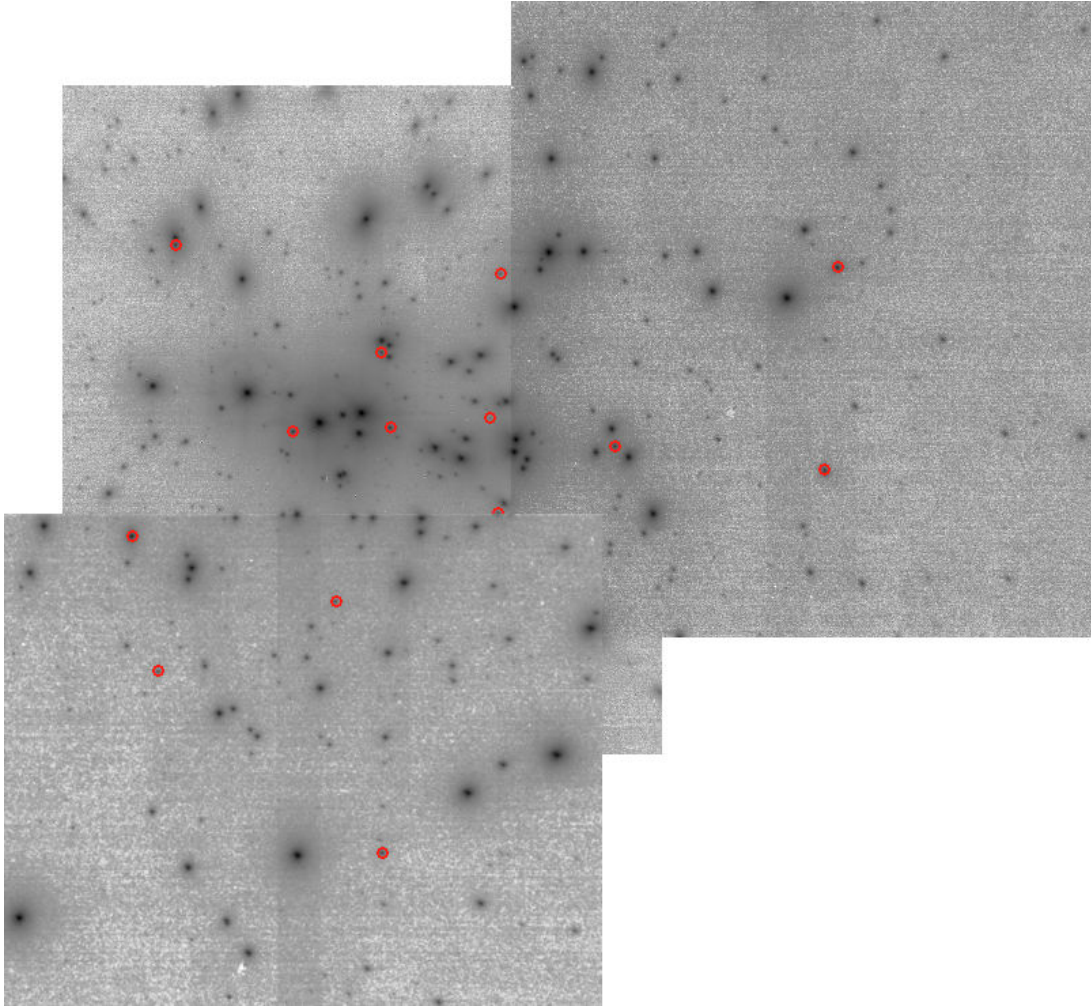


Figure 4.8 The sources with $E(J - K) > 1.8$ in F0, F1 and F2 shown in red circles. The image is a combination of all three fields in IRDIS/B-J.

fit the MF.

$$\log(N) = \Gamma \log\left(\frac{M}{M_{\odot}}\right) + \text{cst.} \quad (4.1)$$

We used the stellar evolution tracks from PARSEC mentioned above to estimate stellar masses at the age of 1.5 Myr. The distance of the cluster was taken as 6 kpc, which fits well with the observed CMD, isochrone, and extinction, and is also in good agreement with [Stolte et al. (2004)], [?], and [Harayama et al. (2008)].

Using grids of stellar evolutionary tracks and extinction for each filter, we can estimate the stellar masses separately from the photometry in each filter. The slope of the mass function Γ can be estimated from Eq. 4.2, where M is the stellar mass and N is the number of stars in the logarithmic mass interval $\log_{10}(M)$ to $\log_{10}(M) + 0.2\log_{10}(M)$. We used a double size bin at the pre-main sequence (PMS) and main sequence (MS) transition, around $4 M_{\odot}$, to smooth out the degeneracy (same as [Harayama et al. (2008)]). We used an implementation of the nonlinear least-squares (NLLS) Marquardt-Levenberg algorithm to fit the MF,

$$\log(N) = \Gamma \log\left(\frac{M}{M_{\odot}}\right) + \text{cst.} \quad (4.2)$$

Mass functions for the two IRDIS BB-J and BB-K filters are shown in Figure 4.9 for the core (F0) and in Figure 4.10 for F1 and F2. One can compare the MF in the very core of the cluster (F0) with the next radial bin (F1 and F2) to check the radial variation of MF. The two latter were observed with similar exposure times and very close conditions as both fields were recorded within one hour slot of a SPHERE/VLT run on 2015-06-07. Also, minimum and maximum magnitudes in both fields are very similar especially in the K band. All these conditions result in similar mass range of detected sources in J and K. Thus we could plot the MF for F1 and F2 together, where 586 sources are detected with masses less than $1 M_{\odot}$ (fainter than 16.5 magnitude) in the K band.

In F0, we were able to reach $0.66 M_{\odot}$ (J=18.7) in the J band and $1.08 M_{\odot}$ (K=16.4) in the K band. Figure 4.9 depicts the MF in F0. Three WR stars (A1, B, C) are located in this region where

two of them (A1 and C) were identified as spectroscopic binaries by [Schnurr et al. (2008)]. The MF can be treated in three possible ways (Table 4.2): 1) considering all WR stars: two as binaries with masses estimated from [Schnurr et al. (2008)] and one (B) as a single star (*All*); 2) considering just two WR stars as two binary systems (*All-B*); and 3) excluding these three WR stars (*All-WRs*).

Figure 4.10 depicts the MF for the next radial bin from the core of NGC3603 (F1 and F2). The mass range covered in K band starts from $0.14 M_{\odot}$, ending at $69 M_{\odot}$. More than 800 sources with a mass smaller than $4 M_{\odot}$ are detected.

The change of the MF slope for the MS and PMS stars occurs around $4 M_{\odot}$. We also fitted a separate line on MF (dash-dotted line in Figure 4.10) for the low-mass PMS stars. The mass function in the low-mass part is corrected for the number of detected sources above an incompleteness level of 80% (black bins in the low-mass part in Figure 4.9 and 4.10).

Table 4.2 lists the derived MF slopes in F0, F1, and F2 regions and derived slopes for MS/PMS stars. MS is a common mass range in J and K and in F0 and F1+F2 with an incompleteness level of 100%. The MF slopes are consistent in the J band and K band and also in the different regions, for the main sequence stars and for the whole mass range.

The MF slopes for the whole mass range is flatter than the main sequence part. The MF slopes even for the massive stars (main sequence) are flatter than Salpeter, $\Gamma_{Salpeter} = -1.35$ [Salpeter (1955)] and Kroupa, $\Gamma_{Kroupa} = -1.3$ [Kroupa (2001)]. The average value agrees with those found in the outer regions of NGC3603 according to previous works. For pre-main sequence stars, the MF slope is flatter than for the whole mass range and for the main sequence.

If we assume that binary properties like binary fraction and mass-ratio distribution do not change strongly with the mass of the primary stars, then the deduced mass function slope should be very similar to the mass function slope of the primary stars.

We could detect 11, 4, and 4 K-excess sources with an E(J-K) that is higher than 1.8 (for MS) and 2.0 (for PMS), in F0, F1, and F2, respectively, corresponding to 14 sources in total (black

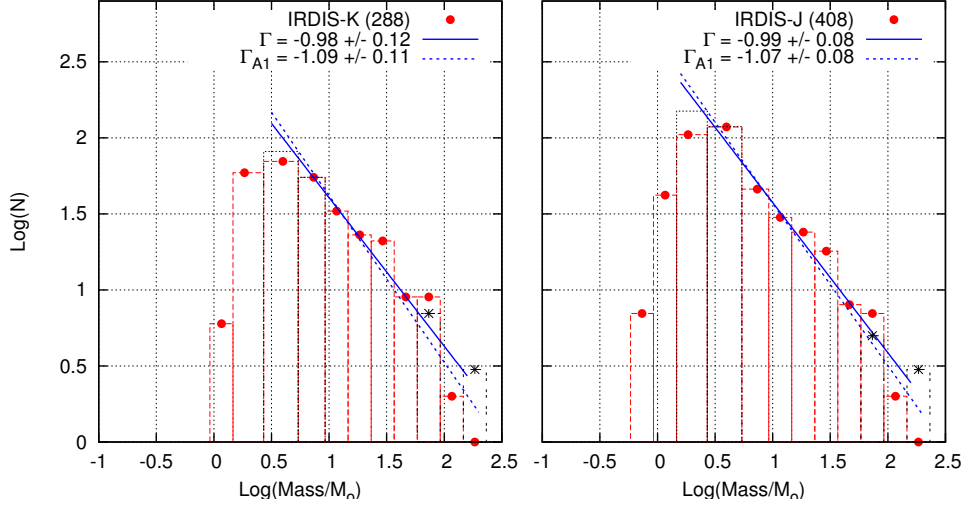


Figure 4.9 Mass functions derived for IRDIS data in BB-J (right) and BB-K (left) in F0 (shown in Figure 4.5 Top). Last three red bins represent the MF considering the A1 and C as a binaries and B as a single source. The last three black stars represent the MF if the WR stars are considered single objects, which is the case for the photometry analysis.

circles in Figure 4.6 and red circles in the bottom panels of Figure 4.5). For these stars, the mass estimated in K is higher than in J because of their K excess. Twelve of these stars are on the sequence parallel to the MS ($M > 4 M_{\odot}$). In this case, the MF slopes for the main sequence part in the J band should be more reliable than in the K band.

4.5 Discussion

NGC 3603 has been observed with various instruments and the slope of its mass function has been calculated in previous works (Table 4.3). These works reach conclusions on the general trend of decreasing MF slopes in the core as the signature of mass segregation. The slopes of the MF in different filters (Table 4.2) in the core of NGC 3603 is steeper than the previous works and does not show a radial dependence in the observed fields. The slope value for the main sequence stars and for the whole mass range is consistent in all observed regions of the core of the cluster.

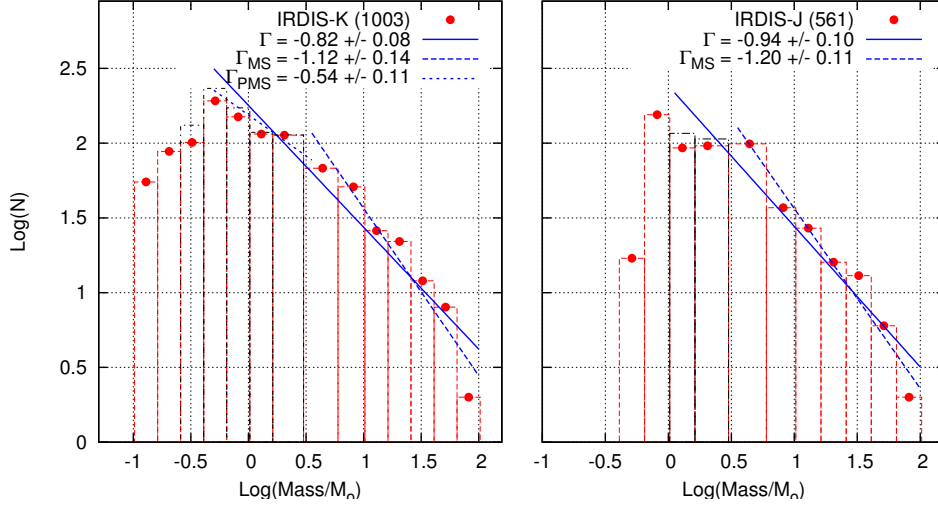


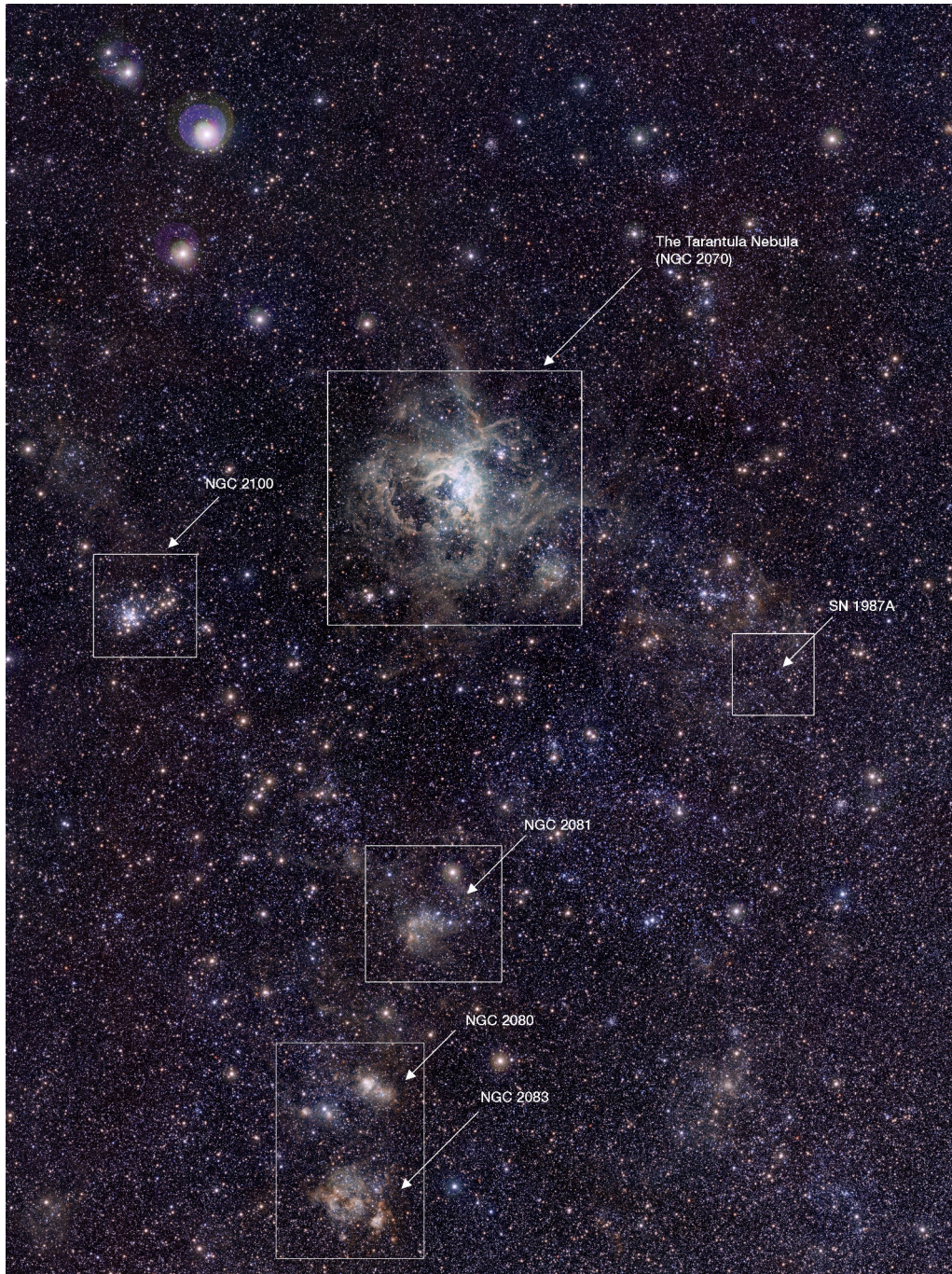
Figure 4.10 Mass functions derived for IRDIS data in BB-J (right) and BB-K (left) in F1 and F2 together. F1 and F2 are shown in Figure 4.5 Top.

Table 4.2 Number of detected stars (N_J and N_K in J and K bands) and MF slopes (Γ_J and Γ_K in J and K bands) using Equation 4.2, at 1.5 Myr in three F0, F1, and F2 fields of NGC 3603 from SPHERE/IRDIS.

F0	N_K	Γ_K	N_J	Γ_J
<i>All</i>	288	-1.09 ± 0.11	408	-1.07 ± 0.08
<i>All-B</i>	287	-0.98 ± 0.12	407	-0.99 ± 0.08
<i>All-WR_s</i>	283	-0.85 ± 0.06	403	-0.98 ± 0.09
F1+F2	N_K	Γ_K	N_J	Γ_J
Total	1003	-0.82 ± 0.08	561	-0.94 ± 0.10
MS	189	-1.12 ± 0.14	200	-1.20 ± 0.11
PMS	814	-0.54 ± 0.11	361	-

Shape of MF at the massive end, can be used as an observational test that may be able to settle the question of which mechanism (accretion or collision) is a dominant route for the formation of the most massive stars [Krumholz (2015)]. According to the accretion models, as the massive stars form by the same accretion processes that produce low-mass stars (normal star formation), the high end of the stellar mass function should be continuous and does not depend radically on the environment [Krumholz (2015)]. On the other hand, collisional formation predicts a large gap in the stellar MF, separating the bulk of the accretion-formed stellar population from the few collisionally formed stars [Baumgardt & Klessen (2011), Moeckel & Clarke (2011)]. This feature should only appear in the most massive and densest clusters. Figure 4.9 shows this signature in the core (F0), but we know that the last bin corresponds to the three WR stars in which two of them have been found to be multiple objects and not single stars [Schnurr et al. (2008)]. Therefore, collisional formation of very massive objects seems unlikely at least for the NGC 3603 cluster. Accretion models also predict that massive stars are likely to have low-mass and high-mass companions [Kratter & Matzner (2006), Kratter et al. (2008), Kratter et al. (2010), Krumholz et al. (2012)], but the collisionally formed stars lack low-mass companions, which provokes segregation.

This study shows no signature of mass segregation in the core of NGC 3603, first, because the MF slope in its very core is not flatter than the next radial bin. Second, both slopes are similar to the MF values found in previous works for the outer regions (references in Table 4.3). Therefore, it appears that nonsegregated clusters with a smooth MF agree better with accretion models for massive star formation. Our SPHERE results demonstrate that, by improved photometric dynamic range and spatial resolution from XAO, we can overcome the effect of confusion that in the past has led to the conclusion of observational segregation (see also [Ascenso et al. (2009)]) as far as NGC 3603 is concerned.



VISTA Magellanic Cloud Survey taken in Y, J and Ks filters in the near-infrared, coloured blue, green and red respectively. The image covers a region of sky about 52 by 70 arcminutes.

Credit: ESO/M.-R. Cioni/VISTA Magellanic Cloud survey.

Table 4.3 Slopes of the mass function derived for NGC3603 in earlier works.

Γ	condition	reference
-0.5 ± 0.1	$r < 6''$, $(1.6-100)M_{\odot}$	[Sung & Bessell (2004)]
-0.31	$0 - 5''$, $(0.4-20)M_{\odot}$	[Harayama et al. (2008)]
-0.26	$0 - 5''$, $(6.3-100)M_{\odot}$	[Pang et al. (2013)]

Chapter 5

VLT/SPHERE Photometry on R136

Abstract: In this chapter I present the results of sharpest near-IR images of the massive cluster R136 to date, based on the extreme adaptive optics of the SPHERE focal instrument implemented on the ESO Very Large Telescope and operated in its IRDIS imaging mode.

The crowded stellar population in the core of the R136 starburst compact cluster remains still to be characterized in terms of individual luminosities, age, mass and multiplicity. SPHERE/VLT and its high contrast imaging possibilities open new windows to make progress on these questions.

Stacking-up a few hundreds of short exposures in J and Ks spectral bands over a Field of View (FoV) of $10.9'' \times 12.3''$ centered on the R136a1 stellar component, enabled us to carry a refined photometric analysis of the core of R136. We detected 1110 and 1059 sources in J and Ks images respectively with 818 common sources that were secured from systematic photometric error analysis and correlation coefficients exceeding 65% and 80%, in Ks and J band, for their reliability.

We found that more than 62.6% (16.5%) of the stars, detected both in J and Ks data, have visual companion closer than 0.2" (0.1"). The closest stars are resolved down to the full width at half maximum (FWHM) of the point spread function (PSF) measured by Starfinder. Among newly resolved and/or detected sources R136a1 and R136c are found to have optical companions

and R136a3 is resolved as two stars (PSF fitting) separated by 59 ± 2 mas. This new companion of R136a3 presents a correlation coefficient of 86% in J and 75% in Ks. The new set of detected sources were used to re-assess the age and extinction of R136 based on 54 spectroscopically stars that have been recently studied with HST slit-spectroscopy [Crowther et al. (2016)] of the core of this cluster. Over 90% of these 54 sources identified visual companions (closer than 0.2"). We found the most probable age and extinction for these sources are $1.8^{+1.2}_{-0.8}$ Myr, $A_J = 1.3 \pm 0.5$ and $A_K = 0.4 \pm 0.5$ within the photometric and spectroscopic error-bars. Additionally, using PARSEC evolutionary isochrones and tracks, we estimated the stellar mass range for each detected source (common in J and K data) and plotted the generalized histogram of mass (MF with error-bars). In the light of these original results we speculate on the true nature of the very core of R136.

5.1 Observations

We obtained data via Guaranteed Time Observation (GTO) runs to image R 136 using the dual mode of IRDIS [Langlois et al. (2014)], enabling simultaneous observations in two spectral bands on the VLT. The observations were performed in September 2015, with high dynamic and spatial resolution imaging in J and K bands with a FoV of $13.5'' \times 13.5''$, centered on the core of the cluster (Figure 5.1 and 5.2).

One can compare these data with HST (WFPC2 and WFC3) in V-band (Figure 5.3 Top). The quality of data is much better than previous data and many stars are resolved thanks to SPHERE/IRDIS resolution in J and K.

Our data consist of 300 frames of 4.0s exposures in both the IRDIS broad-band Ks and J filters (BB-Ks, BB-J). The Wolf-Rayet star R136a1 was used for guiding the AO loop of SPHERE confirming its better than nominal performances surpassing NACO and MAD observations (Figure 5.3).

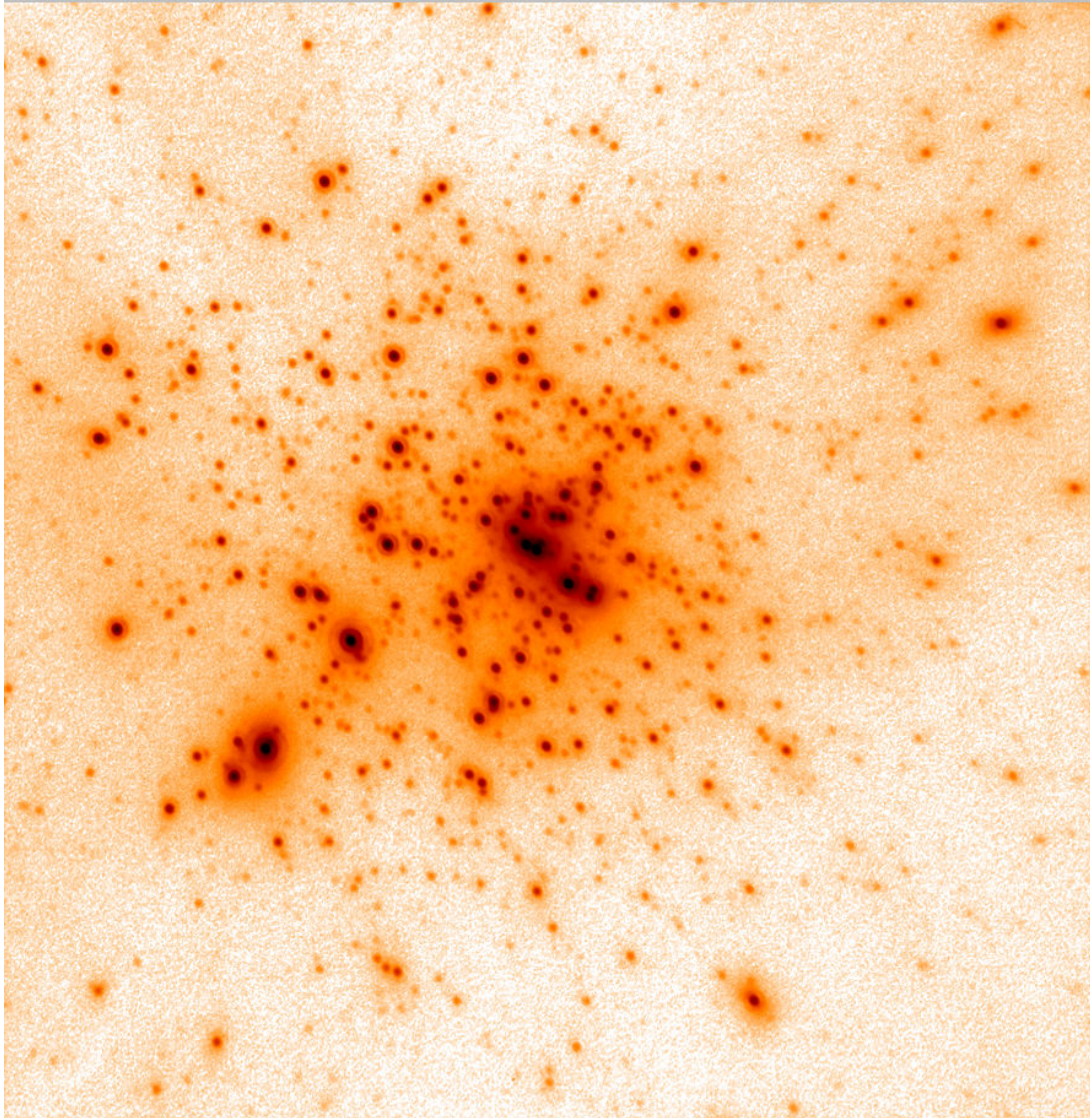


Figure 5.1 SPHERE/IRDIS images of the core of R136 in K-band.

The range of airmass during these observations was 1.54 to 1.67. A log of observations is presented in Table 5.1.

We used the SPHERE pipeline package¹, for correcting dark, flat, distortion, badpixels and

¹http://www.mpia.de/SPHERE/sphere-web/nightly_builds-page.html

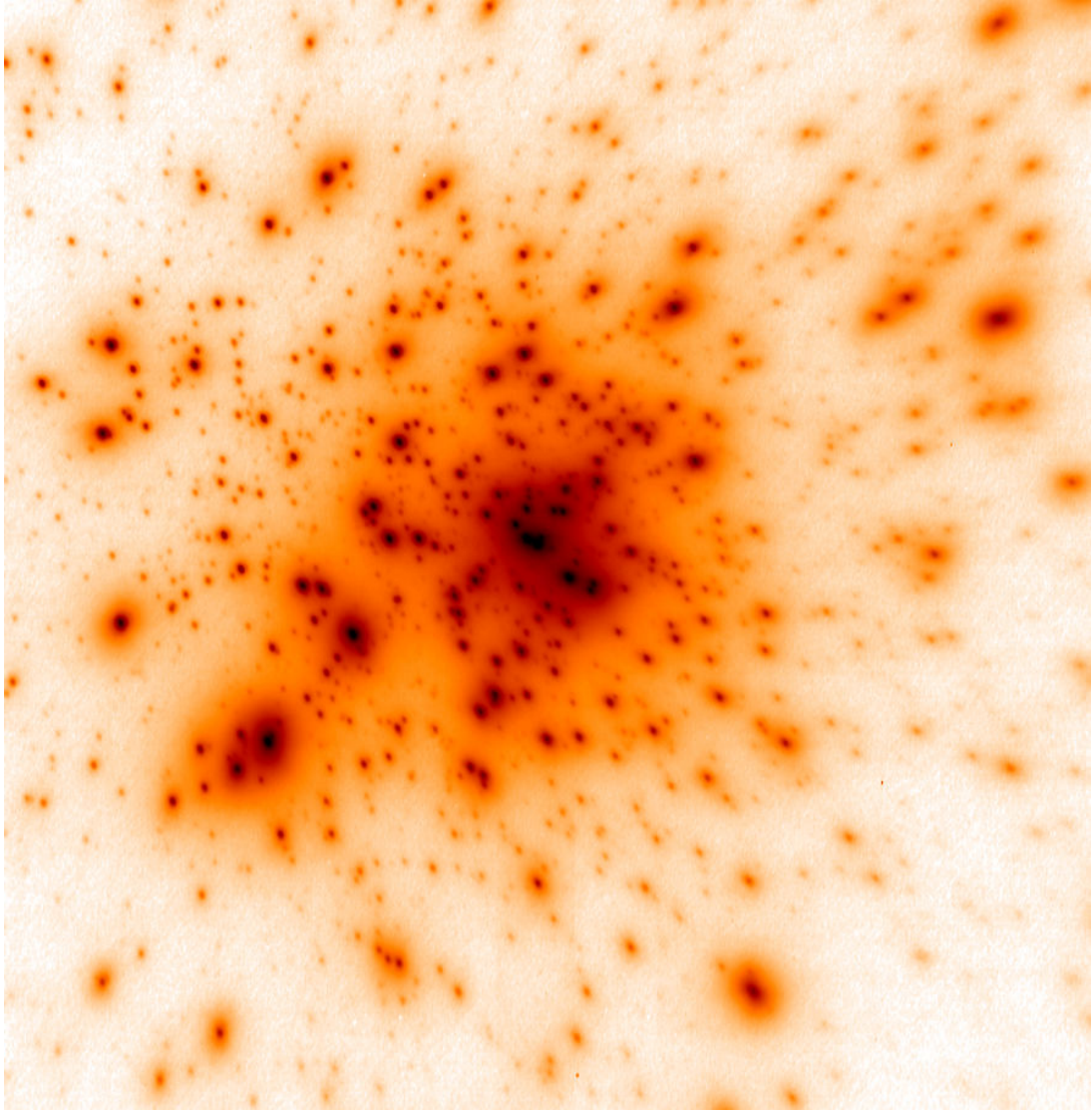


Figure 5.2 SPHERE/IRDIS images of the core of R136 in J-band.

detector thermal emission (in Ks). In order to reach the highest sensitivity and the largest number of detectable sources, additional corrections were carried out onto the images. Based on Gaussian fit using selected stars we estimated and corrected the subpixels images drifts before combining the individual images. This allowed to correct for residual tip tilt errors with a few mas accuracy. Still,

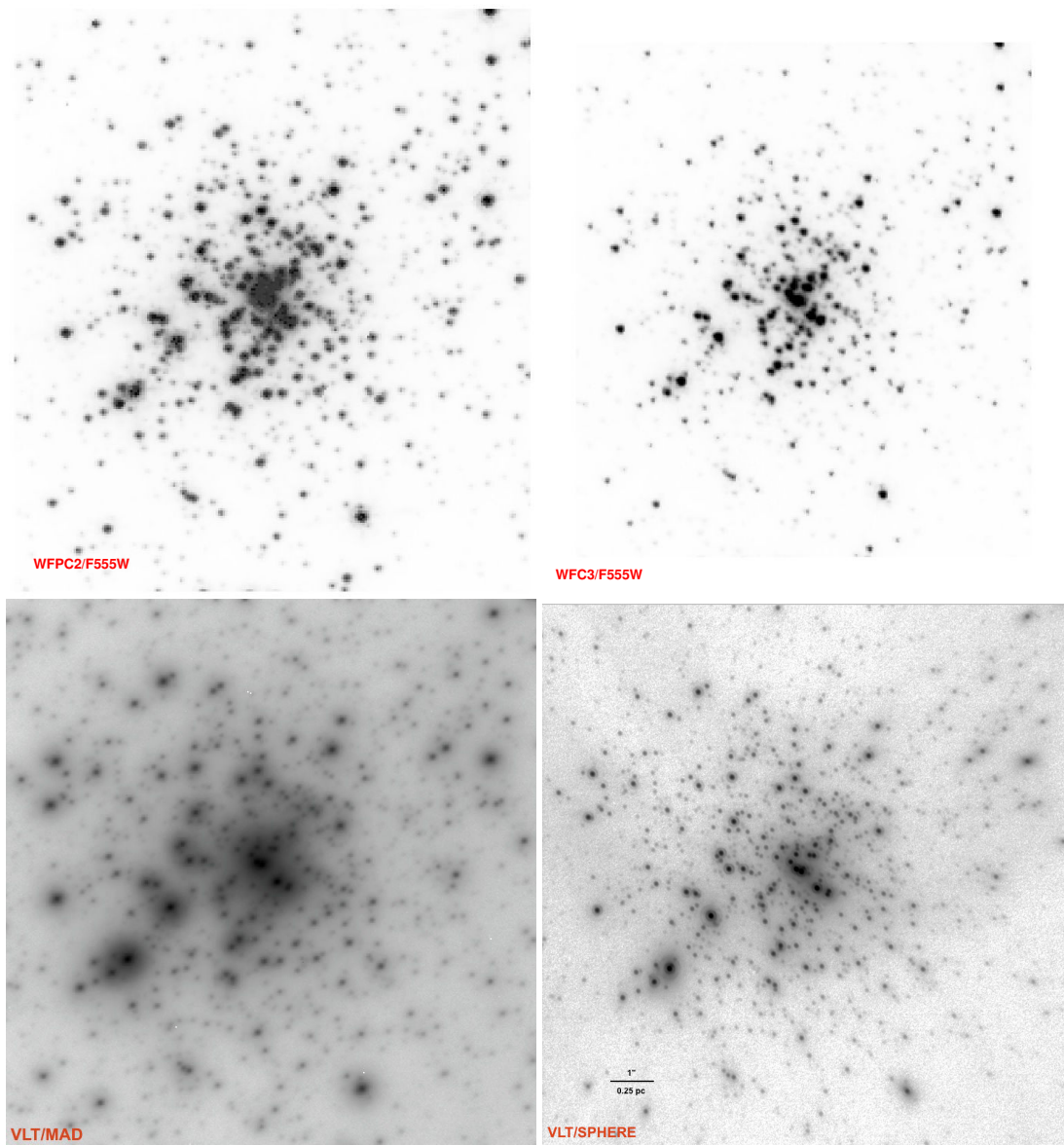


Figure 5.3 Top: HST images in V-band (F555W) from the core of R136, same FoV of SPHERE/IRDIS data. Left: WFPC2, Right:WFC3. Bottom: VLT images of the core of R136 in K band. Left: MAD, Right: SPHERE.

some uncorrected atmospheric leaks persist in our final images due to the adaptive optics residual halo which is more important in J than in Ks, that we accurately considered to estimate correct

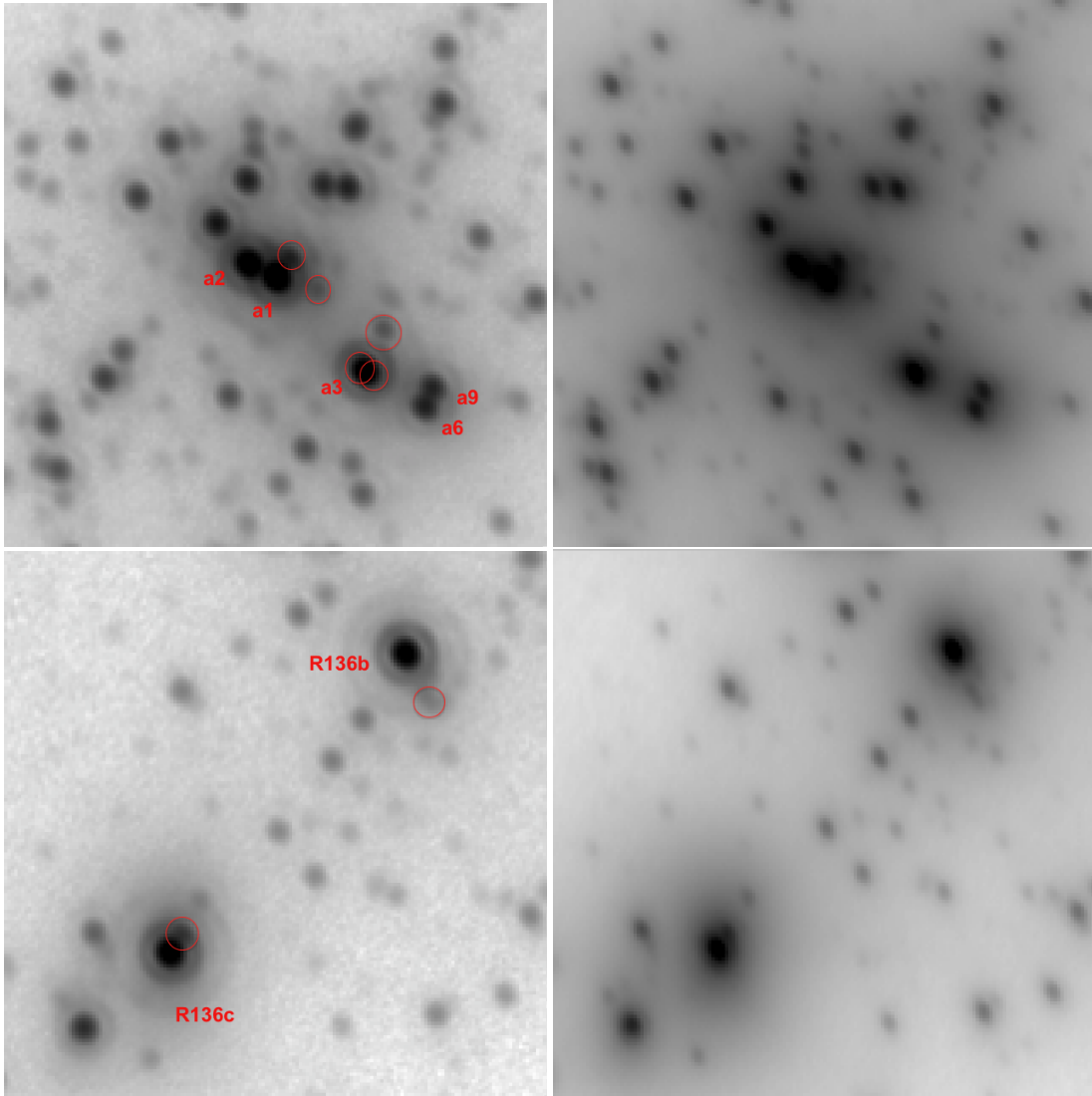


Figure 5.4 Zoom to the WR stars in the core of R136 in K-band (left) and J-band (right). Each frame covers about 2". In the top R136a1, R136a2 and R136a3 can be seen and in Bottom, R136b and R136c with its new companion.

error bars in addition to the Starfinder reduction tool providing photometric errors (see Section 5.2).

Table 5.1 Exposure time log of VLT/SPHERE observations on R136.

Obs. date	Filter	Single/Total Exposure[s]	λ_{cen} [nm]	$\Delta\lambda$ [nm]
2015-09-22	B-J	4.0/1200	1245	240
2015-09-22	B-K	4.0/1200	2182	300

5.2 Photometry of R136's compact core

For the present study we used the Starfinder package implemented in IDL [Diolaiti et al. (2000)]. Starfinder is designed for the analysis of of AO images of crowded fields, like the Galactic Center for instance [Pugliese et al. (2002)]. It determines the empirical local Point Spread Function (PSF) from several isolated sources in the image and uses this PSF to extract other stellar sources across the FoV. Starfinder estimates also the formal error on the estimated photometry based on photon noise, variance due to the sky and the PSF fitting procedure itself. This error is called "**PSF fitting error**" hereafter.

Our photometry analysis of R136 was conducted in two steps: 1) stellar sources detection using Starfinder and 2) the background analysis to obtain realistic error bars on the photometry of individual stars beyond the formal PSF fitting error.

In the first step 1110 and 1059 sources were detected in the J and Ks bands, respectively. Figure 5.25 shows the reconstructed image of SPHERE/IRDIS in Ks band for the 1059 stellar sources detected by Starfinder. We stopped source extraction after we attained a minimum correlation of 65% and 80%, in Ks and J bands, between the extracted star with the locally determined PSF according to Starfinder procedures. Indeed, stars with higher correlation coefficients, i.e. more similarity to the PSF, represent higher reliability on their photometric measure.

Figure 5.5 shows the map of the correlation coefficient across the field of J (left) and Ks (right) images of R136. One can notice that the PSF changes as a function of radial distance and azimuth along the field (Figure 5.5). Actually, the AO correcting efficiency degrades as a function of

distance from R136a1, which is the reference star for the AO loop. At the borders of the FoV one also approaches the isoplanatic limits. Overall the PSF is not centro-symmetric at large distances from R136a1. We took into account these distortions to estimate the local statistical errors, which become significant on the distant sources from the center of the image, typically $>3''$.

In addition to the correlation coefficient criterion, we applied the limit of standard deviation from the sky brightness (σ_{sky}) for stopping the extraction of sources by Starfinder, i.e. the local PSF maximum value must exceed $2\sigma_{sky}$ over the sky. The faintest common detected stars between J and Ks band, present a signal to noise ratio (SNR) better than 2. To convert stellar fluxes to magnitudes, we used the zeropoints of the instrument (IRDIS) itself. One ADU/s in J and Ks, are 25.405 and 24.256 magnitudes, respectively.

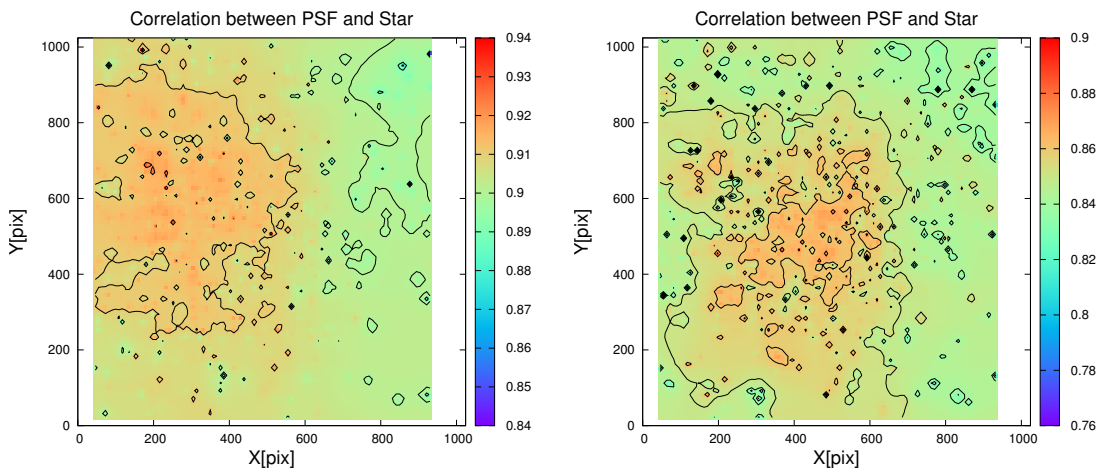


Figure 5.5 Map of the correlation coefficients calculated by starfinder along the FoV in J (left) and in K (right).

In the second step, after extracting sources, the background image was used to estimate the residual errors in addition to the formal photometric PSF fitting errors of Starfinder. The background image contains 1) AO halo from the atmospheric turbulence, 2) residuals from the photometric analysis in the first step and 3) undetected faint stars. We define the residual error as the

fluctuation of the background due to the remaining flux from the photometry using Starfinder and also from the undetected faint sources.

The image of the background is shown in Figure 5.6-Top.

Since the core of R136 is crowded with the brightest stars, the AO halo is the brightest at the center of R136. We removed this large halo in the Fourier space by applying a high bandpass filter (hat function with the diameter equal to the FWHM of the background halo), in order to estimate the fast variations of the background at the scale of the PSF, i.e. 30×30 pixel² area around the source. The final photometric error is set to the quadratic combination of PSF fitting errors and residual errors.

Figure 5.7 shows these errors separately for each detected sources. The PSF fitting errors (red-pluses) are smaller in K-band as the AO works better in larger wavelengths. But the residual errors (blue-crosses) are larger in K-band because the background fluctuation in longer wavelengths is higher. Figure 5.9 shows the maps of these two errors in J and K across the field.

In order to interpret the photometric distribution of the 1110 and 1059 sources in J and Ks bands we conducted an incompleteness test to the core ($r < 3''$) of R136 and outside its core ($r > 3''$) in both J and K-band imaging data. Figure 5.10 shows the result of incompleteness test which is done by putting 500 artificial stars in each image for each flux value (magnitude). In total, 9.45×10^5 and 7.9×10^5 artificial stars were added to the J and K images respectively. Starfinder was used again to extract these artificial stars. The core of the cluster is very crowded so that the incompleteness does not reach 100% even for the bright artificial stars. This effect is more important for J-band data where the core is fuzzy because of a lower AO correction.

5.2.1 Strehl ratio

Strehl ratio (S_r) is a ratio of the peak intensity of the observed PSF to the peak intensity of the ideal diffraction limited PSF of the same optical system. In the AO system data, the flux of each

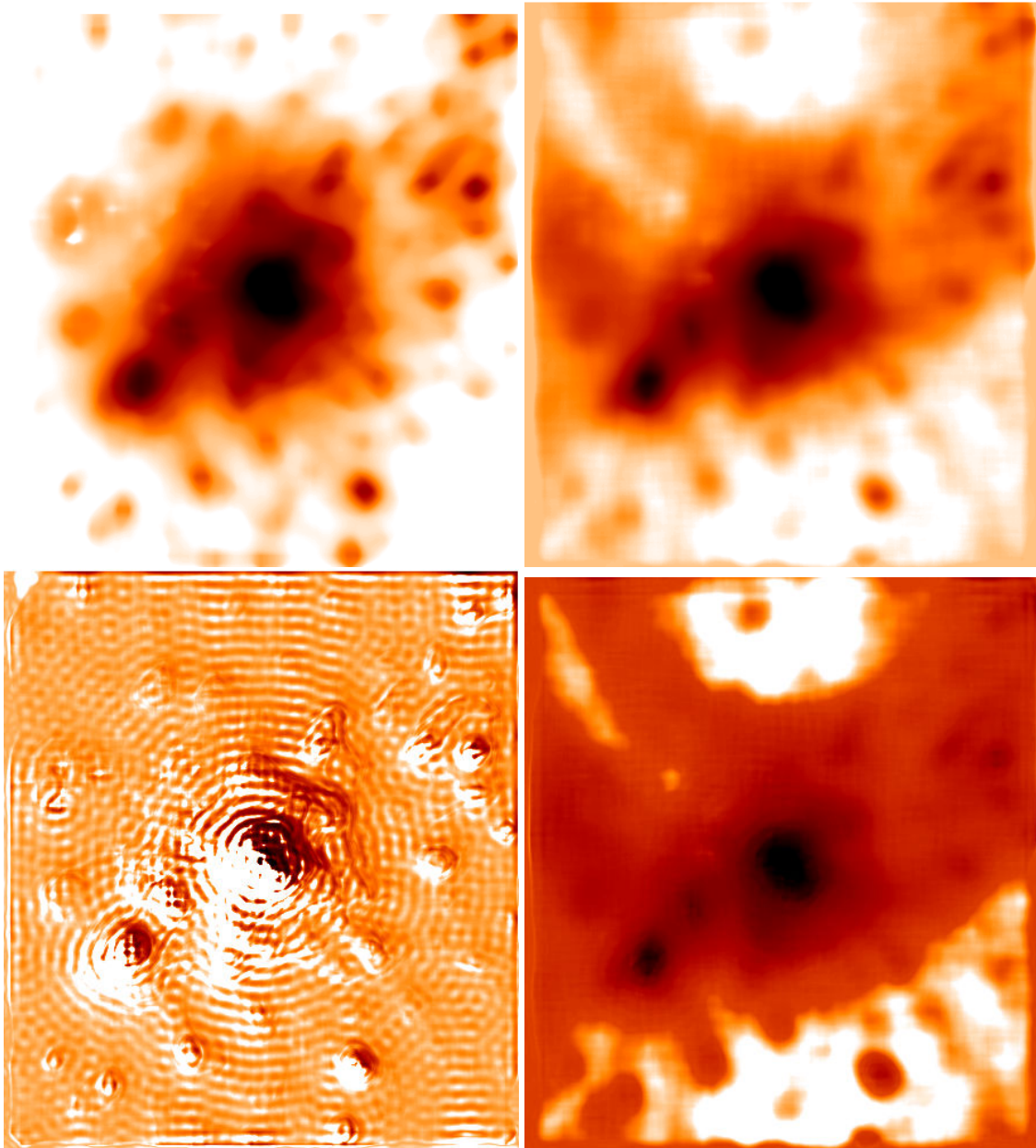


Figure 5.6 Top: Background images in J (left) and in K (right) after removing the detected sources using Starfinder. Bottom: Residual images in J (left) and K (right) after filtering out the AO halo in the background image at Fourier space.

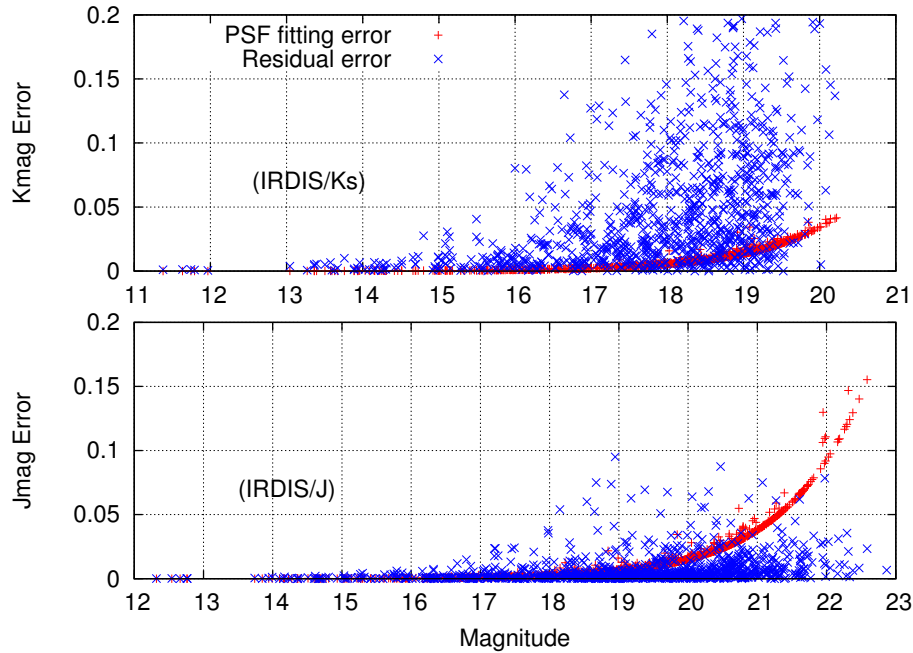


Figure 5.7 PSF fitting errors (red pluses) and residual errors (blue crosses) in J (bottom) and K (top). PSF fitting error is the outcome of the Starfinder. Residual errors is the outcome of the background analysis after removing the stellar sources signals from the image.

stellar object is divided into two parts: 1) corrected airy-pattern with the FWHM of about the diffraction-limited telescope, and 2) AO halo with the FWHM of the seeing, usually with Gaussian distribution. Figure 5.11 depicts the ideal and observed shape of the flux distribution at the cross-section of a simulated image.

The ratio of the integrated flux of the first part (corrected by AO) over the total flux of the star (corrected part plus AO halo), is the S_r . In the IRDIS images, the FWHM of the AO halo (seeing) is about 82. pixels (1"). One can estimate the S_r using aperture photometry of a single star within the 82. pixel aperture. Unfortunately the core of R136 is very crowded, so finding an isolated source is almost impossible. But we used a new method in order to estimate the S_r across the IRDIS FoV. In this method, the minimum value of the S_r is the total flux of the stellar sources (using Starfinder)

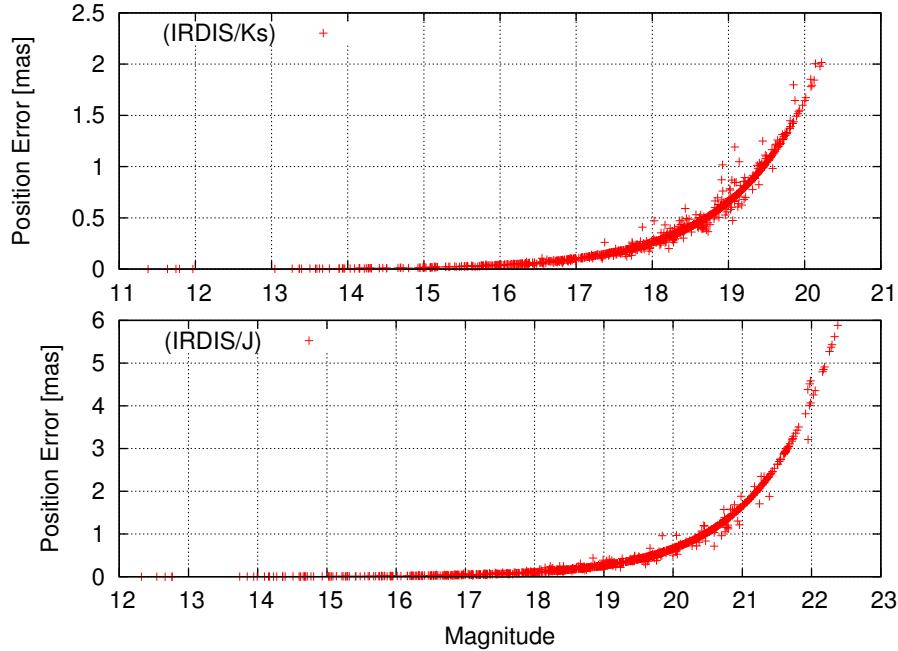


Figure 5.8 Position errors in J (bottom) and K (top), estimated from the photometry.

over the total flux in the image. The key parameter in this calculation is the minimum value of the correlation coefficient (between the input PSF and the stellar source) during the photometry process. We changed this minimum correlation coefficient from 0.8 to 0.0 and calculated the total flux of the detected sources over the total flux of the image (AO halo plus stellar sources signals). Figure 5.12 shows the saturated S_r values at low correlation coefficient. Using this method, the minimum estimated S_r is about 0.86 and 0.54 in K and J images, respectively.

5.3 Age and extinction

To estimate the stellar ages and the extinction of the core of R136, we used the effective temperature (T_{eff}) and luminosity ($\log L$) of 54 stars studied spectroscopically by Crowther et al. (2016). We also chose a grid of isochrones at different ages (from 0.1 up to 8 Myr) with the LMC metallicity

($0.006 Z_{\odot}$), from the latest sets of PARSEC evolutionary model ² [Bressan et al. (2012)] which is a complete theoretical library that includes the latest set of stellar phases from pre-main sequence to main sequence and covering stellar masses from 0.1 to 350 M_{\odot} . Figure 5.13 shows these selected 54 stars with their T_{eff} -logL (with their error-bars) and sets of isochrones covering them.

By fitting the isochrones to each star, we estimated the age and intrinsic color of each star with the error-bars. We adopt the distance modulus of 18.45 magnitude which is consistent with the value suggested by Gibson (2000) for LMC. Table 5.3 shows the estimated age, initial mass and extinction of these 54 spectroscopically known stars. The values of T_{eff} and $\log L/L_{\odot}$ in the second and third column are taken from Crowther et al. 2016. Figure 5.14 shows the generalized histogram of the age of these 54 sources. Note that, the age of each star has a Gaussian distribution with a given σ (error) in the histogram. Also note that the large errors on the age and extinction are coming from the large spectroscopic uncertainties (errors on T_{eff} and $\log L/L_{\odot}$). We were also limited by the evolutionary tracks up to 350 M_{\odot} , which explains the upper mass limit of 348 M_{\odot} for very massive stars like R136a1.

Figure 5.15 shows the histogram of the extinction in J and K and their color-excess.

The age of $1.8^{+1.2}_{-0.8}$ Myr is the most probable age range for these stars. The extinction in J and K is respectively 1.3 ± 0.5 and 0.4 ± 0.5 . Figure 5.16 shows the color magnitude diagram (CMD) of detected sources in J and Ks band IRDIS data with their error-bars. The CMD is plotted for the whole FoV (818 sources), in the very core of the cluster ($r < 3''$) and outside ($r > 3''$), from left to right respectively. The error-bars on each point are the combination of the PSF-fitting errors and the residual errors from the background image after removing the stellar sources signals from the images. The PARSEC isochrones at three different ages (1, 2 and 3 Myr) also are plotted in this Figure. The uncertainties on the photometric analysis is less than those obtained from the spectroscopic analysis of the massive stars. We can clearly see the main sequence and pre-main

²<http://stev.oapd.inaf.it/cgi-bin/cmd>

sequence branch which show a single-age population. The realistic age and extinction can be estimated using the precise photometric analysis for the 818 stellar sources in the core of R136.

Considering these errors on the age and extinction, one can estimate the stellar mass range for each star. The histogram of mass, which is the mass function (MF), is plotted considering a Gaussian distribution for each stellar mass. Gaussian uncertainty in the mass of each star is accounted for, when constructing the MF. Figure 5.17 shows the generalized histogram of the mass (MF) at three different ages (1, 2 and 3 Myr).

Considering these error-bars on the age and extinction, one can estimate the stellar mass range for each star. The histogram of mass (MF) can be plotted considering the Gaussian distribution for each stellar mass in this histogram. Figure 5.17 shows the generalized histogram of the mass (MF) at three different ages (1, 2 and 3 Myr).

Table 5.2 Information on 54 spectroscopically known stars with T_{eff} and $\log L/L_{\odot}$ estimated by Crowther et al. 2016 (second and third columns). Using PARSEC evolutionary isochrones (0.1 to 8 Myr), the age, color excess, extinctions and initial masses are estimated (columns five to eight). N2 and N1 are the number of visual companions for each source in a radius of 0.2" and 0.1" respectively. The identifications (ID) of the sources are from Hunter et al. 1995.

ID	T_{eff} [kK]	$\log L/L_{\odot}$	age[Myr]	E(J-K)	A(K)	A(J)	$M_{initial}$	N2	N1
3	$53.00^{+3.0}_{-3.0}$	$6.94^{+0.09}_{-0.09}$	$0.79^{+1.44}_{-0.00}$	$1.17^{+0.02}_{-0.00}$	$0.27^{+0.01}_{-0.25}$	$1.44^{+0.02}_{-0.25}$	$348.1^{+0.0}_{-80.1}$	3	1
5	$53.00^{+3.0}_{-3.0}$	$6.63^{+0.09}_{-0.09}$	$0.56^{+0.00}_{-0.36}$	$1.14^{+0.00}_{-0.00}$	$-0.39^{+0.25}_{-0.00}$	$0.74^{+0.25}_{-0.00}$	$201.5^{+48.5}_{-0.0}$	3	0
20	$50.00^{+4.0}_{-5.0}$	$6.32^{+0.16}_{-0.15}$	$1.26^{+2.29}_{-0.86}$	$0.95^{+0.01}_{-0.02}$	$0.30^{+0.65}_{-0.29}$	$1.25^{+0.65}_{-0.31}$	$120.0^{+30.2}_{-47.9}$	2	0
24	$46.00^{+4.0}_{-3.0}$	$5.99^{+0.10}_{-0.08}$	$1.78^{+2.69}_{-0.78}$	$0.82^{+0.01}_{-0.01}$	$0.02^{+0.22}_{-0.38}$	$0.84^{+0.21}_{-0.38}$	$75.4^{+14.6}_{-22.2}$	3	0
27	$51.00^{+6.0}_{-6.0}$	$6.28^{+0.13}_{-0.15}$	$1.00^{+2.55}_{-0.90}$	$0.83^{+0.02}_{-0.02}$	$0.79^{+0.54}_{-0.42}$	$1.62^{+0.55}_{-0.41}$	$120.0^{+30.0}_{-47.9}$	1	1
21	$51.00^{+6.0}_{-6.0}$	$6.46^{+0.13}_{-0.15}$	$1.12^{+1.70}_{-1.02}$	$0.85^{+0.01}_{-0.03}$	$1.00^{+0.42}_{-0.32}$	$1.85^{+0.41}_{-0.33}$	$150.2^{+39.9}_{-29.3}$	1	1
86	$46.00^{+4.0}_{-3.0}$	$5.91^{+0.10}_{-0.08}$	$1.78^{+2.69}_{-0.98}$	$0.93^{+0.04}_{-0.04}$	$1.54^{+0.47}_{-0.38}$	$2.47^{+0.44}_{-0.35}$	$67.9^{+11.1}_{-14.8}$	2	0
66	$46.00^{+4.0}_{-3.0}$	$5.70^{+0.10}_{-0.08}$	$1.78^{+0.73}_{-1.68}$	$0.82^{+0.02}_{-0.02}$	$0.70^{+0.27}_{-0.43}$	$1.52^{+0.26}_{-0.42}$	$53.7^{+10.2}_{-4.8}$	2	0
6	$53.00^{+3.0}_{-3.0}$	$6.58^{+0.09}_{-0.09}$	$0.56^{+0.23}_{-0.00}$	$1.25^{+0.00}_{-0.00}$	$-0.28^{+0.00}_{-0.07}$	$0.96^{+0.00}_{-0.08}$	$201.5^{+0.0}_{-24.4}$	2	1

ID	T_{eff} [kK]	$\log L/L_{\odot}$	age[Myr]	E(J-K)	A(K)	A(J)	$M_{initial}$	N2	N1
58	$51.00^{+6.0}_{-6.0}$	$5.93^{+0.13}_{-0.15}$	$0.79^{+3.67}_{-0.69}$	$0.80^{+0.01}_{-0.02}$	$0.48^{+0.43}_{-0.39}$	$1.28^{+0.42}_{-0.38}$	$75.0^{+15.1}_{-21.7}$	0	0
30	$38.00^{+2.0}_{-2.0}$	$5.67^{+0.05}_{-0.06}$	$3.55^{+0.00}_{-0.39}$	$0.89^{+0.01}_{-0.01}$	$0.52^{+0.19}_{-0.11}$	$1.40^{+0.19}_{-0.10}$	$45.0^{+3.1}_{-0.4}$	2	0
70	$42.00^{+2.0}_{-2.0}$	$5.57^{+0.07}_{-0.08}$	$2.51^{+0.65}_{-0.27}$	$0.78^{+0.01}_{-0.01}$	$0.37^{+0.33}_{-0.24}$	$1.15^{+0.32}_{-0.24}$	$44.2^{+1.7}_{-4.2}$	1	1
89	$44.00^{+2.5}_{-2.5}$	$5.99^{+0.08}_{-0.07}$	$4.47^{+0.00}_{-2.69}$	$0.86^{+0.01}_{-0.01}$	$1.86^{+0.20}_{-0.38}$	$2.73^{+0.19}_{-0.37}$	$53.1^{+23.0}_{-0.0}$	2	0
62	$51.00^{+6.0}_{-6.0}$	$5.84^{+0.13}_{-0.15}$	$0.20^{+1.80}_{-0.10}$	$0.84^{+0.03}_{-0.02}$	$0.83^{+0.53}_{-0.46}$	$1.66^{+0.53}_{-0.43}$	$70.0^{+5.0}_{-16.3}$	4	0
19	$46.00^{+4.0}_{-2.0}$	$6.52^{+0.10}_{-0.05}$	$1.26^{+0.00}_{-0.26}$	$1.11^{+0.01}_{-0.00}$	$1.34^{+0.04}_{-0.30}$	$2.46^{+0.04}_{-0.29}$	$170.0^{+20.2}_{-1.8}$	2	1
50	$51.00^{+6.0}_{-6.0}$	$6.02^{+0.15}_{-0.13}$	$4.47^{+0.00}_{-4.37}$	$0.78^{+0.02}_{-0.02}$	$0.80^{+0.53}_{-0.33}$	$1.58^{+0.53}_{-0.31}$	$53.3^{+46.7}_{-0.0}$	2	0
90	$44.00^{+2.5}_{-2.5}$	$5.36^{+0.08}_{-0.07}$	$0.79^{+1.72}_{-0.69}$	$0.97^{+0.02}_{-0.02}$	$0.32^{+0.32}_{-0.11}$	$1.29^{+0.31}_{-0.10}$	$38.6^{+1.4}_{-4.6}$	1	0
141	$41.00^{+3.0}_{-3.0}$	$5.09^{+0.12}_{-0.12}$	$2.00^{+1.99}_{-1.90}$	$0.86^{+0.03}_{-0.03}$	$0.55^{+0.44}_{-0.34}$	$1.41^{+0.42}_{-0.32}$	$28.3^{+5.6}_{-3.4}$	4	0
80	$36.00^{+2.0}_{-2.0}$	$5.20^{+0.08}_{-0.10}$	$4.47^{+1.16}_{-0.00}$	$0.86^{+0.01}_{-0.01}$	$0.51^{+0.22}_{-0.24}$	$1.36^{+0.22}_{-0.23}$	$28.0^{+0.7}_{-3.5}$	1	0
35	$48.00^{+3.0}_{-3.0}$	$5.92^{+0.08}_{-0.09}$	$1.58^{+0.41}_{-1.19}$	$0.97^{+0.01}_{-0.02}$	$0.70^{+0.30}_{-0.31}$	$1.67^{+0.29}_{-0.31}$	$70.0^{+5.4}_{-8.3}$	2	0
78	$44.00^{+2.5}_{-2.5}$	$5.47^{+0.08}_{-0.07}$	$2.24^{+0.58}_{-1.68}$	$1.00^{+0.01}_{-0.01}$	$0.55^{+0.28}_{-0.28}$	$1.55^{+0.27}_{-0.27}$	$40.0^{+5.0}_{-2.2}$	0	0
73	$33.00^{+2.0}_{-2.0}$	$5.21^{+0.09}_{-0.10}$	$6.31^{+0.00}_{-0.69}$	$0.77^{+0.01}_{-0.01}$	$0.54^{+0.11}_{-0.49}$	$1.31^{+0.11}_{-0.48}$	$25.4^{+2.6}_{-1.4}$	2	0
92	$40.00^{+2.0}_{-2.0}$	$5.20^{+0.07}_{-0.08}$	$2.82^{+1.16}_{-1.56}$	$1.01^{+0.01}_{-0.02}$	$0.30^{+0.35}_{-0.27}$	$1.31^{+0.34}_{-0.26}$	$30.0^{+2.1}_{-2.4}$	1	0
143	$39.00^{+3.0}_{-3.0}$	$4.99^{+0.12}_{-0.14}$	$3.16^{+1.85}_{-3.06}$	$0.74^{+0.02}_{-0.01}$	$0.22^{+0.35}_{-0.40}$	$0.96^{+0.35}_{-0.39}$	$24.9^{+5.1}_{-3.3}$	4	0
112	$36.00^{+4.0}_{-4.0}$	$5.01^{+0.10}_{-0.11}$	$4.47^{+2.61}_{-3.47}$	$0.74^{+0.01}_{-0.01}$	$0.07^{+0.42}_{-0.46}$	$0.81^{+0.42}_{-0.46}$	$24.0^{+4.0}_{-4.0}$	3	1
135	$33.00^{+2.0}_{-2.0}$	$4.86^{+0.09}_{-0.10}$	$7.08^{+0.86}_{-2.07}$	$0.77^{+0.01}_{-0.01}$	$0.51^{+0.14}_{-0.35}$	$1.28^{+0.13}_{-0.34}$	$19.4^{+1.9}_{-1.4}$	3	1
69	$42.00^{+2.0}_{-2.0}$	$5.49^{+0.07}_{-0.08}$	$2.82^{+0.34}_{-0.82}$	$0.82^{+0.01}_{-0.01}$	$0.45^{+0.23}_{-0.28}$	$1.28^{+0.22}_{-0.28}$	$40.0^{+1.4}_{-2.2}$	3	0
52	$46.00^{+4.0}_{-3.0}$	$5.74^{+0.10}_{-0.08}$	$2.00^{+0.52}_{-1.80}$	$0.82^{+0.01}_{-0.01}$	$0.62^{+0.32}_{-0.44}$	$1.44^{+0.31}_{-0.43}$	$55.0^{+10.0}_{-5.0}$	2	0
48	$51.00^{+6.0}_{-6.0}$	$5.97^{+0.13}_{-0.15}$	$1.26^{+3.21}_{-1.16}$	$0.76^{+0.00}_{-0.02}$	$0.27^{+0.57}_{-0.33}$	$1.03^{+0.56}_{-0.33}$	$75.0^{+20.0}_{-21.7}$	3	0
94	$43.00^{+3.0}_{-3.0}$	$5.31^{+0.08}_{-0.09}$	$2.00^{+1.17}_{-1.90}$	$0.76^{+0.01}_{-0.01}$	$0.39^{+0.34}_{-0.36}$	$1.15^{+0.33}_{-0.35}$	$34.8^{+5.2}_{-3.5}$	2	0
115	$33.00^{+2.0}_{-2.0}$	$4.82^{+0.09}_{-0.10}$	$7.08^{+0.86}_{-2.07}$	$0.98^{+0.01}_{-0.02}$	$0.52^{+0.27}_{-0.25}$	$1.50^{+0.26}_{-0.23}$	$18.8^{+1.5}_{-1.0}$	1	0
132	$33.00^{+2.0}_{-2.0}$	$4.76^{+0.09}_{-0.10}$	$7.08^{+0.86}_{-2.61}$	$0.93^{+0.01}_{-0.01}$	$0.28^{+0.22}_{-0.30}$	$1.21^{+0.21}_{-0.29}$	$18.1^{+2.2}_{-0.9}$	2	0
36	$46.00^{+4.0}_{-2.0}$	$5.94^{+0.10}_{-0.05}$	$1.78^{+0.22}_{-0.78}$	$0.82^{+0.00}_{-0.00}$	$-0.23^{+0.29}_{-0.29}$	$0.59^{+0.29}_{-0.29}$	$70.0^{+12.9}_{-2.1}$	1	0

ID	T_{eff} [kK]	$\log L/L_{\odot}$	age[Myr]	E(J-K)	A(K)	A(J)	$M_{initial}$	N2	N1
173	$33.00^{+2.0}_{-2.0}$	$4.78^{+0.09}_{-0.10}$	$6.31^{+1.63}_{-1.84}$	$0.98^{+0.01}_{-0.02}$	$0.61^{+0.33}_{-0.36}$	$1.59^{+0.32}_{-0.35}$	$19.2^{+1.1}_{-1.9}$	3	0
75	$44.00^{+2.5}_{-2.5}$	$5.54^{+0.08}_{-0.07}$	$1.58^{+1.23}_{-1.02}$	$0.99^{+0.01}_{-0.01}$	$0.68^{+0.45}_{-0.23}$	$1.67^{+0.44}_{-0.23}$	$45.0^{+1.7}_{-5.0}$	2	0
114	$37.00^{+3.0}_{-3.0}$	$4.99^{+0.12}_{-0.14}$	$3.98^{+1.64}_{-3.19}$	$0.98^{+0.01}_{-0.01}$	$0.44^{+0.43}_{-0.48}$	$1.43^{+0.42}_{-0.46}$	$24.0^{+4.0}_{-2.7}$	1	0
108	$37.00^{+3.0}_{-3.0}$	$5.15^{+0.12}_{-0.14}$	$3.98^{+1.64}_{-1.47}$	$1.03^{+0.02}_{-0.01}$	$1.14^{+0.42}_{-0.42}$	$2.17^{+0.41}_{-0.40}$	$27.6^{+2.6}_{-4.5}$	2	0
31	$51.00^{+6.0}_{-6.0}$	$6.19^{+0.13}_{-0.15}$	$1.26^{+2.72}_{-1.16}$	$1.00^{+0.00}_{-0.02}$	$0.83^{+0.51}_{-0.36}$	$1.83^{+0.50}_{-0.36}$	$100.0^{+21.1}_{-38.8}$	1	0
49	$43.00^{+3.0}_{-3.0}$	$5.60^{+0.08}_{-0.09}$	$2.51^{+0.65}_{-1.39}$	$0.88^{+0.01}_{-0.00}$	$0.19^{+0.35}_{-0.42}$	$1.08^{+0.35}_{-0.41}$	$45.0^{+5.0}_{-5.0}$	1	0
46	$48.00^{+4.0}_{-4.0}$	$6.02^{+0.12}_{-0.09}$	$1.26^{+3.21}_{-0.70}$	$0.75^{+0.00}_{-0.02}$	$0.15^{+0.50}_{-0.28}$	$0.90^{+0.50}_{-0.28}$	$82.9^{+12.1}_{-29.6}$	3	0
47	$48.00^{+4.0}_{-4.0}$	$5.95^{+0.14}_{-0.13}$	$1.41^{+3.05}_{-1.31}$	$0.77^{+0.00}_{-0.02}$	$0.04^{+0.38}_{-0.36}$	$0.81^{+0.38}_{-0.36}$	$73.5^{+16.6}_{-20.2}$	3	0
40	$51.00^{+6.0}_{-6.0}$	$5.97^{+0.13}_{-0.15}$	$1.26^{+3.21}_{-1.16}$	$0.81^{+0.00}_{-0.02}$	$0.41^{+0.57}_{-0.33}$	$1.23^{+0.56}_{-0.33}$	$75.0^{+20.0}_{-21.7}$	1	0
116	$37.00^{+3.0}_{-3.0}$	$4.97^{+0.12}_{-0.14}$	$3.55^{+2.08}_{-3.45}$	$1.33^{+0.01}_{-0.01}$	$0.54^{+0.51}_{-0.51}$	$1.87^{+0.51}_{-0.51}$	$24.0^{+3.1}_{-3.8}$	1	1
118	$39.00^{+3.0}_{-3.0}$	$5.07^{+0.12}_{-0.14}$	$3.16^{+1.85}_{-3.06}$	$0.70^{+0.01}_{-0.00}$	$-0.11^{+0.42}_{-0.41}$	$0.58^{+0.41}_{-0.40}$	$26.5^{+4.0}_{-3.3}$	2	0
42	$46.00^{+4.0}_{-3.0}$	$5.64^{+0.10}_{-0.08}$	$1.58^{+0.93}_{-1.48}$	$1.12^{+0.01}_{-0.01}$	$0.20^{+0.45}_{-0.29}$	$1.32^{+0.44}_{-0.28}$	$50.0^{+10.0}_{-5.8}$	0	0
55	$51.00^{+6.0}_{-6.0}$	$5.93^{+0.13}_{-0.15}$	$0.79^{+3.67}_{-0.69}$	$0.92^{+0.01}_{-0.02}$	$0.73^{+0.43}_{-0.39}$	$1.65^{+0.42}_{-0.38}$	$75.0^{+15.1}_{-21.7}$	0	0
71	$44.00^{+2.5}_{-2.5}$	$5.49^{+0.08}_{-0.07}$	$1.78^{+1.04}_{-1.22}$	$1.03^{+0.01}_{-0.01}$	$0.55^{+0.30}_{-0.18}$	$1.57^{+0.29}_{-0.17}$	$42.3^{+2.7}_{-4.5}$	1	0
121	$33.00^{+1.5}_{-1.5}$	$4.84^{+0.07}_{-0.07}$	$7.08^{+0.86}_{-1.46}$	$0.95^{+0.01}_{-0.01}$	$0.66^{+0.13}_{-0.22}$	$1.61^{+0.13}_{-0.22}$	$19.4^{+0.6}_{-1.4}$	1	0
9	$41.00^{+3.0}_{-3.0}$	$6.30^{+0.11}_{-0.12}$	$1.78^{+0.22}_{-0.19}$	$0.94^{+0.00}_{-0.01}$	$-0.15^{+0.25}_{-0.43}$	$0.78^{+0.25}_{-0.43}$	$119.6^{+17.7}_{-24.6}$	1	0
65	$44.00^{+2.5}_{-2.5}$	$5.56^{+0.08}_{-0.07}$	$2.00^{+0.82}_{-1.20}$	$0.74^{+0.00}_{-0.01}$	$-0.13^{+0.33}_{-0.30}$	$0.62^{+0.33}_{-0.29}$	$45.0^{+5.0}_{-5.0}$	1	0
134	$38.00^{+2.0}_{-2.0}$	$4.91^{+0.05}_{-0.06}$	$2.24^{+2.23}_{-1.44}$	$1.10^{+0.01}_{-0.01}$	$0.60^{+0.21}_{-0.18}$	$1.71^{+0.21}_{-0.18}$	$24.0^{+1.9}_{-2.5}$	1	0
64	$42.00^{+2.0}_{-2.0}$	$5.60^{+0.07}_{-0.08}$	$2.51^{+0.65}_{-0.27}$	$0.77^{+0.00}_{-0.00}$	$0.06^{+0.35}_{-0.11}$	$0.82^{+0.35}_{-0.11}$	$45.0^{+1.6}_{-5.0}$	0	0
45	$43.00^{+3.0}_{-3.0}$	$5.76^{+0.08}_{-0.09}$	$2.24^{+0.58}_{-0.46}$	$0.66^{+0.00}_{-0.00}$	$0.17^{+0.38}_{-0.25}$	$0.83^{+0.38}_{-0.25}$	$55.0^{+5.0}_{-5.0}$	1	0
123	$40.00^{+2.0}_{-2.0}$	$5.04^{+0.07}_{-0.08}$	$1.12^{+2.43}_{-1.02}$	$1.19^{+0.01}_{-0.01}$	$0.63^{+0.24}_{-0.18}$	$1.81^{+0.23}_{-0.17}$	$28.0^{+2.0}_{-3.2}$	0	0

5.4 Visual companions

For each star, detected in both J and K, we determined a distance between the star and its closest neighbor. Figure 5.18-top shows the number of visual close stars, detected both in Ks and J vs their separation in arc-second. More than 250 (pair of) stars have a closest neighbor at the separation less than 0.2". Over 90% of massive objects (brighter than 17 mag in K and 16 mag in J) have a closest neighbor with a separation of less than 0.2". Figure 5.18-bottom shows the separation between the visual close stars versus their distance from R136a1 in the core. This figure indicates that even the sources at larger radii have close visual companions, so that the large number of close visual companions is not just an effect of 2D projection on the sky across the FoV. For the sake of simplicity, regardless of physically bound or not, we call these closely stars **visual companions** hereafter.

The most massive stars R136a1, R136a3 and R136c have visual companions which are detected for the first time. R136a3 is also resolved as two stars with the PSF fitting. Both stars have high correlation coefficient (above 70%) with the input PSF. The separation between R136a3 primary and secondary is about 58.9 ± 2.14 which is larger than the FWHM of the PSF. Note that even the closest visual companions (like R136a3) are physically far from each other (0.059" is 2890 AU). This visual separation produces a period over $P = 10^4 yr$, so probably these sources are not gravitationally bound to each other. Table 5.3 shows the list of the 20 stars, detected in both J and K data, which have companions closer than 0.8". The flux ratio between two companions in K and J band are given in the third and fourth column, respectively. Their separation [in mas] also is given in the last column. Among these stars, we identified visual companions for R136a1 and R136a3, for the first time.

Table 5.3 List of 20 stars which have a companion closer than 0.08". These stars detected in both J- and Ks- band data.

ID1	ID2	<i>FluxRatio_K</i>	<i>FluxRatio_J</i>	Separation[mas]
59	3(a3)	0.044	0.124	58.88 ± 2.14
357	272	0.699	0.577	59.87 ± 0.17
760	519	0.567	0.896	62.62 ± 5.71
643	214	0.208	0.139	63.67 ± 0.31
319	79	0.166	0.177	64.11 ± 4.23
804	517	0.512	0.365	65.06 ± 1.40
380	265	0.630	0.324	66.29 ± 1.61
807	565	0.571	0.830	67.12 ± 3.18
11(a9)	8(a6)	0.878	0.959	70.07 ± 0.88
25	4(c)	0.114	0.095	70.27 ± 0.07
396	56	0.079	0.065	71.25 ± 2.45
635	589	0.870	0.730	72.21 ± 2.30
541	489	0.867	0.964	73.65 ± 4.21
637	539	0.774	1.002	73.84 ± 1.08
312	87	0.197	0.188	74.13 ± 2.37
72	54	0.686	0.714	74.47 ± 0.45
16	1(a1)	0.112	0.152	75.32 ± 2.33
761	655	0.796	0.689	75.65 ± 0.61
353	305	0.819	0.450	75.91 ± 0.94
317	262	0.766	0.413	79.30 ± 0.09

5.5 Density and Surface Brightness Profile

The unexpected number of detected sources in a small FoV and of new resolved companions in R136 indicates that this compact cluster is more crowded than thought before. The error-bars on the stellar masses and also on the age and extinction of the cluster itself are large enough to make it difficult to study the density profile of R136. Instead, one can scrutinize the surface brightness profile (SBP) of this cluster which is less affected by the confusion and crowding. The SBP informs us on the average magnitude per pixel at different radii. Figure 5.19 depicts the SBP of the core of R136 in J and K, centered at R136a1. On average the SBP in Ks is brighter than J, which can be caused by the extinction or the brightness of the stars in Ks. One can notice a number of bumps on the SBP at 0.08, 0.15, 0.46, 1.17 pc radii roughly. These radial distances are the locations of known WR stars. The position of 5 WRs in the FoV is shown in the SBP plot. These stars have extensive emissions in the Ks band because of their wind and mass loss.

Using the stellar masses estimated at the age of 2 Myr and extinction values in J and K ($A_J = 1.3 \pm 0.5$ and $A_K = 0.4 \pm 0.5$), we plotted the two-dimensional (projected) density profile (Figure 5.20). We used an Elson-Fall-Freeman (EFF) profile [Elson et al. (1987)] to fit the projected mass density in the core of R136 (Eq. 5.1). We also fitted another function to the projected number density, given in Eq. 5.2 since this function provides better fitting parameters than Elson-Fall-Freeman profile.

$$\rho[M_{\odot}/pc^2] = \frac{\rho_0}{\left(1 + \frac{r^2}{a^2}\right)^{\frac{\gamma+1}{2}}} \quad (5.1)$$

$$\rho[stars/pc^2] = \frac{\rho_0}{1 + \left(\frac{r}{a}\right)^b} \quad (5.2)$$

We estimate the central mass density of $\rho_0 = 1.15 \times 10^4 [M_{\odot}/pc^2]$ and the parameters $\gamma = 2.04 \pm 0.54$ and $a = 0.45 \pm 0.12$. For the number density, we found $\rho_0 = 288 \pm 27 [stars/pc^2]$ and the parameters $a = 0.87 \pm 0.04$ and $b = 4.55 \pm 0.37$. Total observed mass of the clusters for

$r < 1.4 pc$ is $M_{obs} = (1.06_{0.16}^{0.20}) \times 10^4 M_{\odot}$. We could detect stellar masses down to $2 M_{\odot}$, so total mass of the cluster depends on the shape of MF and the lowest mass limit. The real stellar masses remain open as we are limited to the angular resolution of SPHERE/IRDIS, so the estimated central projected density is a lower limit to the real central density.

Note that the estimated density is projected in two-dimension (2D). In order to estimate the three dimensional (3D) density approximately, we consider R136 is spherically symmetric and has a radius of $R_{cluster}$. The density profiles are estimated for different $R_{cluster}$ values, from 2 pc to 6pc. Hence, 3D central densities, γ and a are computed by fitting EFF profile (Eq. 5.1). Table 5.4, shows the fitting (3D) parameters for R136 considering different values of $R_{cluster}$. Figure 5.22 depicts the 3D density profiles for different values of $R_{cluster}$.

The total mass of the cluster can be estimated by extrapolating to the considered $R_{cluster}$. Figure 5.21 shows the cumulative total mass of the cluster within 6pc. The estimated half-mass radius is $(0.57 \pm 0.04) pc$. The ratio of the observed total mass within $r < 1.4 pc$ to the total mass estimated of the cluster, within a given radius ($R_{cluster}$) also is given in the last column of Table 5.4.

Estimated value of γ and a in 2D and 3D are consistent and the shape of the densities are flatter than Plummer model (close to King model). All the 3D central densities are smaller than the previous values given by Mackey & Gilmore (2003) and Selman & Melnick (2013). Value of γ is consistent with the values derived by these authors. Computed value of a is consistent with the estimated value by Selman & Melnick (2013).

5.6 Discussion and conclusion

In this study we presented photometric analysis of the core of R136 using the VLT/SPHERE instrument in the near-IR. The high quality and resolution of these data open a new perspective on our understandings on R136. For the first time, more than thousand sources have been detected

Table 5.4 Estimation of central density of R136 in three-dimension considering different $R_{cluster}$. First column gives the hypothetical radius of the cluster. The second column is the three-dimensional central mass density. Third and fourth columns are the fitting parameters, γ and a , in the Eq. 5.1. Finally the last column is the ratio of observed mass which is limited by $r < 1.4pc$, to the total mass estimated of the cluster, within a given radius. $M_{obs} = (1.06_{0.16}^{0.20}) \times 10^4 M_{\odot}$.

$R_{cluster}$ [pc]	$\log(\rho_0)$ [M_{\odot}/pc^3]	γ	a	M_{obs}/M_{total}
2	3.49 ± 0.10	1.72 ± 0.34	0.35 ± 0.08	0.91 ± 0.02
3	3.32 ± 0.10	1.97 ± 0.39	0.39 ± 0.09	0.84 ± 0.03
4	3.20 ± 0.10	2.07 ± 0.41	0.40 ± 0.09	0.81 ± 0.03
5	3.11 ± 0.10	2.13 ± 0.42	0.41 ± 0.09	0.79 ± 0.03
6	3.03 ± 0.10	2.17 ± 0.43	0.42 ± 0.10	0.78 ± 0.03

in K and J-band data in the small FoV of IRDIS ($10.9'' \times 12.3''$) covering almost 2.7×3.1 pc of R136's core. HST WFPC2 and WFC3 data, due to a lower resolution and pixel sampling, did not detect such a number of sources in the R136's core. For the ground-based telescopes, the best data comes from VLT/MAD, where the AO quality (Strehl ratios of 15-30% in Ks) is not as good as with SPHERE (Strehl ratios of 80% in Ks). So the confusion, especially in the core remains large enough for the sources being undetectable in its core.

In SPHERE/IRDIS data, more than 60% of stars have companions closer than $0.2''$ ($0.05pc$). 90% of the very massive bright stars which already have been studied spectroscopically by Crowther et al. (2016), have visual companions. The large error-bars on the spectroscopic parameters (T_{eff} and $\log L$) prevent us to estimate the age, extinction and stellar masses accurately. From our analysis, the most probable age of the core is $1.8_{-0.8}^{+1.2}$ Myr and the extinction in J and K are $A_J = (1.3 \pm 0.5) mag$ and $A_K = (0.4 \pm 0.5) mag$, respectively. Considering the photometric errors, the stellar masses are estimated at different ages with a broad extinction range. The MF

slope for 2 Myr isochrone is $\Gamma_{2\text{Myr}} = -1.21 \pm 0.11$ for the mass range of (6 - 160) M_{\odot} . As the core gets better resolved, more stars are detected. The MF slope is consistent with Kroupa value ($\Gamma = -1.3$) and smaller than Salpeter value ($\Gamma = -1.35$). The derived MF is limited to the resolution of the instrument and also on the detection limit of the observation. Higher angular resolution data may resolve binaries and low-mass stars which affects the shape of MF. Figure 5.20 shows the density profile of the R136's core at 2 Myr. The lower limit of the central density of R136 is $\rho_0 = (1.15_{0.24}^{0.29}) \times 10^4 [M_{\odot}/pc^2]$ at 2 Myr which is about $\rho_0 = 288 [stars/pc^2]$. Observed total mass of R136 for $r < 1.4pc$ is $M_{obs} = (1.06_{0.16}^{0.20}) \times 10^4 M_{\odot}$. Considering R136 is a spherically symmetric cluster with Radius $R_{cluster}$ (Table 5.4), we estimated 3D density profile. The 3D central densities are smaller than the values estimated in previous studies. Computed values of γ and a (Eq. 5.1) are consistent in 2D and 3D considering different $R_{cluster}$. All density profiles are flatter than Plummer model ($\gamma = 4.0$).

Very massive stars in R136 have similar characteristics as the galactic WR stars in the core of NGC3603. NGC3603 is almost 8 times closer than R136. One can see the effect of confusion in Figure 5.23 in which we visualize NGC3603 at the distance of R136 (Figure 5.23 Middle). Using Starfinder we detected 408 and 288 stars in J and Ks images respectively [?]. Using the same criteria for Starfinder, we only detect 109 and 52 sources in J and Ks images of NGC3603 at the distance of R136, which means that more than 70% of the stars cannot be detected. This implies that about 1000 detected stars in the R136's core ($r < 6''$) are possibly 30% of the real number. The average density in this region ($r < 6''$) would increase from 71 [$star/pc^2$] to 230 [$star/pc^2$]. The lack of resolution prevents us to accurately estimate stellar masses, core density and density profile, whilst SBP turns out to be less affected. Figure 5.24 shows the SBP of NGC3603 both from IRDIS data in J and Ks band, directly and simulated as would be located at a distance of R136. The general trend is not affected.

Using SPHERE data, we have gone one step further and partially resolved and understood the

core of R136 but this is certainly not the final step. R136 needs to be observed in the future with higher resolution (E-ELT) and/or a more stable PSF (JWST), therefore deeper field imaging. The cluster would then be better characterized for its age, individual and multiple stars and ultimately its kinematics on a long enough temporal baseline of observation.

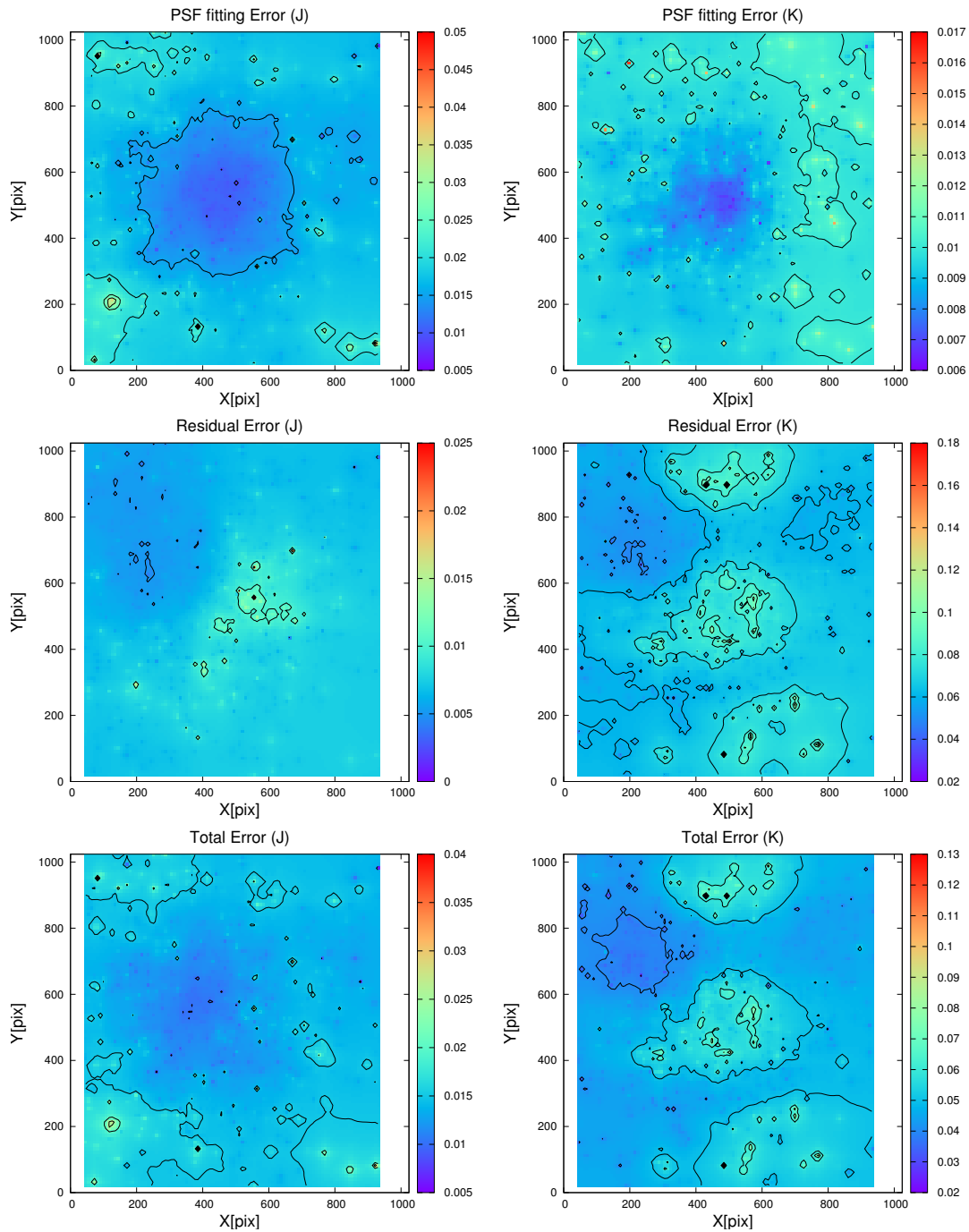


Figure 5.9 Top: map of the PSF fitting errors (outcome of the Satfinder photometry) along the IRDIS FoV. Middle: map of the residual errors, outcome of the background analysis after removing the stellar sources signals from the image. Bottom: map of the total error, combination of the PSF-fitting errors and the residuals background errors. Left: J; Right: K

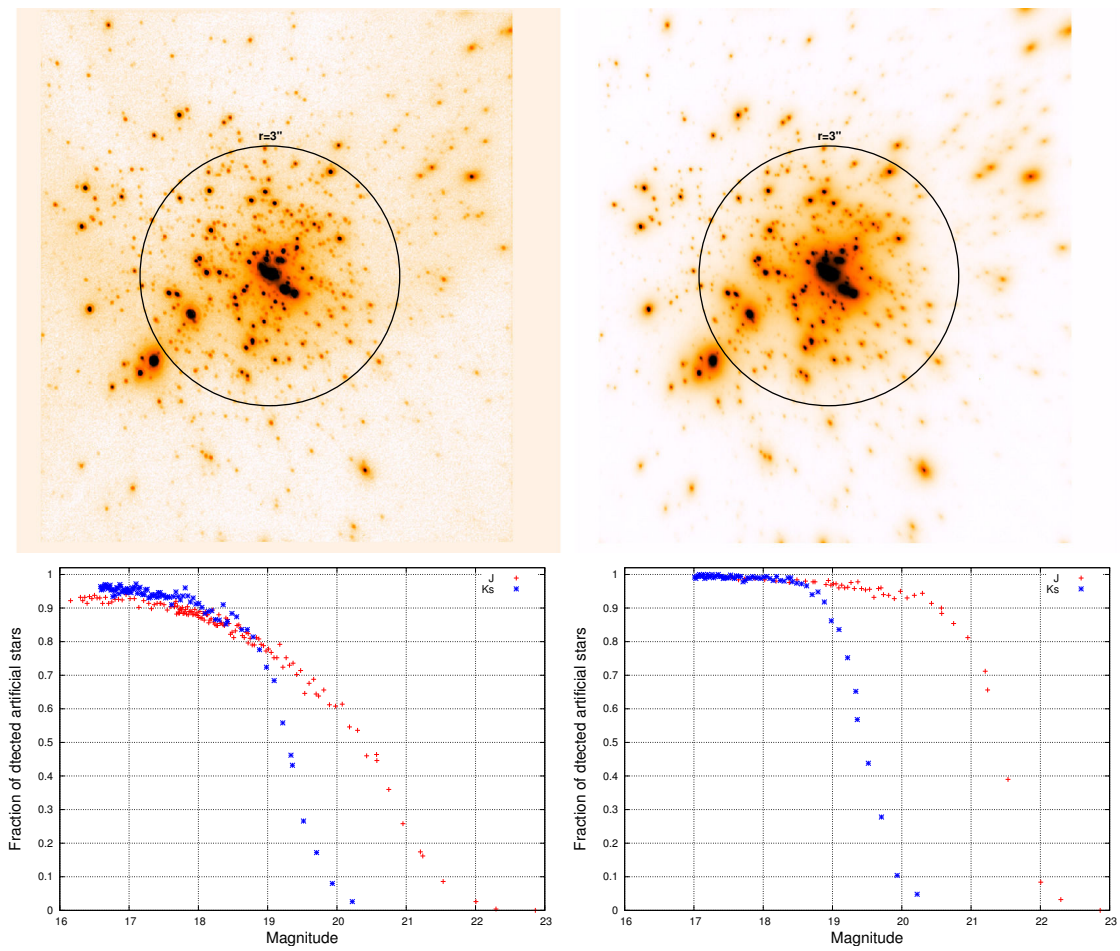


Figure 5.10 Top: r136 in K (left) and J (right) with the circle of 3" radii. Bottom: Incompleteness test in J (red pluses) and K (blue crosses) for two regions: Very core of R136 ($r < 3''$) in the left and outside of the core ($r > 3''$) in the right.

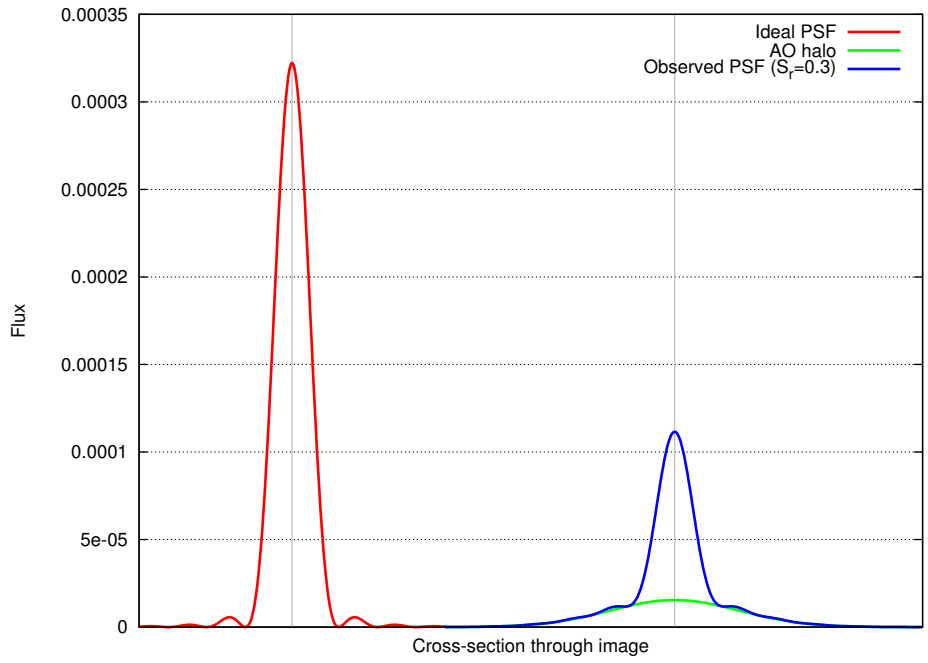


Figure 5.11 Theoretical diffraction pattern PSF (Airy disc) is shown in Red (left) and the simulation of the observed PSF with $S_r=0.3$ is presented in Blue. The green Gaussian profile indicates the AO halo.

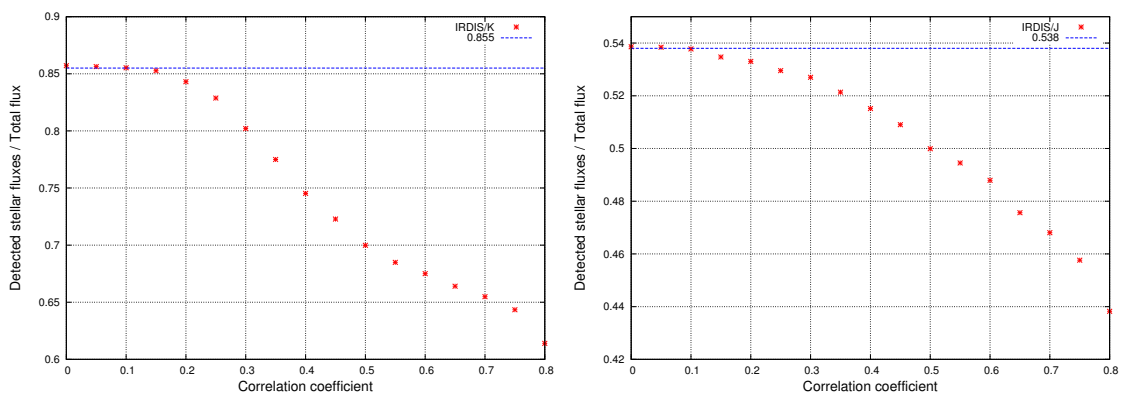


Figure 5.12 The Strehl ratio as a function of minimum correlation coefficient between the input PSF and detected stellar source, in K-band (left) and J-band (right) data of SPHERE/IRDIS from the core of R136.

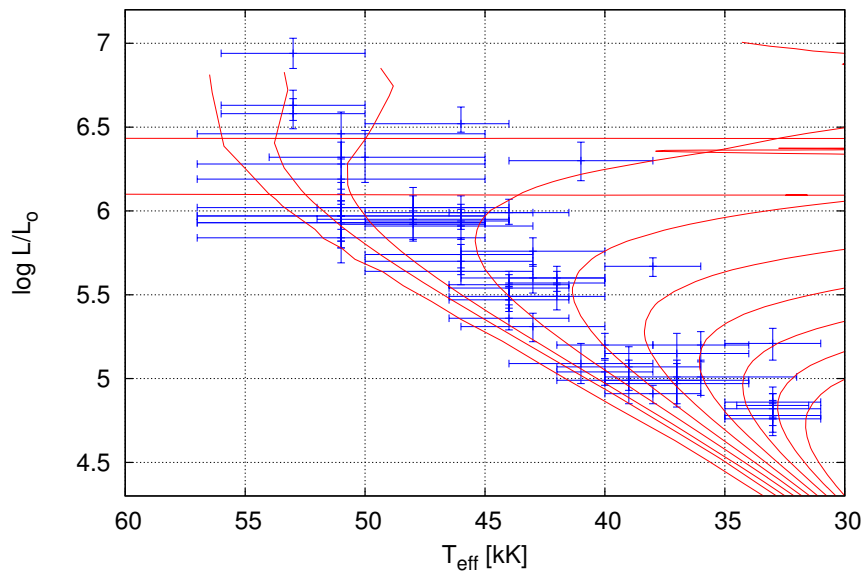
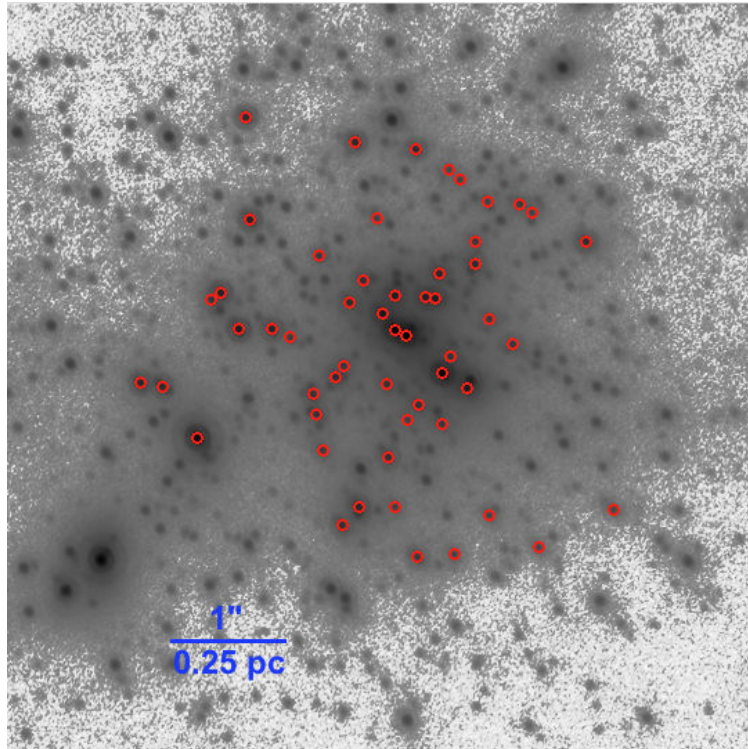


Figure 5.13 The top image corresponds to the IRDIS/Ks on which the 54 spectroscopically known stars from [Crowther et al. (2016)] have been added as red circles. The bottom plot depicts the T_{eff} , $\log L/L_{\odot}$ and corresponding error-bars on these 54 sources taken from Crowther et al. 2016 in blue. The solid red lines indicate the PARSEC isochrones covering ages from 0.1 to 8 Myr.

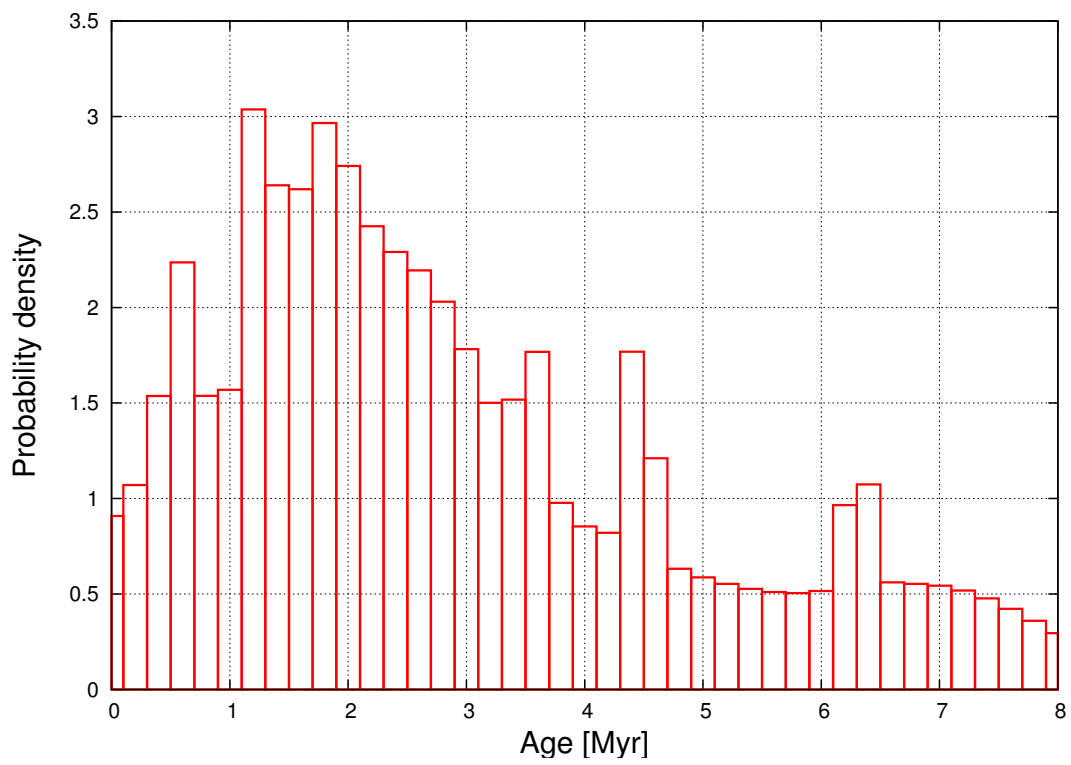


Figure 5.14 generalized histogram of the age of 55 known stars from Crowther et al. 2016.

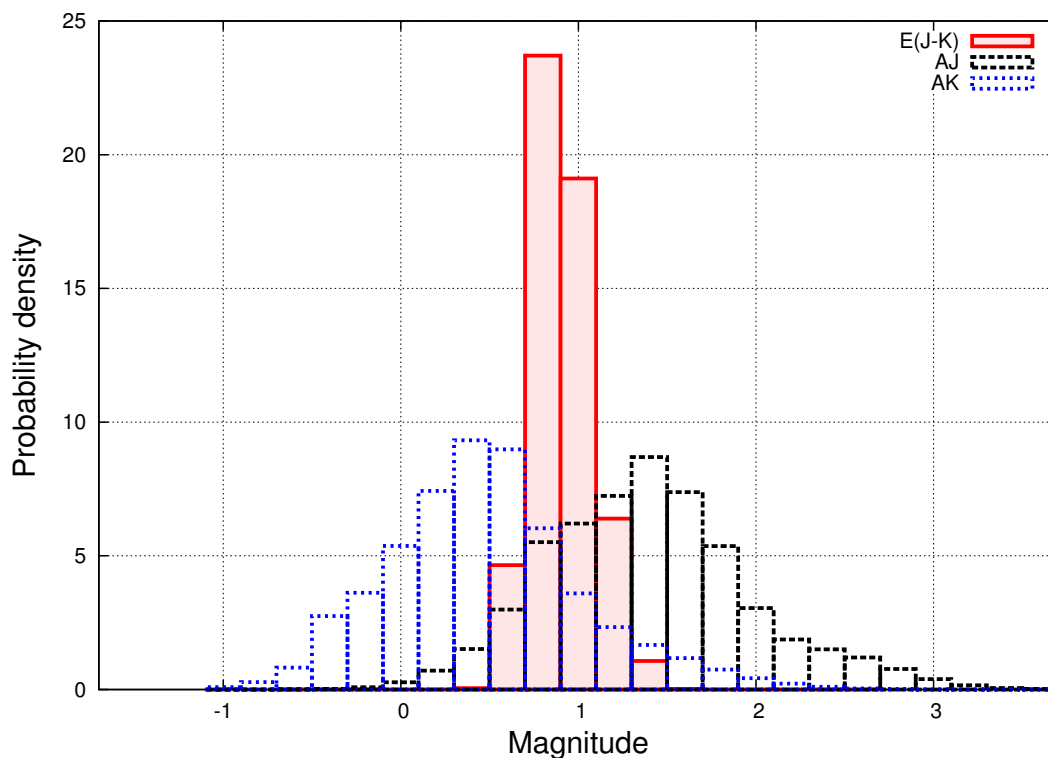


Figure 5.15 Generalized histogram of the extinction of 55 spectroscopically known stars from Crowther et al. 2016.

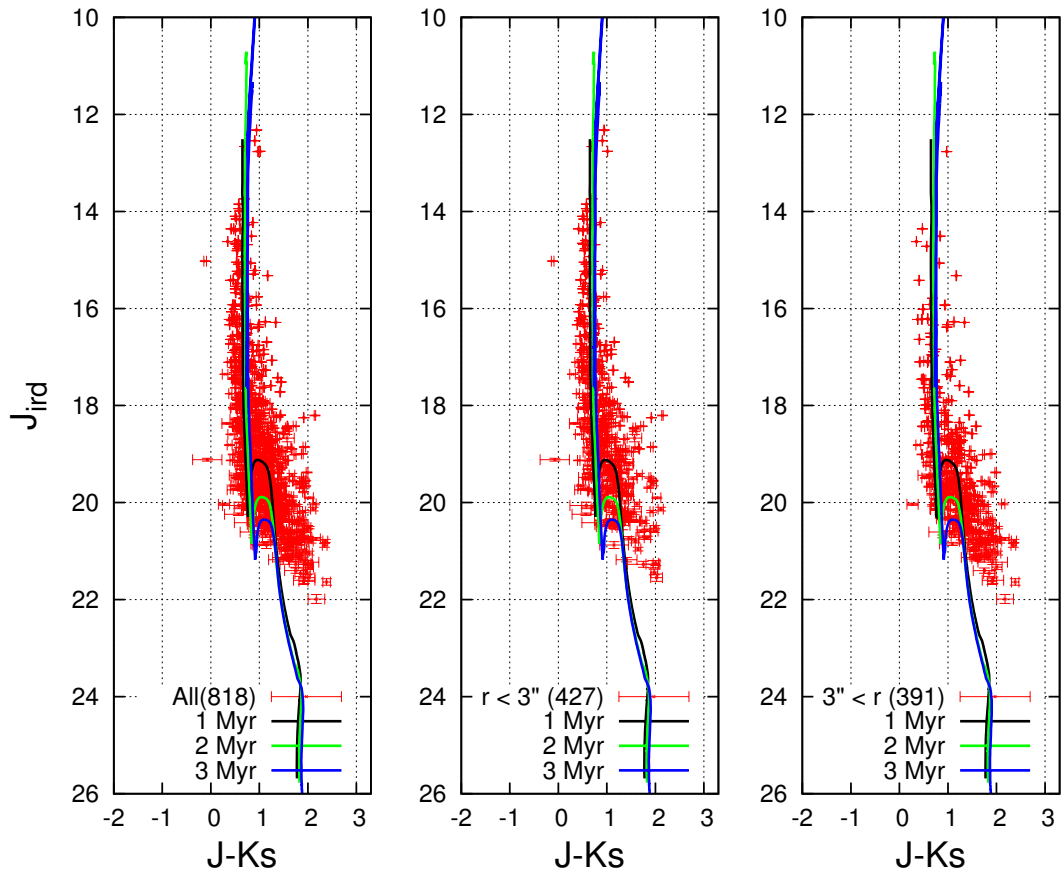


Figure 5.16 isochrones at the ages of 1, 2 and 3 Myr (corrected for distance modulus of 18.45 and central values of extinctions, $A_J = 1.3 \text{ mag}$ and $A_K = 0.4 \text{ mag}$). The CMD is plotted for the whole FoV (818 sources), in the very core of the cluster ($r < 3''$) and outside ($r > 3''$), from left to right respectively. The error-bars on each point is the combination of the PSF-fitting errors and the residual errors from the background image after removing the stellar sources signals from the images.

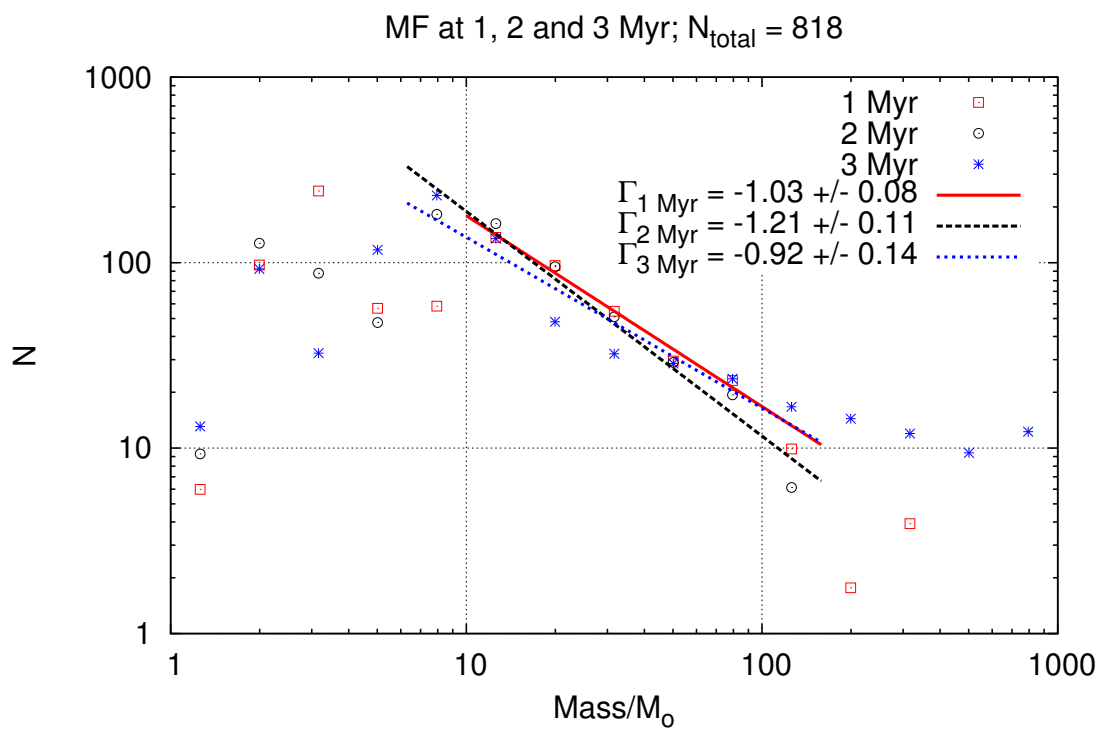


Figure 5.17 Generalized histogram of the MF at 1, 2 and 3 Myr.

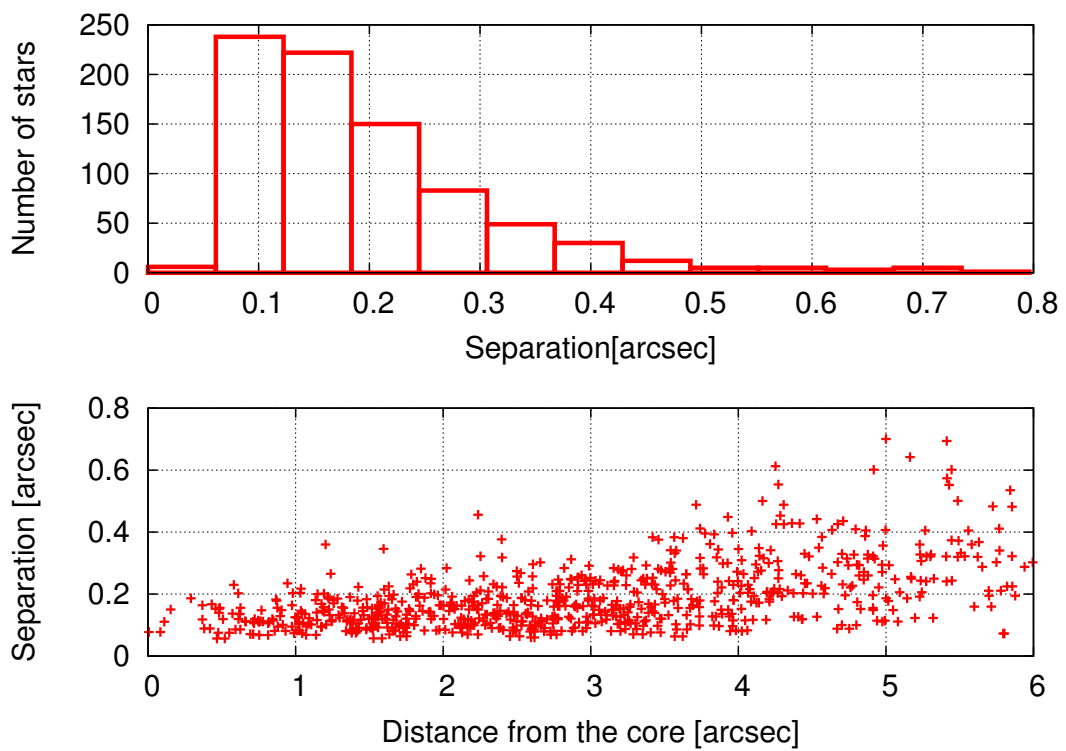


Figure 5.18 Top: Histogram of the separation of the close detected sources. For each star which is detected in both J and K data, we determined a distance between the star and its closest neighbor. Bottom: Separation of the visual close detected sources versus their distance from the core of R136.

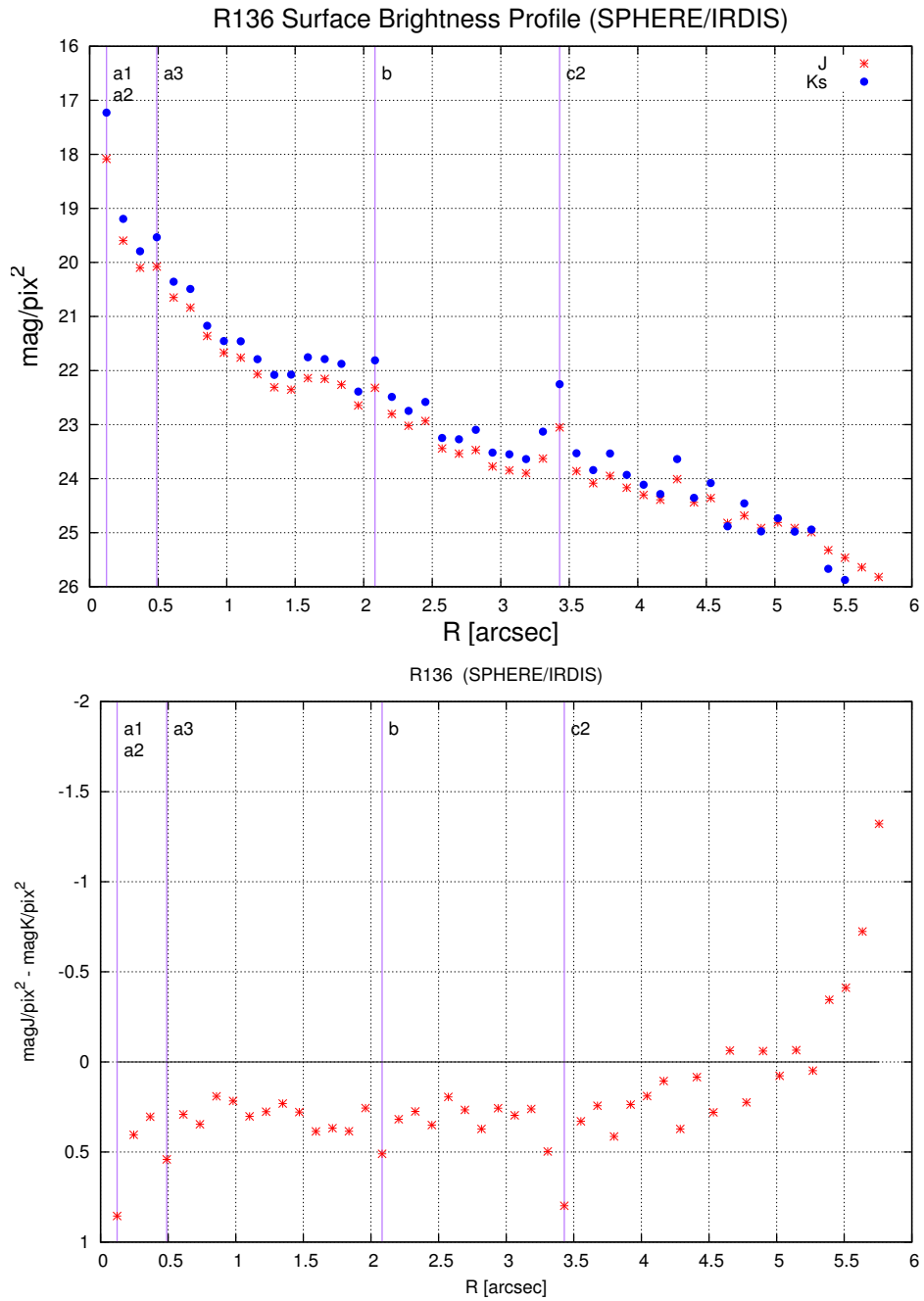


Figure 5.19 Left: Surface brightness profile (mag/pixel) of R136 in IRDIS FoV centered on R136a1. Right: same as Left, but the differences in the Kmag/pixel and Jmag/pixel is shown.

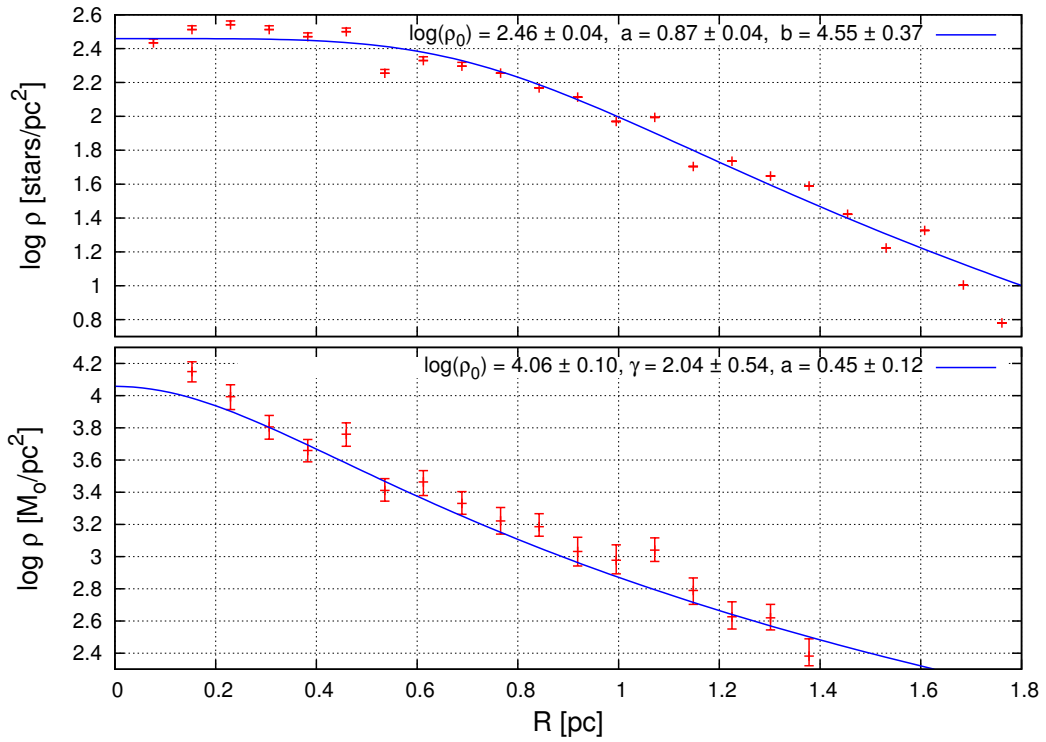


Figure 5.20 Projected density profile of R136 in IRDIS FoV centered on R136a1. Up: number density [stars/pc^2]. Number of stars is taken from the catalog of common stars between IRDIS, J and Ks data. Bottom: mass density [M_{\odot}/pc^2]. The stellar masses are estimated at the age of 2 Myr with extinction values of $A_J = 1.3 \pm 0.5$ and $A_K = 0.4 \pm 0.5$ in J and Ks band. Eq. 5.1 and Eq. 5.2 are used to fit the blue solid line to the data in upper and bottom plots, respectively.

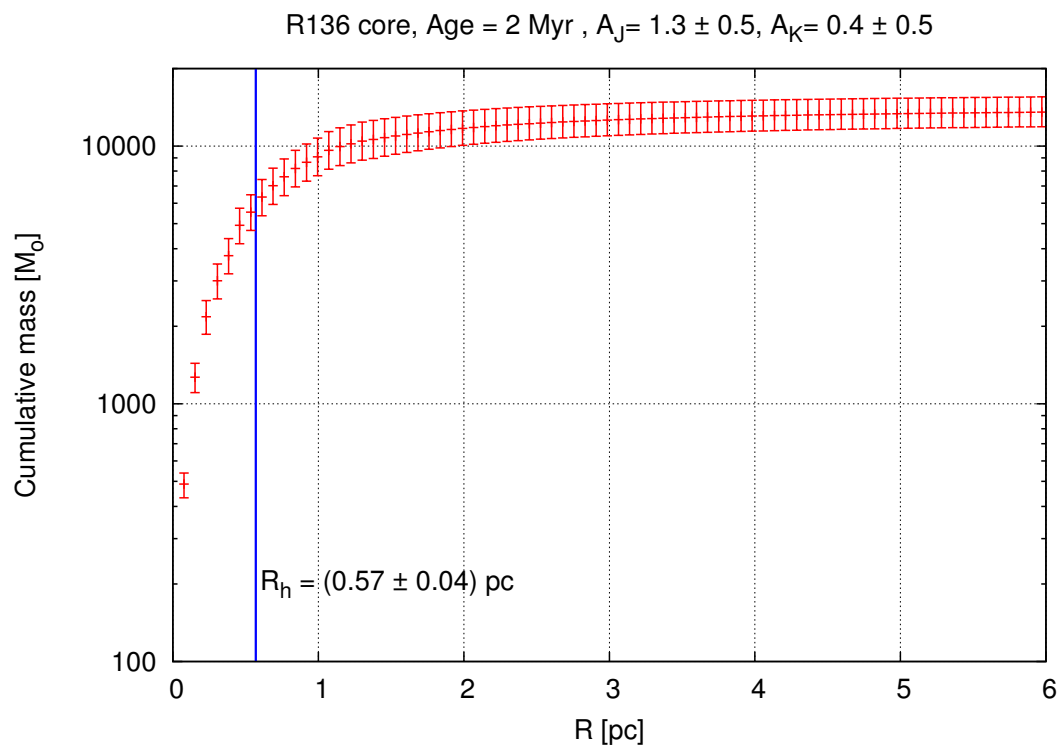


Figure 5.21 Cumulative total mass of R136 using extrapolation in 2D.

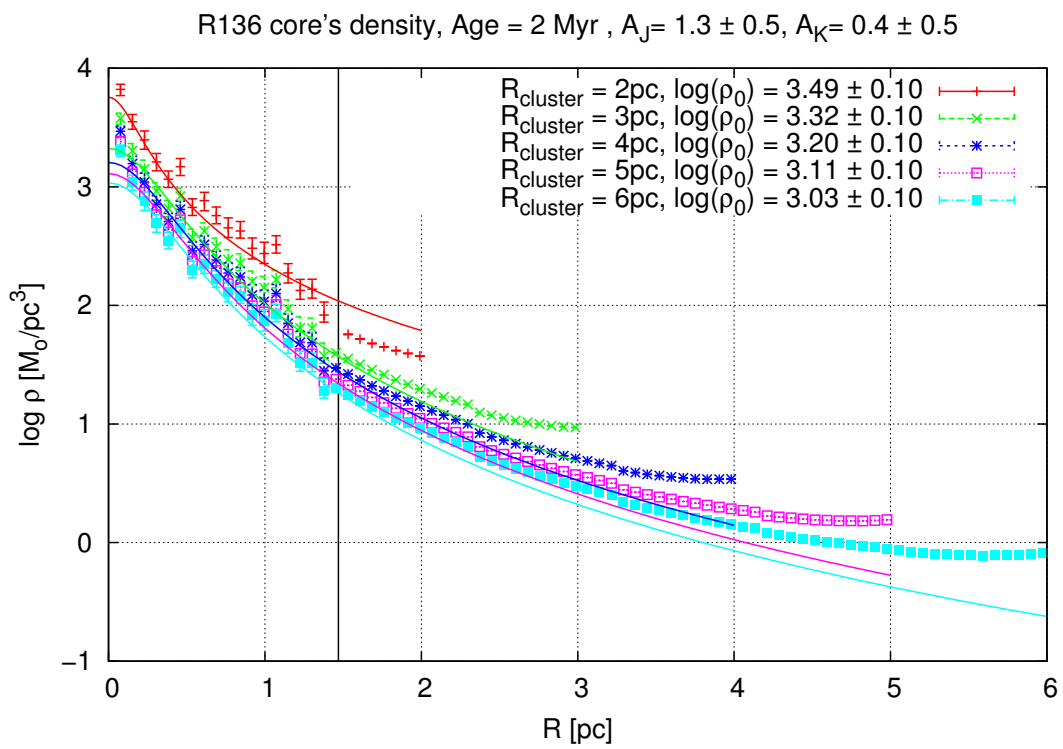


Figure 5.22 The 3D mass density profiles for different values of R_{cluster} . I used Eq. 5.1 for fitting. The fitting parameters, γ and a , are given in Table 5.4.

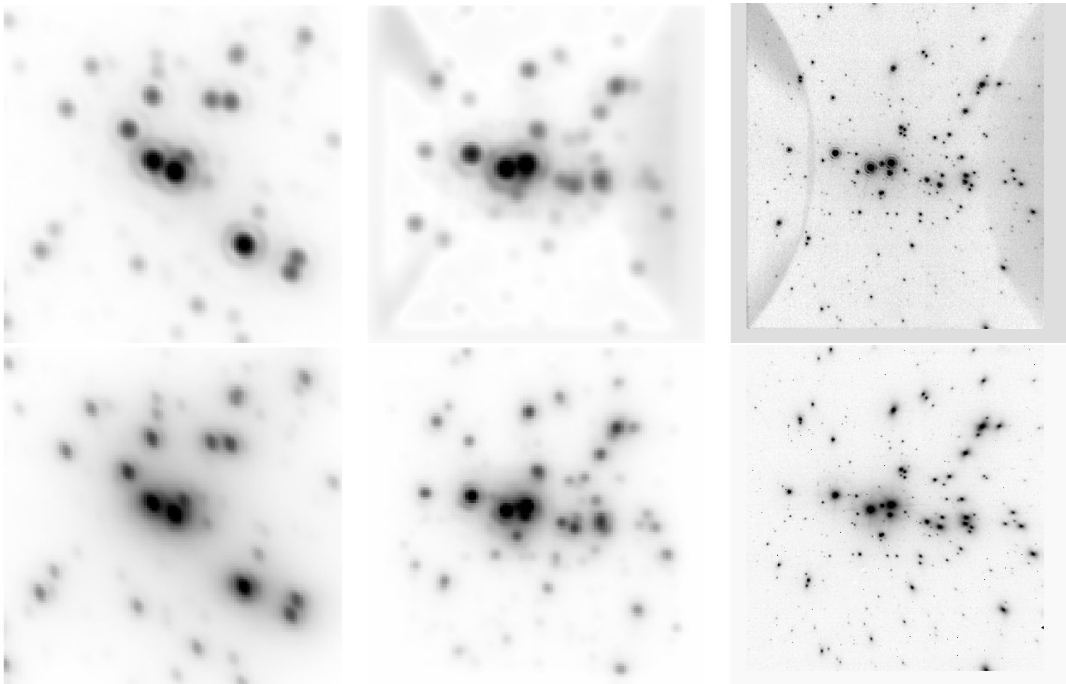


Figure 5.23 Comparison of NGC3603 and R136 images from VLT/SPHERE. Left: Core of R136 ($1.56'' \times 1.56''$) at its real distance. Right: Core of NGC3603 ($12.5'' \times 12.5''$) at its real distance. Middle: NGC3603 as it would appear at the same distance as R136. Upper and bottom panels are in IRDIS Ks and J band bands images, respectively.

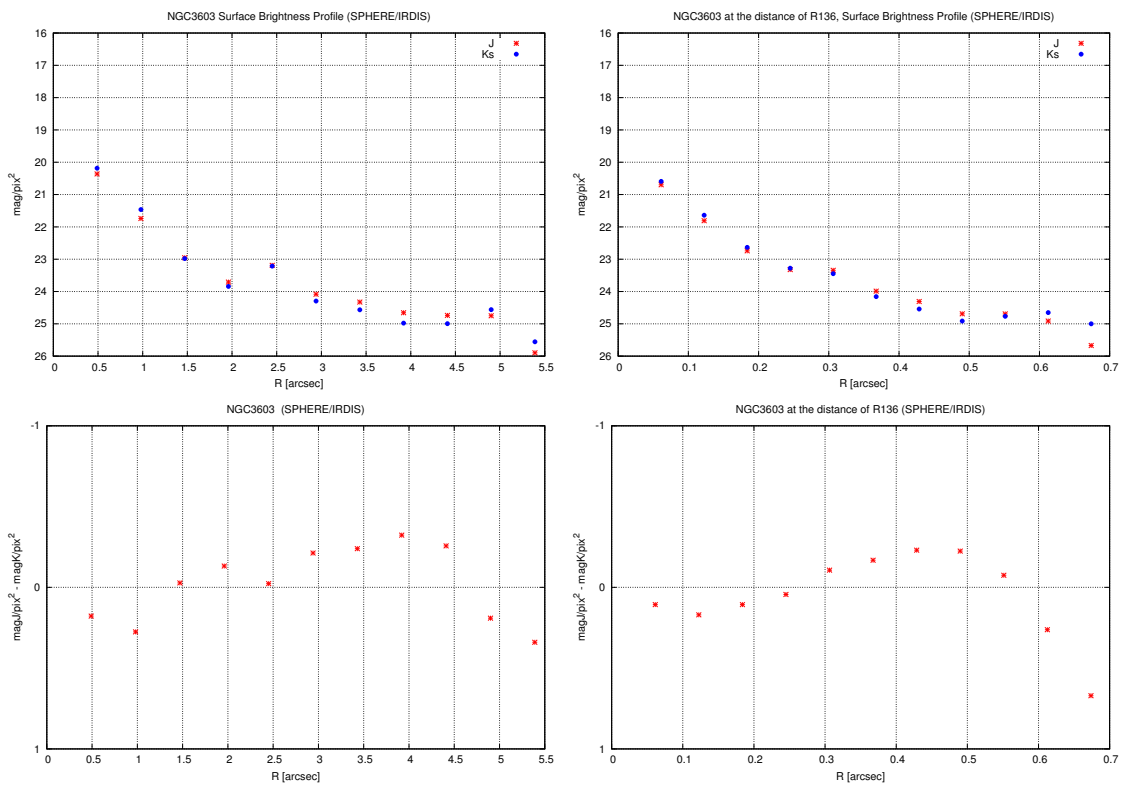


Figure 5.24 Top: SBP of NGC3603 in SPHERE/IRDIS J and K band data. Bottom: the difference of $\text{Kmag/pixel} - \text{Jmag/pixel}$. Left: NGC3603 real images. Right: NGC3603 in the distance of R136.

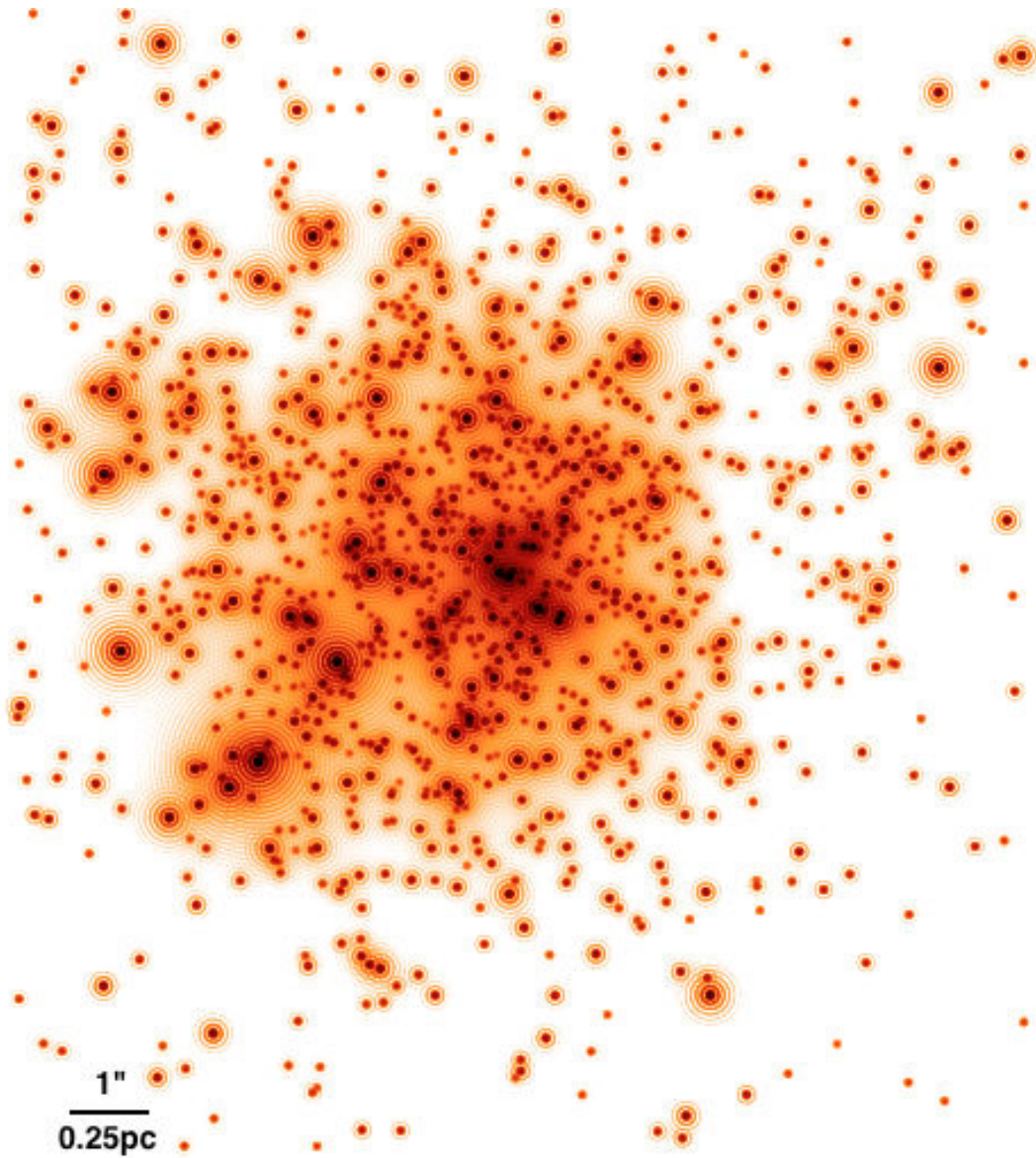


Figure 5.25 Reconstructed image of the R136 taken by IRDIS/Ks. The position and flux of stellar sources is estimated by Starfinder.

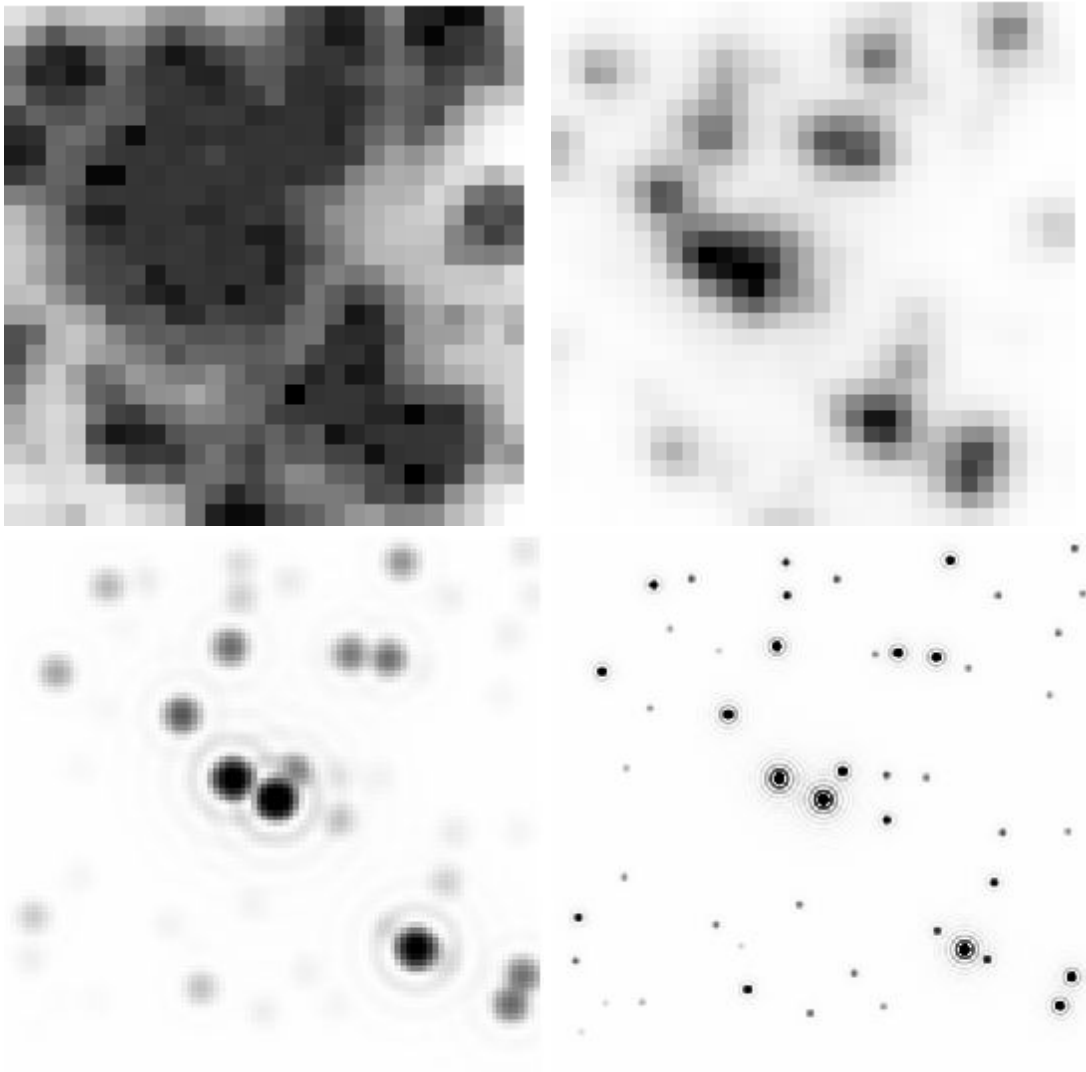


Figure 5.26 FoV: $1.225'' \times 1.225''$ of the core of R136 taken by HST in V-band at the top (Left:WFC2 and Right: WFC3). At Bottom is the reconstructed images of IRDIS/Ks (left) and E-ELT/MICADO/Ks (right), with the same FoV as top images.

Good-bye to Supermassive Stars

THE CASE for supermassive and superluminous stars received a series of body blows recently. For several years astronomers have suspected that stars several thousand times more massive than the Sun might be lurking in giant nebulae. However, new observations have shown that there is no supermassive star in one of the most likely locations for such an object, the mysterious heart of the 30 Doradus nebula in the Large Magellanic Cloud. This nebula, also called the Tarantula or NGC 2070, is a giant cloud of ionized hydrogen (H II), luminous enough to be visible with the unaided eye even though it lies some 180,000 light-years away. At the nebula's center is a cluster of very hot blue stars, with a fuzzy, 10th-magnitude core about 5 arc seconds across. This central patch of light is named R136 (HD 38268), and its brightest part, R136a, is itself a multiple object (see page 134 of the February, 1984, issue).

The 30 Doradus nebula is a relatively nearby example of giant H II regions; one in our own Milky Way galaxy is NGC 3603 in Carina. In the centers of these massive clouds lie bizarre objects indeed. For example, R136a is only a few light-years across, but emits as much energy as 50 to 100 million Suns, or several dozen of the hottest known O-type supergiants.

Clearly something unusual is going on in the centers of 30 Doradus and its kin, but just what kind of objects release energy at such prodigious rates in such small volumes of space? There have been two popular explanations: supermassive objects with masses 1,000 or more times that

of the Sun, or extremely dense clusters of otherwise normal stars. To decide between the different possibilities requires observations with resolution much better than an arc second.

Anthony Moffat of the University of Montreal and collaborators from West Germany and the United States report on CCD (charge-coupled device) direct images and spectra in the August 1, 1985, *Astrophysical Journal*. They found no evidence indicating the presence of a single supermassive body in R136a. Instead, it appears to consist of several stars with absolute visual magnitudes no brighter than -7 or -8 , within the range of previously known stars. The observations are best fitted by the presence of a compact group of O and B stars together with a few — four or five — Wolf-Rayet stars. (These objects are rare but among the hottest and most luminous known. Surrounded by expanding plasma, they are presumably evolved O stars.) Spectra showing a combination of O and Wolf-Rayet features confirm this interpretation.

The central density of stars in this compact grouping is just below the maximum found for globular clusters in our galaxy. After 10 to 100 million years, when all the massive blue-white stars have burned out, the center of the Tarantula should resemble the so-called blue globular clusters found in the Large Magellanic Cloud.

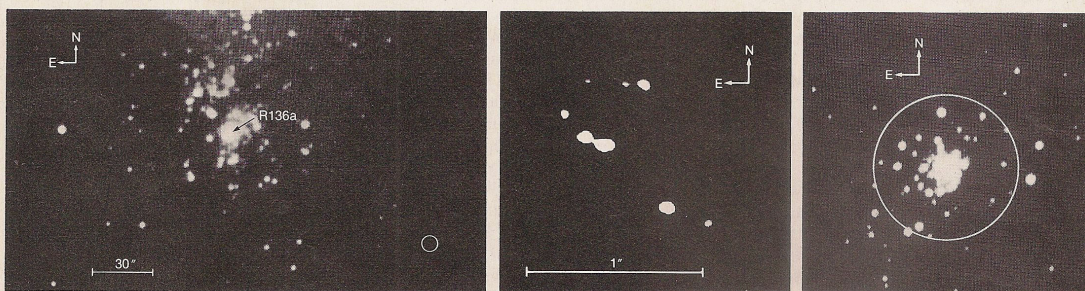
A complementary spectroscopic study carried out in Chile by Jorge Melnich reached similar conclusions. His report, to be published in *Astronomy and Astrophysics*, concludes: "There is no need for

the presence of an exotic object in the core of the cluster. . . ."

Moffat and his co-workers find similar results for NGC 3603, whose core is known as HD 97950. While this is the most massive H II region in the Milky Way that can be studied at visible wavelengths, its stellar mass is only about one third that of the 30 Doradus complex. Here there are only two or three Wolf-Rayet stars, but the activity is concentrated in a much smaller volume. As a result, the central star density in NGC 3603 may be some 300 times greater than in 30 Doradus — possibly due to the greater efficiency of star formation in our galaxy. As Moffat told *Sky & Telescope*, "If you think R136 in 30 Doradus is exotic, then NGC 3603 is beyond this." It is a rare type of object in the Milky Way and may not survive in its present form for long. What it will turn into is uncertain.

The central objects in 30 Doradus and NGC 3603 have been directly resolved by Gerd Weigelt and collaborators from the Physical Institute in Erlangen, West Germany. Their speckle interferometry confirmed that R136a is a dense cluster and showed eight stars within an apparent diameter of 1 arc second. As the illustration below, center, shows, the grouping is dominated by three objects with almost the same brightness: R136a1, a2, and a3. Similarly, the core of NGC 3603 was revealed as a cluster of four stars. Details can be found in the September (I) and October (I), 1985, issues of *Astronomy and Astrophysics*.

RONALD A. SCHORN



Left: R136a and the central area of the 30 Doradus nebula as imaged in blue light at the prime focus of the 4-meter reflector of Cerro Tololo Inter-American Observatory. The small circle shows a region 5.5 light-years across at the distance of the nebula — the same physical size as the circle on the image of NGC 3603. Unless otherwise credited, the illustrations in this article were provided by A. Moffat and first appeared in the *Astrophysical Journal*. Right: The core of NGC 3603, a giant H II region in the Milky Way, is seen here in blue light. The circle has a diameter of 59 arc seconds, corresponding to the same 5.5-light-year circle in the image of 30 Doradus. Note that the central-star density in NGC 3603 far exceeds that of 30 Doradus. Center: R136a, the mysterious object at the center of 30 Doradus, is actually a dense cluster of at least eight stars, as shown in this reconstructed speckle-interferometer image. The three bright objects are, from left to right, R136a2, a1, and a3. Some 4,000 speckle interferograms were taken with the 1.5-meter Danish telescope at the European Southern Observatory by G. Weigelt and C. Baier, and combined to form this image, which was published in *Astronomy and Astrophysics*.

Article written by Schorn, R. A. published in "Sky and Telescope, volume 71, page 13" right after the Weigeldt 1985 observation.

Chapter 6

Summary and prospects

In this chapter we are going to summarize our main results, both from the photometric analysis and Nbody simulations.

6.1 Main results

In this thesis, we carried out a comprehensive photometric study of the core of two young massive star clusters: NGC3603 and R136, located in most massive HII regions. Series of numerical Nbody6 simulations were done in order to study the effect of initial parameters on the evolution of R136-like clusters.

6.1.1 NGC3603

We analyzed the imaging data of the core of NGC3603 using HST/WFPC2 (F547M, F675W, F814W), HST/ACS/HRC (F250W, F330W, F435W, F550M, F658N, F850LP) and VLT/SPHERE/IRDIS (B-J, B-Ks). In each sets of data, we corrected the extinction for O-type stars (class V) in each field for each filter. Then we used Geneva (for HST data) and PARSEC (for SPHERE data) evolutionary

models and proper atmosphere models (TLUSTY for O and B stars and KURUCZ for others), in order to estimate the stellar masses in each image. The mass function and its slope derived for each data in different radial distances from the core of the cluster. HST analysis of the core of NGC3603, shows the effect of mass segregation as the slope in the core is much flatter than the outer regions. This flatten slope of the core is more in WFPC2 data compared to HRC. HRC data have better angular resolution and pixel sampling than WFPC2 data. So the flatten slope of the core can be a signature of the observational confusion. In the Chapter 4 we presented the results of the SPHERE data analysis of the very core of NGC36303 (F0) and the next radial bin (F1 and F2) in J and K band. SPHERE/IRDIS has better resolution and higher pixel sampling. Also the observation were done in near Infrared which the problem of extinction is much less than in the visible. In SPHERE data, we could detect more faint low-mass stars leading to have steeper MF slope for the core. The MF study of the core of NGC3603 with SPHERE/IRDIS data shows no signature of mass segregation for two main reasons: First, MF slope in the very core is not flatter than the next radial bin. Second, both slopes are similar to the MF values found in the previous works for the outer regions. Comparing results of the WFPC2, HRC and SPHERE data, we conclude that the flatten MF slope in the core of NGC3603 can be explain by the observational confusion rather than segregation, as the slope become steeper as the resolution improves.

6.1.2 R136

For R136, we analyzed the HST/WFPC2 data in visible (F555W, F814W) and VLT/SPHERE data in near infrared (B-J and B-Ks). For the HST analysis of the core of R136, we used Geneva with normal and high mass-loss rates and PARSEC evolutionary models. To correct the extinction for the O type stars (class V) we used the TLUSTY atmosphere model. The mass function derived in different color at 1, 1.5 and 2 Myr. Although MF slope in the core is flatter than the outer radii but it is difficult to suggest the mass segregation as an explanation because of the uncertainties due to

the lower resolution from the large distance and due to the extinction.

The resolution of SPHERE data is much better than the HST and we detected over thousands of sources in J and K band data. The majority (above 90%) of massive stars (brighter than 17 mag in K and 16 mag in J) have visual companions closer than 0.2". Among them, R136a1 (most massive star in the Local universe) and r136C have visual companions which are detected for the first time. R136a3 was resolved as two stars (PSF fitting). Considering the spectroscopic and photometric errors on the extinction ($A(J) = 1.3 \pm 0.5$ and $A(K) = 0.4 \pm 0.5$) and the age ($1.8^{+1.2}_{-0.8}$ Myr) of the cluster members, we estimate a mass range for each detected star. The generalized histogram of stellar masses (MF) was plotted at different ages with a given error on each stellar mass. The MF slopes (from generalized histogram of mass) at 1, 1.7 and 2 Myr is steeper than the HST/WFPC2 studies. This gives us a clue that the observed segregation in previous studies might be an observational confusion again. Future instruments with better resolution will clarify this.

In parallel to photometric analysis of R136, we made a series of Nbody6 simulations of young massive R136-like clusters. These clusters have different initial binaries and segregation degree and each cluster is simulated with and without stellar evolution of member stars. In this way we could see the effect of these parameters on the dynamical evolution of R136-like clusters at the early stages of their life (4 Myr). Segregated clusters with stellar evolution expand more. Total mass loss of the clusters with stellar evolution is much higher than the clusters which evolve purely dynamically. Low-mass binaries dissolve very fast (less than 1 Myr) and massive binary systems dissolve because of the stellar evolution. In all the simulations, binaries keep the memory of initial eccentricity distribution during the 4 Myr and only the massive binaries keep the memory of the initial period distribution. To compare the results of the Nbody6 simulations to the HST/WFPC2 images, we wrote a code (ZSCENE) in IDL which calculated the flux of the stars (mass and position is given by Nbody6) in each HST filter using TLUSTY and KURUCZ atmosphere models in combination to the Geneva evolutionary models. The resolution and pixel scale of the synthetic

images are the same as HST/WFPC2. To compare these synthetic images to HST data, we used four methods: SBP, R_{hl} , $R_{neighbor}$ and MF comparison. Using 4 criteria all together, even though they are not completely independent, we conclude that R136 is best represented by non-segregated clusters (in $r < 4\text{pc}$).

6.2 Prospects

We are going to analyze the SPHERE/ZIMPOL data on the core of both clusters which in principle have better resolution and higher pixel sampling. The ZIMPOL observations provide high-contrast polarized imaging to study the structures around these bright targets and detect the presence of dust in polarized light. The asymmetries of objects due to multiplicities and extended atmosphere and winds, can be investigated using ZIMPOL data.

We are going to compare the HST/WFC3 data with VLT/SPHERE as they are complementary in covering visible and infrared wavelengths. For R136, the proper motion of some stars can be estimated by comparing HST data in 1995 and SPHERE data in 2015. In 20 Years, stars with velocity of 200 Km/s will move about 16 mas. So it is feasible to detect the movement of some stars with velocities higher than 200 km/s by comparing HST and SPHERE data. The numerical analysis of R136 will be completed by making the synthetic images with SPHERE/IRDIS resolution to be compared with IRDIS data in J and K band.

6.3 Look into the future

Lack of high-angular-resolution brings confusion and most of the models we actually use are based on the observational data which suffer from this confusion. To overcome this problem, we can either:

- 1) increase the angular resolution of the instruments: switch to bigger telescopes with better

AO systems or use interferometry with longer base-lines.

2) decrease the output of the model's resolution to be compared with the observational data. The method we used to compare the results of the Nbody6 code with HST data, can be applied to any other instrument.

The comprehensive study of R136-like clusters can be done with the imaging and spectroscopic analysis of the future higher angular resolution instruments. Two first-light instruments of E-ELT, a diffraction-limited near-infrared imager (ELT-CAM or MICADO) and a single-field near-infrared wide-band integral field spectrograph (ELT-IFU or HARMONI), can provide a unique data to understand the kinematics and resolve the stellar members of R136-like clusters. With 3mas angular resolution, we can detect the stellar movements with 36 km/s within one month observation using MICADO (see Table 1.2). Using 8000 spectral resolution, we can detect the radial velocity of the stellar objects with 37.5 km/s using HARMONI. Putting these information together, one can find the stellar masses, positions and 3D velocities using MICADO and HARMONI within a month for 50-60 arcsec foV, which perfectly covers the core of R136 cluster. JWST (see Table 1.2) has wider FoV, 2.2-4.4 arcmin which can cover the whole 30Doradus region. But the imaging and spectroscopic data will not have the resolution of E-ELT instruments. For example, Near Infrared Camera (NIRcam) has 22 mas resolution and the Near Infrared Spectrograph (NIRSpec) has 1000 spectral resolution, in the same wavelength bands as E-ELT. So we can detect stars with high radial velocities (more than 300 km/s) using NIRSpec and unfortunately the pixel sampling of NIRcam (32mas/pix) is not as good as E-ELT (3mas/pix). So a star with 300 km/s will move one pixel in the NIRcam within almost 26 years. To sum up, It seems that using E-ELT we can find achieve to the higher angular resolution than JWST and can understand the kinematics of the R136, even the velocity dispersion of the stars within a month. This is not comparable to the all works which have been done on R136!

Appendix A

SPHERE/IRDIS catalog of NGC3603

The SPHERE/IRDIS catalog of the common sources between J and K-band data of NGC3603 in F0, F1 and F2. The IDk, Xpix and Ypix are the identification and pixel position in the IRDIS K-band image. CorrK and CorrJ are the Correlation coefficient between the input PSF and detected star.

IDk	Xpix	Ypix	Kmag	CorrK	Jmag	CorrJ	IDk	Xpix	Ypix	Kmag	CorrK	Jmag	CorrJ
F0							F0						
1	419.67	527.30	10.81	0.98	11.15	0.72	2	481.42	541.53	10.91	0.95	11.11	0.75
3	313.34	571.16	11.66	0.98	11.31	0.86	4	477.77	511.51	12.72	0.96	12.27	0.94
5	755.70	777.97	13.21	0.99	13.48	0.99	6	627.76	474.92	13.24	0.99	13.08	0.99
7	453.80	538.79	13.26	0.99	12.77	1.00	8	488.01	826.72	13.34	0.99	13.11	0.96
9	707.11	502.78	13.48	0.99	13.49	0.93	10	143.49	360.65	13.51	0.95	14.76	0.91
11	174.40	581.22	13.62	0.97	13.10	0.86	12	589.55	490.92	13.63	0.97	13.35	0.98
13	704.56	484.47	13.72	0.94	14.23	0.84	14	705.09	697.66	13.77	0.98	13.69	0.91
15	511.37	648.01	13.78	0.98	13.34	0.91	16	449.61	449.66	14.18	0.92	13.70	0.96
17	207.43	799.27	14.21	0.96	13.84	0.86	18	380.56	513.76	14.27	0.96	15.14	0.97
19	305.87	738.34	14.36	0.98	13.89	0.89	20	231.86	313.99	14.48	1.00	14.12	1.00
21	521.73	641.20	14.58	0.99	14.15	0.93	22	634.89	503.61	14.59	0.98	14.34	0.95
23	693.88	558.52	14.65	0.96	14.59	0.91	24	818.88	224.83	14.66	0.99	14.94	0.93
25	656.55	626.50	14.68	0.94	14.46	0.93	26	908.41	393.61	14.69	0.94	15.20	0.85

IDk	Xpix	Ypix	Kmag	CorrK	Jmag	CorrJ	IDk	Xpix	Ypix	Kmag	CorrK	Jmag	CorrJ
27	523.39	519.68	14.69	0.97	15.52	0.90	28	455.34	452.22	14.77	0.98	14.29	0.86
29	544.44	292.18	14.78	0.97	14.58	0.92	30	806.73	779.12	14.80	0.99	14.91	0.96
31	207.46	788.39	14.83	0.95	15.75	0.87	32	872.39	476.95	14.86	0.96	15.25	0.97
33	723.17	473.54	14.94	0.97	14.87	0.86	34	578.20	874.90	14.94	0.99	14.84	0.89
35	612.83	616.86	14.96	0.99	14.68	0.99	36	386.92	392.65	14.99	0.98	14.54	0.96
37	275.47	548.72	15.17	0.96	15.62	0.93	38	510.41	630.33	15.21	0.96	16.23	0.85
39	569.86	386.66	15.23	0.98	14.94	0.95	40	759.48	915.64	15.29	0.95	15.48	0.95
41	521.76	624.02	15.34	0.99	14.90	0.98	42	244.60	844.25	15.35	0.97	15.06	0.91
43	376.76	568.11	15.36	0.99	14.77	0.97	44	299.43	1009.87	15.37	0.97	15.33	0.96
45	847.81	518.25	15.37	0.99	15.57	0.92	46	742.72	752.43	15.40	0.96	15.55	0.81
47	587.42	863.76	15.43	0.97	15.31	0.96	48	717.72	460.41	15.49	0.97	15.44	0.88
49	226.92	297.54	15.63	0.97	15.35	0.92	50	824.54	483.86	15.66	0.97	15.72	0.95
51	272.27	100.67	15.70	0.98	15.71	0.89	52	852.41	492.93	15.76	0.98	17.16	0.95
53	731.53	511.48	15.79	0.94	16.48	0.88	54	690.67	409.06	15.81	0.99	15.71	0.98
55	568.57	365.83	15.81	0.97	15.55	0.96	56	420.94	137.43	15.98	0.97	15.97	0.92
57	443.19	264.65	16.06	0.98	17.57	0.81	58	649.64	374.53	16.16	0.95	16.22	0.87
59	684.99	746.61	16.23	0.98	17.74	0.91	60	648.02	558.71	16.25	0.99	16.01	0.95
61	262.65	982.73	16.28	0.97	16.29	0.99	62	498.36	387.30	16.28	0.97	15.91	0.90
63	371.86	480.98	16.29	1.00	16.53	0.99	64	639.72	602.94	16.36	0.99	16.22	0.99
65	469.86	388.36	16.42	0.98	16.16	0.93	66	109.47	423.11	16.50	0.97	16.10	0.91
67	761.40	627.71	16.52	0.96	16.67	0.95	68	768.33	621.12	16.53	0.98	16.89	0.93
69	729.17	1008.02	16.54	0.99	16.93	0.89	70	182.27	161.99	16.54	0.99	17.91	0.91
71	520.53	189.05	16.55	0.97	16.50	0.94	73	769.99	803.47	16.64	0.97	16.76	0.85
74	619.96	451.24	16.65	0.99	17.73	0.88	75	222.85	499.66	16.67	0.97	16.83	0.97
76	516.78	65.10	16.78	0.99	17.71	0.98	77	296.37	387.44	16.79	0.95	16.31	0.82
78	569.12	486.69	16.80	0.99	17.17	0.93	79	515.83	732.76	16.83	0.99	16.49	0.99
80	357.35	670.43	16.94	0.95	16.56	0.84	81	607.34	840.35	16.95	0.97	16.84	0.85
82	596.97	447.85	16.95	0.99	17.11	0.96	83	744.77	767.45	16.96	0.95	17.51	0.89
84	72.33	834.01	16.99	0.98	17.35	0.88	85	449.41	434.44	16.99	0.95	16.54	0.85

IDk	Xpix	Ypix	Kmag	CorrK	Jmag	CorrJ	IDk	Xpix	Ypix	Kmag	CorrK	Jmag	CorrJ
86	225.18	332.69	17.00	0.98	16.61	0.92	87	292.62	107.14	17.04	0.97	17.06	0.95
88	366.26	392.07	17.08	0.99	16.62	0.92	89	137.47	321.62	17.13	0.95	17.45	0.92
90	478.22	712.41	17.14	0.97	16.99	0.81	91	781.48	343.84	17.15	0.96	17.41	0.93
92	177.67	507.16	17.17	0.98	16.68	0.97	93	926.57	772.83	17.19	0.97	17.92	0.98
94	682.94	554.88	17.23	0.99	17.07	0.98	95	353.01	571.48	17.23	0.96	17.22	0.88
96	895.05	364.94	17.24	1.00	18.17	0.94	97	682.02	394.52	17.27	0.96	19.38	0.89
98	545.91	563.76	17.28	0.99	17.46	0.97	100	328.02	66.97	17.31	0.99	17.47	0.99
101	344.86	806.58	17.39	0.97	17.89	0.96	103	601.33	474.02	17.40	0.97	17.55	0.95
104	664.55	892.56	17.42	0.94	17.49	0.93	105	911.57	916.34	17.49	0.96	17.92	0.93
106	670.04	533.67	17.52	0.97	19.46	0.93	107	363.67	486.38	17.54	0.95	17.07	0.93
108	407.61	228.09	17.55	0.97	17.60	0.96	109	424.58	445.84	17.56	0.97	17.38	0.96
111	135.99	199.96	17.58	0.99	18.09	0.98	112	874.67	475.63	17.60	0.81	16.10	0.82
113	698.41	209.37	17.62	0.95	18.47	0.88	114	172.55	780.39	17.67	0.94	17.35	0.85
115	615.11	170.25	17.67	0.98	17.97	0.94	116	154.72	597.76	17.67	0.97	17.26	0.93
117	276.29	312.89	17.69	0.98	18.01	0.91	118	273.24	787.39	17.70	0.96	18.16	0.85
119	534.09	658.38	17.71	0.96	18.25	0.81	121	692.46	406.81	17.71	0.89	17.21	0.90
122	251.11	170.16	17.75	0.98	17.73	0.96	123	401.22	182.46	17.77	0.95	17.67	0.89
124	480.83	344.83	17.79	0.98	17.70	0.97	125	131.38	462.33	17.80	0.95	17.97	0.86
126	534.12	655.41	17.81	0.85	18.64	0.83	128	813.55	150.64	17.87	0.94	19.07	0.83
129	826.73	247.49	17.87	0.95	18.16	0.93	130	560.72	964.11	17.89	0.98	17.92	0.96
132	474.57	731.97	17.92	0.96	17.78	0.98	133	160.72	491.51	17.94	0.95	17.45	0.87
134	318.05	76.46	17.94	0.96	17.96	0.94	136	675.62	287.07	18.00	0.97	18.13	0.97
137	434.29	54.47	18.00	0.95	18.93	0.83	138	845.47	348.77	18.02	0.95	18.87	0.94
139	820.17	545.11	18.02	0.98	18.75	0.90	140	580.94	453.57	18.03	0.97	18.75	0.92
141	181.45	734.38	18.03	0.92	18.44	0.87	142	533.79	505.96	18.06	0.98	17.78	0.99
143	514.14	695.42	18.09	0.97	18.12	0.85	144	883.53	614.47	18.09	0.93	18.68	0.83
145	353.32	185.71	18.10	0.96	18.09	0.92	146	867.20	735.66	18.10	0.95	19.08	0.89
147	920.25	131.36	18.10	0.95	18.81	0.88	148	659.68	430.21	18.14	0.96	17.95	0.94
149	170.78	528.98	18.15	0.97	18.40	0.97	150	610.53	999.22	18.16	0.95	19.02	0.84

IDk	Xpix	Ypix	Kmag	CorrK	Jmag	CorrJ	IDk	Xpix	Ypix	Kmag	CorrK	Jmag	CorrJ
151	484.61	490.31	18.17	0.92	18.56	0.84	152	615.96	514.91	18.20	0.97	17.96	0.93
153	462.11	440.63	18.20	0.96	18.60	0.86	154	654.22	671.22	18.21	0.97	18.90	0.92
155	272.60	399.78	18.23	0.95	18.62	0.90	156	217.44	811.06	18.23	0.95	18.74	0.92
157	519.70	584.11	18.23	0.96	18.60	0.98	158	844.48	335.70	18.24	0.94	19.03	0.91
159	858.51	419.58	18.27	0.93	18.96	0.87	160	557.52	708.42	18.27	0.93	18.09	0.91
161	287.39	447.81	18.29	0.95	18.61	0.88	162	616.61	148.20	18.32	0.94	18.60	0.95
163	451.24	748.19	18.33	0.95	18.00	0.93	164	338.40	522.89	18.34	0.95	18.65	0.89
165	838.44	780.12	18.36	0.95	19.14	0.91	166	295.91	600.77	18.38	0.96	18.70	0.83
167	145.74	915.00	18.39	0.96	18.42	0.97	168	218.94	985.75	18.39	0.94	19.88	0.88
169	899.32	677.87	18.39	0.95	19.42	0.92	170	325.49	657.27	18.39	0.93	17.91	0.85
171	280.24	386.12	18.41	0.97	18.77	0.89	172	78.24	371.64	18.42	0.96	18.98	0.85
173	853.15	400.85	18.43	0.98	19.45	0.87	174	121.97	971.66	18.46	0.91	19.37	0.93
175	597.74	565.09	18.46	0.96	19.15	0.88	176	260.78	602.32	18.47	0.95	18.91	0.98
177	458.19	491.59	18.49	0.94	18.04	0.88	178	73.48	656.23	18.49	0.94	21.02	0.82
179	272.39	451.83	18.50	0.93	18.84	0.90	180	368.08	637.73	18.55	0.94	18.81	0.91
181	202.45	234.54	18.57	0.90	19.09	0.90	182	104.33	899.43	18.59	0.90	19.35	0.85
183	744.47	497.84	18.62	0.95	19.24	0.88	185	630.74	564.32	18.63	0.92	19.29	0.97
186	249.63	177.06	18.65	0.92	19.49	0.94	187	430.63	752.95	18.68	0.93	19.11	0.91
189	319.28	42.00	18.69	0.88	19.66	0.85	190	107.84	932.93	18.71	0.94	19.54	0.98
191	203.65	763.82	18.73	0.93	19.34	0.90	192	373.07	470.28	18.76	0.93	19.27	0.86
193	529.28	335.34	18.79	0.88	19.52	0.85	194	209.25	467.34	18.81	0.93	19.24	0.83
196	593.98	206.86	18.82	0.96	18.70	0.96	197	665.35	547.00	18.83	0.92	19.63	0.92
198	85.75	620.67	18.88	0.91	19.27	0.91	199	369.73	776.37	18.88	0.91	19.20	0.85
200	215.05	197.78	18.91	0.91	19.31	0.88	201	246.70	403.63	18.92	0.91	19.48	0.87
202	678.71	795.58	18.92	0.91	19.69	0.93	203	359.98	146.18	18.93	0.93	19.76	0.83
204	746.24	650.66	18.94	0.90	19.53	0.89	205	529.14	561.94	18.94	0.93	19.46	0.90
206	76.78	582.14	18.95	0.93	19.44	0.91	207	358.98	369.49	18.96	0.89	19.41	0.93
209	359.55	570.56	19.04	0.87	19.04	0.95	210	902.06	536.83	19.04	0.94	19.57	0.88
212	232.08	404.60	19.09	0.92	19.77	0.86	213	344.80	610.90	19.11	0.93	19.36	0.91

IDk	Xpix	Ypix	Kmag	CorrK	Jmag	CorrJ	IDk	Xpix	Ypix	Kmag	CorrK	Jmag	CorrJ
215	87.27	703.54	19.12	0.90	19.83	0.90	216	580.59	944.23	19.13	0.88	20.12	0.86
217	146.40	823.34	19.15	0.84	19.94	0.84	218	231.25	699.80	19.16	0.89	19.71	0.96
219	590.18	975.77	19.16	0.90	19.87	0.87	220	518.09	473.83	19.19	0.94	19.64	0.94
221	279.36	643.81	19.20	0.87	19.65	0.92	222	217.07	497.57	19.22	0.86	19.32	0.91
223	729.81	599.43	19.22	0.86	20.67	0.85	224	564.60	465.58	19.22	0.90	19.71	0.88
227	803.10	645.33	19.26	0.91	20.50	0.87	228	595.32	628.04	19.28	0.87	19.86	0.84
229	625.04	771.09	19.28	0.94	20.17	0.88	231	341.03	598.19	19.30	0.93	20.26	0.88
232	250.06	755.61	19.31	0.85	20.04	0.90	234	460.07	688.21	19.31	0.91	19.84	0.84
235	530.94	127.66	19.32	0.86	20.19	0.93	236	876.18	173.81	19.34	0.92	20.29	0.84
237	262.29	671.08	19.35	0.83	20.27	0.82	240	558.39	601.96	19.36	0.89	20.22	0.81
243	601.00	739.18	19.43	0.85	20.15	0.87	247	524.35	466.89	19.43	0.81	19.95	0.83
248	141.08	607.42	19.44	0.83	19.46	0.89	249	655.00	685.66	19.44	0.83	20.24	0.83
251	486.96	763.56	19.47	0.90	19.80	0.93	252	67.12	430.56	19.49	0.83	20.16	0.81
253	693.63	276.02	19.49	0.84	20.29	0.90	254	110.26	963.02	19.49	0.85	20.13	0.85
255	64.27	801.09	19.50	0.82	20.66	0.83	256	419.32	564.51	19.51	0.82	20.12	0.85
260	434.75	741.08	19.57	0.84	19.66	0.90	262	206.62	571.89	19.57	0.83	19.71	0.88
263	421.26	66.49	19.59	0.87	19.60	0.83	267	675.53	469.16	19.66	0.83	20.24	0.82
284	606.74	754.32	20.04	0.82	19.66	0.91							
F1							F1						
1	127.09	581.55	10.77	0.97	12.42	0.95	2	78.50	306.48	11.21	0.94	12.82	0.87
3	477.34	514.44	11.31	0.96	12.96	0.88	4	75.96	288.15	11.44	1.00	13.12	0.95
5	76.41	501.33	11.44	0.96	12.99	0.83	6	178.19	582.66	12.04	0.98	13.62	0.96
7	280.28	197.16	12.09	0.99	13.75	0.88	8	244.21	280.51	12.31	0.96	13.92	0.85
9	367.80	524.52	12.32	0.96	14.22	0.92	10	65.28	362.21	12.38	0.98	14.08	0.91
11	190.52	846.46	12.39	0.94	14.07	0.90	12	551.82	559.18	12.61	0.99	15.46	0.91
13	94.60	277.19	12.62	0.97	14.24	0.97	14	130.78	719.18	12.74	0.99	14.35	0.90
15	219.45	321.87	12.90	0.97	14.52	0.93	16	114.11	556.03	12.97	1.00	14.53	0.97
17	89.16	264.08	13.18	1.00	14.82	0.91	18	196.16	287.50	13.21	0.96	14.81	0.85
19	224.05	296.55	13.27	0.97	16.17	0.87	20	90.42	862.66	13.43	0.96	15.44	0.95

IDk	Xpix	Ypix	Kmag	CorrK	Jmag	CorrJ	IDk	Xpix	Ypix	Kmag	CorrK	Jmag	CorrJ
21	102.98	315.17	13.46	1.00	15.88	0.96	22	62.21	212.65	13.48	0.95	15.13	0.84
23	503.50	614.70	13.56	0.95	15.26	0.94	24	344.60	582.63	13.77	0.96	15.35	0.89
25	532.93	261.70	13.83	0.94	16.80	0.87	26	56.31	550.25	13.85	0.98	17.15	0.84
27	100.41	811.59	13.93	0.95	15.71	0.95	28	132.87	431.37	14.13	0.98	15.73	0.91
29	141.43	607.00	14.14	0.97	15.77	0.87	30	139.83	424.70	14.15	0.98	16.10	0.98
31	440.52	957.54	14.23	0.94	16.08	0.98	32	574.65	728.64	14.23	0.96	16.06	0.93
33	116.15	570.94	14.42	0.99	16.56	0.94	34	533.51	257.59	14.57	0.90	16.75	0.82
35	298.20	576.30	14.58	0.98	16.52	0.90	36	266.75	168.58	14.64	0.97	16.98	0.91
37	153.04	147.44	14.69	0.97	16.48	0.87	38	283.02	719.72	14.75	0.99	16.39	1.00
39	706.85	453.53	14.77	0.97	17.45	0.85	40	511.72	110.98	14.78	0.99	17.14	0.97
41	205.38	867.68	14.79	0.97	16.86	1.00	42	316.67	836.62	14.82	0.96	16.70	0.92
43	54.28	358.50	14.96	0.96	16.59	0.84	44	53.47	198.19	14.96	0.96	16.74	0.96
46	911.26	311.24	15.05	0.98	17.24	0.95	47	587.99	94.84	15.08	1.00	17.25	0.96
48	144.06	848.92	15.11	1.00	17.52	0.96	49	435.18	413.69	15.15	0.98	17.58	0.96
50	615.48	679.18	15.17	0.96	17.26	0.94	51	295.14	885.86	15.19	0.99	17.35	0.97
52	198.34	51.07	15.32	0.99	17.10	0.93	53	102.59	869.49	15.34	0.95	17.16	0.88
54	798.78	314.84	15.43	0.99	17.69	0.89	55	273.76	827.97	15.44	0.99	17.94	0.86
56	238.83	539.09	15.46	1.00	17.91	0.97	57	709.31	869.47	15.46	0.95	17.46	0.92
58	217.17	152.51	15.48	0.96	17.94	0.82	59	501.08	179.08	15.52	1.00	17.88	0.96
60	610.05	922.00	15.55	1.00	17.54	0.90	61	127.67	973.83	15.57	0.98	18.16	0.83
62	191.69	348.60	15.60	0.96	17.66	0.95	63	47.32	90.75	15.60	0.95	17.35	0.89
64	630.56	644.62	15.63	0.94	18.21	0.91	65	230.19	223.15	15.63	0.99	18.09	0.89
66	444.19	837.70	15.67	0.98	17.72	0.97	67	255.17	418.13	15.68	0.99	17.29	0.94
68	216.07	139.54	15.70	0.97	18.09	0.83	69	310.35	115.35	15.74	0.97	18.38	0.88
70	630.11	610.31	15.75	0.98	17.64	0.89	71	914.40	909.04	15.75	0.98	18.62	0.95
72	209.85	583.68	15.77	0.98	18.06	0.97	73	334.90	407.66	15.78	0.98	18.35	0.96
74	271.04	481.26	15.80	0.99	18.16	0.90	75	311.56	901.56	15.81	0.94	18.51	0.95
76	577.57	355.12	15.85	0.97	17.75	0.89	77	460.44	762.38	15.88	0.95	17.71	0.89
78	63.59	210.11	15.92	0.86	17.49	0.90	79	224.87	204.38	15.93	0.98	18.54	0.93

IDk	Xpix	Ypix	Kmag	CorrK	Jmag	CorrJ	IDk	Xpix	Ypix	Kmag	CorrK	Jmag	CorrJ
80	534.01	453.02	16.00	1.00	18.34	0.98	82	385.59	803.59	16.05	0.95	18.61	0.86
83	306.10	99.96	16.10	1.00	18.47	0.93	84	139.21	985.66	16.23	0.98	18.94	0.91
85	359.55	391.04	16.24	0.97	18.83	0.92	86	115.80	301.47	16.28	0.95	18.63	0.92
87	588.17	565.91	16.31	0.99	18.17	0.99	88	475.65	743.28	16.35	0.97	18.92	0.83
90	803.18	102.02	16.42	0.99	18.79	0.92	91	505.44	166.41	16.45	0.95	19.13	0.84
92	117.50	454.55	16.52	0.94	19.06	0.87	93	49.84	599.21	16.52	0.99	19.18	0.91
94	274.14	340.52	16.59	0.97	18.47	0.87	95	436.75	238.77	16.59	0.98	19.15	0.90
98	360.53	338.77	16.65	0.96	19.15	0.84	99	365.26	378.99	16.66	0.99	19.07	0.81
100	286.79	87.99	16.67	0.94	19.40	0.94	101	515.26	593.14	16.74	0.98	18.74	0.92
102	561.44	633.12	16.75	0.97	19.68	0.82	105	101.35	403.44	16.88	0.96	20.23	0.83
106	129.88	139.57	16.90	0.97	19.63	0.86	108	206.99	293.07	16.93	0.97	19.64	0.87
109	684.62	103.44	16.93	0.95	19.79	0.86	110	243.93	724.05	16.96	1.00	19.60	0.83
116	65.33	79.52	17.05	0.95	19.76	0.86	119	175.11	448.60	17.08	0.97	19.64	0.84
120	520.60	741.91	17.08	0.97	19.67	0.85	121	744.22	692.79	17.08	0.98	19.89	0.85
123	452.41	120.97	17.12	0.97	19.95	0.82	125	151.09	485.12	17.16	0.99	19.60	0.86
129	180.40	755.53	17.23	0.92	19.81	0.86	145	643.81	242.88	17.39	0.98	20.05	0.86
150	144.82	87.71	17.46	0.98	20.34	0.87	156	435.25	310.82	17.54	0.98	20.18	0.82
162	113.57	444.49	17.63	0.93	20.16	0.81	173	145.82	934.98	17.74	0.99	19.95	0.82
182	498.24	132.31	17.86	0.96	20.02	0.82	195	200.26	455.06	17.96	0.97	20.26	0.88
F2							F2						
1	67.68	422.60	11.21	0.94	12.89	0.99	2	233.40	983.67	11.48	0.94	14.93	0.92
3	477.27	514.61	11.52	0.95	13.29	0.93	4	859.03	662.54	11.66	0.94	13.79	0.95
5	728.12	606.59	12.23	0.95	14.26	0.97	6	909.23	848.57	12.33	0.94	14.54	0.96
7	321.76	937.08	12.42	0.99	14.22	0.86	8	634.57	915.64	12.68	0.93	14.67	0.95
9	104.49	998.74	13.03	0.93	14.79	0.82	10	248.14	149.36	13.13	0.96	14.83	0.83
11	362.24	723.45	13.34	0.94	15.07	0.93	12	316.36	496.84	13.48	0.97	15.15	0.92
13	601.75	518.38	13.51	0.95	16.87	0.88	14	316.79	920.57	13.54	0.94	15.41	0.97
15	83.83	929.79	13.55	0.98	15.34	0.90	16	510.94	760.43	13.68	0.95	15.50	0.95
17	405.02	371.11	13.75	1.00	15.44	0.92	18	658.75	989.50	13.79	0.93	15.82	0.90

IDk	Xpix	Ypix	Kmag	CorrK	Jmag	CorrJ	IDk	Xpix	Ypix	Kmag	CorrK	Jmag	CorrJ
19	533.24	887.93	13.93	0.99	17.57	0.96	20	660.02	1010.49	14.03	0.95	15.25	0.91
21	476.88	1015.22	14.11	0.93	15.53	0.86	22	779.87	648.23	14.16	0.99	16.32	0.88
23	272.29	784.75	14.20	0.97	17.35	0.92	24	610.62	812.33	14.31	0.95	16.24	0.85
25	606.91	688.19	14.34	0.99	17.01	0.90	26	739.89	998.28	14.48	0.98	16.64	0.83
27	382.60	729.89	14.65	0.96	16.44	0.93	28	372.68	418.71	14.68	0.92	16.39	0.96
29	747.10	444.08	14.70	1.00	16.83	0.96	30	685.11	298.79	14.77	0.99	17.54	0.98
31	315.03	955.72	14.84	0.98	16.73	0.96	32	418.06	689.77	14.91	0.99	16.75	0.99
33	871.68	967.66	14.93	0.95	17.23	0.92	34	227.46	944.58	15.04	0.91	17.55	0.91
35	588.43	1010.99	15.08	0.96	16.28	0.95	36	263.51	578.76	15.11	0.93	16.81	0.97
37	559.89	1012.04	15.23	1.00	16.38	0.92	38	373.75	414.83	15.27	0.90	17.04	1.00
39	225.92	822.67	15.30	0.97	17.76	0.99	40	788.62	832.94	15.37	0.97	17.65	0.91
41	705.30	793.58	15.38	0.94	17.67	0.97	42	497.58	851.21	15.39	0.95	17.52	0.83
43	903.81	774.30	15.44	0.97	18.47	0.84	44	341.11	793.00	15.47	1.00	17.37	0.92
45	408.04	699.18	15.47	0.99	17.33	0.89	46	402.73	183.44	15.48	0.94	18.05	0.90
47	491.23	805.42	15.51	0.95	17.41	0.96	48	696.59	981.96	15.51	0.96	18.58	0.93
49	917.01	871.20	15.52	0.99	17.83	0.88	50	524.41	677.33	15.58	0.94	18.26	0.86
52	386.23	1010.80	15.61	0.97	16.67	0.98	53	885.64	403.62	15.61	0.94	18.51	0.88
54	366.16	936.02	15.64	0.99	18.19	0.89	55	530.18	139.37	15.66	0.96	18.12	0.81
56	645.33	109.90	15.66	0.97	17.80	0.90	57	825.49	55.52	15.73	0.89	17.98	0.86
58	570.85	968.25	15.74	0.98	17.98	0.84	59	765.88	910.76	15.81	0.98	18.00	0.94
60	443.14	808.63	15.85	0.96	17.86	0.99	61	359.32	224.76	15.90	0.96	18.43	0.94
62	579.92	348.05	15.90	1.00	17.86	0.97	64	456.21	1014.79	16.03	0.94	17.47	0.94
65	706.83	771.58	16.07	0.95	18.25	0.93	66	598.18	537.39	16.17	0.95	19.48	0.88
67	604.28	442.87	16.19	0.98	19.02	0.94	68	409.21	664.19	16.26	0.98	19.03	0.87
69	68.76	234.57	16.34	0.94	18.09	0.96	72	123.33	49.70	16.44	0.95	19.80	0.98
73	168.12	994.33	16.44	0.97	19.24	0.98	74	292.47	857.26	16.44	0.94	19.06	0.87
75	684.13	830.25	16.46	0.98	18.53	0.88	76	247.00	169.57	16.51	0.95	19.24	0.88
77	602.80	586.68	16.51	0.97	19.28	0.95	78	335.56	566.45	16.51	0.91	19.17	0.93
79	339.62	799.92	16.54	0.96	19.34	0.85	80	304.96	820.40	16.54	0.96	19.13	0.98

IDk	Xpix	Ypix	Kmag	CorrK	Jmag	CorrJ	IDk	Xpix	Ypix	Kmag	CorrK	Jmag	CorrJ
81	88.67	923.15	16.55	0.96	19.13	0.92	82	146.96	555.34	16.55	0.97	19.09	0.91
83	142.31	728.85	16.56	0.97	19.15	0.90	84	233.97	261.29	16.57	0.97	19.35	0.84
85	70.68	908.75	16.58	0.96	18.48	0.94	86	302.77	191.61	16.58	0.95	19.38	0.95
87	492.45	960.57	16.58	0.91	19.45	0.96	88	807.15	413.36	16.61	0.96	19.70	0.85
89	808.61	49.02	16.65	0.97	19.82	0.95	90	605.15	650.46	16.72	0.94	19.73	0.97
91	119.22	166.49	16.75	0.95	19.43	0.85	92	450.34	768.73	16.75	0.96	19.42	0.95
93	517.40	338.61	16.77	0.93	19.63	0.88	94	321.58	390.69	16.77	0.94	19.41	0.97
96	252.71	752.52	16.80	0.92	19.48	0.95	98	619.30	958.73	16.85	0.96	19.98	0.96
99	59.44	811.19	16.87	0.95	19.40	0.87	101	511.41	689.38	16.96	0.93	18.98	0.83
102	449.13	992.46	16.97	0.94	19.70	0.98	103	530.36	855.89	16.98	0.97	19.91	0.93
104	137.35	775.16	16.98	0.97	20.44	0.82	105	637.61	816.14	17.05	0.96	19.85	0.80
106	820.01	807.17	17.05	0.99	20.28	0.82	107	620.97	750.50	17.06	0.94	19.94	0.97
108	761.25	500.51	17.08	0.93	19.87	0.89	110	619.45	310.46	17.10	0.90	20.89	0.85
111	509.32	111.15	17.11	0.97	20.14	0.85	112	848.65	959.72	17.12	0.95	20.39	0.87
114	552.87	311.04	17.18	0.99	19.45	0.96	115	784.17	899.50	17.22	0.93	20.47	0.90
116	665.57	850.91	17.23	0.96	20.11	0.87	117	786.64	515.85	17.24	0.95	20.38	0.87
118	125.09	791.50	17.25	0.94	19.84	0.96	119	371.62	849.97	17.28	0.97	20.12	0.87
120	762.89	838.09	17.32	0.99	20.26	0.87	121	208.65	747.58	17.34	0.93	20.06	0.96
122	370.13	1009.19	17.35	0.86	19.24	0.88	123	510.75	833.82	17.35	0.98	19.58	0.92
125	756.54	776.37	17.42	0.92	20.35	0.82	127	199.05	906.32	17.42	0.97	20.21	0.97
128	98.32	564.55	17.44	0.93	19.97	0.90	129	609.22	166.71	17.45	0.97	20.42	0.89
130	625.61	929.95	17.45	0.96	20.38	0.84	131	466.08	746.24	17.50	0.98	20.28	0.90
132	590.65	817.64	17.52	0.94	20.37	0.96	133	795.77	797.56	17.52	0.95	20.67	0.89
134	281.38	635.46	17.53	0.92	20.23	0.83	135	715.78	370.80	17.55	0.98	20.79	0.87
136	599.28	748.27	17.55	0.96	20.58	0.85	137	375.91	911.72	17.55	0.98	20.44	0.93
139	909.84	946.90	17.58	0.99	21.07	0.81	140	192.44	463.59	17.59	0.92	20.22	0.88
141	449.92	802.58	17.60	0.96	20.34	0.94	142	167.88	283.72	17.61	0.97	20.13	0.92
143	177.47	128.77	17.62	0.93	20.30	0.94	144	423.64	801.50	17.66	0.91	20.20	0.88
145	496.97	315.56	17.67	0.95	20.17	0.92	147	55.95	985.40	17.67	0.96	20.20	0.95

IDk	Xpix	Ypix	Kmag	CorrK	Jmag	CorrJ	IDk	Xpix	Ypix	Kmag	CorrK	Jmag	CorrJ
148	863.42	907.83	17.69	0.96	20.79	0.89	149	290.17	655.49	17.69	0.94	20.22	0.87
150	932.69	323.67	17.70	0.89	20.78	0.88	151	888.26	510.22	17.71	0.97	20.14	0.89
152	411.77	534.08	17.72	0.99	20.48	0.81	153	289.30	925.80	17.73	0.96	20.35	0.83
156	905.46	803.83	17.75	0.95	20.59	0.87	157	298.23	629.53	17.76	0.94	20.52	0.83
160	440.11	825.69	17.79	0.97	20.81	0.83	162	452.03	434.11	17.81	1.00	20.29	0.87
163	507.49	584.06	17.81	0.95	20.40	0.89	164	136.40	359.14	17.82	0.96	20.13	0.84
165	880.81	588.62	17.82	0.95	20.87	0.83	166	136.18	596.04	17.82	0.99	20.18	0.83
169	726.59	254.13	17.91	0.96	21.07	0.82	170	99.40	974.80	17.93	0.95	20.89	0.81
171	615.69	656.86	17.93	0.97	20.75	0.82	172	914.10	358.89	17.93	0.99	21.12	0.89
175	172.16	726.38	17.94	0.96	20.86	0.86	176	426.54	625.12	17.96	0.95	21.04	0.88
177	97.95	611.69	17.97	0.97	20.75	0.97	180	371.13	609.29	17.98	0.98	20.81	0.86
181	225.50	486.86	17.99	0.94	20.73	0.87	182	237.65	624.58	18.00	0.93	20.74	0.92
184	226.43	841.45	18.00	0.90	20.78	0.82	185	316.21	709.87	18.01	0.98	20.68	0.82
188	834.77	510.20	18.04	0.98	21.08	0.83	189	864.44	477.88	18.04	0.95	20.98	0.84
194	341.96	895.09	18.08	0.99	20.78	0.85	198	625.95	771.25	18.11	0.98	20.86	0.86
199	555.10	478.89	18.13	0.99	21.07	0.95	203	773.49	980.88	18.16	0.95	20.62	0.88
204	783.22	647.38	18.16	0.87	18.50	0.88	205	460.20	298.69	18.17	0.97	20.79	0.83
209	275.55	491.39	18.21	0.93	20.88	0.85	210	110.45	773.76	18.21	0.94	20.61	0.91
217	204.03	880.35	18.30	0.97	20.97	0.88	221	324.41	868.35	18.32	0.93	20.84	0.91
223	568.09	882.03	18.33	0.99	21.30	0.85	225	534.15	58.21	18.35	0.98	21.17	0.81
228	895.01	768.80	18.45	0.98	21.33	0.81	246	74.56	877.57	18.59	0.91	21.02	0.85
252	295.26	1007.87	18.64	0.86	20.63	0.91	255	814.44	612.61	18.67	0.91	21.15	0.87
258	480.31	467.28	18.69	0.94	21.76	0.80	260	286.13	1008.73	18.69	0.87	20.36	0.81
261	177.84	657.19	18.69	0.97	21.04	0.82	263	535.22	400.48	18.70	0.93	21.77	0.85
275	495.42	842.39	18.76	0.93	21.20	0.83	278	188.87	414.46	18.80	0.93	21.14	0.83
281	289.96	594.45	18.82	0.94	21.46	0.91	311	922.25	592.01	19.05	0.98	21.77	0.86
314	382.80	232.04	19.07	0.97	21.27	0.82	367	771.28	430.94	19.33	0.97	21.33	0.82
464	708.48	793.77	19.86	0.81	20.29	0.81							

Appendix B

SPHERE/IRDIS catalog of R136

The SPHERE/IRDIS catalog of the common sources between J and K-band data of R136. The IDk, Xpix and Ypix are the identification and pixel position in the IRDIS K-band image. ΔK_{mag} and ΔJ_{mag} are the total error (combination of PSF-fitting error and Residual errors) in K and J images. CorreK and CorreJ are the Correlation coefficient between the input PSF and detected star.

IDk	Xpix	Ypix	Kmag	ΔK_{mag}	CorreK	Jmag	ΔJ_{mag}	CorreJ
1	478.266	522.470	11.38	0.001	0.96	12.32	0.000	0.96
2	470.107	526.343	11.63	0.001	0.98	12.54	0.000	0.97
3	504.482	494.600	11.75	0.001	0.95	12.76	0.000	0.92
4	257.553	359.908	11.79	0.001	0.97	12.77	0.000	0.95
5	327.123	448.150	11.97	0.001	0.99	12.66	0.000	0.99
6	460.611	538.220	13.04	0.004	0.97	13.74	0.001	0.93
7	357.086	526.528	13.27	0.001	0.97	13.85	0.000	0.98
8	522.197	484.147	13.36	0.004	0.80	14.23	0.000	0.89
9	469.639	550.932	13.36	0.005	0.98	13.94	0.001	0.92
10	499.285	548.864	13.40	0.005	0.96	13.99	0.001	0.97
11	524.383	489.511	13.50	0.005	0.96	14.27	0.001	0.94
12	492.103	549.675	13.58	0.007	0.98	14.17	0.001	0.94
13	344.141	553.064	13.60	0.001	1.00	14.10	0.000	0.99

IDk	Xpix	Ypix	Kmag	Δ Kmag	CorreK	Jmag	Δ Jmag	CorreJ
14	365.280	605.847	13.63	0.001	0.99	14.16	0.000	0.97
15	232.160	337.616	13.67	0.002	0.98	14.51	0.001	0.96
16	481.845	527.701	13.76	0.010	0.95	14.36	0.000	0.96
17	136.616	457.448	13.89	0.001	0.96	14.36	0.000	0.93
18	381.012	526.742	13.89	0.002	0.99	14.40	0.000	0.95
19	443.589	397.910	13.93	0.002	0.95	14.68	0.000	0.91
20	285.956	487.961	13.94	0.001	1.00	14.36	0.000	0.96
21	501.747	566.902	13.96	0.007	0.98	14.61	0.002	0.90
22	441.452	662.068	14.03	0.001	0.97	14.60	0.000	0.97
23	467.622	678.184	14.09	0.001	0.98	14.69	0.000	0.93
24	128.735	685.507	14.15	0.001	0.96	14.72	0.000	0.93
25	260.288	364.945	14.15	0.007	0.93	15.32	0.001	0.89
26	362.330	680.188	14.15	0.001	0.98	14.68	0.000	0.98
27	301.541	485.359	14.16	0.002	0.95	14.66	0.000	0.94
28	437.161	546.192	14.22	0.006	0.99	14.77	0.001	0.99
29	305.721	822.525	14.24	0.000	0.96	15.06	0.000	0.94
30	427.486	492.318	14.27	0.005	0.94	14.81	0.001	0.97
31	121.779	613.061	14.27	0.001	0.99	14.62	0.000	0.92
32	485.088	656.736	14.29	0.002	0.99	14.93	0.000	0.96
33	590.992	715.909	14.30	0.001	1.00	15.22	0.000	0.99
34	527.541	573.652	14.31	0.006	0.94	15.03	0.002	0.91
35	607.919	590.156	14.42	0.003	1.00	15.29	0.001	0.98
36	431.568	384.703	14.46	0.003	0.96	15.14	0.001	0.92
37	446.685	562.359	14.51	0.008	0.98	15.05	0.000	0.96
38	465.289	434.096	14.51	0.005	0.99	15.09	0.000	0.99
39	486.825	471.576	14.66	0.011	0.97	15.27	0.003	0.94
40	410.561	479.515	14.69	0.005	0.95	15.23	0.001	0.92
41	413.377	465.485	14.70	0.005	0.92	15.28	0.001	0.93
42	464.206	487.264	14.73	0.012	0.98	15.30	0.004	0.99

IDk	Xpix	Ypix	Kmag	Δ Kmag	CorreK	Jmag	Δ Jmag	CorreJ
43	490.096	518.608	14.80	0.028	0.93	15.76	0.002	0.84
44	306.510	666.040	14.92	0.001	0.96	15.48	0.000	0.96
45	856.866	706.746	14.95	0.004	0.97	16.29	0.001	0.92
46	337.299	547.951	14.95	0.003	0.97	15.41	0.000	0.97
47	655.594	154.739	14.99	0.002	0.95	15.93	0.000	0.90
48	554.945	515.720	14.99	0.011	0.98	15.75	0.004	0.96
49	432.796	500.489	15.00	0.010	0.96	15.61	0.003	0.94
50	486.374	361.883	15.01	0.004	0.98	15.79	0.001	0.82
51	197.075	669.137	15.01	0.001	0.99	15.42	0.000	0.98
52	445.297	425.774	15.03	0.008	0.98	15.55	0.001	0.97
53	503.642	458.195	15.08	0.013	0.97	15.70	0.003	0.93
54	471.547	560.360	15.09	0.022	0.89	15.80	0.004	0.91
55	560.248	617.461	15.09	0.006	0.96	15.83	0.001	0.95
56	415.109	579.558	15.09	0.006	0.97	15.60	0.000	0.97
57	235.422	365.404	15.10	0.011	0.93	15.79	0.001	0.96
58	509.976	507.096	15.11	0.031	0.98	15.79	0.006	0.98
59	508.723	492.738	15.14	0.027	0.74	15.02	0.001	0.86
60	538.375	534.337	15.14	0.016	0.96	15.87	0.005	0.96
61	179.286	311.062	15.15	0.002	0.99	16.28	0.001	1.00
62	417.736	438.744	15.16	0.007	0.98	15.68	0.001	0.92
63	528.102	590.142	15.18	0.010	1.00	15.95	0.003	0.99
64	433.977	332.108	15.28	0.003	0.99	15.91	0.001	0.81
65	258.358	784.500	15.29	0.001	0.95	15.92	0.000	0.97
66	423.695	338.897	15.33	0.003	0.98	15.95	0.001	0.92
67	606.066	765.381	15.34	0.002	0.98	16.33	0.001	0.96
68	172.064	992.013	15.41	0.002	1.00	16.38	0.001	0.98
69	394.440	520.540	15.42	0.009	0.94	15.92	0.001	0.94
70	235.429	501.651	15.47	0.004	0.96	15.92	0.001	0.95
72	471.355	566.473	15.49	0.027	0.96	16.16	0.006	0.95

IDk	Xpix	Ypix	Kmag	Δ Kmag	CorreK	Jmag	Δ Jmag	CorreJ
73	221.485	529.480	15.53	0.003	0.94	16.02	0.001	0.96
74	500.502	467.417	15.53	0.023	0.94	16.32	0.007	0.92
75	474.062	701.195	15.54	0.004	0.99	16.69	0.002	0.91
76	389.769	808.552	15.56	0.001	0.97	16.23	0.001	0.94
77	469.858	398.369	15.57	0.011	0.98	16.32	0.001	0.82
78	524.573	731.125	15.58	0.003	0.97	16.41	0.001	0.93
79	456.589	606.742	15.63	0.010	0.96	16.16	0.001	0.91
80	201.837	353.801	15.63	0.007	0.99	16.21	0.001	0.93
81	401.430	817.454	15.64	0.001	0.94	16.34	0.001	0.96
82	343.513	540.687	15.64	0.005	0.94	16.07	0.001	0.92
83	516.755	634.793	15.67	0.008	0.98	16.37	0.001	0.93
84	479.181	461.082	15.71	0.022	0.99	16.32	0.006	0.99
85	295.642	459.762	15.73	0.010	0.97	16.20	0.001	0.92
86	360.450	714.888	15.74	0.002	0.97	16.23	0.001	0.97
87	538.043	392.066	15.76	0.007	0.99	16.85	0.002	0.99
88	254.089	625.095	15.76	0.001	0.99	16.22	0.001	0.98
89	536.527	619.321	15.77	0.011	0.90	16.52	0.002	0.93
90	363.693	476.668	15.77	0.012	0.96	16.76	0.001	0.90
91	512.573	363.641	15.78	0.006	0.95	16.49	0.001	0.91
92	314.468	428.664	15.78	0.013	0.94	16.30	0.001	0.93
93	781.661	723.792	15.81	0.006	0.97	17.07	0.002	0.92
94	332.521	436.170	15.82	0.016	0.86	16.25	0.001	0.86
95	466.798	759.774	15.82	0.003	0.99	16.55	0.001	0.94
96	492.566	417.612	15.82	0.014	0.95	16.50	0.001	0.92
97	447.997	630.637	15.83	0.008	0.98	16.37	0.001	0.96
98	72.077	654.013	15.84	0.004	1.00	16.22	0.001	0.98
99	357.025	590.610	15.85	0.005	0.98	16.94	0.001	0.96
100	146.709	665.663	15.87	0.004	0.97	16.51	0.001	0.91
101	589.047	634.821	15.89	0.008	0.99	16.75	0.003	0.98

IDk	Xpix	Ypix	Kmag	Δ Kmag	CorreK	Jmag	Δ Jmag	CorreJ
102	568.781	611.113	15.90	0.012	0.96	16.70	0.003	0.96
103	627.864	396.283	15.92	0.004	0.98	16.87	0.001	0.97
104	267.814	283.913	15.94	0.004	0.99	16.59	0.001	0.94
105	509.236	642.484	15.94	0.009	0.96	16.69	0.001	0.96
106	278.497	593.642	15.95	0.003	0.94	16.34	0.001	0.93
107	568.213	427.938	15.95	0.010	0.99	16.71	0.001	0.98
108	592.002	444.194	15.97	0.011	0.99	16.97	0.003	0.84
109	261.266	437.068	15.98	0.010	0.97	16.60	0.001	0.96
110	305.461	416.608	15.98	0.014	0.95	16.54	0.001	0.95
111	398.500	717.743	15.99	0.003	0.96	16.54	0.001	0.94
113	419.366	562.357	16.00	0.018	0.96	16.57	0.001	0.97
114	573.634	368.732	16.02	0.005	0.96	16.89	0.001	0.91
115	466.425	734.446	16.05	0.004	0.94	17.43	0.002	0.92
116	615.984	485.248	16.06	0.012	0.99	18.20	0.007	0.98
117	681.889	358.620	16.06	0.003	0.97	17.10	0.001	0.94
118	391.044	615.273	16.07	0.006	0.99	17.51	0.002	0.99
119	478.761	243.710	16.09	0.001	0.98	16.84	0.001	0.93
120	205.418	322.312	16.10	0.009	0.95	16.74	0.004	0.98
121	546.544	605.556	16.11	0.018	0.96	16.78	0.002	0.92
122	372.590	591.929	16.12	0.008	0.97	16.57	0.001	0.91
123	665.969	465.036	16.14	0.008	0.99	17.27	0.003	0.98
125	363.964	370.767	16.16	0.008	0.99	16.82	0.001	0.95
126	204.042	814.912	16.18	0.001	1.00	16.89	0.001	0.97
127	929.793	981.620	16.18	0.004	0.80	17.26	0.002	0.81
128	320.326	832.559	16.18	0.002	0.96	16.89	0.001	0.95
129	615.395	459.441	16.19	0.013	0.94	17.09	0.002	0.93
130	480.794	563.367	16.19	0.058	0.97	16.80	0.015	0.94
131	495.066	439.925	16.21	0.026	0.98	16.82	0.004	0.97
133	143.296	626.366	16.23	0.006	0.90	16.64	0.001	0.95

IDk	Xpix	Ypix	Kmag	Δ Kmag	CorreK	Jmag	Δ Jmag	CorreJ
134	371.276	618.880	16.24	0.004	0.97	16.73	0.001	0.94
135	549.487	485.848	16.26	0.040	0.94	17.05	0.007	0.90
136	218.011	120.952	16.27	0.002	0.99	16.96	0.001	0.97
137	216.345	720.069	16.29	0.001	0.98	16.98	0.001	0.98
138	364.984	178.149	16.29	0.003	0.99	16.96	0.001	0.98
139	856.621	949.028	16.29	0.006	0.96	17.72	0.002	0.83
140	336.260	341.698	16.29	0.006	0.97	16.91	0.001	0.96
141	465.926	602.539	16.32	0.021	0.97	16.94	0.003	0.97
142	453.533	563.806	16.32	0.046	0.94	16.73	0.002	0.89
143	544.717	449.902	16.33	0.024	0.98	17.16	0.001	0.93
144	292.909	680.327	16.33	0.004	0.98	18.25	0.003	0.98
145	289.615	395.700	16.34	0.022	0.97	16.85	0.002	0.92
146	760.281	708.309	16.35	0.007	0.98	17.39	0.003	0.91
147	804.154	513.441	16.35	0.007	0.96	17.59	0.002	0.92
148	475.802	482.745	16.36	0.056	0.86	17.22	0.024	0.90
149	404.803	561.546	16.37	0.020	0.96	17.21	0.002	0.94
150	429.492	591.936	16.38	0.019	0.96	16.87	0.001	0.96
151	439.030	963.448	16.39	0.004	0.97	17.36	0.001	0.95
152	303.719	465.528	16.39	0.020	0.96	17.00	0.002	0.92
153	300.362	382.357	16.43	0.020	0.96	17.31	0.003	0.99
154	594.844	489.808	16.43	0.022	0.98	17.35	0.004	0.95
155	536.770	652.431	16.44	0.013	0.97	17.11	0.005	0.96
156	388.270	588.697	16.45	0.013	0.98	16.91	0.001	0.95
157	510.666	560.369	16.45	0.067	0.96	17.20	0.018	0.91
158	572.795	508.746	16.46	0.031	0.97	17.21	0.009	0.91
159	521.925	552.937	16.48	0.064	0.90	17.45	0.023	0.84
160	149.839	721.068	16.53	0.003	0.99	17.11	0.001	0.94
161	618.133	330.247	16.53	0.003	0.99	17.62	0.002	0.97
162	266.123	375.589	16.53	0.050	0.82	17.08	0.008	0.94

IDk	Xpix	Ypix	Kmag	Δ Kmag	CorreK	Jmag	Δ Jmag	CorreJ
163	434.863	324.685	16.55	0.008	0.98	17.29	0.002	0.95
164	443.326	703.519	16.55	0.007	0.93	17.18	0.002	0.95
165	499.369	621.531	16.55	0.021	0.96	17.30	0.003	0.97
167	469.567	449.307	16.56	0.039	0.95	17.19	0.007	0.93
168	379.368	621.104	16.57	0.007	0.97	17.10	0.001	0.97
169	342.173	623.549	16.58	0.005	0.97	17.06	0.001	0.97
170	548.879	631.745	16.60	0.020	0.97	17.64	0.008	0.94
172	431.624	725.695	16.64	0.007	0.95	17.29	0.002	0.92
174	506.256	578.079	16.66	0.060	0.93	17.26	0.018	0.95
175	477.403	640.784	16.67	0.018	0.97	17.30	0.001	0.96
176	157.179	618.852	16.68	0.008	0.99	17.10	0.001	0.96
177	571.058	579.745	16.70	0.030	0.96	18.43	0.006	0.98
178	458.257	499.266	16.71	0.073	0.93	17.20	0.024	0.94
179	588.006	455.227	16.71	0.024	0.99	17.53	0.002	0.98
181	415.332	456.979	16.73	0.033	0.96	17.11	0.005	0.95
182	411.120	548.131	16.74	0.035	0.96	17.21	0.003	0.99
183	618.524	625.614	16.75	0.015	0.91	17.59	0.007	0.90
184	355.862	181.532	16.75	0.004	0.96	17.48	0.002	0.96
185	916.908	572.591	16.76	0.007	0.95	18.20	0.004	0.92
186	356.444	347.448	16.76	0.009	0.94	17.37	0.002	0.94
187	307.362	697.372	16.76	0.002	0.95	17.28	0.001	0.97
188	404.092	551.462	16.77	0.031	0.96	17.96	0.006	0.97
189	407.991	519.097	16.78	0.038	0.96	17.31	0.007	0.99
190	75.640	919.845	16.79	0.005	0.97	17.45	0.002	0.91
191	121.346	162.754	16.80	0.002	0.96	17.52	0.002	0.93
192	571.826	501.095	16.81	0.044	0.97	17.77	0.011	0.97
193	457.566	395.797	16.81	0.034	0.95	17.45	0.002	0.94
194	647.013	669.600	16.81	0.007	0.97	18.07	0.007	0.95
195	527.541	622.107	16.82	0.029	0.95	17.91	0.005	0.91

IDk	Xpix	Ypix	Kmag	Δ Kmag	CorreK	Jmag	Δ Jmag	CorreJ
196	590.841	504.629	16.82	0.032	0.96	17.59	0.008	0.92
197	419.689	774.820	16.82	0.005	0.96	17.90	0.003	0.94
198	331.102	596.314	16.83	0.010	0.98	17.32	0.001	0.99
199	417.616	789.186	16.83	0.004	0.97	17.61	0.002	0.92
200	220.269	591.219	16.85	0.006	0.98	18.42	0.004	0.99
201	397.385	463.058	16.85	0.033	0.96	18.24	0.009	0.99
202	634.448	48.442	16.88	0.002	0.93	17.89	0.004	0.91
203	134.703	897.262	16.88	0.006	0.98	17.65	0.002	0.93
204	402.254	752.333	16.89	0.007	0.94	17.68	0.002	0.97
205	251.723	328.580	16.89	0.052	0.95	17.61	0.009	0.90
206	591.690	566.789	16.90	0.028	0.97	17.85	0.002	0.93
207	507.512	391.995	16.90	0.027	0.96	18.46	0.004	0.97
208	665.148	434.655	16.90	0.012	0.97	17.94	0.004	0.96
209	291.843	933.620	16.91	0.009	0.97	17.74	0.002	0.93
210	371.625	535.543	16.91	0.024	0.93	17.55	0.003	0.91
211	641.428	689.120	16.92	0.008	0.95	18.22	0.013	0.81
212	462.982	662.330	16.93	0.019	0.97	17.99	0.003	0.96
213	628.492	481.631	16.93	0.024	0.94	18.86	0.009	0.94
214	309.441	284.358	16.93	0.006	0.95	17.57	0.002	0.97
215	526.447	560.944	16.94	0.082	0.90	17.98	0.038	0.92
216	178.766	469.840	16.94	0.016	0.96	17.47	0.002	0.87
217	381.399	510.311	16.94	0.033	0.95	17.54	0.003	0.95
218	535.278	599.704	16.95	0.043	0.97	18.52	0.018	0.93
219	422.719	485.118	16.96	0.051	0.97	17.44	0.013	0.93
220	199.270	681.138	16.96	0.005	0.98	17.45	0.002	0.99
221	441.302	508.052	16.97	0.075	0.93	17.49	0.024	0.90
222	488.327	440.038	16.99	0.053	0.96	17.65	0.008	0.96
223	393.120	573.812	16.99	0.029	0.86	17.89	0.004	0.89
224	532.155	642.555	16.99	0.025	0.95	17.78	0.007	0.96

IDk	Xpix	Ypix	Kmag	Δ Kmag	CorreK	Jmag	Δ Jmag	CorreJ
227	151.751	644.996	17.00	0.011	0.98	17.46	0.002	0.93
228	525.817	864.405	17.00	0.029	0.97	17.94	0.002	0.95
229	619.982	427.232	17.03	0.021	0.98	17.90	0.002	0.96
230	459.972	440.667	17.06	0.057	0.96	17.35	0.005	0.81
231	656.473	533.137	17.07	0.014	0.96	18.16	0.006	0.93
232	112.883	687.594	17.07	0.011	0.97	17.84	0.002	0.96
233	489.467	484.003	17.07	0.119	0.75	18.15	0.054	0.83
234	537.542	565.808	17.08	0.073	0.96	17.98	0.036	0.90
235	305.397	310.657	17.08	0.013	0.96	17.82	0.003	0.98
236	364.490	784.739	17.09	0.006	0.95	18.58	0.004	0.95
237	520.263	541.874	17.10	0.129	0.97	18.67	0.075	0.86
238	795.812	845.866	17.11	0.007	0.97	18.35	0.004	0.93
239	174.786	753.537	17.11	0.017	0.95	19.00	0.006	0.96
240	218.864	572.783	17.13	0.010	0.98	17.64	0.002	0.92
241	190.115	480.638	17.13	0.018	0.97	17.73	0.002	0.98
242	387.981	727.635	17.15	0.009	0.95	18.42	0.008	0.91
243	510.271	808.091	17.16	0.009	0.97	18.10	0.003	0.97
244	279.573	674.312	17.16	0.007	0.95	17.84	0.002	0.94
245	197.269	455.692	17.17	0.018	0.97	18.46	0.004	0.97
246	542.550	347.946	17.18	0.009	0.94	18.22	0.006	0.96
247	475.341	583.242	17.18	0.083	0.92	17.77	0.021	0.96
248	348.599	188.934	17.18	0.005	0.96	17.91	0.002	0.90
249	356.444	546.873	17.20	0.023	0.92	18.36	0.007	0.84
250	818.184	761.054	17.20	0.015	0.98	18.55	0.004	0.93
251	394.326	370.329	17.20	0.019	0.94	17.83	0.003	0.96
252	575.776	708.348	17.21	0.018	0.96	18.04	0.004	0.93
253	234.801	720.703	17.21	0.003	0.97	17.91	0.002	0.94
254	651.868	245.540	17.21	0.017	0.95	18.20	0.003	0.93
255	342.938	521.654	17.22	0.029	0.91	18.28	0.004	0.94

IDk	Xpix	Ypix	Kmag	Δ Kmag	CorreK	Jmag	Δ Jmag	CorreJ
256	513.924	312.181	17.23	0.005	0.98	18.89	0.006	0.97
257	586.895	587.845	17.23	0.042	0.98	18.10	0.004	0.95
259	626.320	541.524	17.25	0.024	0.94	18.21	0.005	0.92
260	278.627	450.429	17.25	0.035	0.95	18.87	0.011	0.98
261	555.043	190.962	17.26	0.036	0.98	18.15	0.003	0.97
262	324.261	376.854	17.27	0.031	0.87	17.97	0.003	0.98
263	129.763	512.779	17.28	0.019	0.97	19.01	0.006	0.91
265	462.743	457.280	17.28	0.079	0.81	17.95	0.015	0.87
266	256.085	504.111	17.31	0.022	0.97	17.83	0.003	0.98
267	369.038	377.929	17.32	0.024	0.97	18.02	0.003	0.97
268	591.036	671.651	17.33	0.016	0.96	18.28	0.006	0.95
269	405.412	734.914	17.33	0.012	0.96	18.69	0.005	0.91
270	712.771	794.495	17.33	0.007	0.95	18.50	0.004	0.90
271	48.069	409.039	17.34	0.003	0.97	17.87	0.002	0.97
272	380.904	710.262	17.34	0.010	0.84	17.89	0.003	0.93
273	577.386	581.442	17.34	0.050	0.94	18.12	0.004	0.96
274	183.611	656.650	17.35	0.013	0.86	18.34	0.004	0.88
275	513.161	686.440	17.35	0.022	0.92	18.29	0.009	0.92
276	551.906	701.046	17.35	0.017	0.98	18.44	0.004	0.99
277	366.040	548.402	17.35	0.031	0.92	17.76	0.004	0.94
278	385.933	648.747	17.36	0.014	0.97	17.99	0.002	0.93
279	883.373	773.311	17.37	0.017	0.67	18.33	0.004	0.85
280	308.216	338.277	17.38	0.024	0.96	18.01	0.003	0.99
281	601.011	477.401	17.38	0.047	0.95	18.36	0.011	0.88
282	233.377	670.102	17.39	0.004	0.97	17.98	0.002	0.98
283	625.907	619.292	17.39	0.026	0.93	18.37	0.013	0.95
284	491.770	214.138	17.40	0.015	0.98	19.38	0.009	0.92
285	168.864	82.260	17.41	0.004	0.96	18.34	0.005	0.92
286	250.788	563.274	17.41	0.013	0.97	17.95	0.002	0.93

IDk	Xpix	Ypix	Kmag	Δ Kmag	CorreK	Jmag	Δ Jmag	CorreJ
287	429.412	470.460	17.43	0.076	0.85	18.31	0.023	0.84
288	581.633	677.172	17.43	0.018	0.95	18.95	0.006	0.98
289	541.656	851.286	17.43	0.038	0.94	18.72	0.005	0.91
290	868.746	632.986	17.43	0.021	0.94	18.64	0.005	0.91
291	630.463	510.080	17.43	0.034	0.93	18.38	0.005	0.95
292	521.276	989.330	17.44	0.060	0.96	18.56	0.004	0.94
294	208.288	492.060	17.44	0.023	0.97	17.99	0.002	1.00
296	96.286	770.673	17.45	0.006	0.96	18.71	0.005	0.96
298	330.724	663.357	17.46	0.007	0.95	18.05	0.003	0.94
299	866.449	337.785	17.46	0.009	0.94	18.71	0.005	0.91
300	310.366	395.375	17.47	0.050	0.94	18.31	0.003	0.98
301	583.955	376.779	17.47	0.019	0.97	18.35	0.004	0.94
302	883.513	832.221	17.47	0.013	0.92	18.93	0.006	0.85
303	230.044	558.104	17.49	0.015	0.97	18.75	0.005	0.99
304	596.513	557.755	17.49	0.043	0.94	18.42	0.004	0.92
305	455.709	634.846	17.49	0.038	0.82	18.08	0.003	0.90
306	273.660	777.938	17.50	0.005	0.95	18.59	0.005	0.94
307	661.295	374.314	17.51	0.011	0.87	18.40	0.004	0.82
308	114.675	340.708	17.51	0.008	0.94	18.16	0.003	0.94
309	583.568	496.009	17.52	0.068	0.91	18.47	0.015	0.90
310	573.393	620.485	17.52	0.048	0.89	18.29	0.014	0.93
311	510.940	116.819	17.52	0.040	0.96	18.49	0.004	0.94
312	542.573	396.364	17.52	0.038	0.93	18.66	0.005	0.90
313	774.307	526.203	17.52	0.020	0.95	18.71	0.005	0.93
314	233.005	627.868	17.53	0.009	0.98	18.07	0.003	0.97
315	175.269	945.114	17.54	0.007	0.96	19.13	0.007	0.99
316	453.131	469.396	17.55	0.105	0.95	18.65	0.052	0.94
317	318.458	379.708	17.56	0.044	0.91	18.93	0.007	0.91
318	789.116	599.376	17.56	0.014	0.96	18.78	0.005	0.90

IDk	Xpix	Ypix	Kmag	Δ Kmag	CorreK	Jmag	Δ Jmag	CorreJ
319	454.505	611.917	17.57	0.052	0.83	18.04	0.007	0.80
320	413.426	154.484	17.57	0.054	0.93	18.39	0.004	0.94
322	447.425	371.620	17.58	0.047	0.94	18.91	0.018	0.93
323	356.030	663.207	17.58	0.013	0.97	18.75	0.006	0.98
325	483.802	452.964	17.58	0.106	0.96	18.93	0.041	0.84
326	274.319	650.241	17.58	0.004	0.93	18.60	0.004	0.86
327	366.199	555.776	17.59	0.040	0.93	18.54	0.007	0.91
328	402.171	515.994	17.59	0.074	0.92	18.07	0.013	0.93
329	209.459	355.804	17.59	0.047	0.93	19.08	0.030	0.89
330	675.119	395.716	17.60	0.013	0.98	19.49	0.015	0.93
331	296.494	502.124	17.60	0.040	0.94	18.52	0.006	0.90
332	399.900	301.036	17.61	0.006	0.96	19.55	0.016	0.96
333	390.592	961.303	17.62	0.049	0.95	18.79	0.005	0.93
335	734.812	823.429	17.64	0.007	0.94	18.87	0.006	0.88
336	555.737	648.093	17.64	0.038	0.96	19.60	0.053	0.90
337	444.880	484.707	17.65	0.122	0.96	18.89	0.074	0.91
338	392.641	256.144	17.65	0.021	0.94	18.68	0.005	0.93
339	693.326	771.284	17.66	0.008	0.94	18.78	0.005	0.89
340	365.072	966.807	17.66	0.064	0.96	18.87	0.005	0.97
341	567.021	239.789	17.67	0.043	0.97	18.63	0.004	0.94
342	876.284	638.029	17.67	0.026	0.92	18.92	0.008	0.85
343	60.064	878.792	17.67	0.004	0.97	18.43	0.004	0.94
344	518.131	724.719	17.67	0.022	0.95	18.70	0.007	0.86
345	536.341	692.028	17.67	0.024	0.96	18.44	0.004	0.97
346	194.965	717.041	17.67	0.004	0.98	18.35	0.004	0.96
347	256.063	493.700	17.68	0.033	0.95	18.26	0.004	0.96
348	487.569	759.405	17.69	0.015	0.93	18.51	0.005	0.92
349	356.455	462.272	17.70	0.076	0.91	18.33	0.006	0.91
350	849.287	634.400	17.70	0.024	0.82	19.02	0.009	0.85

IDk	Xpix	Ypix	Kmag	Δ Kmag	CorreK	Jmag	Δ Jmag	CorreJ
351	733.992	280.906	17.70	0.024	0.95	18.75	0.005	0.96
352	285.456	643.270	17.71	0.004	0.93	18.89	0.005	0.95
353	461.671	633.461	17.71	0.048	0.94	18.94	0.006	0.92
354	306.473	796.576	17.71	0.009	0.93	18.44	0.004	0.95
355	846.482	796.703	17.72	0.021	0.89	18.89	0.007	0.89
356	432.796	249.793	17.72	0.020	0.96	19.67	0.012	0.90
357	376.016	709.899	17.73	0.015	0.77	18.49	0.004	0.95
358	718.796	601.849	17.73	0.016	0.97	19.57	0.010	0.97
359	549.217	367.903	17.73	0.028	0.94	19.03	0.008	0.95
362	235.915	567.237	17.73	0.016	0.97	18.32	0.003	0.94
363	558.360	574.468	17.74	0.091	0.94	19.19	0.035	0.94
364	517.174	928.283	17.74	0.082	0.97	18.90	0.006	0.97
365	798.140	494.628	17.74	0.020	0.90	18.91	0.008	0.91
366	409.234	615.843	17.75	0.036	0.94	18.77	0.005	0.87
367	182.800	630.647	17.76	0.019	0.95	18.70	0.005	0.92
368	598.462	621.561	17.76	0.049	0.92	19.43	0.032	0.94
369	788.469	628.956	17.76	0.020	0.93	18.93	0.006	0.91
370	332.354	421.716	17.77	0.082	0.89	18.37	0.006	0.80
371	233.299	656.063	17.77	0.008	0.95	18.34	0.003	0.98
373	410.384	283.870	17.77	0.005	0.95	18.99	0.009	0.97
374	467.857	588.234	17.77	0.117	0.90	18.29	0.028	0.93
375	203.244	233.934	17.77	0.010	0.96	18.44	0.004	0.99
376	347.464	496.850	17.78	0.070	0.94	19.09	0.008	0.93
377	544.595	412.444	17.78	0.054	0.92	18.58	0.004	0.94
378	233.889	996.588	17.78	0.005	0.95	18.89	0.005	0.97
379	419.223	587.005	17.78	0.063	0.91	18.67	0.006	0.89
380	466.153	461.650	17.79	0.131	0.88	19.18	0.063	0.85
381	569.017	733.457	17.79	0.026	0.95	19.01	0.006	0.97
382	485.261	428.977	17.79	0.099	0.94	18.71	0.009	0.98

IDk	Xpix	Ypix	Kmag	Δ Kmag	CorreK	Jmag	Δ Jmag	CorreJ
383	519.012	154.353	17.79	0.067	0.96	18.73	0.005	0.97
385	179.832	689.287	17.80	0.015	0.95	18.79	0.006	0.97
386	699.089	859.259	17.80	0.006	0.96	18.95	0.006	0.93
387	333.031	253.661	17.80	0.007	0.92	18.58	0.004	0.95
388	628.179	525.267	17.81	0.044	0.92	18.75	0.008	0.94
389	629.529	175.340	17.81	0.005	0.92	19.28	0.009	0.95
390	488.702	87.860	17.82	0.051	0.96	19.62	0.011	0.93
391	446.875	612.590	17.82	0.061	0.75	18.63	0.008	0.89
392	501.365	356.314	17.83	0.037	0.92	19.69	0.014	0.89
393	229.540	687.300	17.83	0.005	0.92	18.41	0.005	0.92
394	665.534	368.300	17.83	0.014	0.94	18.73	0.005	0.87
395	727.420	761.139	17.84	0.010	0.94	19.08	0.007	0.89
396	421.123	579.386	17.84	0.077	0.81	18.56	0.004	0.89
397	444.119	468.191	17.84	0.126	0.90	18.69	0.038	0.88
398	415.077	331.650	17.85	0.025	0.95	18.49	0.013	0.96
399	329.739	246.342	17.86	0.007	0.94	19.56	0.010	0.96
400	374.872	331.010	17.87	0.018	0.95	18.84	0.007	0.95
401	844.803	867.916	17.87	0.015	0.94	19.26	0.008	0.82
402	310.376	658.354	17.87	0.005	0.92	18.56	0.004	0.88
403	362.307	469.083	17.87	0.084	0.86	19.90	0.016	0.85
404	742.394	439.715	17.87	0.014	0.94	19.78	0.013	0.95
405	577.696	897.578	17.88	0.088	0.93	18.99	0.006	0.94
406	339.489	418.361	17.88	0.085	0.91	18.44	0.005	0.91
407	504.539	635.294	17.88	0.060	0.82	18.79	0.010	0.94
408	489.842	326.499	17.89	0.017	0.95	19.32	0.012	0.94
409	356.678	375.564	17.89	0.041	0.88	18.67	0.005	0.91
410	200.066	826.352	17.89	0.006	0.94	18.67	0.004	0.98
411	843.601	630.002	17.89	0.027	0.93	19.15	0.011	0.83
412	155.212	494.491	17.89	0.039	0.92	18.69	0.006	0.98

IDk	Xpix	Ypix	Kmag	Δ Kmag	CorreK	Jmag	Δ Jmag	CorreJ
413	301.528	180.294	17.89	0.030	0.93	20.03	0.017	0.93
414	396.198	530.542	17.90	0.085	0.89	19.15	0.023	0.93
415	313.904	408.585	17.91	0.079	0.95	18.53	0.008	0.95
416	429.299	578.468	17.91	0.095	0.89	19.12	0.009	0.94
418	416.965	640.729	17.92	0.035	0.87	18.48	0.005	0.92
419	687.647	67.028	17.92	0.060	0.93	19.06	0.007	0.90
420	588.171	323.631	17.93	0.007	0.95	18.81	0.006	0.93
421	368.277	464.496	17.94	0.087	0.92	18.81	0.007	0.95
422	228.401	495.896	17.94	0.035	0.94	18.43	0.004	0.97
423	88.522	644.632	17.95	0.031	0.89	18.44	0.004	0.92
424	715.509	466.345	17.95	0.025	0.92	19.14	0.008	0.89
426	73.329	309.562	17.96	0.012	0.94	18.58	0.004	0.96
427	376.279	650.057	17.96	0.021	0.94	18.44	0.004	0.97
429	501.831	612.381	17.97	0.087	0.94	19.50	0.030	0.91
430	437.395	716.088	17.97	0.025	0.94	18.68	0.005	0.95
431	576.101	279.726	17.97	0.009	0.97	19.06	0.006	0.95
432	331.578	614.051	17.98	0.021	0.92	19.02	0.008	0.91
433	430.324	666.192	17.99	0.035	0.86	19.14	0.009	0.85
435	928.342	894.451	17.99	0.009	0.84	19.39	0.009	0.81
436	624.390	761.027	17.99	0.024	0.94	19.10	0.014	0.96
437	481.078	615.739	18.00	0.078	0.93	18.73	0.014	0.99
438	631.179	28.870	18.01	0.005	0.91	19.19	0.008	0.94
439	610.802	531.693	18.02	0.059	0.95	19.22	0.009	0.96
440	531.753	528.201	18.02	0.244	0.83	18.95	0.095	0.92
441	273.028	566.241	18.02	0.026	0.94	19.11	0.007	0.99
443	472.867	346.855	18.03	0.040	0.95	20.14	0.038	0.90
444	381.535	409.318	18.03	0.062	0.89	19.38	0.013	0.92
445	470.016	627.724	18.03	0.069	0.92	18.97	0.006	0.94
446	399.349	491.840	18.03	0.104	0.85	18.37	0.016	0.95

IDk	Xpix	Ypix	Kmag	Δ Kmag	CorreK	Jmag	Δ Jmag	CorreJ
447	446.427	416.707	18.04	0.117	0.89	18.95	0.006	0.82
448	600.994	412.894	18.05	0.048	0.95	19.05	0.008	0.95
450	274.880	587.660	18.05	0.021	0.95	19.26	0.008	0.86
451	324.127	402.491	18.07	0.085	0.92	19.27	0.011	0.91
452	290.924	445.059	18.08	0.087	0.96	18.75	0.011	0.95
454	380.500	454.034	18.09	0.094	0.92	18.91	0.008	0.94
455	361.323	724.716	18.09	0.017	0.89	19.22	0.007	0.96
456	278.565	556.746	18.10	0.032	0.92	18.99	0.006	0.92
458	508.927	863.120	18.11	0.098	0.92	19.39	0.009	0.92
459	367.396	761.627	18.11	0.017	0.90	18.76	0.005	0.95
460	836.911	658.295	18.11	0.035	0.92	19.52	0.011	0.91
461	345.702	514.635	18.11	0.073	0.82	18.87	0.008	0.83
462	365.966	566.945	18.11	0.062	0.92	18.69	0.006	0.95
463	361.871	648.443	18.11	0.023	0.95	19.39	0.009	0.93
464	518.953	613.326	18.11	0.102	0.73	18.81	0.010	0.92
465	556.007	710.819	18.13	0.036	0.95	19.04	0.007	0.95
466	633.415	313.338	18.13	0.006	0.90	19.19	0.008	0.90
467	342.829	303.974	18.13	0.010	0.93	19.60	0.011	0.94
468	384.919	718.475	18.13	0.022	0.92	19.35	0.009	0.97
469	362.595	846.546	18.13	0.062	0.89	19.08	0.007	0.96
470	632.659	656.761	18.13	0.027	0.90	19.22	0.009	0.91
471	346.605	260.241	18.14	0.007	0.93	19.66	0.012	0.93
472	499.106	302.224	18.14	0.010	0.95	19.24	0.008	0.97
473	383.138	561.313	18.14	0.082	0.85	19.61	0.011	0.81
474	611.192	269.108	18.14	0.039	0.94	19.25	0.008	0.94
476	379.064	601.223	18.15	0.043	0.70	18.96	0.006	0.88
477	463.104	270.565	18.16	0.008	0.93	19.14	0.007	0.97
478	271.697	273.513	18.17	0.022	0.88	19.09	0.009	0.94
479	299.256	398.155	18.17	0.102	0.88	19.16	0.007	0.97

IDk	Xpix	Ypix	Kmag	Δ Kmag	CorreK	Jmag	Δ Jmag	CorreJ
480	61.829	858.751	18.17	0.007	0.93	18.77	0.005	0.92
481	409.063	451.562	18.17	0.109	0.88	18.95	0.023	0.94
482	335.546	522.653	18.18	0.066	0.93	18.59	0.005	0.92
484	358.350	455.839	18.18	0.115	0.92	19.23	0.010	0.90
486	381.930	759.417	18.19	0.021	0.90	18.97	0.007	0.94
487	740.144	580.615	18.19	0.023	0.90	19.88	0.014	0.89
488	60.852	313.284	18.19	0.010	0.84	19.19	0.007	0.94
489	271.899	606.610	18.20	0.017	0.82	19.13	0.007	0.99
491	300.882	356.864	18.22	0.083	0.90	19.67	0.028	0.92
492	559.461	305.438	18.22	0.008	0.88	19.35	0.008	0.93
493	398.733	172.513	18.23	0.057	0.89	19.13	0.008	0.90
494	789.328	368.460	18.23	0.062	0.87	19.42	0.009	0.90
495	459.750	701.002	18.23	0.040	0.80	19.24	0.013	0.91
497	515.393	817.602	18.24	0.046	0.90	19.19	0.007	0.93
499	301.846	624.493	18.25	0.016	0.80	19.51	0.010	0.95
501	673.774	623.905	18.26	0.023	0.91	20.19	0.023	0.92
502	285.173	509.387	18.27	0.064	0.83	18.87	0.006	0.81
503	472.105	725.708	18.27	0.036	0.88	19.64	0.015	0.94
504	756.695	518.908	18.27	0.033	0.92	19.38	0.010	0.93
505	801.517	443.544	18.27	0.009	0.88	19.40	0.009	0.89
507	555.023	557.038	18.28	0.166	0.84	19.37	0.070	0.81
508	547.191	783.630	18.28	0.015	0.93	19.26	0.008	0.95
509	557.276	365.482	18.28	0.040	0.91	19.48	0.012	0.96
510	769.625	738.677	18.28	0.043	0.90	20.06	0.021	0.87
511	409.943	865.053	18.28	0.124	0.94	19.70	0.013	0.93
512	324.143	728.789	18.28	0.011	0.95	18.95	0.006	0.97
513	755.598	247.393	18.29	0.041	0.88	19.52	0.010	0.88
514	294.506	533.956	18.29	0.057	0.74	19.28	0.008	0.88
515	738.285	616.511	18.29	0.030	0.86	19.65	0.011	0.89

IDk	Xpix	Ypix	Kmag	Δ Kmag	CorreK	Jmag	Δ Jmag	CorreJ
516	591.739	728.920	18.29	0.051	0.90	19.33	0.012	0.85
517	419.217	648.568	18.29	0.048	0.85	18.99	0.007	0.92
519	424.308	634.620	18.29	0.058	0.87	19.39	0.011	0.87
520	526.221	422.833	18.30	0.112	0.92	19.33	0.010	0.95
521	348.977	36.165	18.30	0.039	0.90	19.87	0.014	0.95
522	123.672	760.032	18.31	0.009	0.93	19.85	0.013	0.92
524	269.682	403.212	18.31	0.140	0.88	18.96	0.023	0.88
525	427.389	300.012	18.31	0.019	0.87	19.53	0.018	0.86
526	369.540	261.444	18.31	0.025	0.89	19.96	0.015	0.91
527	324.968	816.584	18.31	0.015	0.92	19.05	0.007	0.98
528	112.352	599.608	18.31	0.050	0.88	19.03	0.006	0.87
529	630.289	825.048	18.31	0.007	0.89	20.05	0.018	0.91
530	60.885	793.989	18.31	0.009	0.91	19.56	0.010	0.94
531	401.131	725.363	18.32	0.028	0.91	19.54	0.011	0.96
532	189.217	691.064	18.32	0.018	0.90	19.16	0.007	0.98
534	349.389	376.758	18.33	0.065	0.92	19.02	0.006	0.95
535	653.551	668.633	18.33	0.024	0.81	19.24	0.011	0.87
536	349.685	594.122	18.33	0.043	0.75	19.15	0.010	0.93
537	529.037	253.902	18.33	0.052	0.95	19.84	0.013	0.96
538	204.034	614.051	18.34	0.025	0.92	19.56	0.010	0.98
539	215.908	915.813	18.34	0.009	0.76	19.70	0.014	0.95
540	488.802	97.896	18.35	0.074	0.94	19.35	0.008	0.95
541	270.846	612.180	18.35	0.018	0.90	19.17	0.009	0.96
542	197.992	564.671	18.36	0.042	0.87	18.97	0.006	0.96
545	519.412	1013.991	18.36	0.008	0.89	19.73	0.012	0.89
546	153.112	186.077	18.36	0.052	0.90	19.02	0.006	0.97
548	460.030	340.115	18.37	0.052	0.89	19.60	0.011	0.90
549	488.378	292.257	18.37	0.012	0.88	19.48	0.009	0.96
551	291.481	610.694	18.37	0.021	0.85	19.44	0.010	0.94

IDk	Xpix	Ypix	Kmag	Δ Kmag	CorreK	Jmag	Δ Jmag	CorreJ
552	555.419	823.118	18.38	0.048	0.86	19.49	0.010	0.94
554	341.839	392.002	18.39	0.089	0.93	19.62	0.013	0.93
556	682.547	619.863	18.40	0.025	0.91	19.86	0.017	0.90
557	55.364	675.411	18.40	0.016	0.85	20.21	0.019	0.96
558	449.669	290.970	18.40	0.014	0.89	19.83	0.014	0.92
559	561.376	497.406	18.41	0.216	0.82	19.70	0.068	0.83
561	604.612	611.841	18.41	0.094	0.87	19.75	0.036	0.90
563	337.768	571.572	18.41	0.056	0.82	19.10	0.007	0.81
564	719.171	375.033	18.41	0.010	0.84	19.59	0.013	0.95
565	404.618	330.095	18.41	0.032	0.84	20.04	0.045	0.89
566	796.113	878.918	18.42	0.025	0.87	20.05	0.029	0.91
567	651.506	578.922	18.42	0.043	0.91	19.53	0.016	0.95
568	783.985	782.686	18.42	0.028	0.90	19.80	0.013	0.93
569	208.412	526.170	18.43	0.051	0.83	18.81	0.005	0.99
570	241.253	454.696	18.43	0.064	0.87	19.06	0.009	0.96
571	417.571	598.523	18.43	0.092	0.87	19.84	0.014	0.82
574	785.728	661.491	18.43	0.038	0.88	20.79	0.033	0.84
575	396.130	745.964	18.44	0.029	0.91	19.66	0.012	0.95
576	241.772	255.391	18.44	0.013	0.88	19.90	0.019	0.96
577	197.847	703.003	18.44	0.012	0.91	19.39	0.009	0.96
578	331.062	200.123	18.44	0.009	0.91	19.16	0.008	0.99
579	393.160	398.954	18.44	0.082	0.91	19.38	0.014	0.92
580	385.590	472.553	18.44	0.136	0.88	19.85	0.025	0.82
583	470.620	660.640	18.45	0.076	0.78	19.69	0.019	0.83
584	482.552	811.031	18.46	0.053	0.88	19.50	0.010	0.96
585	200.034	528.081	18.46	0.054	0.86	19.55	0.013	0.93
586	439.491	918.370	18.46	0.131	0.88	19.70	0.012	0.94
587	357.624	745.798	18.46	0.022	0.85	19.58	0.010	0.91
588	528.990	762.227	18.47	0.029	0.87	20.34	0.022	0.89

IDk	Xpix	Ypix	Kmag	Δ Kmag	CorreK	Jmag	Δ Jmag	CorreJ
589	407.186	360.030	18.47	0.060	0.76	19.65	0.027	0.91
590	167.566	478.910	18.47	0.066	0.85	19.61	0.013	0.93
591	379.445	162.805	18.48	0.009	0.88	20.04	0.016	0.88
592	220.767	389.861	18.48	0.099	0.93	19.56	0.010	0.94
593	577.650	803.697	18.48	0.009	0.89	20.38	0.022	0.89
595	454.828	804.884	18.48	0.035	0.91	19.41	0.010	0.91
596	188.436	785.386	18.49	0.027	0.88	20.52	0.024	0.93
597	689.132	368.817	18.49	0.027	0.89	19.61	0.019	0.91
598	62.710	926.364	18.50	0.011	0.83	19.52	0.010	0.92
600	430.211	283.101	18.51	0.011	0.90	19.81	0.019	0.97
602	923.955	422.060	18.51	0.012	0.85	19.95	0.016	0.92
603	451.868	280.849	18.51	0.011	0.89	20.50	0.028	0.86
604	357.544	576.834	18.51	0.072	0.81	19.14	0.007	0.88
605	294.412	739.457	18.53	0.012	0.87	19.28	0.008	0.97
606	609.344	34.741	18.53	0.024	0.84	19.53	0.019	0.89
607	348.931	231.330	18.53	0.011	0.85	19.32	0.009	0.93
609	745.052	670.109	18.54	0.030	0.84	20.88	0.039	0.90
610	140.993	1018.010	18.54	0.010	0.79	19.01	0.007	0.95
611	360.424	562.722	18.54	0.085	0.76	19.55	0.017	0.90
612	708.360	858.330	18.55	0.012	0.83	19.74	0.012	0.86
614	715.619	589.192	18.55	0.031	0.88	19.80	0.013	0.89
615	561.357	393.802	18.55	0.085	0.76	19.42	0.011	0.85
616	79.320	875.033	18.56	0.041	0.89	19.88	0.014	0.95
617	275.411	860.137	18.56	0.014	0.81	20.17	0.018	0.97
618	674.598	720.138	18.57	0.020	0.88	19.61	0.011	0.90
620	778.644	260.950	18.58	0.081	0.87	20.75	0.031	0.82
621	184.659	436.366	18.58	0.059	0.82	20.46	0.023	0.88
622	295.118	1000.180	18.58	0.024	0.88	19.63	0.014	0.98
623	740.335	350.959	18.59	0.049	0.87	20.02	0.016	0.93

IDk	Xpix	Ypix	Kmag	Δ Kmag	CorreK	Jmag	Δ Jmag	CorreJ
624	187.279	494.909	18.60	0.068	0.85	19.95	0.015	0.92
625	594.901	215.048	18.60	0.143	0.82	20.05	0.019	0.93
626	249.945	420.837	18.60	0.114	0.92	19.87	0.015	0.95
627	422.258	704.776	18.60	0.041	0.80	19.24	0.010	0.97
628	815.181	533.832	18.60	0.048	0.80	19.77	0.024	0.89
629	399.078	361.402	18.60	0.063	0.71	19.73	0.027	0.84
631	179.477	491.866	18.61	0.071	0.78	19.17	0.007	0.94
632	662.825	449.774	18.61	0.070	0.88	20.59	0.028	0.86
633	367.982	148.276	18.61	0.015	0.87	19.41	0.010	0.94
634	720.693	703.778	18.62	0.024	0.88	20.38	0.024	0.87
635	404.800	354.845	18.62	0.063	0.73	19.99	0.037	0.83
636	771.651	760.200	18.62	0.040	0.83	20.12	0.017	0.91
637	220.525	919.550	18.62	0.011	0.85	19.70	0.012	0.93
638	653.042	630.883	18.62	0.039	0.88	20.40	0.032	0.93
639	604.272	503.630	18.63	0.135	0.84	20.19	0.058	0.82
640	613.695	966.795	18.63	0.150	0.88	19.82	0.013	0.84
641	277.239	262.385	18.63	0.020	0.86	19.44	0.012	0.95
642	394.466	777.442	18.63	0.029	0.82	20.09	0.017	0.93
643	304.652	282.405	18.63	0.031	0.83	19.71	0.012	0.91
644	212.912	505.498	18.64	0.065	0.83	19.45	0.009	0.95
646	193.714	90.033	18.64	0.012	0.83	19.81	0.013	0.96
647	456.747	199.490	18.64	0.133	0.85	19.96	0.016	0.90
649	180.571	665.536	18.65	0.041	0.85	19.24	0.008	0.97
650	259.259	509.789	18.66	0.074	0.83	19.86	0.015	0.93
651	280.952	849.081	18.66	0.016	0.92	20.08	0.016	0.97
654	413.254	255.771	18.67	0.043	0.86	20.09	0.017	0.96
655	645.353	502.653	18.67	0.091	0.73	19.77	0.021	0.91
657	835.032	348.167	18.67	0.082	0.82	19.92	0.015	0.89
658	258.586	519.251	18.67	0.069	0.84	19.71	0.017	0.93

IDk	Xpix	Ypix	Kmag	Δ Kmag	CorreK	Jmag	Δ Jmag	CorreJ
659	701.600	744.474	18.67	0.017	0.79	20.15	0.018	0.88
660	317.032	559.207	18.67	0.072	0.79	19.46	0.010	0.93
662	566.043	388.998	18.68	0.087	0.87	19.42	0.012	0.92
665	800.232	751.981	18.68	0.065	0.88	19.98	0.018	0.92
666	173.780	826.698	18.68	0.016	0.86	19.65	0.011	0.95
667	347.913	203.901	18.69	0.018	0.86	19.73	0.012	0.88
668	570.073	787.822	18.69	0.019	0.86	20.59	0.028	0.96
669	221.682	808.166	18.69	0.013	0.85	19.94	0.014	0.93
670	660.204	672.082	18.69	0.030	0.81	19.66	0.016	0.83
671	241.484	629.534	18.69	0.023	0.79	19.44	0.010	0.95
672	321.883	507.574	18.70	0.121	0.87	19.47	0.010	0.93
673	608.303	901.372	18.70	0.148	0.87	20.22	0.019	0.95
675	211.941	283.884	18.70	0.035	0.89	19.61	0.019	0.98
676	704.246	970.569	18.70	0.034	0.84	20.08	0.016	0.85
677	365.937	579.129	18.70	0.092	0.78	19.31	0.008	0.92
678	657.298	312.814	18.70	0.033	0.83	20.43	0.023	0.91
679	647.871	457.359	18.71	0.093	0.83	19.80	0.015	0.94
680	306.948	628.863	18.71	0.024	0.86	19.13	0.009	0.96
681	607.394	820.323	18.71	0.012	0.81	20.00	0.019	0.90
682	137.156	912.893	18.72	0.012	0.80	19.96	0.015	0.96
683	719.135	802.670	18.72	0.022	0.81	19.68	0.012	0.87
684	136.645	872.668	18.73	0.075	0.78	19.69	0.012	0.97
685	209.060	956.922	18.73	0.013	0.78	20.79	0.041	0.94
688	778.487	673.553	18.73	0.049	0.83	20.74	0.036	0.86
689	384.817	632.284	18.74	0.049	0.83	20.22	0.019	0.92
691	756.229	817.867	18.74	0.020	0.80	20.26	0.020	0.92
692	404.042	672.239	18.74	0.053	0.87	20.57	0.026	0.93
695	483.916	255.573	18.75	0.018	0.75	19.56	0.011	0.91
696	137.405	318.703	18.75	0.028	0.80	19.43	0.010	0.99

IDk	Xpix	Ypix	Kmag	Δ Kmag	CorreK	Jmag	Δ Jmag	CorreJ
697	283.726	612.854	18.76	0.027	0.89	19.39	0.010	0.87
698	487.636	870.733	18.76	0.239	0.80	19.95	0.015	0.95
699	367.783	453.635	18.76	0.175	0.86	20.38	0.022	0.90
701	623.106	492.045	18.77	0.132	0.88	19.66	0.020	0.90
702	760.302	455.342	18.77	0.034	0.82	20.65	0.028	0.90
703	566.599	291.576	18.78	0.012	0.84	20.11	0.017	0.92
704	621.764	346.971	18.79	0.023	0.82	20.19	0.019	0.94
705	176.393	580.078	18.79	0.063	0.88	19.82	0.013	0.95
707	80.564	345.827	18.81	0.027	0.72	19.94	0.014	0.96
708	84.889	105.415	18.81	0.065	0.78	20.15	0.017	0.95
710	312.933	588.136	18.81	0.061	0.91	19.41	0.009	0.99
711	55.257	838.479	18.81	0.012	0.76	19.92	0.014	0.98
712	587.531	358.883	18.81	0.040	0.72	20.27	0.023	0.80
714	661.054	748.370	18.82	0.025	0.83	20.03	0.016	0.95
715	511.336	654.815	18.82	0.112	0.72	20.30	0.071	0.85
719	101.288	969.193	18.82	0.027	0.84	20.04	0.016	0.92
721	616.935	236.670	18.83	0.127	0.76	20.36	0.021	0.93
722	821.361	777.575	18.83	0.064	0.84	20.38	0.025	0.89
723	354.306	698.758	18.83	0.030	0.85	19.69	0.012	0.81
725	244.269	620.343	18.83	0.027	0.76	19.47	0.009	0.95
727	672.299	342.603	18.84	0.021	0.81	20.77	0.047	0.92
728	602.399	661.802	18.84	0.062	0.81	20.14	0.029	0.94
729	480.572	729.192	18.84	0.058	0.81	19.69	0.017	0.96
732	534.459	265.118	18.85	0.045	0.85	19.80	0.013	0.94
733	598.628	573.707	18.85	0.154	0.86	20.38	0.029	0.80
734	151.053	738.823	18.85	0.013	0.81	19.85	0.014	0.96
735	630.828	968.295	18.85	0.132	0.86	20.62	0.028	0.91
736	661.282	911.427	18.85	0.092	0.78	20.37	0.021	0.90
739	242.813	400.811	18.86	0.190	0.77	19.44	0.023	0.89

IDk	Xpix	Ypix	Kmag	Δ Kmag	CorreK	Jmag	Δ Jmag	CorreJ
743	338.227	315.263	18.87	0.032	0.80	19.76	0.013	0.96
744	534.979	419.042	18.87	0.164	0.74	20.38	0.022	0.82
748	166.688	730.172	18.88	0.016	0.85	20.13	0.018	0.98
749	564.919	676.597	18.89	0.071	0.83	20.59	0.026	0.96
750	388.896	547.748	18.89	0.176	0.72	19.48	0.012	0.83
753	618.262	682.234	18.89	0.056	0.86	20.73	0.034	0.92
755	755.848	629.036	18.89	0.050	0.87	20.77	0.031	0.82
756	49.055	462.110	18.90	0.013	0.76	19.93	0.016	0.90
757	607.842	827.063	18.90	0.026	0.79	20.35	0.024	0.91
759	257.467	464.443	18.90	0.110	0.82	20.27	0.030	0.86
760	422.351	638.834	18.91	0.093	0.67	19.50	0.011	0.80
761	650.906	505.466	18.91	0.103	0.78	20.17	0.031	0.80
764	313.672	620.626	18.92	0.036	0.81	19.84	0.013	0.94
765	520.605	744.727	18.92	0.054	0.78	20.16	0.023	0.91
766	819.028	445.689	18.92	0.031	0.68	19.85	0.014	0.90
767	696.800	250.552	18.93	0.169	0.83	20.15	0.018	0.91
768	281.134	871.413	18.93	0.018	0.77	19.63	0.011	0.96
769	341.967	703.370	18.93	0.029	0.83	19.52	0.010	0.98
770	575.737	686.855	18.94	0.076	0.83	20.18	0.021	0.94
771	629.114	436.824	18.94	0.116	0.85	20.72	0.033	0.90
772	588.832	352.144	18.94	0.036	0.82	20.11	0.018	0.87
773	305.355	68.881	18.94	0.113	0.74	19.92	0.014	0.95
774	500.594	778.594	18.95	0.030	0.75	19.97	0.018	0.91
775	698.127	422.831	18.95	0.039	0.84	20.29	0.020	0.95
776	279.013	956.538	18.95	0.056	0.76	19.85	0.013	0.98
777	363.228	484.102	18.96	0.207	0.73	19.78	0.016	0.86
778	85.197	543.885	18.96	0.075	0.73	19.49	0.010	0.98
779	300.664	754.545	18.96	0.018	0.80	19.84	0.016	0.94
780	448.727	783.131	18.96	0.028	0.86	19.61	0.011	0.95

IDk	Xpix	Ypix	Kmag	Δ Kmag	CorreK	Jmag	Δ Jmag	CorreJ
781	220.100	964.735	18.96	0.015	0.67	20.59	0.033	0.93
783	461.974	843.134	18.97	0.261	0.86	20.60	0.027	0.91
784	288.307	300.350	18.97	0.081	0.81	20.30	0.021	0.89
785	341.792	327.432	18.97	0.044	0.80	20.38	0.030	0.89
787	288.842	426.001	18.98	0.198	0.77	19.98	0.027	0.87
789	832.465	823.262	18.98	0.045	0.76	20.75	0.031	0.87
791	287.537	884.453	18.98	0.018	0.70	20.34	0.025	0.94
793	381.619	798.883	18.99	0.028	0.71	20.18	0.019	0.90
795	594.450	410.597	18.99	0.112	0.72	20.32	0.021	0.81
797	158.279	548.231	19.00	0.091	0.70	19.66	0.011	0.95
799	173.715	503.421	19.00	0.100	0.76	20.26	0.020	0.90
801	236.770	644.809	19.01	0.028	0.71	19.82	0.017	0.97
802	195.176	258.318	19.01	0.014	0.76	20.62	0.031	0.92
803	138.911	993.238	19.02	0.025	0.74	20.63	0.030	0.86
804	421.288	653.335	19.02	0.090	0.78	20.08	0.018	0.93
805	47.032	151.283	19.02	0.014	0.71	20.85	0.034	0.86
806	680.727	914.485	19.02	0.056	0.81	21.04	0.040	0.83
807	406.117	335.095	19.02	0.064	0.81	20.24	0.059	0.83
809	265.565	521.732	19.03	0.098	0.72	19.82	0.014	0.95
811	245.106	719.001	19.03	0.014	0.74	20.38	0.022	0.90
812	461.487	909.051	19.03	0.276	0.82	20.76	0.031	0.91
813	248.354	576.254	19.04	0.048	0.81	20.23	0.019	0.94
817	663.419	526.904	19.04	0.078	0.65	20.08	0.027	0.87
819	528.055	681.657	19.05	0.093	0.80	19.91	0.029	0.96
820	425.967	741.838	19.05	0.055	0.73	20.04	0.016	0.94
823	118.893	553.104	19.05	0.093	0.73	19.90	0.014	0.98
824	401.987	634.629	19.06	0.084	0.79	19.75	0.012	0.97
825	314.368	252.741	19.06	0.021	0.82	20.32	0.022	0.96
826	572.797	914.961	19.07	0.260	0.71	20.15	0.018	0.94

IDk	Xpix	Ypix	Kmag	Δ Kmag	CorreK	Jmag	Δ Jmag	CorreJ
827	212.565	635.955	19.07	0.047	0.72	19.67	0.011	0.91
828	599.631	384.080	19.07	0.074	0.81	19.92	0.014	0.91
829	74.582	638.572	19.07	0.076	0.76	20.55	0.026	0.87
830	879.381	530.156	19.08	0.022	0.78	20.48	0.024	0.82
833	251.947	644.742	19.08	0.023	0.68	19.96	0.015	0.84
835	287.869	794.062	19.08	0.030	0.72	20.81	0.037	0.92
838	739.402	533.006	19.09	0.060	0.70	20.32	0.020	0.90
839	192.525	22.011	19.09	0.017	0.78	20.32	0.023	0.92
841	641.314	527.042	19.09	0.117	0.88	20.20	0.036	0.88
842	244.046	637.578	19.10	0.030	0.71	20.45	0.027	0.81
843	532.908	774.952	19.10	0.039	0.81	19.97	0.017	0.94
844	85.836	365.532	19.10	0.032	0.76	20.52	0.024	0.94
845	615.403	254.689	19.10	0.123	0.74	21.00	0.038	0.89
851	418.069	671.583	19.11	0.083	0.71	19.99	0.015	0.92
852	693.552	324.704	19.12	0.015	0.79	20.47	0.031	0.94
854	584.456	285.875	19.12	0.020	0.85	20.78	0.031	0.86
856	284.362	92.637	19.13	0.159	0.68	20.28	0.020	0.88
858	54.567	582.070	19.14	0.044	0.78	20.59	0.027	0.94
859	487.727	634.931	19.14	0.177	0.73	19.72	0.018	0.82
861	564.012	654.610	19.14	0.118	0.68	20.47	0.090	0.82
862	839.128	837.677	19.14	0.047	0.71	20.37	0.021	0.88
863	737.356	887.169	19.15	0.019	0.77	20.56	0.026	0.86
865	82.948	895.459	19.15	0.073	0.69	20.10	0.017	0.95
866	793.019	531.971	19.15	0.090	0.79	20.45	0.036	0.91
868	179.562	856.533	19.16	0.016	0.66	20.82	0.032	0.94
869	118.906	364.393	19.16	0.038	0.65	19.83	0.013	0.92
870	154.522	509.196	19.16	0.113	0.74	20.47	0.025	0.91
871	419.593	911.019	19.16	0.253	0.75	20.36	0.021	0.96
872	492.165	395.827	19.16	0.233	0.78	19.74	0.013	0.95

IDk	Xpix	Ypix	Kmag	Δ Kmag	CorreK	Jmag	Δ Jmag	CorreJ
873	714.939	772.102	19.17	0.038	0.75	20.80	0.032	0.90
875	739.169	464.225	19.17	0.063	0.76	20.44	0.023	0.91
877	240.131	527.552	19.18	0.088	0.67	19.73	0.013	0.89
878	332.766	631.605	19.18	0.051	0.77	19.65	0.014	0.91
880	70.106	562.442	19.18	0.082	0.71	19.93	0.014	0.95
881	423.577	451.368	19.19	0.301	0.76	19.11	0.029	0.84
884	579.513	870.677	19.20	0.267	0.68	20.86	0.034	0.83
885	812.349	557.781	19.20	0.064	0.74	20.79	0.035	0.87
886	452.957	231.711	19.20	0.065	0.71	20.63	0.039	0.81
887	222.640	418.719	19.20	0.133	0.72	20.59	0.035	0.91
888	366.446	877.694	19.21	0.213	0.68	20.96	0.038	0.92
889	324.365	612.495	19.21	0.061	0.68	20.79	0.039	0.90
893	356.527	655.096	19.22	0.059	0.73	20.05	0.016	0.93
894	769.573	431.211	19.22	0.030	0.76	21.09	0.041	0.88
895	631.087	939.435	19.22	0.188	0.78	20.45	0.023	0.83
896	591.512	220.663	19.22	0.235	0.80	20.74	0.032	0.89
898	780.436	888.481	19.22	0.036	0.66	20.56	0.026	0.85
901	324.149	709.312	19.24	0.027	0.78	21.25	0.048	0.84
903	176.723	516.446	19.25	0.116	0.70	20.02	0.016	0.94
905	203.883	506.771	19.25	0.114	0.72	20.61	0.027	0.95
906	742.106	428.321	19.25	0.037	0.75	21.64	0.067	0.81
907	59.325	437.405	19.25	0.023	0.74	20.57	0.025	0.98
909	504.547	283.048	19.26	0.022	0.66	20.05	0.019	0.90
910	218.681	46.097	19.26	0.052	0.73	20.12	0.017	0.87
913	449.692	346.717	19.29	0.144	0.78	20.74	0.034	0.92
915	233.994	604.867	19.29	0.047	0.72	20.87	0.034	0.85
917	616.011	926.509	19.29	0.252	0.74	20.31	0.020	0.86
919	578.203	341.140	19.30	0.037	0.67	20.42	0.028	0.86
920	207.486	595.798	19.30	0.062	0.70	21.06	0.040	0.87

IDk	Xpix	Ypix	Kmag	Δ Kmag	CorreK	Jmag	Δ Jmag	CorreJ
921	501.103	424.233	19.31	0.319	0.76	20.37	0.039	0.84
922	457.861	833.537	19.31	0.300	0.69	21.23	0.047	0.84
923	312.130	91.361	19.31	0.187	0.66	20.13	0.018	0.94
924	376.274	762.744	19.32	0.056	0.68	20.41	0.023	0.89
925	257.666	608.809	19.32	0.045	0.76	20.96	0.037	0.81
926	678.307	483.698	19.32	0.121	0.71	21.27	0.077	0.88
927	143.842	726.584	19.32	0.038	0.70	20.79	0.035	0.81
928	880.301	616.396	19.32	0.091	0.72	21.33	0.052	0.83
930	213.458	577.407	19.32	0.075	0.68	20.51	0.025	0.94
932	922.226	506.184	19.33	0.019	0.70	21.13	0.043	0.87
934	356.748	488.873	19.33	0.281	0.70	20.09	0.021	0.94
936	173.500	110.132	19.34	0.022	0.76	20.56	0.025	0.93
941	506.749	289.251	19.35	0.026	0.80	20.37	0.022	0.90
942	491.330	714.433	19.35	0.111	0.79	20.14	0.031	0.95
943	656.450	356.202	19.35	0.035	0.72	20.51	0.037	0.81
948	108.795	279.011	19.38	0.032	0.76	20.06	0.016	0.96
949	384.557	751.165	19.38	0.063	0.67	20.33	0.021	0.92
951	198.807	574.479	19.38	0.094	0.67	20.22	0.019	0.94
954	107.940	494.395	19.39	0.107	0.66	20.14	0.017	0.94
961	808.787	613.963	19.42	0.082	0.74	20.96	0.037	0.93
964	198.040	927.654	19.42	0.024	0.72	20.55	0.025	0.93
966	617.593	563.554	19.43	0.190	0.81	20.46	0.034	0.83
967	194.427	525.399	19.43	0.128	0.73	21.08	0.042	0.82
969	274.342	424.578	19.44	0.274	0.79	20.50	0.029	0.91
971	388.065	835.217	19.44	0.126	0.67	20.33	0.021	0.93
974	284.683	621.908	19.45	0.040	0.70	21.43	0.058	0.82
977	726.461	609.482	19.46	0.083	0.66	20.96	0.038	0.83
981	575.312	549.397	19.48	0.331	0.73	20.06	0.066	0.87
983	641.777	491.357	19.49	0.203	0.71	20.45	0.034	0.89

IDk	Xpix	Ypix	Kmag	Δ Kmag	CorreK	Jmag	Δ Jmag	CorreJ
985	347.775	934.742	19.50	0.319	0.66	21.16	0.044	0.84
986	197.677	292.317	19.50	0.089	0.82	21.07	0.084	0.81
989	573.421	456.259	19.52	0.319	0.70	21.27	0.061	0.84
990	501.700	744.422	19.52	0.094	0.66	21.55	0.076	0.89
995	227.408	768.774	19.52	0.025	0.70	20.80	0.032	0.84
997	416.251	797.015	19.54	0.038	0.71	20.62	0.030	0.91
999	393.959	760.545	19.55	0.072	0.81	20.69	0.029	0.82
1000	514.213	190.091	19.55	0.298	0.72	21.13	0.043	0.91
1002	567.918	588.901	19.57	0.357	0.83	20.41	0.052	0.88
1009	293.953	756.555	19.61	0.032	0.70	21.16	0.046	0.84
1012	724.356	620.803	19.62	0.092	0.69	21.46	0.060	0.85
1016	637.568	221.259	19.65	0.227	0.70	21.40	0.055	0.85
1019	494.255	632.680	19.67	0.284	0.67	20.24	0.026	0.93
1020	327.070	967.964	19.67	0.325	0.71	20.60	0.026	0.94
1021	230.979	423.033	19.67	0.211	0.69	21.60	0.066	0.82
1027	717.654	426.026	19.71	0.064	0.66	21.62	0.066	0.81
1030	467.653	365.991	19.73	0.286	0.75	20.88	0.071	0.85
1033	321.526	934.851	19.76	0.262	0.71	20.85	0.033	0.91
1034	104.545	444.059	19.76	0.113	0.72	20.03	0.021	0.92
1036	337.944	367.487	19.77	0.211	0.69	21.18	0.045	0.83
1038	266.861	887.410	19.81	0.040	0.72	20.70	0.029	0.88
1039	95.240	959.233	19.81	0.145	0.67	21.99	0.092	0.81

Appendix C

Papers

L E

VLT/SPHERE deep insight of NGC 3603's core: Segregation or confusion?*

Z. Khorrani¹, T. Lanz¹, F. Vakili¹, E. Lagadec¹, M. Langlois^{2,3}, W. Brandner⁴, O. Chesneau¹, M. R. Meyer⁵,
M. Carillet¹, L. Abe¹, D. Mouillet⁶, J. L. Beuzit⁶, A. Boccaletti⁷, C. Perrot⁷, C. Thalmann⁵, H.-M. Schmid⁵,
A. Pavlov⁴, A. Costille³, K. Dohlen³, D. Le Mignant³, C. Petit⁸, and J. F. Sauvage⁸

¹ Laboratoire Lagrange, Université Côte d'Azur, Observatoire de la Côte d'Azur, CNRS, 06304 Nice, France
e-mail: zeinab.khorrani@oca.eu

² Univ. Lyon 1, ENS de Lyon, CNRS, CRAL UMR 5574, 69230 Saint-Genis-Laval, France

³ Aix-Marseille Université, CNRS, LAM – Laboratoire d'Astrophysique de Marseille, UMR 7326, 13388 Marseille, France

⁴ Max-Planck-Institut für Astronomie, Königstuhl 17, 69117 Heidelberg, Germany

⁵ Institute for Astronomy, ETH Zurich, Wolfgang-Pauli-Strasse 27, 8093 Zurich, Switzerland

⁶ Université Grenoble Alpes, CNRS, IPAG, 38000 Grenoble, France

⁷ LESIA, Observatoire de Paris, CNRS, Université Paris 7, Université Paris 6, 5 place Jules Janssen, 92190 Meudon, France

⁸ ONERA – Optics Department, 29 avenue de la Division Leclerc, 92322 Chatillon Cedex, France

Received 11 January 2016 / Accepted 25 February 2016

ABSTRACT

We present new near-infrared photometric measurements of the core of the young massive cluster NGC 3603 obtained with extreme adaptive optics. The data were obtained with the SPHERE instrument mounted on ESO's Very Large Telescope, and cover three fields in the core of this cluster. We applied a correction for the effect of extinction to our data obtained in the *J* and *K* broadband filters and estimated the mass of detected sources inside the field of view of SPHERE/IRDIS, which is $13.5'' \times 13.5''$. We derived the mass function (MF) slope for each spectral band and field. The MF slope in the core is unusual compared to previous results based on HST and VLT observations. The average slope in the core is estimated as -1.06 ± 0.26 for the main sequence stars with $3.5 M_{\odot} < M < 120 M_{\odot}$. Thanks to the SPHERE extreme adaptive optics, 814 low-mass stars were detected to estimate the MF slope for the pre-main sequence stars with $0.6 M_{\odot} < M < 3.5 M_{\odot}$, $\Gamma = -0.54 \pm 0.11$ in the *K*-band images in two fields in the core of the cluster. For the first time, we derive the MF of the very core of the NGC 3603 young cluster for masses in the range $0.6\text{--}120 M_{\odot}$. Previous studies were either limited by crowding, lack of dynamic range, or a combination of both.

Key words. open clusters and associations: individual: NGC 3603 – stars: luminosity function, mass function – stars: massive – instrumentation: adaptive optics

1. Introduction

Among Galactic spiral arm clusters, the NGC 3603 young cluster, located in its namesake giant HII region (Kennicutt 1984), is the most compact and youngest cluster with an age of 1 Myr (Brandl et al. 1999; Stolte et al. 2004; Sung & Bessell 2004) and a central density of $6 \times 10^4 M_{\odot} \text{pc}^{-3}$ (Harayama et al. 2008). The cluster is known to contain three massive and luminous central stars with spectral types as early as O2V (Walborn et al. 2002; Moffat et al. 2004), and up to 50 O-type stars in total (Drissen et al. 1995). The most massive stars exhibit both characteristics of WN6 stars and Balmer absorption lines (Drissen et al. 1995), suggesting that they are actually core hydrogen burning rather than evolved stars (Conti et al. 1995; de Koter et al. 1997). Two of these three Wolf-Rayet (WR) stars are very close binaries (Schnurr et al. 2008). The total mass of the cluster is estimated as $10^4 M_{\odot}$ (Harayama et al. 2008), with an upper limit to the dynamical mass of $17\,600 \pm 3800 M_{\odot}$ (Rochau et al. 2010). NGC 3603 provides a unique opportunity to study the formation of massive stars embedded in clusters at their early

stages. Studying such clusters is not generally straightforward owing to the limited angular resolution of telescopes in addition to uncertainties from existing models (Ascenso et al. 2009). Besides, extinction from the Galactic plane and the birth place of massive stars, which is immersed in dust and gas, play an important role.

All these combined effects can introduce an observational bias that hampers differentiating models of massive star and cluster formation: i.e., singular collapse of a rotating molecular cloud core with subsequent fragmentation in a flattened disk or competitive accretion, or, for example, external triggering by cloud-cloud collision (ref., e.g., Johnston et al. 2014). To test these models, high angular resolution observation in the infrared are the best strategy as they minimize the effects of source confusion and spatial extinction variations.

In this context, the extreme adaptive optics (XAO) of the new instrument SPHERE (Beuzit et al. 2008) on the Very Large Telescope (VLT), enabled us to observe deeper in the core of NGC 3603 in the near-infrared *J*- and *K*-bands to better probe the massive star cluster at a high resolution in the range of 20–40 mas resolution, which is comparable to the *Hubble* Space Telescope (HST) in the visible.

* Based on data collected at the European Southern Observatory, Chile (guaranteed time observation 095.D-0309(A) and 095.D-0309(E))

Table 1. Exposure time log and faintest stars ($S/N > 4.2$) of VLT/SPHERE observations.

Field (Filter)	Single/total exposure [s]	λ_{cen} [nm]	Δ_{J} [nm]	mag_{max}	Mass [M_{\odot}]	Δ_{mag}
F0 (<i>J</i>)	4.0/1600	1245	240	18.7	0.66	10.6
F0 (<i>K</i>)	0.83/335.0	2182	300	16.4	1.08	9.5
F1 (<i>J</i>)	2.0/300.0	1245	240	18.9	0.57	9.0
F1 (<i>K</i>)	0.83/251.3	2182	300	18.1	0.29	9.8
F2 (<i>J</i>)	2.0/320.0	1245	240	18.9	0.58	9.3
F2 (<i>K</i>)	0.83/269.0	2182	300	18.8	0.14	9.6

Notes. Δ_{mag} is the difference between the maximum and minimum magnitudes in F0, F1, and F2 fields.

2. Data and photometry

We obtained data via guaranteed time observation (GTO) runs to image NGC 3603 using the dual mode of IRDIS (Langlois et al. 2014), enabling simultaneous observations in two spectral bands on the VLT. The observations were performed in two epochs in 2015 (March and June), with high dynamic and spatial resolution imaging of three regions, each with a field of view (FoV) of $13.5'' \times 13.5''$, one centered on the core of the cluster (F0) and two regions (F1 and F2) to cover the radial extent of the cluster (Fig. 1, top). To facilitate homogeneous photometric calibrations, F1 and F2 partially overlap with F0. The data consist of 400, 300, and 320 frames of 0.8s exposures in the IRDIS broadband *K* filter (IRDIS/BB-K) for F0, F1, and F2, respectively, and 400, 150, and 160 frames of 4.0, 2.0, and 2.0s exposures in IRDIS broadband *J* (IRDIS/BB-J), respectively, during the two observing epochs. Neutral density (ND) filters were used for the IRDIS/BB-J data to avoid saturating the brightest stars. The average airmass during these observations was 1.25–1.26. A log of the observations is presented in Table 1.

We used the SPHERE pipeline package¹, for correcting dark, flat, distortion, and bad pixels. As SPHERE filters in BB-J and BB-K are similar to ESO's Nasmyth Adaptive Optics System Near-Infrared Imager and Spectrograph (NACO), we corrected the photometric zero-points of SPHERE by comparing them to the magnitudes of spectroscopically known stars (preferentially isolated sources) in NACO (Harayama et al. 2008) *J* and *K* filters.

For the photometry, we used the STARFINDER package implemented in IDL (Diolaiti et al. 2000) to derive the local point spread function (PSF) to detect stellar objects, while estimating instrumental magnitudes, i.e., before the photometric zero-point corrections. For this, each field is divided into subregions to extract the empirical local PSFs from isolated sources in the image itself. Local PSFs are then used to extract the flux of the sources to compensate for the local distortion effect. This is particularly suitable for AO-assisted imaging data where one can face locally distorted PSFs that hamper photometric measurements along different parts of the IRDIS FoV.

Consequently, 410 (290), 149 (364), and 445 (682) sources were detected in the *J*- and *K*-bands in F0, F1, and F2, respectively, by limiting them to a minimum correlation of 0.8 with the PSF. We also put a threshold limit of one standard deviation of sky brightness. Table 2 gives the details of the total number of detected sources in each field for a given filter.

The high Strehl ratio, and the resulting high dynamic range close to bright stars, enabled us to detect stellar sources that are 10.6 and 9.8 mag fainter than the brightest sources in *J*- and

¹ http://www.mpia.de/SPHERE/sphere-web/nightly_builds-page.html

Table 2. Number of detected stars (N_J and N_K in *J* and *K*-bands) and MF slopes (Γ_J and Γ_K in *J* and *K*-bands) using Eq. (1), at 1.5 Myr in three F0, F1, and F2 fields of NGC 3603 from SPHERE/IRDIS.

	F0	N_K	Γ_K	N_J	Γ_J
<i>All</i>	288		-1.09 ± 0.11	408	-1.07 ± 0.08
<i>All-B</i>	287		-0.98 ± 0.12	407	-0.99 ± 0.08
<i>All-WRs</i>	283		-0.85 ± 0.06	403	-0.98 ± 0.09
	F1+F2	N_K	Γ_K	N_J	Γ_J
Total	1003		-0.82 ± 0.08	561	-0.94 ± 0.10
MS	189		-1.12 ± 0.14	200	-1.20 ± 0.11
PMS	814		-0.54 ± 0.11	361	-

K-bands, respectively. Sources with *K* magnitude of 18.8 and *J* magnitude of 18.9 could be detected in the core of NGC 3603. Our test experiments for completeness correction (500 artificial star per flux) suggest that we should reach a completeness level $\geq 80\%$ for stars brighter than 17.5 mag in F1 and F2 in both *J*- and *K*-bands. The quality (signal-to-noise ratio – S/N) of data in F0 in *K*-band (in March 2015) was not as good as in F1 and F2 in the second run (June 2015), thus the dynamic range is lower. In F0, stars brighter than 15.3 in *K*-band and 16.5 in *J*-band have a completeness level of $\geq 80\%$. Table 1 gives the faintest magnitudes obtained in the different fields F0, F1, and F2 by SPHERE within the exposure time limits of the run.

3. Extinction and CMD

In order to correct for extinction, 31 O stars on or close to the main sequence (class V) were selected from Harayama et al. (2008). These stars are encircled in green in the top panel of Fig. 1. To estimate their intrinsic magnitude, their T_{eff} were estimated from Table 4 of Martins et al. (2005) and their $\log g$ as a function of age (1.5 Myr) according to the PARSEC² stellar evolution models (Bressan et al. 2012), adopting Galactic metallicity. We assumed a distance of 6 kpc (Sect. 4) for these O stars.

We derived the color excess for selected O stars in the two IRDIS-BB *J* and *K* filters at the distance of 6 kpc. We adopted the maximum weighted value for $E(J - K)$, which is 0.76 ($A_V = 4.5$). This value results in A_J and A_K as 1.269 and 0.504, respectively, (from Rieke & Lebofsky 1985). We found 239, 118, and 191 sources detected in both *J* and *K* data in F0, F1, and F2, respectively. The color magnitude diagrams (CMDs) for these different fields are shown in Fig. 2.

4. Mass functions (MF)

We used the stellar evolution tracks from PARSEC mentioned above to estimate stellar masses at the age of 1.5 Myr. The distance of the cluster was taken as 6 kpc, which fits well with the observed CMD, isochrone, and extinction, and is also in good agreement with Stolte et al. (2004), De Pree et al. (1999), and Harayama et al. (2008).

Using grids of stellar evolutionary tracks and extinction for each filter, we can estimate the stellar masses separately from the photometry in each filter. The slope of the MF Γ can be estimated from Eq. (1), where M is the stellar mass and N is the number of stars in the logarithmic mass interval $\log_{10}(M)$ to $\log_{10}(M) + 0.2 \log_{10}(M)$. We used a double size bin at the pre-main sequence (PMS) and main sequence (MS) transition, around $4 M_{\odot}$, to smooth out the degeneracy (same as Harayama et al. 2008). We used an implementation of the nonlinear

² <http://stev.oapd.inaf.it/cgi-bin/cmd>

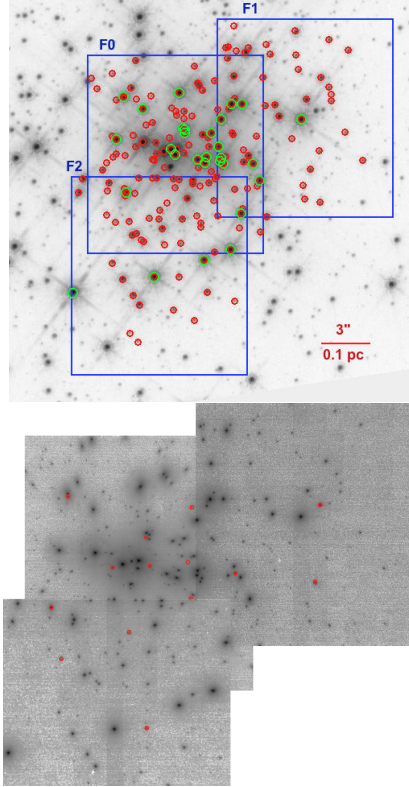


Fig. 1. *Top:* HST/WFPC2-PC/F814W core of NGC 3603; blue squares depict the three fields observed with SPHERE-IRDIS. Green circles refer to the known O-type stars from Harayama et al. (2008). Red circles show the stars in Harayama et al. (2008) catalog, which we used for calibrating zero-points in different fields. There are 113, 45, and 51 stars common between Harayama et al. (2008) in the SPHERE F0, F1, and F2 fields. *Bottom:* sources with $E(J - K) > 1.8$ in F0, F1, and F2 shown in red circles. The image is a combination of all three fields in IRDIS/B-J.

least-squares (NLLS) Marquardt-Levenberg algorithm to fit the MF,

$$\log(N) = \Gamma \log\left(\frac{M}{M_{\odot}}\right) + \text{cst.} \quad (1)$$

MFs for the two IRDIS BB-J and BB-K filters are shown in Fig. 3 for the core (F0) and in Fig. 4 for F1 and F2. One can compare the MF in the very core of the cluster (F0) with the next radial bin (F1 and F2) to check the radial variation of MF. The two latter were observed with similar exposure times and very close conditions as both fields were recorded within one hour slot of a SPHERE/VLT run on 2015-06-07. Also, minimum and maximum magnitudes in both fields are very similar especially in the K -band. All these conditions result in similar mass range of detected sources in J and K . Thus we could plot the MF for F1 and F2 together, where 586 sources are detected with masses less than $1 M_{\odot}$ (fainter than 16.5 mag) in the K -band.

In F0, we were able to reach $0.66 M_{\odot}$ ($J = 18.7$) in the J -band and $1.08 M_{\odot}$ ($K = 16.4$) in the K -band. Figure 3 depicts

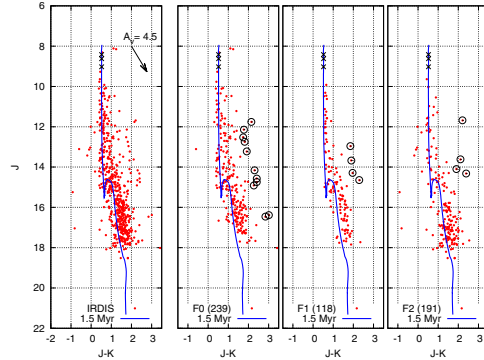


Fig. 2. CMD of the core of NGC 3603 in IRDIS J - and K -band for the whole FoV (*left*) followed to the right for the three fields F0, F1, and F2. Black circles show the K -excess stars. Three black crosses represent stellar models with initial masses of 100, 120, and $150 M_{\odot}$. The black arrow signifies the effect of extinction, $A_V = 4.5$.

the MF in F0. Three WR stars (A1, B, C) are located in this region where two of them (A1 and C) were identified as spectroscopic binaries by Schnurr et al. (2008). The MF can be treated in three possible ways (Table 2): 1) considering all WR stars: two as binaries with masses estimated from Schnurr et al. (2008) and one (B) as a single star (*All*); 2) considering just two WR stars as two binary systems (*All-B*); and 3) excluding these three WR stars (*All-WRs*).

Figure 4 depicts the MF for the next radial bin from the core of NGC 3603 (F1 and F2). The mass range covered in K -band starts from $0.14 M_{\odot}$, ending at $69 M_{\odot}$. More than 800 sources with a mass smaller than $4 M_{\odot}$ are detected.

The change of the MF slope for the MS and PMS stars occurs around $4 M_{\odot}$. We also fitted a separate line on MF (dash-dotted line in Fig. 4) for the low-mass PMS stars. The MF in the low-mass part is corrected for the number of detected sources above an incompleteness level of 80% (black bins in the low-mass part in Figs. 3 and 4).

Table 2 lists the derived MF slopes in F0, F1, and F2 regions and derived slopes for MS/PMS stars. MS is a common mass range in J and K and in F0 and F1+F2 with an incompleteness level of 100%. The MF slopes are consistent in the J -band and K -band and also in the different regions, for the main sequence stars and for the whole mass range.

The MF slopes for the whole mass range is flatter than the main sequence part. The MF slopes even for the massive stars (main sequence) are flatter than Salpeter, $\Gamma_{\text{Salpeter}} = -1.35$ (Salpeter 1955) and Kroupa, $\Gamma_{\text{Kroupa}} = -1.3$ (Kroupa 2001). The average value agrees with those found in the outer regions of NGC 3603 according to previous works. For PMS stars, the MF slope is flatter than for the whole mass range and for the main sequence.

If we assume that binary properties like binary fraction and mass-ratio distribution do not change strongly with the mass of the primary stars, then the deduced MF slope should be very similar to the MF slope of the primary stars.

We could detect 11, 4, and 4 K -excess sources with an $E(J - K)$ that is higher than 1.8 (for MS) and 2.0 (for PMS), in F0, F1, and F2, respectively, corresponding to 14 sources in total (black circles in Fig. 2 and red circles in the bottom panels of Fig. 1). For these stars, the mass estimated in K is higher than in J because of their K -excess. Twelve of these stars are on

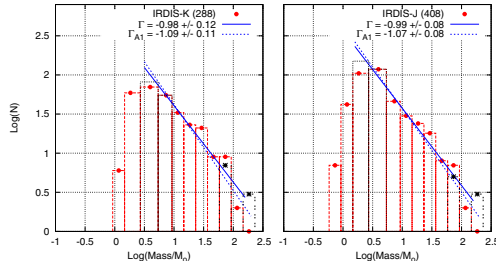


Fig. 3. MFs derived for IRDIS data in BB-J (*right*) and BB-K (*left*) in F0 (shown in Fig. 1, top). Last three red bins represent the MF considering the A1 and C as binaries and B as a single source. The last three black stars represent the MF if the WR stars are considered single objects, which is the case for the photometry analysis.

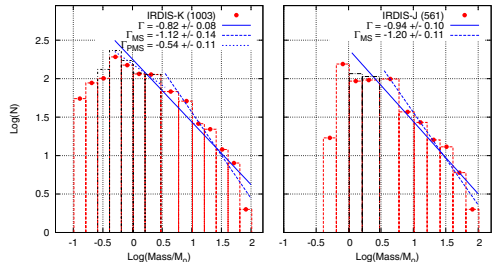


Fig. 4. MFs derived for IRDIS data in BB-J (*right*) and BB-K (*left*) in F1 and F2 together. F1 and F2 are shown in Fig. 1, top.

the sequence parallel to the MS ($M > 4 M_{\odot}$). In this case, the MF slopes for the main sequence part in the *J*-band should be more reliable than in the *K*-band.

5. Discussion and conclusion

NGC 3603 has been observed with various instruments and the slope of its MF has been calculated in previous works (Table 3). These works reach conclusions on the general trend of decreasing MF slopes in the core as the signature of mass segregation. The slopes of the MF in different filters (Table 2) in the core of NGC 3603 is steeper than the previous works and does not show a radial dependence in the observed fields. The slope value for the main sequence stars and for the whole mass range is consistent in all observed regions of the core of the cluster.

Shape of MF at the massive end, can be used as an observational test that may be able to settle the question of which mechanism (accretion or collision) is a dominant route for the formation of the most massive stars (Krumholz 2015). According to the accretion models, as the massive stars form by the same accretion processes that produce low-mass stars (normal star formation), the high end of the stellar MF should be continuous and does not depend radically on the environment (Krumholz 2015). On the other hand, collisional formation predicts a large gap in the stellar MF, separating the bulk of the accretion-formed stellar population from the few collisionally formed stars (Baumgardt & Klessen 2011; Moeckel & Clarke 2011). This feature should only appear in the most massive and densest clusters. Figure 3 shows this signature in the core (F0), but we know that the last bin corresponds to the three WR stars in which two of them have been found to be multiple objects and not single stars (Schnurr et al. 2008). Therefore, collisional formation of very

Table 3. Slopes of the MF derived for NGC 3603 in earlier works.

Γ	Condition	Reference
-0.5 ± 0.1	$r < 6''$, $(1.6-100) M_{\odot}$	Sung & Bessell (2004)
-0.31	$0-5''$, $(0.4-20) M_{\odot}$	Harayama et al. (2008)
-0.26	$0-5''$, $(6.3-100) M_{\odot}$	Pang et al. (2013)

massive objects seems unlikely at least for the NGC 3603 cluster. Accretion models also predict that massive stars are likely to have low-mass and high-mass companions (Kratter & Matzner 2006; Kratter et al. 2008, 2010; Krumholz et al. 2012), but the collisionally formed stars lack low-mass companions, which provokes segregation.

This study shows no signature of mass segregation in the core of NGC 3603, first, because the MF slope in its very core is not flatter than the next radial bin. Second, both slopes are similar to the MF values found in previous works for the outer regions (references in Table 3). Therefore, it appears that non-segregated clusters with a smooth MF agree better with accretion models for massive star formation. Our SPHERE results demonstrate that, by improved photometric dynamic range and spatial resolution from XAO, we can overcome the effect of confusion that in the past has led to the conclusion of observational segregation (see also Ascenso et al. 2009) as far as NGC 3603 is concerned.

Acknowledgements. Z.K. is supported by the Erasmus Mundus Joint Doctorate Program by Grant Number 2012-1710 from the EACEA of the European Commission. We warmly thank Alain Chelli for useful discussions. We thank the anonymous referee for constructive comments, which improved the paper.

References

- Ascenso, J., Alves, J., & Lago, M. T. V. T. 2009, *A&A*, 495, 147
 Baumgardt, H., & Klessen, R. S., 2011, *MNRAS*, 413, 1810
 Beuzit, J.-L., Feldt, M., Dohlen, K., et al. 2008, *Proc. SPIE*, 7014, 701418
 Brandl, B., Sams, B. J., Bertoldi, F., et al. 1996, *ApJ*, 466, 254
 Brandl, B., Brandner, W., Eisenhauer, F., et al. 1999, *A&A*, 352, L69
 Bressan, A., Marigo, P., Girardi, L., et al. 2012, *MNRAS*, 427, 127
 Conti, P. S., Hanson, M. M., Morris, P. W., et al. 1995, *ApJ*, 445, L35
 de Koter, A., Heap, S. R., & Hubeny, I. 1997, *ApJ*, 477, 792
 De Pree, C. G., Nysewander, M. C., & Goss, W. M. 1999, *AJ*, 117, 2902
 Diolaiti, E., Bendinelli, O., Bonaccini, D., et al. 2000, *A&AS*, 147, 335
 Drissen, L., Moffat, A. F. J., Walborn, N. R., & Shara, M. M. 1995, *AJ*, 110, 2235
 Eisenhauer, F., Quirrenbach, A., Zinnecker, H., & Genzel, R. 1998, *ApJ*, 498, 278
 Harayama, Y., Eisenhauer, F., & Martins, F. 2008, *ApJ*, 675, 1319
 Johnston, K. G., Beuther, H., Linz, H., et al. 2014, *A&A*, 568, A56
 Kennicutt, R. C., Jr. 1984, *ApJ*, 287, 116
 Kratter, K. M., & Matzner, C. D. 2006, *MNRAS*, 373, 1563
 Kratter, K. M., Matzner, C. D., & Krumholz, M. R. 2008, *ApJ*, 681, 375
 Kratter, K. M., Matzner, C. D., Krumholz, M. R., & Klein, R. I. 2010, *ApJ*, 708, 1585
 Kroupa, P. 2001, *MNRAS*, 322, 231
 Krumholz, M. R. 2015, *Very Massive Stars in the Local Universe*, 412, 43
 Krumholz, M. R., Klein, R. I., & McKee, C. F. 2012, *ApJ*, 754, 71
 Langlois, M., Vigan, A., Dohlen, K., et al. 2014, *SPIE*, 9147, 91479
 Lejeune T., & Schaerer D. 2001, *A&A*, 366, 538
 Malumuth, E. M., & Heap, S. R. 1994, *AJ*, 107, 1054
 Martins, F., Schaerer, D., & Hillier, D. J. 2005, *A&A*, 436, 1049
 Massey, P. 2003, *ARA&A*, 41, 15
 Massey, P., & Hunter Deidre, A. 1998, *ApJ*, 493, 180
 Moeckel, N., & Clarke, C. J. 2011, *MNRAS*, 410, 2799
 Moffat, A. F. J., Poitras, V., Marchenko, S. V., et al. 2004, *AJ*, 128, 2854
 Pang, X., Grebel, E. K., Allison, R. J., Goodwin S. P., et al. 2013, *ApJ*, 764, 9
 Rieke, G. H., & Lebofsky, M. J. 1985, *ApJ*, 288, 618
 Rochau, B., Brandner, W., Stolte, A., et al. 2010, *ApJ*, 716, L90
 Salpeter, E. E. 1955, *ApJ*, 121
 Schnurr, O., Casoli, J., Chene, A.-N., et al. 2008, *MNRAS*, 389, L38
 Stolte, A., Brandner, W., Brandl, B., et al. 2004, *AJ*, 128, 765
 Sung, H., & Bessell, M. S. 2004, *AJ*, 127, 1014
 Walborn, N. R., Howarth, I. D., Lennon, D. J., et al. 2002, *AJ*, 123, 2754

THE MASSIVE STARS NURSERY R136

Zeinab Khorrami¹, Farrokh Vakili¹, Olivier Chesneau² and Thierry Lanz¹

Abstract. As most stars are born in a clustered mode, young massive star clusters are the best places to find and study the formation and evolution of massive stars. R136 is one of the most massive nearby clusters in the LMC. It contains at least 72 known O and Wolf-Rayet stars. These young stars are usually embedded in dust and gas so that correcting the local extinction plays an important role to estimate their mass from their luminosity. The extinction is derived for 26 O stars in different HST filters using TLUSTY model atmospheres of O stars. We derived the stellar masses, and hence the Mass Function (MF), using HST multi-color photometry. In parallel, we simulated series of R136-like clusters using the NBODY6 code to test the segregation scenario for R136. We could check whether massive stars are preferentially formed in the cluster core or formed homogeneously. By comparing the surface brightness profiles (SBP) of simulated clusters mimicking R136 with HST data, we could determine which scenario best represents R136. We present here a method that we used to connect the results of the NBODY6 simulations to R136 HST imaging data. The results of these studies bring a new insight to the understanding of R136 and similar clusters, pending future VLT and E-ELT high-contrast imaging observations at the diffraction limit at visible and IR wavelengths.

1 Introduction

R136 is a very massive ($10^5 M_{\odot}$) young ($2 \pm 1 Myr$) star cluster in LMC. This cluster provides a unique opportunity to study the formation and evolution of massive stars and also massive star clusters at their early stages of life. In this work, we present the results of the HST photometry on the core of this cluster (Section 2). In Section 3 we explain the results from the simulation of clusters similar to R136 using NBODY6 code. We also introduce a method that we devised for converting the results from the NBODY6 simulation to be compared to HST imaging data. Combining observations and simulations, we may then conclude

¹ Laboratoire Lagrange, Université Côte d'Azur, Observatoire de la Côte d'Azur, France;
e-mail: zeinab.khorrami@oca.eu

² Olivier Chesneau passed away before being able to see the final results of this work

whether the initially segregated or the non-segregated clusters could better explain the present-day structure of R136.

2 Observation

We used the highest resolution deep imaging data of R136 obtained by the HST¹, extracted from the STScI MAST archive. Observations of R136 were carried out on 1994-09-25 (PI: Westphal) using the WFPC2-PC detector. They are a combination of shallow, intermediate and long exposures, ranging from 3–5 s to 80–120 s in the F555W and F814W filters.

For the image analysis we used the STARFINDER package implemented in IDL Diolaiti et al. (2000) that is well suited for the crowded field photometry. To extract sources from the data, we used precomputed Point Spread Function (PSF) based on analytical models with a detector-dependent FWHM instead of choosing empirical PSFs extracted from sources in the image itself that is more suitable for AO-assisted imaging. We found 2509 and 2660 sources in the F555W and F814W images respectively. The Field of View (FoV) of the images (after applying mask to avoid boarder noise) is about $32.5'' \times 32.5''$.

To estimate the stellar masses, we need their intrinsic magnitudes in HST filters. For this aim we created Bolometric Correction (BC) tables from the combination of model atmosphere SEDs and stellar evolution models. From these tables we derived the intrinsic magnitude of different stars in HST/WFPC2 filters leading to an estimate of their masses. For the stellar evolution models, we used Geneva isochrones² Lejeune & Schaerer (2001) at 1.0, 1.5 and 2 Myr for LMC metallicity. We used TLUSTY Hubeny & Lanz (1995), Lanz & Hubeny (2003), Lanz & Hubeny (2007) model atmospheres for O and B-type stars and Kurucz Castelli et al. (1997) for the other stellar types. Note that the metallicity, T_{eff} and $\log g$ are the common entries between the SEDs and the stellar evolution models.

To correct the extinction in the two HST filters, we selected 26 O-type stars classified by Massey & Hunter (1998). We then adopted effective temperatures from the spectral type– T_{eff} relation in Table 1 of Simon-Diaz et al. (2014). Surface gravities, $\log g$, (hence luminosities) are assigned using isochrones (1.0, 1.5 and 2 Myr) in the Geneva stellar evolution models. Using BC tables, we derived the extinction and color excess of two HST filters (F814W, F555W) at 1, 1.5 and 2 Myr. We adopted a LMC distance of 48.4 kpc that agrees well with Selman et al. (1999) and Gieren et al. (1998).

Finally we plotted the mass function and its slopes in F814W and F555W data using different evolutionary models (at 1, 1.5 and 2 Myr). Full results are presented in a recent paper submitted by Khorrami et al. (2015)

¹Based on observations made with the NASA/ESA Hubble Space Telescope, obtained from the data archive at the Space Telescope Institute. STScI is operated by the association of Universities for Research in Astronomy, Inc. under the NASA contract NAS 5-26555.

²<http://webast.ast.obs-mip.fr/equipe/stellar/>

3 Model

In parallel to the observational study of R136, we carried out a grid of NBODY6 simulations³ (Aarseth *et al.* (2003)) using the initial parameters (Kupper *et al.* (2011)) adequate for R136 (total cluster mass of $1.0 \times 10^5 M_{\odot}$ with half-mass radius of 0.8 pc and LMC metallicity). These simulated clusters differ in the degree of mass segregation, in binary fraction and in the evolution of the member stars during their dynamical evolution in the clusters. The simulation time was limited to 4 Myr with 0.1 Myr time-steps.

We found that in all cases segregated clusters expand more than non-segregated clusters. Clusters with stellar evolution expand significantly around 3 Myr because of the evolution of very massive stars. On the other hand, segregated clusters lose more binaries than non-segregated ones. Almost half of the low-mass binaries dissolve within 1 Myr. Clusters with stellar evolution lose their massive binaries according since their massive components evolve themselves. In all cases, binaries keep the memory of initial eccentricities distribution during the first 4 Myr. During this period, only the massive binaries keep the memory of initial period distribution.

4 Synthetic Images

Unlike to the common practice of comparing the results of NBODY6 simulations directly to observation, we preferred to create synthetic images from the output of NBODY6 simulations and compare these simulated images with the HST data.

We produced the simulated imaging data with a spatial resolution similar to R136 HST/WFPC2 data. We developed a program that reads the information of stars from the simulations as an input and creates the synthetic scenes that mimic HST/WFPC2 resolution in different HST filters. We used the BC-tables (see Sect. 2) to compute the flux of stars in the F814W and F555W filters at 2 Myr. The simulated images are 800x800 pixels scenes corresponding to a field of $32.5'' \times 32.5''$ on the detector where a star with a given flux falls on the detector with a Gaussian distribution as the PSF profile. Fig. 1 depicts some synthetic images generated by our program.

One question remains: what can be the best criterion to select that closest simulated image to R136?

One useful way is to compare the Surface Brightness Profile (SBP) the Half-Light radius (R_{hl}) of R136 to those of synthetic scenes. It is also possible to compare the Mass Function (MF) slopes of R136 with the MF slopes from simulations. The MF is not directly derived from simulations. The mass of stars in the FoV is estimated from the photometry of the synthetic scenes and we used the BC-tables for finding the mass of each detected star in a given field.

³<http://www.ast.cam.ac.uk/~sverre/web/pages/nbody.htm>

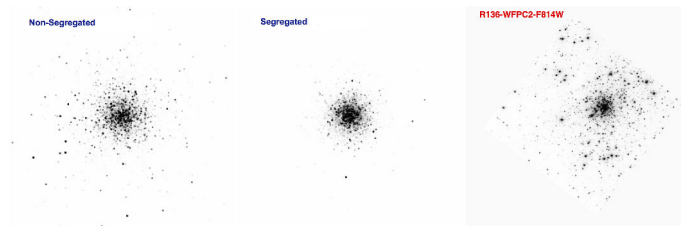


Fig. 1. Synthetic images from simulation of clusters with the mass range of $(0.2-150)M_{\odot}$ and 0% initial binaries at 2 Myr. *Left:* Non-segregated; *Middle:* Segregated; *Right:* HST/WFPC2-PC image of R136 in F814W filter.

5 Conclusion

We analyzed the highest resolution with longest exposures imaging HST data on R136. We estimate the mass of extracted sources in F814W and F555W filter using our BC-tables that are a combination of SEDs from NLTE model atmospheres and Geneva stellar evolution models. Considering standard and high mass-loss models at three different ages (1, 1.5 and 2 Myr) we found no signature of mass segregation comparing the MF slopes locally ($r < 4.5''$, $4.5'' < r < 9''$, $9'' < r < 13.5''$). After creating synthetic images from the output of NBODY6 simulations of R136, we compared the synthesized images (with HST/WFPC2/F814W resolution) to HST data using three different methods. The results show that simulated images from the clusters without no initial mass segregation resemble the most to R136 as observed by HST/WFPC2.

References

- Aarseth, S. J. 2003, *Gravitational N-Body Simulations* (Cambridge Univ. Press)
- Castelli, F., Gratton, R. G., Kurucz, R. L. 1997, *A&A*, 318, 841
- Kupper, A. H. W., Maschberger, T., Baumgardt, H., Kroupa, 2011, *MNRAS*, 417, 2300
- Diolaiti, E., Bendinelli, O., Bonaccini, D., et al. 2000, *A&AS*, 147, 335
- Gieren, W. P., Fouqué, P., Gomez, M. 1998, *ApJ* 496, 17
- Hubeny I., Lanz T. 1995, *ApJ*, 439, 875
- Khorrani Z., Lanz T., Vakili F. 2015, *MNRAS* (submitted)
- Lejeune T., Schaerer D. 2001, *A&A*, 366, 538
- Lanz T., Hubeny I. 2003, *ApJS*, 146, 417
- Lanz T., Hubeny I. 2007, *ApJS*, 169, 83
- Massey P., Hunter D. A. 1998, *ApJ*, 493, 180
- Selman, F., Melnick, J., Bosch, G., Terlevich, R., 1999, *A&A*, 347, 532
- Simon-Diaz S., Herrero A., Sabin-Sanjulian C., et al. 2014, *A&A*, 570, L6

Image modeling of compact starburst clusters *: I. R136

Z. Khorrami¹, F. Vakili¹, and O. Chesneau¹

Laboratoire Lagrange, Université Côte d'Azur, Observatoire de la Côte d'Azur, CNRS,
Boulevard de l'Observatoire, F-06304 Nice, France
e-mail: zeinab.khorrami@oca.eu

ABSTRACT

Context. Continuous progress in data quality from HST, recent multiwavelength high resolution spectroscopy and high contrast imaging from ground adaptive optics on large telescopes need exhaustive modeling of R136 to better understand its nature and evolutionary stage.

Aims. To produce the best synthesized multiwavelength images of R136 we need to simulate the effect of dynamical and stellar evolution, mass segregation and binary stars fraction on the survival of young massive clusters with the initial parameters of R136 in the LMC, being set to the state of the art knowledge of this famous cluster.

Methods. We produced a series of 32 young massive clusters using the NBODY6 code. Each cluster was tracked with adequate temporal samples to correctly follow the evolution of R136 during its early stages. To compare the results of the NBODY6 simulations with observational imaging data, we created the synthetic images from the output of the code. We used the TLUSTY (for massive O and B stars) and KURUCZ (for other spectral types) model atmospheres to produce the fluxes in HST/WFPC2 filters. GENEVA isochrones grids were used to track the evolution of stars. Then, we derived the observable parameters from synthetic scenes at the spatial resolution of HST/WFPC2 in the F814W filter corresponding to 790.48nm central wavelength. Surface brightness profile of the cluster, half-light radius, mass function and neighbor radius were used as criteria to select the best representation of R136.

Results. We compared the simulations of R136 to its HST imagery in recent years by creating synthetic scenes at the same resolution, pixel scale and FOV of the HST. We applied the same photometric analysis of the images as of the real ones. Having extracted the stellar sources, we estimated the mass-function (MF), the surface brightness profile (SBP), the half-light radius and the neighbor radius, $R_{neighbor}$ across R136. The interpretation of these four criteria point to the fact that an initially non-segregated cluster scenario is more representative of R136. This result pleads for the formation of massive stars by accretion rather than by collision.

Key words. open clusters and associations: individual: R136 - Galaxies: star clusters: individual: R136 - Stars: kinematics and dynamics - Methods: numerical - Stars: imaging

arXiv:1605.07533v1 [astro-ph.SR] 24 May 2016

1. Introduction

R136 is known to be a very massive ($10^5 M_{\odot}$), young star cluster at the center of 30 Doradus star forming region in the LMC. This cluster is remarkable for its large number of massive stars formed in a relatively small volume (Hunter et al. (1995)). The total number of O3 stars in this cluster, at least 41, exceeds the total number known elsewhere in the Milky Way or Magellanic Clouds (Massey & Hunter (1998)). The WN stars in R136 are presumably core H-burning stars that mimic WR-like spectra due to their very high intrinsic luminosity. Here the individual luminosities are a factor of 10 higher than those of normal WN stars of similar type, only encountered in the Galactic cluster NGC3603, that they also resemble spectroscopically (Massey & Hunter (1998)).

R136 is outranking among other clusters in three aspects:

1) It is massive enough to produce such very massive stars as a relationship appears between the mass of a cluster and its highest-mass stars (Weidner & Kroupa (2006), Weidner et al. (2010)).

2) It is young enough for its massive members to be observed. The age of the cluster in the core is 2 ± 1 Myr (de Koter et al. (1998), Massey & Hunter (1998), Crowther et al. (2010)).

3) It is close enough to be spatially resolved. We considered the distance of 48.5 kpc for our simulations which agrees well with Selman et al. (1999) and Gieren et al. (1998).

Therefore R136 can provide clues to understand the unsolved problems of formation and evolution of massive stars and star clusters, initial distribution of stellar masses at birth (IMF), if the massive stars tend to be formed locally in the center of the cloud (mass segregation) and the binary-multiple fraction of these stars as this property can impact the rate of SNe produced soon after a few Myr evolution of such clusters.

In the present study, unlike usual studies of R136 in the literature (Banerjee & Kroupa (2013)), we have adopted a new approach to unveil the different facets of R136. Our approach is primarily motivated by the fact that presently operated 8-10m class optical telescopes and foreseen extremely large telescopes like E-ELT should deliver diffraction limited visible and IR images of crowded field clusters such as R136.

Having this in mind we created a series of simulated multi-color images of R136 from the output of the numerical dynamical model (NBODY6 code, Aarseth et al. (2003)). In this work, we present the results from the comparison of the HST/WFPC2 imaging data with synthesized images from the output of the NBODY6 simulations at the age of 2 Myr. For this we used

Send offprint requests to: zeinab.khorrami@oca.eu

* The effect of primordial mass segregation, binary fraction and stellar evolution on the evolution of massive clusters on their early life-stages

Geneva stellar evolution models (Lejeune & Schaerer (2001)) and TLUSTY (Lanz & Hubeny (2003)) or KURUCZ (Castelli et al. (1997)) model atmospheres depending on the spectral type of stars to calculate their flux in WFPC2/F814W filter at the age of 2 Myr.

The present paper is organized as followings. In Section 2 we shortly describe the NBODY6 code with special emphasis on the options and parameters that are relevant to the present work. We outline the initial conditions from which the evolution of R136 can be simulated and recorded following different tracks. Section 3 describes the results of these simulations, including their observational aspects. These results are compared to the HST observations¹ in Section 4. We introduce our method to create the synthetic images from the output of the NBODY6 code. For this comparison we define a number of criteria applied to simulated scenes from HST versus observed scenes. The relevance of the comparisons is then discussed in the Section 5. While we derive some general and preliminary results in perspective of high dynamic, high dynamic and spatially resolved images of R136 to become soon available with SPHERE and GPI in the coming years in Section 6.

2. Modeling a young massive star cluster

We used NBODY6² code which includes the individual stellar equations of motion for all members of the cluster without any simplifying assumption and approximation (Aarseth et al. (2003)). We remind that NBODY6 integrates the particle orbits using the highly accurate fourth-order Hermite scheme and deals with the diverging gravitational forces in close encounters through regularizations. In addition, this code can track the evolution of the individual stars since it employs the well-tested Single Star Evolution (SSE) and Binary Star Evolution (BSE) recipes (Hurley et al. (2000) and Hurley et al. (2002)).

The whole modeling intends to better understand the nature of R136 as it can be imaged nowadays, by taking into account the parameters and different mechanisms that drive the evolution of the cluster such as the degree of initial mass segregation, initial binary fraction, lower/upper stellar masses and stellar evolution. The initial parameters for R136 have been set to the values that represent the best this cluster according to its general properties.

2.1. Physical conditions and Mechanisms

Stellar clusters are born embedded in giant molecular clouds, with a few percent of them surviving and becoming bound clusters (Lada & Lada (2003)). It is generally admitted that the fate of the clusters must occur during the early stages of their evolution. In massive star-burst clusters, such as R136, dynamical evolution of the cluster can be affected by their significant number of massive stars. The initial distribution of these massive stars (mass segregation) in space, specially if they form in binary systems, plays an important role on the evolution of the cluster.

In order to include such effects, we simulated full segregated clusters (in which most massive stars are located deeper in the core) versus non-segregated clusters (in which the massive stars are randomly distributed in space). The result of these simulations can tell us if R136 is more similar to an initially segregated

cluster or not. A result that should put important constraints on theories of massive star formation and the cluster consequent evolution as a whole.

Following clusters without initial binaries, we also considered clusters with 30 and 60 % initial binaries which is not far from the observation as lower-limit of the spectroscopic binaries detected in the clusters of 30 Dor is found to be 45% (Bosch et al. (2009)).

Finally, by comparing the results from clusters with and without stellar evolution, one can check for the effect of stellar evolution on the binaries and the dynamical effect of the binaries themselves on the evolution of the cluster.

2.2. Initial conditions

Initial setup of the clusters made by MCLUSTER³ (Kupper et al. (2011)). The simulation time is limited to an age of 4 Myr with 0.1Myr time-steps. The total mass of the cluster is estimated (Selman & Melnick 2013) to be in the range of:

$$4.6 \times 10^4 M_{\odot} < M_{\odot} < 1.3 \times 10^5 M_{\odot}$$

Therefore we adopt the total mass of the cluster to be $1.0 \times 10^5 M_{\odot}$. Kroupa IMF with mass ranging between $0.2 M_{\odot}$ or $0.5 M_{\odot}$ to $150 M_{\odot}$. For the density profile we adopted Plummer model (Aarseth et al. (1974)). Simulated clusters are assumed isolated and not impacted by tidal fields ($t_f=0$). The initial half mass radius of the clusters is 0.8 pc. And finally the metallicity of LMC (R136) is taken as half of the solar metallicity. All the clusters are in virial equilibrium as Hnault-Brunet et al. (2012) find that R136 is in virial equilibrium.

The set-up of the numerical experimentations is as follows: half of the clusters are segregated ($s=1.0$) and the others are non-segregated ($s=0.0$). We adopted 60%, 30% and 0% percent of initial binary for the simulated clusters. There will be two groups of clusters. These groups are totally similar to each other (even the initial position and velocity of stars) but for one group stellar evolution is ON and for other group stellar evolution is OFF to see the effect of stellar evolution (Table 1).

Table 1 depicts the main characteristics of simulated clusters. The first column is the name of the cluster. The second column says if stellar evolution is ON or OFF. Column 3 corresponds to the degree of mass segregation, 0.0 means non-segregation and 1.0 means the cluster is fully segregated. The fourth column corresponds to the binary fraction. The fifth column defines the number of initial binaries. M_{min} and M_{max} are the lower and upper mass cutoff respectively of initial mass function (The canonical Kroupa, Kroupa (2001)) and N is the initial number of stars.

For the initial number of binaries we used random pairing but separate pairing for components with $m > m_{sort}$. In this way, pairing of primary and secondary components of binary stars above m_{sort} are randomly paired among each other. The motivation for this lies in extensive observational data showing that massive O, B stars are more likely to be found in an equal mass binary system (sana & Evans (2011)). m_{sort} is equal to $5 M_{\odot}$ in agreement with Kobulnicky & Fryer (2007). More detail about semi-major axis and period distribution of binaries can be found in section 3.3.

The period distribution was taken from the Kroupa (1995) period distribution since it unifies the observed Galactic field and pre-main sequence populations (see also Kroupa (2008)). But for massive binaries with $M_{primary} > m_{sort}$ we used the period distribution from Sana & Evans 2011 since the period distribution of

¹ Based on observations made with the NASA/ESA Hubble Space Telescope, obtained from the data archive at the Space Telescope Institute. STScI is operated by the association of Universities for Research in Astronomy, Inc. under the NASA contract NAS 5-26555.

² <http://www.ast.cam.ac.uk/~sverre/web/pages/nbody.htm>

³ <https://ahwkuepper.wordpress.com/mcluster/>

massive O,B spectroscopic binaries has been found to be significantly different from what is observed for low-mass binaries (sana & Evans (2011)). Massive binaries are found to have short periods in the range from 2 days to 10 years with a peak at 10 days.

Eccentricities are assumed to have a thermal distribution i.e. $f(e)=2e$ (Kroupa (2008)) and for the eccentricities of high mass binaries the distribution is taken according to sana & Evans (2011), leading to the computation of the semi-major axis (a) of each binary.

3. Results of the simulations

3.1. Expansion of the cluster

Figure 1 shows the evolution of half mass radii of 24 simulated clusters in 4 Myr. The upper plots correspond to clusters with a mass distribution in the range of $0.5M_{\odot} - 150M_{\odot}$ and bottom plots correspond to clusters with mass distribution in the range of $0.2M_{\odot} - 150M_{\odot}$. From left to right the plots depict clusters with 0%, 30% and 60% initial binaries. It can be seen in all plots that segregated clusters expand more than non-segregated ones. Stellar evolution plays also an important role in the expansion of the cluster, especially around 3-3.5 Myr on the evolution of massive stars and their high mass-loss. Clusters which contain more massive stars, present a larger expansion. This can be checked by comparing the half-mass radius evolution of clusters with pure dynamical evolution (D-clusters). At the same time, changing the binary fraction does not affect the expansion of the clusters in a significant way.

3.2. Escapers and cluster's mass loss

Clusters lose mass due to escaping stars and also if stellar evolution is ON, which drives the mass-loss of massive stars. Figure 2 shows the total mass loss of each cluster per time-step. Left plots correspond to clusters in the mass range of $0.5M_{\odot} - 150M_{\odot}$ and right plots for $0.2M_{\odot} - 150M_{\odot}$. Upper, middle and bottom plots represent clusters with 0%, 30% and 60% initial binaries.

The mass-loss of the clusters with stellar evolution (hereafter call S-clusters) is much larger than the clusters without stellar evolution (here after call D-clusters) especially around time 3.5 Myr which is a time when massive stars ($M > 60M_{\odot}$) turn out to supernova events. Clusters on the left with $M_{min} = 0.5M_{\odot}$ contain indeed more massive stars than clusters at the right (with $M_{min} = 0.2M_{\odot}$), so for these clusters mass loss is more than for clusters with $M_{min} = 0.2M_{\odot}$. that for D-clusters the number of escapers increases with the increasing binary fraction.

3.3. Binary fraction

Figure 3 shows the fraction of bound binary systems for different clusters versus time. Segregated clusters lose less binaries than non-segregated clusters. It seems that the segregated clusters are safer places for binaries to be survive. It can be explain by two main reasons: Location of the binaries and their neighbors.

In segregated clusters binaries are located deeper in the cluster and they interact mostly with the same-mass neighbors so the chance to be disrupted by single massive star and massive binaries decreases in segregated clusters. Also when a binary is disrupted in the segregated cluster, If it is going to be ejected/evaporated from cluster, It has to pass from a outer layer of the cluster which is contaminated by single stars. This star still has a chance to interact with single stars and remain in the

cluster which decreases the evaporation probability. This is not a case for Non-segregated clusters.

For clusters with 30% binaries it can be seen that if they contain more low mass stars and less massive binaries (the case of clusters with $M_{min} = 0.2M_{\odot}$), they lose more binaries than clusters with $M_{min} = 0.5M_{\odot}$.

3.4. Periods and eccentricities

Figure 4 shows the histogram of periods in units of days (logarithmic) in six time-steps for 16 clusters which contain 30% and 60% initial binaries. Different colors represent different times. For example red plot is at the time of 0.0 Myr which is the initial distribution of periods that we have chosen according to observations reported in literature (see Section 2.2). It is a bimodal distribution, for low mass binaries it is Kroupa distribution and for massive O, B binaries it is Sana&Evans 2011 which exhibits in its a first part a peak around 10 days.

Evolution of the first part is according to stellar evolution, that is why it is not visible in D-clusters. Evolution of second part is according to the dynamics of the cluster, that is why we see this for both S-clusters and D-clusters.

Almost half of the low-mass binaries dissolve within 1 Myr. Figure 5 shows the evolution of eccentricity distributions in 6 time-steps for 16 clusters which contain 30% and 60% initial binaries. Initial distribution ($T = 0.0$ Myr) is the red plot. Like the period distribution, eccentricities also have a bimodal distributions, for low-mass and massive binaries (with a peak close to $e=0.0$). Stellar evolution, affects the evolution of the first peak (for massive binaries) that is why for D-clusters the peak does not evolve. For low-mass binaries, during the evolution (in different time-steps) the distribution keeps the memory of the initial distribution for different eccentricities.

For period distribution, after 2-3 Myr the new distribution could keep the memory of initial distribution of massive binaries not for low-mass binaries. But for eccentricity distribution, cluster keeps the memory of initial distribution of eccentricities.

4. Comparison with observations

For R136, the main observational data result from imaging in different filters. From these data, one can estimate the mass of stars and compare the density profile with simulations. In such an approach errors can dramatically increase from converting magnitudes to mass as the theoretical evolutionary models may not provide enough information for very massive and Wolf-Rayet stars specially. On the other hand, we probably cannot detect many low mass stars during the photometry. Moreover, if the detected object is a binary then estimated mass is biased.

At this point of our study we prefer to produce the imaging data from the simulations with the spatial resolution of HST/WFPC2 data from R136. HST/WFPC2 observations of R136 were carried out on 1994-09-25 (PI: Westphal), from which we use a combination of shallow, intermediate and long exposures ranging from 3–5 s to 80–120 s with the planetary camera (PC) and the F814W filter. So we wrote a code which reads the information of stars from the NBODY6 simulations as an input and creates the synthetic scenes that mimic HST/WFPC2 resolution in different HST filters. During this simulation we also need proper stellar evolution models and atmospheric models for calculating Bolometric Correction (BC) of different HST/WFPC2 filters. We created sets of BC tables at the age of 2 Myr using Geneva stellar evolution mod-

Model	SE	Seg	BF	N_{bin}	M_{min}	M_{max}	N
S00seg00bin05m150	ON	0.0	0.0	0	0.5	150	55992
D00seg00bin05m150	OFF	0.0	0.0	0	0.5	150	55992
S10seg00bin05m150	ON	1.0	0.0	0	0.5	150	55815
D10seg00bin05m150	OFF	1.0	0.0	0	0.5	150	55815
S00seg03bin05m150	ON	0.0	0.3	8404	0.5	150	56032
D00seg03bin05m150	OFF	0.0	0.3	8404	0.5	150	56032
S10seg03bin05m150	ON	1.0	0.3	8536	0.5	150	56908
D10seg03bin05m150	OFF	1.0	0.3	8536	0.5	150	56908
S00seg06bin05m150	ON	0.0	0.6	17000	0.5	150	56669
D00seg06bin05m150	OFF	0.0	0.6	17000	0.5	150	56669
S10seg06bin05m150	ON	1.0	0.6	16686	0.5	150	55622
D10seg06bin05m150	OFF	1.0	0.6	16686	0.5	150	55622
S00seg00bin02m150	ON	0.0	0.0	0	0.2	150	105666
D00seg00bin02m150	OFF	0.0	0.0	0	0.2	150	105666
S10seg00bin02m150	ON	1.0	0.0	0	0.2	150	107722
D10seg00bin02m150	OFF	1.0	0.0	0	0.2	150	107722
S00seg03bin02m150	ON	0.0	0.3	16134	0.2	150	107565
D00seg03bin02m150	OFF	0.0	0.3	16134	0.2	150	107565
S10seg03bin02m150	ON	1.0	0.3	16084	0.2	150	107230
D10seg03bin02m150	OFF	1.0	0.3	16084	0.2	150	107230
S00seg06bin02m150	ON	0.0	0.6	32225	0.2	150	107419
D00seg06bin02m150	OFF	0.0	0.6	32225	0.2	150	107419
S10seg06bin02m150	ON	1.0	0.6	32309	0.2	150	107698
D10seg06bin02m150	OFF	1.0	0.6	32309	0.2	150	107698

Table 1. Different simulated clusters grouped by minimum mass. Total mass of the clusters is $10^5 M_{\odot}$. Summary of naming convention for these simulated clusters is explained hereafter:

$$\underbrace{S}_{1} \underbrace{10 \text{ seg}}_{2} \underbrace{03 \text{ bin}}_{3} \underbrace{01 \text{ m } 100}_{4}$$

- 1 : **S** means Stellar evolution is ON and **D** means Stellar evolution is OFF (Pure Dynamically evolution).
- 2 : Number before **seg** shows the degree of mass segregation. **10 seg** means fully segregated and **00 seg** means non-segregated.
- 3 : Number before **bin** shows the initial binary fraction. **03 bin** means 0.3 binary fraction (30 percent of binaries) and **00 bin** means no initial binaries.
- 4 : The numbers before and after **m** shows the mass range. The first number before **m** can be **01** which means the low mass cutoff is $0.1M_{\odot}$ or it can be **10** which means the low mass cutoff is $1.0M_{\odot}$ and the second number after **m** can be **100** which means the maximum mass of the particles is $100M_{\odot}$ or it can be **300** which mean the maximum mass is $300M_{\odot}$.

So name **S10seg03bin01m100** stand for a cluster with stellar evolution is ON and it is fully segregated with 0.3 binary fraction and mass range between $0.1M_{\odot}$ to $100M_{\odot}$. Also **D00seg00bin10m300** means this cluster evolves just Dynamically without stellar evolution and it is not initially segregated without any initial binaries and mass range between $1.0M_{\odot}$ to $300M_{\odot}$.

els⁴ (Lejeune & Schaerer, 2001). For calculating BCs we used SEDs from TLUSTY atmosphere models for O and B stars⁵ (Hubeny & Lanz, 1995), Lanz & Hubeny (2003), Lanz & Hubeny (2007)) and KURUCZ⁶ (Castelli et al. (1997)) for the rest of the stellar types with a half-solar metallicity appropriate for LMC stars. TLUSTY provides grids of non-LTE, metal line blanketed, plane-parallel, hydrostatic model atmospheres which is well suited for the very massive stars specially in visible and near-IR.

At a given time (2 Myr) it is possible to calculate the flux (in different HST filters) for each star in the simulation using computed BC tables. We simulated a 800×800 pixels scene corresponding to a field of $32.5'' \times 32.5''$ on the detector where a star with a given flux falls on the detector with a Gaussian distribution as the PSF profile.

Figure A.1-A.4 show synthetic scenes of 12 simulated clusters at time 2 Myr both in XY and XZ plane. One can compare the synthetic images with real HST/WFPC2 data on R136 shown in Figure 6. Both images are in F814W filters.

⁴ <http://webast.ast.obs-mip.fr/equipe/stellar/>

⁵ Model atmospheres and source codes are available at <http://nova.astro.umd.edu>

⁶ ATLAS9 Kurucz ODFNEW/NOVER models

However the question is at what degree a simulated cluster with thousands of stars within a given volume projected once on the sky to reproduce HST image of R136. What is the best criterion to select the closest simulated cluster to R136?

One useful way is to compare the Surface Brightness Profile (SBP) of R136 to those of synthetic scenes (Section 4.1). It is also possible to compare the Half-Light radius (R_{hl}) of R136 and synthetic scenes (Section 4.3). In Section 4.2 we compared the Mass Function (MF) slopes of R136 with the MF slopes from simulations. The MF is not directly derived from simulation. The mass of stars in the FoV is estimated by the photometry on the synthetic scenes and we used the BC-tables for finding the mass of each detected star in a given field. In Section 4.4 we introduce a new definition for double checking. In this section we calculate a neighbor radius ($R_{neighbor}$) of each star in each cluster which is a radius containing for example, 100 neighbor stars. In a crowded regions (in the core) this radius is very short for each star while in outer regions it can be larger.

4.1. SBP of R136

Figure 7 shows the SBP of R136. It can be seen that at some radial distances from the core of the cluster the SBP suddenly

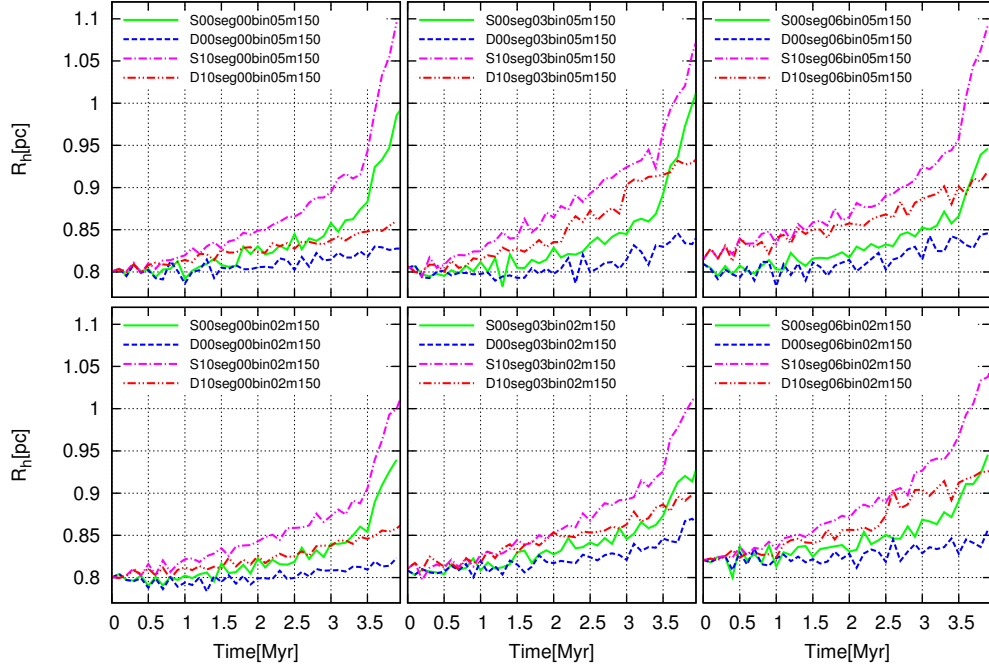


Fig. 1. Half-mass radius evolution of different clusters within 4 Myr. Up: mass range of $0.5M_{\odot} - 150M_{\odot}$. Down: $0.2M_{\odot} - 150M_{\odot}$. Left: No initial binaries, Middle: 30% initial binaries, Right: 60% initial binaries. Green and Blue: Non-segregated; Pink and Red: Segregated.

increases with a significant deviation from the general trend. We checked for the distribution of the spectral type of R136 stars in the FoV of HST/WFPC2-PC imaging data and we found 9 WR stars. Figure 7 shows the radii at which a given WR is detected.

For synthetic scenes we have calculated the SBPs in the same regions as R136. Figure 8 shows the SBPs of the simulated R136 versus its simulated twin (pink stars).

To determine the closest SBP value of the simulated to the observed R136 we calculated the χ^2 for each cluster in three regions in addition to the whole cluster. Table 2 (simulated scenes in XZ plane) and Table 3 (simulated scenes in XY plane) depict the χ^2 values. Clusters with the smallest value have an SBP more closer to that of R136. Thus the non-segregated clusters match better R136 in all regions.

One can consider the cumulative SBP of R136 and compare it with cumulative SBP of R136. As this cumulative value smooths the SBP, it hides the details of the profile but we calculate this function for both R136 HST data and simulations. The results are given as an example in Appendix C.

4.2. MF slopes

After having created series of synthetic scenes, in the first step photometry on each image have to be done. For the photometry on HST/WFPC2 data and also on the synthetic images we used STARFINDER (Diolaiti et al. (2000)) to extract the sources using analytical prepared Point Spread Function (PSF)

related to the F814W filter. For HST/WFPC2-F814W we extracted 2660 stars and for the synthetic images, we extracted from 1759 up to 3193 sources depending on the scene. Using BC tables (explained in Section 4), we estimated the photometric mass of detected stars in each imaging data for different clusters. Furthermore we computed the MF for each simulated cluster at the evolution time of 2 Myr as following:

$$\log(N) = a \log\left(\frac{M}{M_{\odot}}\right) + b$$

Table 4 and 5, for the scenes in XZ and XY planes respectively, show the MF slopes for three regions ($r < 4''.5$, $4''.5 < r < 9''$, $9'' < r < 13.5''$) and also for the whole cluster at time of 2 Myr. MF slope of R136 in the same filter is as follow:

$$r < 4''.5 : a = -0.39 \pm 0.24$$

$$4''.5 < r < 9'' : a = -1.18 \pm 0.21$$

$$9'' < r < 13.5'' : a = -0.97 \pm 0.09$$

$$\text{For the whole FoV: } a = -0.89 \pm 0.14$$

To better compare the slopes Figure 9 on can compare them MF between simulations and R136 (Black solid line). In region 2 and 3 non-segregated simulated clusters exhibit closer values to the observed MF of R136.

4.3. Half-light radius

In a next step, we estimated the half-light radius (R_{hl}) of R136 versus those of synthetic scenes from the simulations at time 2 Myr.

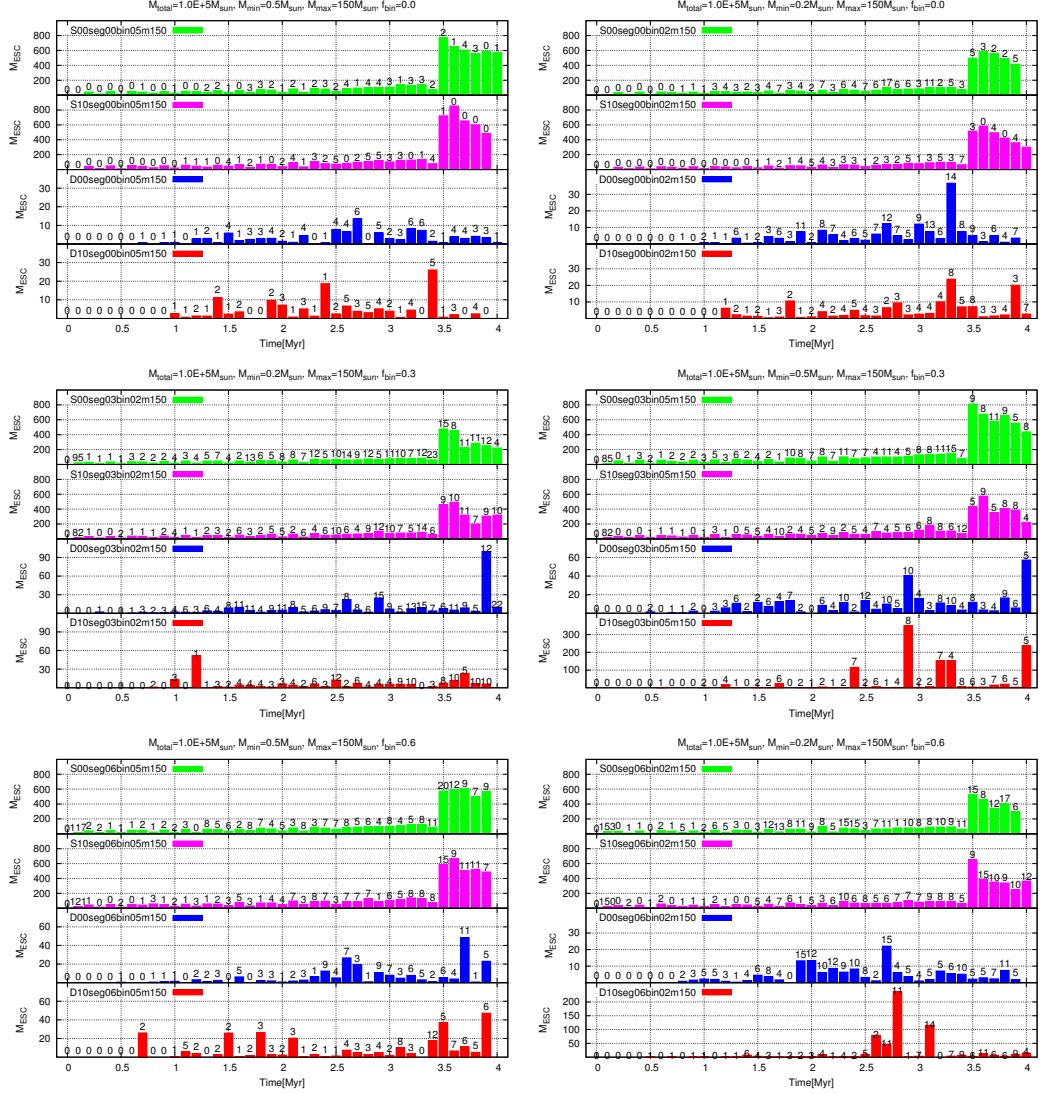


Fig. 2. Total mass loss of the clusters per time-step. Left: mass range of $0.5M_{\odot} - 150M_{\odot}$. Right: mass range of $0.2M_{\odot} - 150M_{\odot}$. Upper, middle and bottom plots represent clusters with 0%, 30% and 60% initial binaries. The numbers at the top of each bin correspond to the number of escapers. Green and Blue: non-segregated; Pink and Red: Segregated. Stellar evolution is ON for Green and Red, and OFF for blue and Red.

In order to compare the simulated scenes to the observed R136 we computed R_{hl} in the same FoV as HST imaging data ($32.5'' \times 32.5''$ in terms of PC). Corresponding results are outlined in Table 6. It can be seen that, unlike what $R_{half-mass}$ shows in the simulations, non-segregated clusters have larger half light radii than segregated ones.

At time 2Myr, clusters with $M_{min} = 0.5M_{\odot}$ have larger R_{hl} than clusters with $M_{min} = 0.2M_{\odot}$. It means that clusters

with larger number of low-mass (high-mass) stars have smaller (larger) half-light radius. Also R_{hl} of the clusters with 0% and 60% initial binaries are more close together and both are larger than clusters with 30% initial binaries.

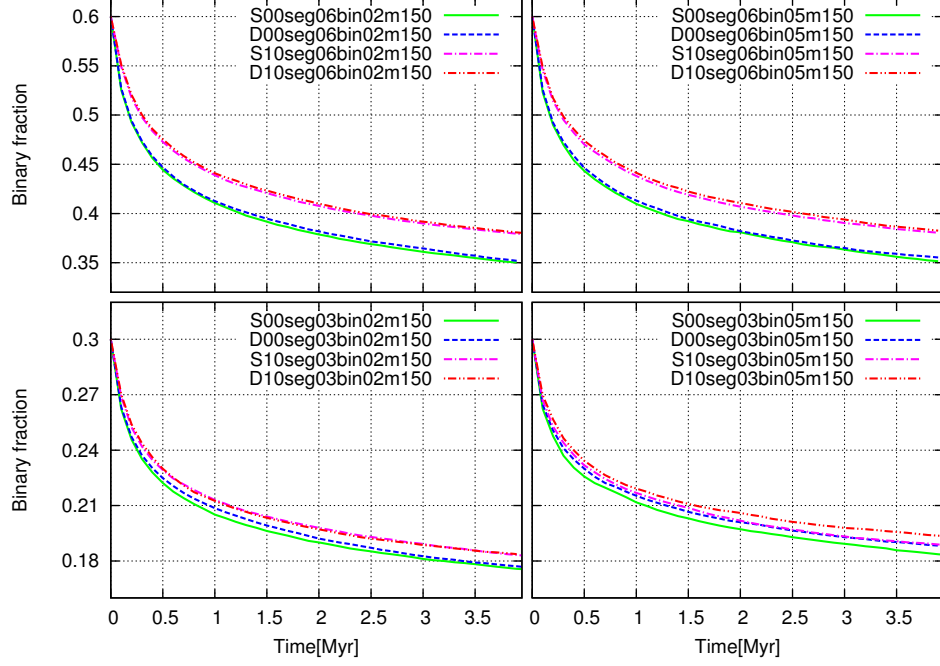


Fig. 3. Fraction of bound binary systems for different clusters in each time-steps. Left, Up: clusters with mass range of $1.0M_{\odot} - 100M_{\odot}$ and 30% Initial binaries. Right, Up: clusters with mass range of $1.0M_{\odot} - 300M_{\odot}$ and 30% Initial binaries. Left, Down: clusters with mass range of $0.5M_{\odot} - 150M_{\odot}$ and 30% Initial binaries. Right, Down: clusters with mass range of $0.5M_{\odot} - 150M_{\odot}$ and 60% Initial binaries. Green and Blue: non-segregated; Pink and Red: Segregated. Stellar evolution is ON for Green and Red, and OFF for blue and Red.

0.2 – 150 M_{\odot}						
Non segregated			Segregated			
Binary:	0%	30%	60%	0%	30%	60%
reg1:	0.165324	0.105162	0.113661	0.243965	0.338743	0.275119
reg2:	0.310922	0.592480	0.420130	3.60058	3.51407	3.23245
reg3:	2.00193	2.23264	2.25797	8.67890	11.7996	8.54216
total:	2.46867	2.68223	2.60257	12.4118	14.6848	11.3888
0.5 – 150 M_{\odot}						
Non segregated			Segregated			
Binary:	0%	30%	60%	0%	30%	60%
reg1:	0.234170	0.278665	0.199646	0.315313	0.327533	0.378822
reg2:	0.282935	0.481584	0.310920	1.56187	1.53784	1.77578
reg3:	1.36780	1.53290	1.33918	8.44827	7.46168	4.86113
total:	1.83876	2.18597	1.84632	10.0084	9.22575	6.49839

Table 2. χ^2 of SBP of simulated scenes at 2 Myr in XZ plane in three different regions and for the whole cluster. The smallest value is the closest one to SBP of R136.

4.4. Neighbor radius

Neighbor radius ($R_{neighbor}$) is an arbitrary distance to find 100 neighbor stars from a given star. In the core of the cluster that has a higher stellar density, this radius is smaller than in the outer regions of the cluster. For R136 we calculated this radius for all the sources that have been detected in the HST image. We carried the same procedure on every simulated scene, with different characteristics, i.e. segregated or not, different binary frac-

tions, etc... both in XY and XZ planes. Figure C.1 and B.2 depict the corresponding results. Red dots in each plot correspond to R136, Green and Blue dots correspond to not-segregated and segregated clusters. One can conclude that for all the simulated scenes, non-segregated clusters better fit to the R136 by HST considering the general trend of the slope.

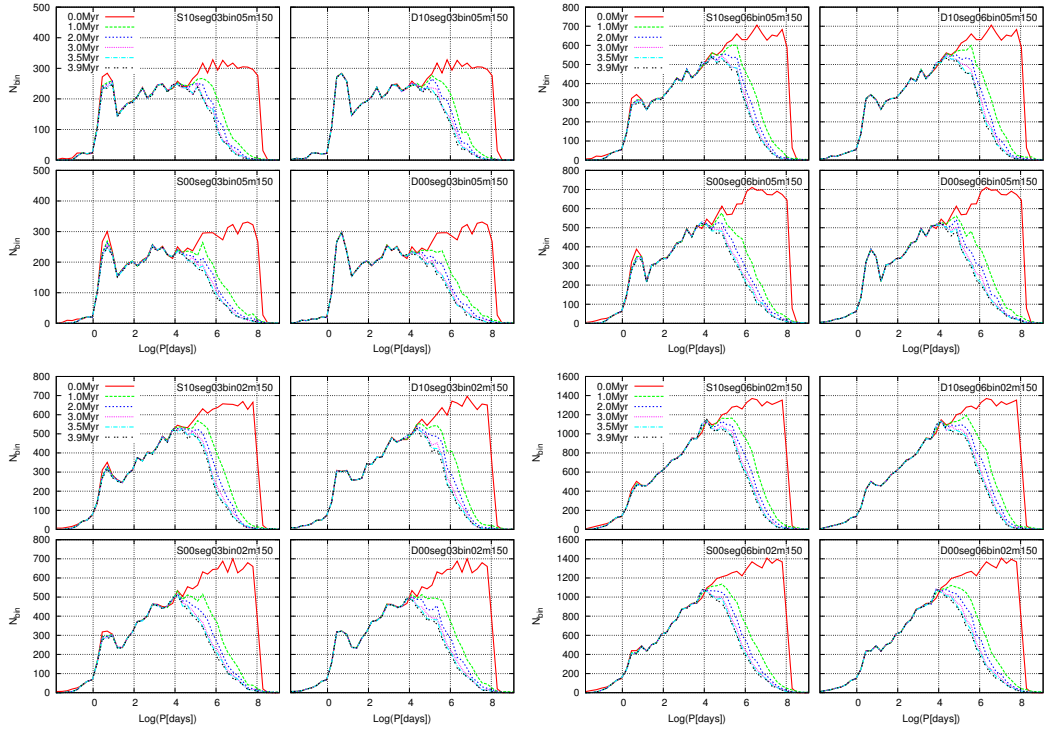


Fig. 4. Histogram of the Log(period [days]) of bound binary systems for different clusters in 6 time-steps (0.0, 1.0, 2.0, 3.0, 3.5 and 3.9 Myr). Left, Up: 4 clusters with mass range of $0.5M_{\odot} - 150M_{\odot}$ and 30% Initial binaries. Right, Up: 4 clusters with mass range of $0.5M_{\odot} - 150M_{\odot}$ and 60% Initial binaries. Left, Down: 4 clusters with mass range of $0.2M_{\odot} - 150M_{\odot}$ and 30% Initial binaries. Right, Down: 4 clusters with mass range of $0.2M_{\odot} - 150M_{\odot}$ and 60% Initial binaries.

0.2 – 150 M_{\odot}						
Non segregated			Segregated			
Binary:	0%	30%	60%	0%	30%	60%
reg1:	0.134300	0.121093	0.109488	0.296658	0.288149	0.291632
reg2:	0.313673	0.345682	0.233337	3.53505	3.24678	3.14732
reg3:	2.24570	2.98828	2.46877	9.67167	11.5166	11.6881
total:	2.64560	3.44385	2.80842	12.8372	14.2383	14.1527
0.5 – 150 M_{\odot}						
Non segregated			Segregated			
Binary:	0%	30%	60%	0%	30%	60%
reg1:	0.199056	0.277567	0.201168	0.364366	0.311924	0.352169
reg2:	0.268080	0.388363	0.334479	2.08545	2.05616	1.62055
reg3:	1.24983	1.71160	2.10933	8.94076	7.85162	7.39265
total:	1.68033	2.27788	2.64436	10.9022	9.82424	9.14485

Table 3. χ^2 of SBP of simulated scenes at 2 Myr in XY plane in three different regions and for the whole cluster. The smallest value is the closest one to SBP of R136.

5. Discussion of the results

We carried out a study of R136 in two steps. In a first and as exhaustive as possible step based on the NBODY6 code, we simulated a grid of synthetic young starburst compact clusters similar to R136, starting from its state-of-the-art basic parameters: i.e. age, distance, luminosity of individual member stars. In a second step we selected the likeliest synthesized images of R136

that match the observed visible wavelengths data from HST. The choice of this image provides a set of physical properties that explain best the expansion, the mass loss of the stellar populations in R136 as well as their binary fraction for instance.

Regarding the expansion of the cluster we found that in all cases segregated clusters expand more than non-segregated clusters, and that the former have larger R_t than the latter. Clusters with stellar evolution (S-clusters) expand significantly around 3

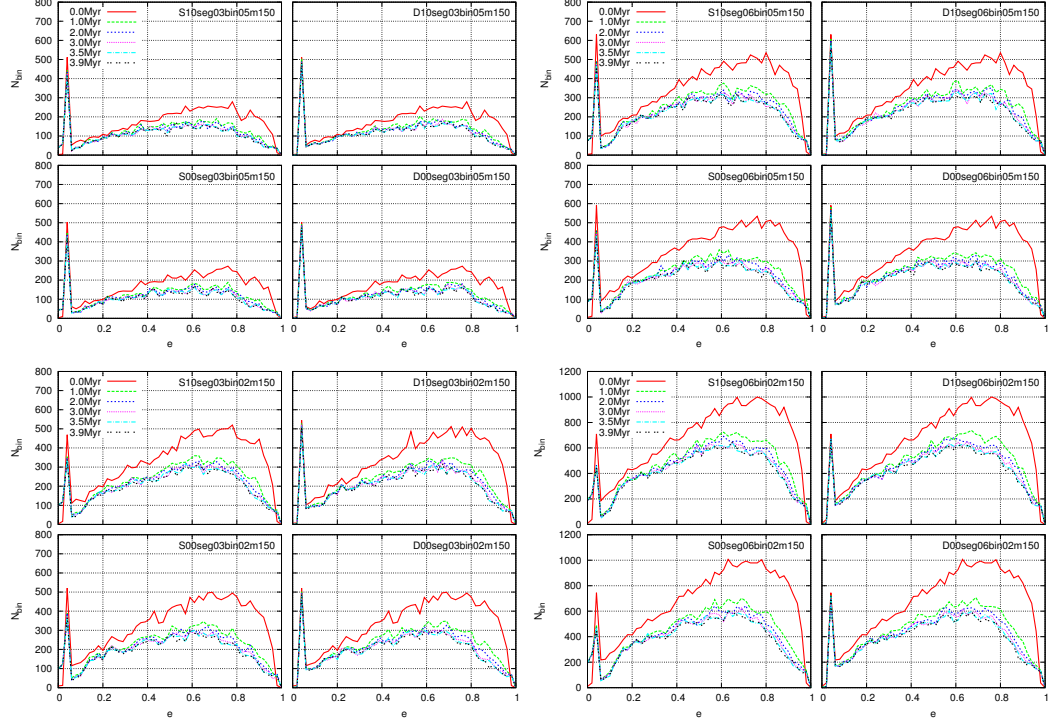


Fig. 5. Histogram of the eccentricity of bound binary systems for different clusters in 6 time-steps (0.0, 1.0, 2.0, 3.0, 3.5 and 3.9 Myr). Left, Up: 4 clusters with mass range of $0.5M_{\odot} - 150M_{\odot}$ and 30% Initial binaries. Right, Up: 4 clusters with mass range of $0.5M_{\odot} - 150M_{\odot}$ and 60% Initial binaries. Left, Down: 4 clusters with mass range of $0.2M_{\odot} - 150M_{\odot}$ and 30% Initial binaries. Right, Down: 4 clusters with mass range of $0.2M_{\odot} - 150M_{\odot}$ and 60% Initial binaries.

		0.2 - 150M _⊙					
		Not segregated			Segregated		
Binary:		0%	30%	60%	0%	30%	60%
reg1:		0.06 ± 0.67	-0.06 ± 0.32	-0.03 ± 0.35	-0.23 ± 0.26	-0.31 ± 0.15	-0.19 ± 0.24
reg2:		-1.43 ± 0.15	-1.14 ± 0.17	-1.16 ± 0.28	-1.65 ± 0.02	-1.64 ± 0.13	-1.68 ± 0.15
reg3:		-1.32 ± 0.14	-1.06 ± 0.23	-1.31 ± 0.20	-1.44 ± 0.02	-1.58 ± 0.05	-1.47 ± 0.58
total:		-0.77 ± 0.09	-0.69 ± 0.15	-0.68 ± 0.19	-0.64 ± 0.06	-0.67 ± 0.16	-0.67 ± 0.67
		0.5 - 150M _⊙					
		Non-segregated			Segregated		
Binary:		0%	30%	60%	0%	30%	60%
reg1:		0.13 ± 0.60	0.31 ± 0.54	0.11 ± 0.49	-0.04 ± 0.59	-0.08 ± 0.36	-0.09 ± 0.24
reg2:		-1.18 ± 0.11	-1.26 ± 0.40	-1.01 ± 0.14	-1.89 ± 0.24	-1.64 ± 0.26	-1.69 ± 0.29
reg3:		-1.17 ± 0.06	-1.33 ± 0.22	-1.22 ± 0.13	-1.79 ± 0.01	-2.54 ± 0.17	-1.20 ± 0.69
total:		-0.72 ± 0.04	-0.61 ± 0.22	-0.65 ± 0.10	-0.70 ± 0.04	-0.71 ± 0.15	-0.70 ± 0.12

Table 4. MF's slopes from simulated scenes at 2 Myr in XZ plane in three different regions and also for the the whole cluster.

Myr because of the evolution of very massive stars, that possess for some of them extreme winds of $10^{-8} - 10^{-5}[M_{\odot}/\text{yr}]$ (Lamers & Cassinelli (1999)). Clusters with dynamical evolution (D-clusters) alone expand more due to the presence of more massive stars.

Regarding the mass loss of the cluster and escapers: the total mass loss of S-clusters is larger than for D-clusters. This is due to the evolution of massive stars themselves whilst D-clusters

undergo escapers loss only. S-clusters containing more massive stars, present a larger mass loss in their early stages of evolution. D-clusters lose more escapers as the binary fraction increases.

On the other hand segregated clusters lose more binaries than non-segregated ones and in the special case of clusters with 30% initial binaries made of low-mass stars, the binary loss is significantly larger.

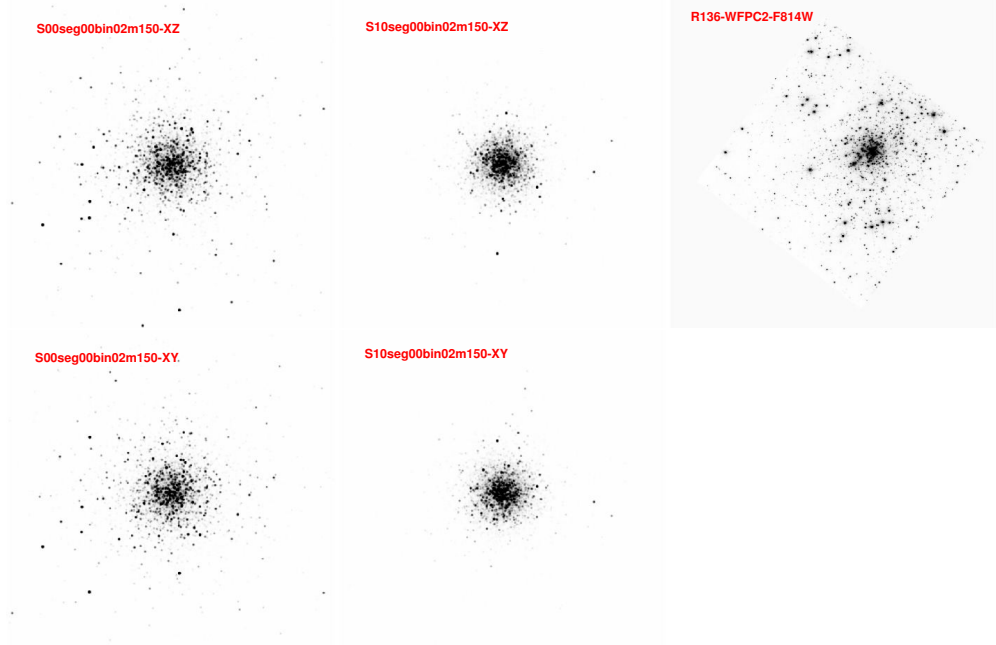


Fig. 6. Synthetic scenes from simulation of S-clusters with the mass range of $(0.2 - 150)M_{\odot}$ and 0% initial binaries at time 2 Myr. Not segregated: Left images; Segregated clusters: Middle images; Top is in XZ plane and bottom is in XY plane. R136 image taken by HST/WFPC2-PC in F814W filter is in the Right top.

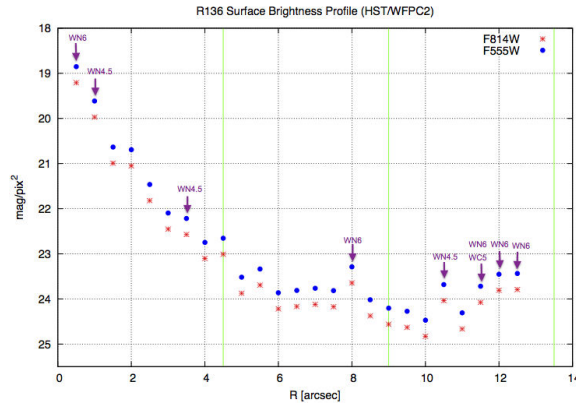


Fig. 7. SBP of R136 in two filters F814W and F555W. 9 WR stars are shown in the plot.

Concerning periods and eccentricities: almost half of the low-mass binaries dissolve within 1 Myr. Clusters with stellar evolution lose their massive binaries according to the evolution of massive stars themselves. In all cases binaries keep the memory of initial eccentricities distribution during the first 4 Myr. For this period, only the massive binaries keep the memory of initial period distribution.

Having these general properties in mind we used synthetic scenes with the same observational resolution as HST/WFPC2-PC/F814W. For this purpose we computed a grid of bolometric correction tables which provide the flux of different stars in F814W filter using Geneva stellar evolution models and model atmosphere (TLUSTY for O,B stars and Kurucz for other spectral types). These synthetic images have the same pixel scale, spatial resolution and FoV of WFPC2 data on R136.

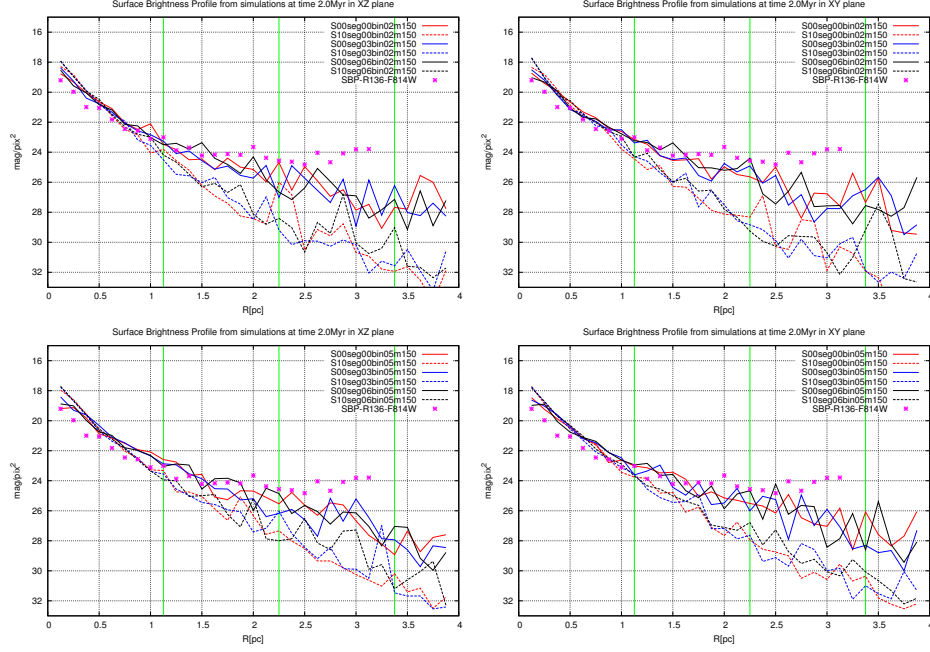


Fig. 8. SBP from simulations at time 2 Myr for different sets of clusters in a mass range of $(0.2 - 150)M_{\odot}$ (upper plots) and $(0.5 - 150)M_{\odot}$ (bottom plots). Right is the synthetic scenes created in XY plan and Left belongs to XZ plan. Solid lines belong to initial non-segregated clusters and dashed lines represent initial segregated clusters. Pink stars shows the SBP of R136 from WFPC2-PC data. Reddening is corrected for the HST data.

0.2 - 150 M_{\odot}						
Non-segregated			Segregated			
Binary:	0%	30%	60%	0%	30%	60%
reg1:	0.01 ± 0.43	-0.05 ± 0.37	0.00 ± 0.54	-0.24 ± 0.23	-0.28 ± 0.29	-0.21 ± 0.21
reg2:	-1.42 ± 0.26	-1.18 ± 0.29	-1.26 ± 0.84	-2.03 ± 0.49	-1.64 ± 0.47	-1.61 ± 0.30
reg3:	-1.28 ± 0.01	-1.29 ± 0.29	-1.38 ± 0.43	-1.60 ± 0.44	-1.78 ± 0.28	-1.37 ± 0.29
total:	-0.75 ± 0.03	-0.70 ± 0.17	-0.73 ± 0.19	-0.66 ± 0.08	-0.68 ± 0.17	-0.65 ± 0.07
0.5 - 150 M_{\odot}						
Non-segregated			Segregated			
Binary:	0%	30%	60%	0%	30%	60%
reg1:	0.12 ± 0.62	0.11 ± 0.29	0.17 ± 0.46	-0.10 ± 0.41	-0.10 ± 0.35	0.01 ± 0.40
reg2:	-1.22 ± 0.11	-1.23 ± 0.15	-1.12 ± 0.20	-1.69 ± 0.10	-1.80 ± 0.28	-1.73 ± 0.35
reg3:	-1.32 ± 0.12	-1.29 ± 0.27	-1.06 ± 0.42	-1.99 ± 0.02	-1.49 ± 1.11	-1.93 ± 0.65
total:	-0.75 ± 0.05	-0.66 ± 0.12	-0.62 ± 0.13	-0.71 ± 0.07	-0.72 ± 0.14	-0.68 ± 0.13

Table 5. MF's slopes from simulated scenes at 2 Myr in XY plane in three different regions and also for the the whole cluster.

To conclude on the best R136 from its synthesized images we used 4 different criteria based on: SBP, MF's slopes, R_{hl} and R_{conf} .

We calculated the surface brightness profiles (SBP) of R136 and the synthetic scenes (in both XY and XZ planes). A χ^2 criterion on the SBP permits to chose can the most probable synthesized R136 in three different regions and also for the whole cluster. SBP, R_{hl} can easily be driven for each scene. Thus, using the photometry on each synthesized R136 image, we derived the mass of detected sources and plotted the mass function (MF) and $R_{neighbor}$.

Using the 4 criteria all together, even though they are not completely independent, we conclude that R136 is best represented by a non-segregated cluster (in $r < 4pc$).

This result can explain the dominant mechanism for the formation of very massive stars among two main formation scenarii of gas accretion and collision between less massive stars that are explained in details by Krumholz (2015). Initially a non-segregated cluster cannot provide sufficient dense conditions and a higher mean stellar mass in the core, for collisions to occur before the final stages of massive stars evolution. Presently, no convincing evidence exists such as fragmentation, radiation pressure, photoionization and stellar winds to stop the

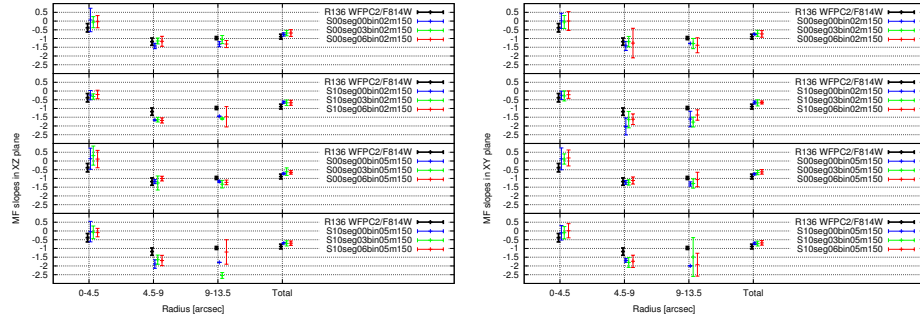


Fig. 9. MF Slopes from simulated synthetic scenes at 2 Myrs in XY (Right plots) and XZ (Left plots) plane. Black solid lines belong to R136 from HST/WFPC2 data taken in F814W filter. Blue, Green and Red represents clusters with 0%, 30% and 60% initial binaries.

Model	Seg	BF	M_{min} [M_{\odot}]	M_{max} [M_{\odot}]	R_{hl} (XY) [pc]	R_{hl} (XZ) [pc]
S00seg00bin05m150	0.0	0.0	0.5	150	0.43	0.50
S10seg00bin05m150	1.0	0.0	0.5	150	0.30	0.28
S00seg03bin05m150	0.0	0.3	0.5	150	0.40	0.43
S10seg03bin05m150	1.0	0.3	0.5	150	0.26	0.26
S00seg06bin05m150	0.0	0.6	0.5	150	0.46	0.48
S10seg06bin05m150	1.0	0.6	0.5	150	0.29	0.26
S00seg00bin02m150	0.0	0.0	0.2	150	0.42	0.43
S10seg00bin02m150	1.0	0.0	0.2	150	0.27	0.27
S00seg03bin02m150	0.0	0.3	0.2	150	0.36	0.38
S10seg03bin02m150	1.0	0.3	0.2	150	0.23	0.25
S00seg06bin02m150	0.0	0.6	0.2	150	0.42	0.43
S10seg06bin02m150	1.0	0.6	0.2	150	0.25	0.27

Table 6. R_{hl} calculated for different simulated scenes at 2Myr in XY and XZ plane.

growth of stars by accretion (Krumholz (2015)). So initially non-segregated clusters may better explain the formation of massive stars by accretion.

Effectively, accretion based models predict the low-mass companions, in addition to their massive companions, at separation of 100-1000 AU (Kratter & Matzner (2008), Kratter et al. (2008), Kratter et al. (2010), Krumholz et al. (2012)) while the collisionally-formed stars will lack low-mass companions. These companions can be observationally detected by using high angular resolution and high contrast instruments like VLT/SPHERE (Zurlo et al. (2014)), the future E-ELT where R136 would be resolved as NGC3603 by the VLT and NGC3603 resolved by the VLT as the Trapezium cluster in Orion by a 1-2m class telescope.

Note that for the comparison of synthesized versus observed images of R136, we considered the median value of the extinction (in F814W filter) derived from 26 known O-type stars in the FoV of the HST data (Khorrami et al. in prep). If the spatial distribution of dust were taken into account according to the real position of massive stars in the cluster, the effect of confusion would even be worse. Since massive stars are expected to clear out dust from their neighborhood, the extinction would affect the low mass stars specially. This would make them undetectable in the visible wavelengths, that introduces an additional bias on the HST images reinforcing the segregation scenario for R136 (Ascenso et al. (2003)).

6. Conclusion

In this work we proposed a new approach to compare the results of the NBODY6 code with data from high contrast imaging observations obtained on large optical telescopes at their diffraction limit. In previous studies, the direct output of the code is compared with observational material where one compares for example the density profile of hundred thousands of stars with the density of a few thousands of them extracted from observations in practice. Our method is rather based on synthesizing the observations directly from NBODY6 itself. These synthesized images are matched to real observations in a final step for their likeness.

We based our study on data taken from HST/WFPC2 archives. For this we produced simulated scenes at the resolution of HST/WFPC2-pc/F814W images) and created BC tables which provide the flux of different stars in F814W filter using Geneva stellar evolution models and TLUSTY atmosphere model for O,B stars and Kurucz model for other spectral types. These synthetic images have the same pixel scale, spatial resolution and FoV as the WFPC2 data of R136 from HST. Note that our modeling of stellar members atmospheres could be improved by considering more appropriate atmosphere codes for the WR components of R136, for example using grids of model atmosphere like TLUSTY but including winds (Neugent et al. (2015)). On the other hand our synthesized R136 clusters could be improved for their evolution by adding time-space depend-

ing gas potential to the model. This could ideally be included in NBODY6 code itself (private communication R. Wunsch).

In summary our study is in favor of the R136 to be a non-segregated cluster: a result contradicting the generally accepted picture. A result that deserves more exhaustive and systematic observations of R136 to be conclusive. Such observations should be carried out in as many spectral bands as possible: from the visible to optical and thermal IR wavelengths to overcome the confusion effect specially. This becomes possible using the VLT and high contrast AO imaging in the optical, future observations from space (JWST) or the E-ELT (Zinnecker (2006)). Ultimately long baseline imaging interferometry from the ground should enable us to resolve the stellar binary components of R136 or similar compact clusters.

Acknowledgements. ZK is supported by the Erasmus Mundus Joint Doctorate Program by Grant Number 2012-1710 from the EACEA of the European Commission. We warmly thank Marcel Carillet, Sambaran Banerjee, Andreas Kupper, Richard Wunsch for useful discussions and Frédéric Thévenin for his careful reading of the original paper.

References

- S.J. Aarseth, M. Hénon, R. Wielen, 1974, *A&A*, 37, 183-187
 Aarseth, S. J. 2003, *Gravitational N-Body Simulations* (Cambridge: Cambridge Univ. Press)
 Ascenso, J.; Alves, J.; Lago, M. T. V. T., 2009, *A&A*, 495, 147-155
 Sambarab Banerjee and Pavel Kroupa, 2013, *ApJ*, 764:29
 Bonnell, I. A., Davies, M. B. 1998, *MNRAS*, 295, 691
 Bonnell, I. A., Clarke, C. J., Bate, M. R., Pringle, J. E. 2001, *MNRAS*, 324, 573
 Bonnell, I. A., Bate, M. R. 2006, *MNRAS*, 370, 488
 Bosch, G., Terlevich, E., Terlevich, R. 2009, *AJ*, 137, 3437
 Castelli, F.; Gratton, R. G.; Kurucz, R. L., 1997, *A&A*, 318, 841
 Paul A. Crowther, Olivier Schnurr, Raphael Hirschi, Norhasliza Yusof, Richard J. Parker, Simon P. Goodwin, Hasan Abu Kassim, 2010, *MNRAS*, 408, 731-751
 de Koter, A., Heap, S. R., Hubeny, I. 1997, *AJ*, 509, 879
 Diolaiti, E., Bendinelli, O., Bonaccini, D., Close, L., Currie, D., Parmeggiani, G. 2000, *A&AS*, 147, 335
 Gieren W.P., Fouque P., Go mez M., 1998, *ApJ*, 496, 17
 Henny J. G. L. M. Lamers, Joseph P. Cassinelli, Cambridge University Press, Jun 17, 1999
 Hnault-Brunet V., Evans C. J., Sana H., Gieles M., Bastian N., Maz Apellniz J., Markova N., Taylor W. D., Bressert E., Crowther P. A., van Loon J. T., 2012, *A&A*, 546, A73
 Hubeny I., Lanz T. 1995, *ApJ*, 439, 875
 Hunter Deidre A., Shaya Edward J., Holtzman Jon A., Light Robert M., O'Neil Earl J. Jr., Lynds Roger, 1995, *ApJ*, 448, 179
 Hurley, J. R., Pols, O. R., Tout, C. A. 2000, *MNRAS*, 315, 543
 Hurley, J. R., Tout, C. A., Pols, O. R. 2002, *MNRAS*, 329, 897
 /Kobulnicky H. A., Fryer C. L., 2007, *ApJ*, 670, 747
 Kratter, Kaitlin M.; Matzner, Christopher D., 2006, *MNRAS*, 373, 1563
 Kratter, Kaitlin M.; Matzner, Christopher D.; Krumholz, Mark R., 2008, *The Astrophysical Journal*, 681, 375
 Kratter, Kaitlin M.; Matzner, Christopher D.; Krumholz, Mark R.; Klein, Richard I., 2010, *The Astrophysical Journal*, 708, 1585
 Kroupa P., 2001a, *MNRAS*, 322, 231
 Kroupa P., 1995a, *MNRAS*, 277, 1491
 Kroupa P., 2008, *LNP*, 760, 181
 Krumholz, Mark R.; Klein, Richard I.; McKee, Christopher F., 2012, *The Astrophysical Journal*, 754
 Krumholz, Mark R., "The Formation of Very Massive Stars", 2015, SPRINGER, P43
 Kupper, A. H. W., Mascherberger, T., Baumgardt, H., Kroupa, P. 2011, *MNRAS*, 417, 2300
 Lada, C. J. & Lada, E. A. ,2003, *Annu. Rev. Astron. Astrophys.* 41, 57115.
 Lanz T., Hubeny I., 2003, *ApJS*, 146, 417
 Lanz T., Hubeny I., 2007, *ApJS*, 169, 83
 Lejeune T., Schaerer D. 2001, *A&A*, 366, 538
 Massey P., 2003, *ARA&A*, 41, 15
 Massey P., Hunter Deidre A., 1998, *ApJ*, 493, 180
 Neugent, K. F.; Massey, P.; Hillier, D. J.; Morrell, N. I., 2015, To be published by Universitätsverlag Potsdam as part of the International Workshop on Wolf-Rayet Stars conference proceedings

- Sana H., Evans C. J., 2011, *IAUS*, 272, 474
 Selman, F., Melnick, J., Bosch, G., Terlevich, R., 1999, *A&A*, 347, 532
 Remi Soummer, Anand Sivaramakrishnan, Ben R. Oppenheimer, Robin Roberts, Douglas Brenner, Alexis Carlotti, Laurent Pueyo, Bruce Macintosh, Brian Bauman, Les Saddlemyer, David Palmer, Darren Erickson, Christophe Dorrer, Kris Caputa, Christian Marois, Kent Wallace, Emily Griffiths, Jacob Mey, Proc. SPIE 7440, Techniques and Instrumentation for Detection of Exoplanets IV, 74400R (August 19, 2009)
 Weidner, C., Kroupa, P. 2006, *MNRAS*, 365, 1333
 Weidner, C., Kroupa, P., Bonnell, I. A. D., 2010 *MNRAS* 401, 275
 Zinnecker, Hans, The Scientific Requirements for Extremely Large Telescopes, Proceedings of the 232nd Symposium of the International Astronomical Union, Held in Cape Town, South Africa, November 14-18, 2005, Edited by Patricia Ann Whitelock; Michel Dennefeld; Bruno Leibundgut. Cambridge: Cambridge University Press, 2006., pp.324-327
 A. Zurlo, A. Vigan, D. Mesa, R. Gratton, C. Moutou, M. Langlois, R. U. Claudi, L. Pueyo, A. Boccaletti, A. Baruffolo et al. (19 more), 2014, *A&A*, 572, A85

Appendix A: Synthetic scenes

Appendix B: Neighbor Radius

Appendix C: Cumulative Surface brightness Profiles

Uncrowding R136 from VLT/SPHERE extreme adaptive optics [★]

Z. Khorrami¹, F. Vakili¹, T. Lanz¹, M. Langlois^{2,3}, E. Lagadec¹, M. R. Meyer⁴, S. Robbe-Dubois¹, L. Abe¹, H. Avenhaus⁵, J.L. Beuzit⁶, R. Gratton⁷, and D. Mouillet⁶

¹ Université Côte d'Azur, OCA, CNRS, Lagrange, France e-mail: zeinab.khorrami@oca.eu

² Univ Lyon, Univ Lyon1, Ens de Lyon, CNRS, CRAL UMR5574, F-69230, Saint-Genis-Laval, France

³ Aix Marseille Université, CNRS, LAM - Laboratoire d'Astrophysique de Marseille, UMR 7326, 13388, Marseille, France

⁴ Institute for Astronomy, ETH Zurich, Wolfgang-Pauli-Strasse 27, CH-8093 Zurich, Switzerland

⁵ Departamento de Astronomia, Universidad de Chile, Casilla 36-D, Santiago, Chile

⁶ Université Grenoble Alpes, CNRS, IPAG, 38000 Grenoble, France

⁷ INAF - Astronomical Observatory of Padua

ABSTRACT

Context. This paper presents the sharpest near-IR images of the massive cluster R136 to date, based on the extreme adaptive optics of the SPHERE focal instrument implemented on the ESO Very Large Telescope and operated in its IRDIS imaging mode.

Aims. The crowded stellar population in the core of the R136 starburst compact cluster remains still to be characterized in terms of individual luminosities, age, mass and multiplicity. SPHERE/VLT and its high contrast imaging possibilities open new windows to make progress on these questions.

Methods. Stacking-up a few hundreds of short exposures in J and Ks spectral bands over a Field of View (FoV) of 10.9"×12.3" centered on the R136a1 stellar component, enabled us to carry a refined photometric analysis of the core of R136. We detected 1110 and 1059 sources in J and Ks images respectively with 818 common sources.

Results. We found that more than 62.6% (16.5%) of the stars, detected both in J and Ks data, have visual companion closer than 0.2" (0.1").

The closest stars are resolved down to the full width at half maximum (FWHM) of the point spread function (PSF) measured by Starfinder. Among newly resolved and/or detected sources R136a1 and R136c are found to have optical companions and R136a3 is resolved as two stars (PSF fitting) separated by 59 ± 2 mas. This new companion of R136a3 presents a correlation coefficient of 86% in J and 75% in Ks. The new set of detected sources were used to re-assess the age and extinction of R136 based on 54 spectroscopically stars that have been recently studied with HST slit-spectroscopy (Crowther et al. 2016) of the core of this cluster.

Over 90% of these 54 sources identified visual companions (closer than 0.2"). We found the most probable age and extinction for these sources are $1.8^{+1.2}_{-0.8}$ Myr, $A_J = (1.3 \pm 0.5)$ mag and $A_K = (0.4 \pm 0.5)$ mag within the photometric and spectroscopic error-bars. Additionally, using PARSEC evolutionary isochrones and tracks, we estimated the stellar mass range for each detected source (common in J and K data) and plotted the generalized histogram of mass (MF with error-bars).

Using SPHERE data, we have gone one step further and partially resolved and studied the IMF and density in the core of R136. We show that the stars in the core are still unresolved due to crowding, and the results we obtained are upper limits. Higher angular resolution is mandatory to overcome these difficulties.

Key words. open clusters and associations: individual: RMC136 - Stars: luminosity function, mass function - Stars: massive - Instrumentation: adaptive optics

1. Introduction

*"The two Magellanic clouds, Nubecula major and Nebecula minor, are very remarkable objects... In no other portion of the heavens are so many nebulous and stellar masses thronged together in an equally small space."*¹

R136 is a very massive young star cluster that lies at the center of the Tarantula nebula in the Large Magellanic Cloud (LMC). Hosting the most massive stars known in the Local universe (Crowther et al.2010), R136 provides a unique opportunity to study the formation of massive stars and clusters in their early stages of evolution.

Our understanding of the true nature of R136 has constantly improved with increasing resolution of telescopes.

[★] Based on data collected at the European Southern Observatory, Chile, Guaranteed Time Observation 095.D-0309(K)

¹ From a letter of Sir John Herschel, Feldhuysen, at the Cape of Good Hope, 13th June, 1836.

The fuzzy object in the core of the cluster was initially thought to be a super-massive star with a mass in excess of 1000 M_{\odot} (Feitzinger et al. 1980; Cassinelli et al. 1981; Savage et al. 1983). Image sharpening techniques such as speckle interferometry (Weigelt & Baier 1985) revealed though that this object had many individual stars coined as R136a's Weigelt components. R136a was clearly resolved into hundreds of sources by the Hubble Space Telescope (HST, Hunter et al. 1995; Campbell et al. 1992) that opened routes to better study each of Weigelt components at various wavelengths and resolutions. More recent multi-conjugate Adaptive Optics (AO, Campbell et al. 2010) on the VLT attempted to better resolve the core of R136 with relative success (AO, Campbell et al. 2010).

Combination of photometry, ultraviolet spectrometry (STIS/MAMA, Crowther et al. 2016), visible (HST/FOS, Massey & Hunter 1998) and near-infrared (VLT/SINFONI, Schnurr et al. 2009) observations have resulted in more constraints on the R136 stellar population and its most luminous

stars. Still, questions subsist on the true nature of these stars: e.g. their multiplicity, their mass and the age of the cluster as a whole.

This paper presents the first observations of R136 in the infrared by the second generation ESO's Very Large Telescope (VLT) instrument Spectro-Polarimetric High-contrast Exoplanet Research (SPHERE²) (Beuzit et al. 2008) aiming at uncrowding the compact core of R136 in the near-infrared (near-IR). Thanks to SPHERE's extreme AO system, we reached the same resolution as HST in the visible with the VLT 8.2m Melipal telescope in the K_s band and have surpassed it in J band thanks to the angular resolution, namely 0.035-0.055 arcsec in near-IR and with a better pixel sampling (12.25 mas/pix).

2. Observations

We collected data via Guaranteed Time Observation (GTO) runs to image R136 using the classical imaging mode of IRDIS (Langlois et al. 2014). For our purpose we use the same spectral band splitted into two channels to correct for residual detector hot pixels and uncorrelated detector noise among other instrumental effects. With this method we indeed keep the same photometric efficiency as on single frames. Observations were performed in September 2015, with high dynamic and high angular resolution imaging in J and K_s bands, over a FoV of 10.9"×12.3", centered on the core of the cluster (Figure 1 - Bottom).

In order to qualify our data we compared the reduced J and K_s band images with published images of R136 from HST (WFPC2 and WFC3) in V-band and the VLT/MAD imaging (Campbell et al. 2010) in K-band (Figure 1-Top). This comparison confirms that our data present better spatial resolution and PSF sampling more suitable for applying deconvolution techniques.

Our data consist of 300 frames of 4.0s exposures in both the IRDIS broad-band K_s and J filters (BB-K_s, BB-J). The Wolf-Rayet star R136a1 was used for guiding the AO loop of SPHERE confirming its better than nominal performances surpassing NACO and MAD observations (Figure 1).

The range of airmass during these observations was 1.54 to 1.67. A log of observations is presented in Table 1. We used

Table 1. Exposure time log of VLT/SPHERE observations on R136.

Obs. date	Filter	Single/Total Exposure[s]	λ_{cen} [nm]	$\Delta\lambda$ [nm]
2015-09-22	BB-J	4.0/1200	1245	240
2015-09-22	BB-K	4.0/1200	2182	300

the SPHERE pipeline package³, for correcting dark, flat, distortion, badpixels and detector thermal emission (in K_s). In order to reach the highest sensitivity and the largest number of detectable sources, additional corrections were carried out onto the images. Based on Gaussian fit using selected stars we estimated and corrected the subpixels images drifts before combining the individual images. This allowed to correct for residual tip tilt errors with a few mas accuracy. Still, some uncorrected atmospheric leaks persist in our final images due to the adaptive optics residual halo which is more important in J than in K_s, that

² <https://www.eso.org/sci/facilities/paranal/instruments/sphere.html>

³ http://www.mpaia.de/SPHERE/sphere-web/nightly_builds-page.html

we accurately considered to estimate correct error bars in addition to the Starfinder reduction tool providing photometric errors (see Section 3).

3. Photometry of R136's compact core

For the present study we used the Starfinder package implemented in IDL (Diolaiti et al.2000). Starfinder is designed for the analysis of AO images of crowded fields, like the Galactic Center for instance (Pugliese et al. 2002). It determines the empirical local Point Spread Function (PSF) from several isolated sources in the image and uses this PSF to extract other stellar sources across the FoV. Starfinder estimates also the formal error on the estimated photometry based on photon noise, variance due to the sky and the PSF fitting procedure itself. This error is called "PSF fitting error" hereafter.

Our photometry analysis of R136 was conducted in two steps: 1) stellar sources detection using Starfinder and 2) the background analysis to obtain realistic error bars on the photometry of individual stars beyond the formal PSF fitting error.

In the first step 1110 and 1059 sources were detected in the J and K_s bands, respectively. We stopped source extraction after we attained a minimum correlation of 65% and 80%, in K_s and J bands, between the extracted star with the locally determined PSF according to Starfinder procedures. Indeed, stars with higher correlation coefficients, i.e. more similarity to the PSF, represent higher reliability on their photometric measure. We notice that the PSF changes as a function of radial distance and azimuth along the field. Actually, the AO correcting efficiency degrades as a function of distance from R136a1, which is the reference star for the AO loop. At the borders of the FoV one also approaches the isoplanatic limits. Overall the PSF is not centro-symmetric at large distances from R136a1. We took into account these distortions to estimate the local statistical errors, which become significant on the distant sources from the center of the image, typically $>3''$.

In addition to the correlation coefficient criterion, we applied the limit of standard deviation from the sky brightness (σ_{sky}) for stopping the extraction of sources by Starfinder, i.e. the local PSF maximum value must exceed $2\sigma_{sky}$ over the sky. The faintest common detected stars between J and K_s band, present a signal to noise ratio (SNR) better than 2. To convert stellar fluxes to magnitudes, we used the zeropoints of the instrument (IRDIS) itself. One ADU/s in J and K_s, are 25.405 and 24.256 magnitudes, respectively.

In the second step, after extracting sources, the background image was used to estimate the residual errors in addition to the formal photometric PSF fitting errors of Starfinder. The background image contains 1) AO halo from the atmospheric turbulence, 2) residuals from the photometric analysis in the first step and 3) undetected faint stars. We define the residual error as the fluctuation of the background due to the remaining flux from the photometry using Starfinder and also from the undetected faint sources.

Since the core of R136 is crowded with the brightest stars, the AO halo is the brightest at the center of R136. We removed this large halo in the Fourier space by applying a high bandpass filter (hat function with the diameter equal to the FWHM of the background halo), in order to estimate the fast variations of the background at the scale of the PSF, i.e. 30×30 pixel² area around the source. The final photometric error is set to the quadratic combination of PSF fitting errors and residual errors.

Figure 2 shows these errors separately for each detected sources. The PSF fitting errors (red-pluses) are smaller in K-

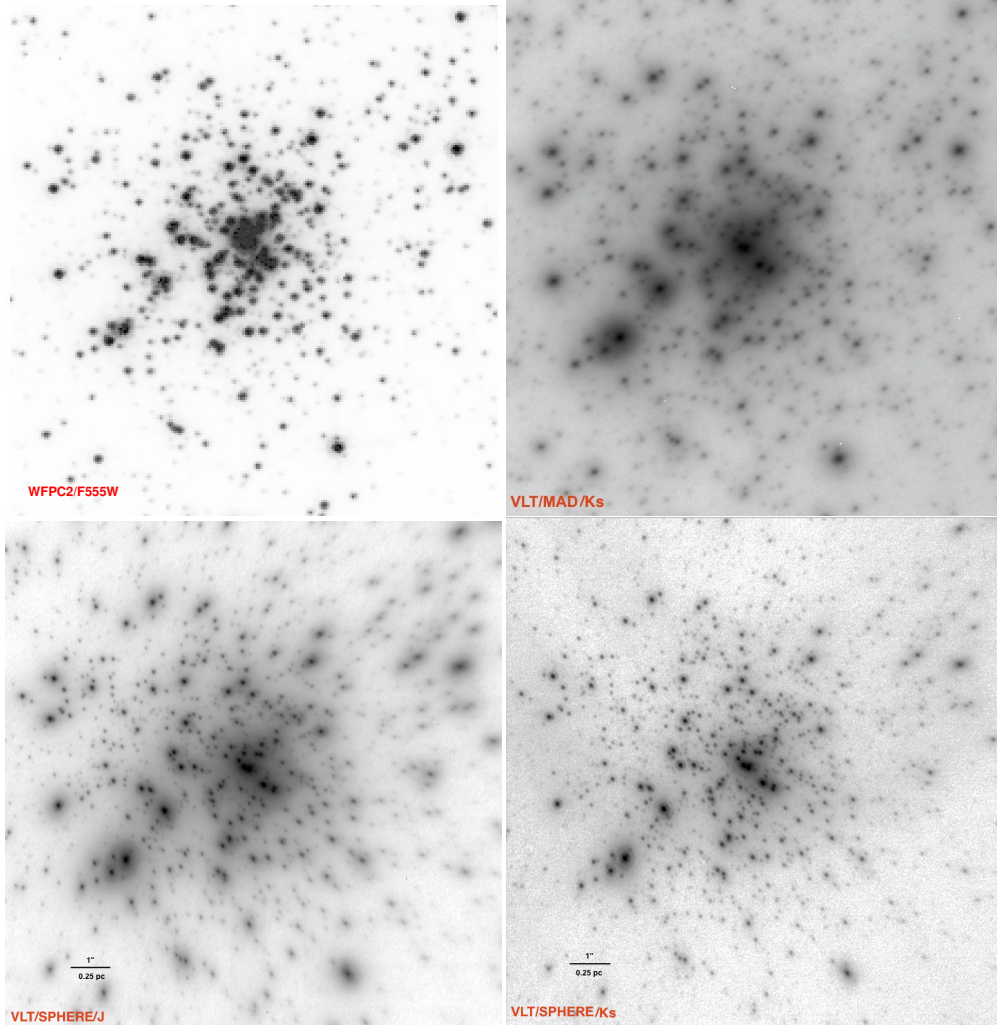


Fig. 1. Comparison of R136's core images at different wavelengths with the highest available angular resolution telescopes. The FoV of all images is the same as IRDIS data ($10.9'' \times 12.3''$). Top-left: HST/WFPC2 in V-band ($\lambda_{cen} 526\text{nm}$), Top-right: VLT/MAD in Ks-band ($\lambda_{cen} 2200\text{nm}$), Bottom-right: SPHERE/IRDIS/Ks ($\lambda_{cen} 2182\text{nm}$); Bottom-left: SPHERE/IRDIS/J ($\lambda_{cen} 1245\text{nm}$)

band as the AO works better in larger wavelengths. But the residual errors (blue-crosses) are larger in K-band because the background fluctuation in longer wavelengths is higher. Figure 5 shows the maps of these two errors in J and K across the field.

The error on the position of the detected stars is shown in Figure 3. All stars brighter than 17 magnitude in ks and 18 magnitude in J, have position errors less than 0.1mas (about 5 AU).

In order to interpret the photometric distribution of the 1110 and 1059 sources in J and Ks bands we conducted an incompleteness test to the core ($r < 3''$) of R136 and outside its core ($r > 3''$) in both J and K-band imaging data. Figure 4 shows the result of incompleteness test which is done by putting 500 artificial stars in each image for each flux value (magnitude). This

experiment was repeated, 9.45×10^5 and 7.9×10^5 times to the J and K images, respectively. Each time one artificial star was added to these images and Starfinder was used again to detect the artificial star. The core of the cluster is very crowded so that the incompleteness does not reach 100% even for the bright artificial stars. This effect is more important for J-band data where the core is fuzzy because of a lower AO correction.

4. Age and extinction

To estimate the stellar ages and the extinction of the core of R136, we used the effective temperature (T_{eff}) and luminosity ($\log L$) of 54 stars studied spectroscopically by Crowther

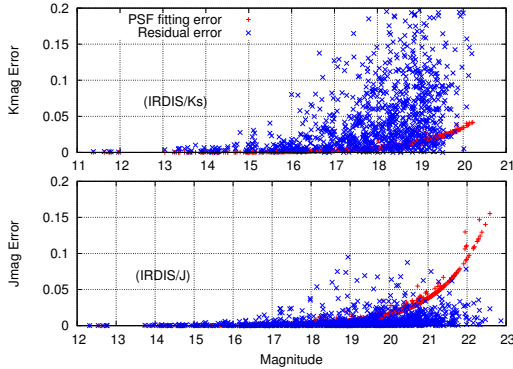


Fig. 2. PSF fitting errors (red pluses) and residual errors (blue crosses) in Ks (top) and J (bottom). PSF fitting error is the outcome of the Starfinder. Residual errors is the outcome of the background analysis after removing the stellar sources from the image.

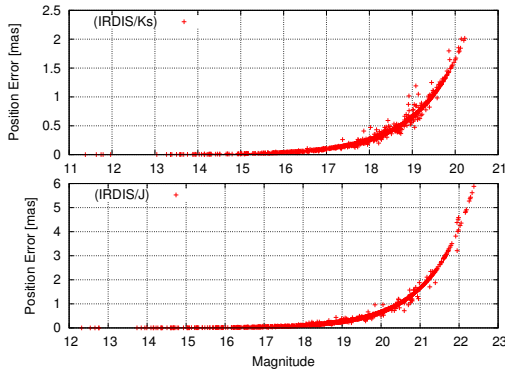


Fig. 3. Error in the position of the stars, in Ks (top) and J (bottom) data. This error is the outcome of the Starfinder and decreases for the bright stars.

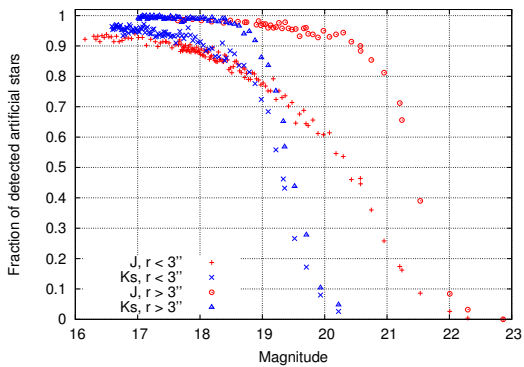


Fig. 4. Incompleteness test in J (red) and K (blue) for two regions: Very core of R136 ($r < 3''$), shown in pluses and crosses, and outside of the core ($r > 3''$), shown in circles and triangles. For each magnitude we used 500 artificial star in order to find the completeness value.

et al. (2016). We also chose a grid of isochrones at different ages (from 0.1 up to 8 Myr) with the LMC metallicity ($Z=0.006$), from the latest sets of PARSEC evolutionary model⁴ (Bressan et al. 2012) which is a complete theoretical library that includes the latest set of stellar phases from pre-main sequence to main sequence and covering stellar masses from 0.1 to 350 M_{\odot} . Figure 7 shows these selected 54 stars with their T_{eff} - $\log L$ (with their error-bars) and sets of isochrones covering them.

By fitting the isochrones to each star, we estimated the age and intrinsic color of each star with the error-bars. We adopt the distance modulus (DM) of 18.45 magnitude which is consistent with the value suggested by Gibson (2000) for LMC.

Table 4 shows the estimated age, initial mass and extinction of these 54 spectroscopically known stars. The values of T_{eff} and $\log L/L_{\odot}$ in the second and third column are taken from Crowther et al. 2016. Figure 8 shows the generalized histogram of the age of these 54 sources. Note that, the age of each star has a Gaussian distribution with a given σ (error) in the histogram. Also note that the large errors on the age and extinction are coming from the large spectroscopic uncertainties (errors on T_{eff} and $\log L/L_{\odot}$). We were also limited by the evolutionary tracks up to 350 M_{\odot} , which explains the upper mass limit of 348 M_{\odot} for very massive stars like R136a1.

Figure 9 shows the histogram of the extinction in J and K and their color-excess.

The age of $1.8^{+1.2}_{-0.8}$ Myr is the most probable age range for these stars. The extinction in J and K is respectively 1.3 ± 0.5 and 0.4 ± 0.5 magnitude. Figure 6 shows the color magnitude diagram (CMD) of detected sources in J and Ks band IRDIS data with their error-bars. The CMD is plotted for the whole FoV (818 sources), in the very core of the cluster ($r < 3''$) and outside ($r > 3''$), from left to right respectively. The error-bars on each point are the combination of the PSF-fitting errors and the residual errors from the background image after removing the stellar sources signals from the images. The PARSEC isochrones at three different ages (1, 2 and 3 Myr) also are plotted in this Figure using DM=18.45 and central values of extinctions in J (1.3 mag) and K (0.4 mag). The uncertainties on the photometric analysis is less than those obtained from the spectroscopic analysis of the massive stars. We can clearly see the main sequence and pre-main sequence branch which show a single-age population. The realistic age and extinction can be estimated using the precise photometric analysis for the 818 stellar sources in the core of R136.

Considering these errors on the age and extinction, one can estimate the stellar mass range for each star. The histogram of mass, which is the mass function (MF), is plotted considering a Gaussian distribution for each stellar mass. Gaussian uncertainty in the mass of each star is accounted for, when constructing the MF. Figure 10 shows the generalized histogram of the mass (MF) at three different ages (1, 2 and 3 Myr). The MF slope for 2 Myr isochrone is $\Gamma_{2Myr} = -1.21 \pm 0.11$ for the mass range of (6 - 160) M_{\odot} . The MF slope is consistent with Kroupa value ($\Gamma = -1.3$) and smaller than Salpeter value ($\Gamma = -1.35$). The derived MF is limited to the resolution of the instrument and also on the detection limit of the observation. In future, using higher angular resolution data, we may resolve binaries and low-mass stars which affects the shape of MF.

⁴ <http://stev.oapd.inaf.it/cgi-bin/cmd>

Table 2. Information on 54 spectroscopically known stars with T_{eff} and $\log L/L_{\odot}$ estimated by Crowther et al. 2016 (second and third columns). Using PARSEC evolutionary isochrones (0.1 to 8 Myr), the age, color excess, extinctions and initial masses are estimated (columns five to eight). N2 and N1 are the number of visual companions for each source in a radius of 0.2" and 0.1" respectively. The identifications (ID) of the sources are from Hunter et al. 1995. Note that we are also limited by the evolutionary tracks up to 350 M_{\odot} which explains zero error-bars for very bright stars.

ID	T_{eff} [kK]	$\log L/L_{\odot}$	age[Myr]	E(J-K)	A(K)	A(J)	$M_{initial}[M_{\odot}]$	N2	N1
3	53.00 ^{+3.0} _{-3.0}	6.94 ^{+0.09} _{-0.09}	0.79 ^{+1.44} _{-0.00}	1.17 ^{+0.02} _{-0.00}	0.27 ^{+0.01} _{-0.25}	1.44 ^{+0.02} _{-0.25}	348.1 ^{+0.0} _{-80.1}	3	1
5	53.00 ^{+3.0} _{-3.0}	6.63 ^{+0.09} _{-0.09}	0.56 ^{+0.00} _{-0.36}	1.14 ^{+0.00} _{-0.00}	-0.39 ^{+0.25} _{-0.00}	0.74 ^{+0.25} _{-0.00}	201.5 ^{+48.5} _{-30.2}	3	0
20	50.00 ^{+4.0} _{-5.0}	6.32 ^{+0.16} _{-0.15}	1.26 ^{+2.29} _{-0.86}	0.95 ^{+0.01} _{-0.02}	0.30 ^{+0.65} _{-0.39}	1.25 ^{+0.65} _{-0.31}	120.0 ^{+30.2} _{-17.9}	2	0
24	46.00 ^{+4.0} _{-3.0}	5.99 ^{+0.10} _{-0.08}	1.78 ^{+2.89} _{-0.78}	0.82 ^{+0.01} _{-0.01}	0.02 ^{+0.22} _{-0.38}	0.84 ^{+0.21} _{-0.38}	75.4 ^{+14.6} _{-22.2}	3	0
27	51.00 ^{+6.0} _{-6.0}	6.28 ^{+0.13} _{-0.13}	1.00 ^{+2.55} _{-0.70}	0.83 ^{+0.02} _{-0.01}	0.79 ^{+0.34} _{-0.42}	1.62 ^{+0.35} _{-0.41}	120.0 ^{+30.0} _{-39.9}	1	1
21	51.00 ^{+6.0} _{-6.0}	6.46 ^{+0.13} _{-0.15}	1.12 ^{+0.70} _{-1.02}	0.85 ^{+0.01} _{-0.03}	1.00 ^{+0.42} _{-0.32}	1.85 ^{+0.41} _{-0.33}	150.2 ^{+39.9} _{-29.3}	1	1
86	46.00 ^{+4.0} _{-3.0}	5.91 ^{+0.10} _{-0.08}	1.78 ^{+2.69} _{-0.98}	0.93 ^{+0.04} _{-0.02}	1.54 ^{+0.47} _{-0.39}	2.47 ^{+0.44} _{-0.35}	67.9 ^{+11.1} _{-14.8}	2	0
66	46.00 ^{+4.0} _{-3.0}	5.70 ^{+0.08} _{-0.08}	1.78 ^{+2.69} _{-1.68}	0.82 ^{+0.02} _{-0.02}	0.70 ^{+0.39} _{-0.43}	1.52 ^{+0.26} _{-0.42}	53.7 ^{+14.8} _{-4.8}	2	0
6	53.00 ^{+3.0} _{-3.0}	6.58 ^{+0.09} _{-0.09}	0.56 ^{+0.23} _{-0.00}	1.25 ^{+0.00} _{-0.00}	-0.28 ^{+0.00} _{-0.07}	0.96 ^{+0.00} _{-0.08}	201.5 ^{+0.0} _{-13.4}	2	1
58	51.00 ^{+6.0} _{-6.0}	5.93 ^{+0.15} _{-0.05}	0.79 ^{+0.69} _{-0.69}	0.80 ^{+0.00} _{-0.02}	0.48 ^{+0.07} _{-0.39}	1.28 ^{+0.08} _{-0.38}	75.0 ^{+13.4} _{-21.7}	0	0
30	38.00 ^{+2.0} _{-2.0}	5.67 ^{+0.05} _{-0.06}	3.55 ^{+0.00} _{-0.39}	0.89 ^{+0.01} _{-0.01}	0.52 ^{+0.19} _{-0.11}	1.40 ^{+0.19} _{-0.10}	45.0 ^{+3.1} _{-0.4}	2	0
70	42.00 ^{+2.0} _{-2.0}	5.57 ^{+0.08} _{-0.08}	2.51 ^{+0.65} _{-0.27}	0.78 ^{+0.01} _{-0.01}	0.37 ^{+0.32} _{-0.24}	1.15 ^{+0.32} _{-0.24}	44.2 ^{+1.7} _{-4.2}	1	1
89	44.00 ^{+2.5} _{-2.5}	5.99 ^{+0.08} _{-0.07}	4.47 ^{+0.00} _{-2.60}	0.86 ^{+0.01} _{-0.01}	1.86 ^{+0.01} _{-0.38}	2.73 ^{+0.19} _{-0.37}	53.1 ^{+23.0} _{-0.0}	2	0
62	51.00 ^{+6.0} _{-6.0}	5.84 ^{+0.15} _{-0.10}	0.20 ^{+0.10} _{-0.10}	0.84 ^{+0.02} _{-0.02}	0.83 ^{+0.33} _{-0.46}	1.66 ^{+0.33} _{-0.43}	70.0 ^{+5.0} _{-16.3}	4	0
19	46.00 ^{+4.0} _{-2.0}	6.52 ^{+0.10} _{-0.05}	1.26 ^{+0.00} _{-0.26}	1.11 ^{+0.01} _{-0.00}	1.34 ^{+0.04} _{-0.30}	2.46 ^{+0.04} _{-0.29}	170.0 ^{+20.2} _{-1.8}	2	1
50	51.00 ^{+6.0} _{-6.0}	6.02 ^{+0.15} _{-0.13}	4.47 ^{+0.00} _{-0.77}	0.78 ^{+0.02} _{-0.02}	0.80 ^{+0.33} _{-0.33}	1.58 ^{+0.33} _{-0.33}	53.3 ^{+46.7} _{-0.0}	2	0
90	44.00 ^{+2.5} _{-2.5}	5.36 ^{+0.08} _{-0.07}	0.79 ^{+1.72} _{-0.69}	0.97 ^{+0.02} _{-0.02}	0.32 ^{+0.32} _{-0.11}	1.29 ^{+0.31} _{-0.10}	38.6 ^{+1.4} _{-4.6}	1	0
141	41.00 ^{+3.0} _{-3.0}	5.09 ^{+0.12} _{-0.12}	2.00 ^{+1.99} _{-1.99}	0.86 ^{+0.03} _{-0.03}	0.55 ^{+0.44} _{-0.44}	1.41 ^{+0.42} _{-0.42}	28.3 ^{+5.6} _{-0.0}	4	0
80	36.00 ^{+2.0} _{-2.0}	5.20 ^{+0.08} _{-0.10}	4.47 ^{+1.16} _{-0.00}	0.86 ^{+0.01} _{-0.01}	0.51 ^{+0.22} _{-0.24}	1.36 ^{+0.22} _{-0.23}	28.0 ^{+0.7} _{-3.5}	1	0
35	48.00 ^{+3.0} _{-3.0}	5.92 ^{+0.08} _{-0.09}	1.58 ^{+0.41} _{-1.19}	0.97 ^{+0.01} _{-0.02}	0.70 ^{+0.30} _{-0.28}	1.67 ^{+0.29} _{-0.27}	70.0 ^{+5.4} _{-3.0}	2	0
78	44.00 ^{+2.5} _{-2.5}	5.47 ^{+0.08} _{-0.07}	2.24 ^{+0.38} _{-1.68}	1.00 ^{+0.01} _{-0.01}	0.55 ^{+0.28} _{-0.28}	1.55 ^{+0.27} _{-0.27}	40.0 ^{+3.0} _{-2.2}	0	0
73	33.00 ^{+2.0} _{-2.0}	5.21 ^{+0.09} _{-0.10}	6.31 ^{+0.00} _{-0.69}	0.77 ^{+0.01} _{-0.01}	0.54 ^{+0.11} _{-0.14}	1.31 ^{+0.11} _{-0.14}	25.4 ^{+2.6} _{-1.4}	2	0
92	40.00 ^{+2.0} _{-2.0}	5.20 ^{+0.07} _{-0.08}	2.82 ^{+1.16} _{-1.56}	1.01 ^{+0.01} _{-0.02}	0.30 ^{+0.35} _{-0.27}	1.31 ^{+0.34} _{-0.26}	30.0 ^{+2.1} _{-2.4}	1	0
143	39.00 ^{+3.0} _{-3.0}	4.99 ^{+0.12} _{-0.14}	3.16 ^{+1.85} _{-3.06}	0.74 ^{+0.02} _{-0.01}	0.22 ^{+0.35} _{-0.40}	0.96 ^{+0.35} _{-0.42}	24.9 ^{+5.1} _{-3.3}	4	0
112	36.00 ^{+4.0} _{-4.0}	5.01 ^{+0.11} _{-0.11}	4.47 ^{+3.47} _{-3.47}	0.74 ^{+0.01} _{-0.01}	0.07 ^{+0.46} _{-0.46}	0.81 ^{+0.46} _{-0.46}	24.0 ^{+4.0} _{-4.0}	3	1
135	33.00 ^{+2.0} _{-2.0}	4.86 ^{+0.09} _{-0.10}	7.08 ^{+0.86} _{-0.97}	0.77 ^{+0.01} _{-0.01}	0.51 ^{+0.14} _{-0.35}	1.28 ^{+0.13} _{-0.34}	19.4 ^{+1.9} _{-1.4}	3	1
69	42.00 ^{+2.0} _{-2.0}	5.49 ^{+0.10} _{-0.08}	2.82 ^{+0.82} _{-0.82}	0.82 ^{+0.01} _{-0.01}	0.45 ^{+0.35} _{-0.28}	1.28 ^{+0.34} _{-0.28}	40.0 ^{+1.4} _{-2.2}	3	0
52	46.00 ^{+4.0} _{-4.0}	5.74 ^{+0.10} _{-0.08}	2.00 ^{+1.80} _{-1.80}	0.82 ^{+0.01} _{-0.01}	0.62 ^{+0.32} _{-0.44}	1.44 ^{+0.31} _{-0.43}	55.0 ^{+10.0} _{-5.0}	2	0
48	51.00 ^{+6.0} _{-6.0}	5.97 ^{+0.13} _{-0.15}	1.26 ^{+1.16} _{-1.16}	0.76 ^{+0.02} _{-0.02}	0.27 ^{+0.33} _{-0.33}	1.03 ^{+0.33} _{-0.33}	75.0 ^{+21.7} _{-21.7}	3	0
94	43.00 ^{+3.0} _{-3.0}	5.31 ^{+0.08} _{-0.09}	2.00 ^{+1.17} _{-1.90}	0.76 ^{+0.01} _{-0.01}	0.39 ^{+0.34} _{-0.35}	1.15 ^{+0.33} _{-0.35}	34.8 ^{+5.2} _{-3.5}	2	0
115	33.00 ^{+2.0} _{-2.0}	4.82 ^{+0.09} _{-0.09}	7.08 ^{+0.86} _{-2.07}	0.98 ^{+0.01} _{-0.01}	0.52 ^{+0.27} _{-0.25}	1.50 ^{+0.26} _{-0.23}	18.8 ^{+1.0} _{-1.0}	1	0
132	33.00 ^{+2.0} _{-2.0}	4.76 ^{+0.09} _{-0.10}	7.08 ^{+0.86} _{-2.61}	0.93 ^{+0.01} _{-0.01}	0.28 ^{+0.22} _{-0.30}	1.21 ^{+0.21} _{-0.29}	18.1 ^{+2.2} _{-0.9}	2	0
36	46.00 ^{+4.0} _{-4.0}	5.94 ^{+0.10} _{-0.05}	1.78 ^{+0.22} _{-0.78}	0.82 ^{+0.00} _{-0.00}	-0.23 ^{+0.29} _{-0.29}	0.59 ^{+0.29} _{-0.29}	70.0 ^{+12.9} _{-5.0}	1	0
173	33.00 ^{+2.0} _{-2.0}	4.78 ^{+0.09} _{-0.10}	6.31 ^{+1.63} _{-1.84}	0.98 ^{+0.01} _{-0.02}	0.61 ^{+0.33} _{-0.36}	1.59 ^{+0.32} _{-0.35}	19.2 ^{+1.1} _{-1.9}	3	0
75	44.00 ^{+2.5} _{-2.5}	5.54 ^{+0.08} _{-0.07}	1.58 ^{+1.23} _{-1.02}	0.99 ^{+0.01} _{-0.01}	0.68 ^{+0.45} _{-0.23}	1.67 ^{+0.44} _{-0.23}	45.0 ^{+1.7} _{-5.0}	2	0
114	37.00 ^{+3.0} _{-3.0}	4.99 ^{+0.12} _{-0.14}	3.98 ^{+1.64} _{-3.19}	0.98 ^{+0.01} _{-0.01}	0.44 ^{+0.43} _{-0.48}	1.43 ^{+0.42} _{-0.46}	24.0 ^{+4.0} _{-2.7}	1	0
108	37.00 ^{+3.0} _{-3.0}	5.15 ^{+0.12} _{-0.12}	3.98 ^{+1.64} _{-1.47}	1.03 ^{+0.02} _{-0.01}	1.14 ^{+0.42} _{-0.42}	2.17 ^{+0.41} _{-0.40}	27.6 ^{+2.6} _{-4.5}	2	0
31	51.00 ^{+6.0} _{-6.0}	6.19 ^{+0.13} _{-0.15}	1.26 ^{+1.42} _{-1.16}	1.00 ^{+0.00} _{-0.02}	0.83 ^{+0.31} _{-0.36}	1.83 ^{+0.30} _{-0.36}	100.0 ^{+21.1} _{-38.8}	1	0
49	43.00 ^{+3.0} _{-3.0}	5.60 ^{+0.08} _{-0.09}	2.51 ^{+0.65} _{-1.39}	0.88 ^{+0.01} _{-0.00}	0.19 ^{+0.35} _{-0.42}	1.08 ^{+0.35} _{-0.41}	45.0 ^{+3.0} _{-5.0}	1	0
46	48.00 ^{+4.0} _{-4.0}	6.02 ^{+0.12} _{-0.09}	1.26 ^{+3.21} _{-0.70}	0.75 ^{+0.00} _{-0.02}	0.15 ^{+0.50} _{-0.28}	0.90 ^{+0.50} _{-0.28}	82.9 ^{+21.1} _{-29.6}	3	0
47	48.00 ^{+4.0} _{-4.0}	5.95 ^{+0.14} _{-0.13}	1.41 ^{+3.05} _{-1.31}	0.77 ^{+0.00} _{-0.02}	0.04 ^{+0.38} _{-0.36}	0.81 ^{+0.38} _{-0.36}	73.5 ^{+16.6} _{-20.0}	3	0
40	51.00 ^{+6.0} _{-6.0}	5.97 ^{+0.13} _{-0.15}	1.26 ^{+1.42} _{-1.16}	0.81 ^{+0.02} _{-0.02}	0.41 ^{+0.36} _{-0.33}	1.23 ^{+0.36} _{-0.33}	75.0 ^{+21.7} _{-21.7}	1	0
116	37.00 ^{+3.0} _{-3.0}	4.97 ^{+0.12} _{-0.12}	3.55 ^{+2.08} _{-1.45}	1.33 ^{+0.01} _{-0.01}	0.54 ^{+0.31} _{-0.31}	1.87 ^{+0.31} _{-0.31}	24.0 ^{+3.1} _{-4.5}	1	1
118	39.00 ^{+3.0} _{-3.0}	5.07 ^{+0.12} _{-0.14}	3.16 ^{+1.85} _{-3.06}	0.70 ^{+0.01} _{-0.00}	-0.11 ^{+0.12} _{-0.41}	0.58 ^{+0.31} _{-0.40}	26.5 ^{+3.8} _{-3.3}	2	0
42	46.00 ^{+4.0} _{-4.0}	5.64 ^{+0.10} _{-0.08}	1.58 ^{+0.93} _{-1.48}	1.12 ^{+0.01} _{-0.01}	0.20 ^{+0.45} _{-0.29}	1.32 ^{+0.44} _{-0.28}	50.0 ^{+10.0} _{-5.8}	0	0
55	51.00 ^{+6.0} _{-6.0}	5.93 ^{+0.13} _{-0.15}	0.79 ^{+1.04} _{-0.69}	0.92 ^{+0.01} _{-0.02}	0.73 ^{+0.33} _{-0.39}	1.65 ^{+0.38} _{-0.38}	75.0 ^{+21.7} _{-21.7}	0	0
71	44.00 ^{+2.5} _{-2.5}	5.49 ^{+0.08} _{-0.07}	1.78 ^{+1.04} _{-1.22}	1.03 ^{+0.01} _{-0.01}	0.55 ^{+0.30} _{-0.18}	1.57 ^{+0.29} _{-0.17}	42.3 ^{+2.7} _{-4.5}	1	0
121	33.00 ^{+2.0} _{-2.0}	4.84 ^{+0.09} _{-0.07}	7.08 ^{+0.86} _{-1.46}	0.95 ^{+0.01} _{-0.01}	0.66 ^{+0.22} _{-0.22}	1.61 ^{+0.22} _{-0.22}	19.4 ^{+1.4} _{-1.4}	1	0
9	41.00 ^{+3.0} _{-3.0}	6.30 ^{+0.11} _{-0.12}	1.78 ^{+0.22} _{-0.19}	0.94 ^{+0.00} _{-0.01}	-0.15 ^{+0.25} _{-0.43}	0.78 ^{+0.25} _{-0.43}	119.6 ^{+17.7} _{-24.6}	1	0
65	44.00 ^{+2.5} _{-2.5}	5.56 ^{+0.08} _{-0.07}	2.00 ^{+0.82} _{-1.20}	0.74 ^{+0.01} _{-0.01}	-0.13 ^{+0.30} _{-0.30}	0.62 ^{+0.33} _{-0.29}	45.0 ^{+3.0} _{-1.9}	1	0
134	38.00 ^{+2.0} _{-2.0}	4.91 ^{+0.05} _{-0.06}	2.24 ^{+2.23} _{-1.44}	1.10 ^{+0.01} _{-0.01}	0.60 ^{+0.21} _{-0.18}	1.71 ^{+0.21} _{-0.18}	24.0 ^{+1.9} _{-2.5}	1	0
64	42.00 ^{+2.0} _{-2.0}	5.60 ^{+0.07} _{-0.08}	2.51 ^{+0.65} _{-0.27}	0.77 ^{+0.00} _{-0.01}	0.06 ^{+0.35} _{-0.35}	0.82 ^{+0.35} _{-0.35}	45.0 ^{+1.6} _{-1.6}	0	0
45	43.00 ^{+3.0} _{-3.0}	5.76 ^{+0.08} _{-0.09}	2.24 ^{+0.58} _{-0.46}	0.66 ^{+0.00} _{-0.00}	0.17 ^{+0.38} _{-0.25}	0.83 ^{+0.38} _{-0.25}	55.0 ^{+3.0} _{-5.0}	1	0
123	40.00 ^{+2.0} _{-2.0}	5.04 ^{+0.07} _{-0.08}	1.12 ^{+2.43} _{-1.02}	1.19 ^{+0.01} _{-0.01}	0.63 ^{+0.24} _{-0.18}	1.81 ^{+0.23} _{-0.17}	28.0 ^{+2.0} _{-3.2}	0	0

Table 3. List of 20 stars which have a companion closer than $0.08''$. These stars detected in both J- and Ks- band data.

ID1	ID2	$FluxRatio_K$	$FluxRatio_J$	Separation[mas]
59	3(a3)	0.044	0.124	58.88 ± 2.14
357	272	0.699	0.577	59.87 ± 0.17
760	519	0.567	0.896	62.62 ± 5.71
643	214	0.208	0.139	63.67 ± 0.31
319	79	0.166	0.177	64.11 ± 4.23
804	517	0.512	0.365	65.06 ± 1.40
380	265	0.630	0.324	66.29 ± 1.61
807	565	0.571	0.830	67.12 ± 3.18
11(a9)	8(a6)	0.878	0.959	70.07 ± 0.88
25	4(c)	0.114	0.095	70.27 ± 0.07
396	56	0.079	0.065	71.25 ± 2.45
635	589	0.870	0.730	72.21 ± 2.30
541	489	0.867	0.964	73.65 ± 4.21
637	539	0.774	1.002	73.84 ± 1.08
312	87	0.197	0.188	74.13 ± 2.37
72	54	0.686	0.714	74.47 ± 0.45
16	1(a1)	0.112	0.152	75.32 ± 2.33
761	655	0.796	0.689	75.65 ± 0.61
353	305	0.819	0.450	75.91 ± 0.94
317	262	0.766	0.413	79.30 ± 0.09

5. Visual companions

For each star, detected in both J and K, we determined a distance between the star and its closest neighbor. Figure 11 shows the number of close detected stars in K (red) and J (blue) vs their separation in arc-second. More than 250 (pair of) stars have a closest neighbor at the separation less than $0.2''$. Over 90% of massive objects (brighter than 17 mag in K and 16 mag in J) have a closest neighbor with a separation of less than $0.2''$. Figure 11 shows the separation between the visual close stars versus their distance from R136a1 in the core. This figure indicates that even the sources at larger radii have close visual companions, so that the large number of close visual companions in not just an effect of 2D projection on the sky across the FoV. For the sake of simplicity, regardless of physically bound or not, we call these closely stars **visual companions** hereafter.

The most massive stars R136a1, R136a3 and R136c have visual companions which are detected for the first time. R136a3 is also resolved as two stars with the PSF fitting. Both stars have high correlation coefficient (above 70%) with the input PSF. The separation between R136a3 primary and secondary is about $58.9 \pm 2.14 mas$ which is larger than the FWHM of the PSF. Note that even the closest visual companions (like R136a3) are physically far from each other ($0.059''$ is 2890 AU). This visual separation produces a period over $P = 10^4 yr$, so probably these sources are not gravitationally bound to each other. Table 3 shows the list of the 20 stars, detected in both J and K data, which have companions closer than $0.08''$. The flux ratio between two companions in K and J band are given in the third and fourth column, respectively. Their separation [in mas] also is given in the last column. Among these stars, we identified visual companions for R136a1 and R136a3, for the first time.

6. Density and surface brightness profile

The unexpected number of detected sources in a small FoV and of new resolved companions in R136 indicates that this compact cluster is more crowded than thought before. The error-bars on the stellar masses and also on the age and extinction of the clus-

ter itself are large enough to make it difficult to study the density profile of R136. Instead, one can scrutinize the surface brightness profile (SBP) of this cluster which is less affected by the confusion and crowding. We obtained the SBP by measuring radial profiles for J and Ks images, centered at R136a1. The SBP informs us on the average magnitude per pixel at different radii. Figure 12 depicts the SBP of the core of R136 in J and K. On average the SBP in Ks is brighter than J, which can be caused by the extinction or brighter stars in Ks. One can notice a number of bumps on the SBP at 0.08, 0.15, 0.46, 1.17 pc radii roughly. These radial distances are the locations of known WR stars. The position of 5 WRs in the FoV is shown in the SBP plot. These stars have extensive emissions in the Ks band because of their wind and mass loss.

Using the stellar masses estimated at the age of 2 Myr and extinction values in J and K, $A_J = (1.3 \pm 0.5) mag$ and $A_K = (0.4 \pm 0.5) mag$, we plotted the two-dimensional (projected) density profile (Figure 13). We used an Elson-Fall-Freeman (EFF) profile (Elson et al. 1987) to fit the projected mass density in the core of R136 (Eq. 1).

$$\rho[M_\odot/pc^2] = \frac{\rho_0}{(1 + \frac{r^2}{a^2})^{\frac{\gamma+1}{2}}} \quad (1)$$

We estimate the central mass density of $\rho_0 = (1.15_{0.24}^{0.29}) \times 10^4 [M_\odot/pc^2]$ and the parameters $\gamma = 2.04 \pm 0.54$ and $a = 0.45 \pm 0.12$. Total observed mass of the clusters for $r < 1.4 pc$ is $M_{obs} = (1.06_{0.16}^{0.20}) \times 10^4 M_\odot$. We could detect stellar masses down to $2 M_\odot$, so total mass of the cluster depends on the shape of MF and the lowest mass limit. The real stellar masses remain open as we are limited to the angular resolution of SPHERE/IRDIS, so the estimated central projected density is a lower limit to the real central density.

Note that the estimated density is projected in two-dimension (2D). In order to estimate the three dimensional (3D) density approximately, we consider R136 is spherically symmetric and has a radius of $R_{cluster}$. The density profiles are estimated for different $R_{cluster}$ values, from 2 pc to 6pc. Hence, 3D central densities, γ and a are computed by fitting EFF profile (Eq. 1). Table 4, shows the fitting (3D) parameters for R136 considering different values of $R_{cluster}$. The total mass of the cluster can be estimated by extrapolating to the considered $R_{cluster}$. The ratio of the observed total mass within $r < 1.4 pc$ to the total mass estimated of the cluster, within a given radius ($R_{cluster}$) also is given in the last column of Table 4.

Estimated value of γ and a in 2D and 3D are consistent and the shape of the densities are flatter than Plummer model (close to King model). All the 3D central densities are smaller than the previous values given by Mackey & Gilmore (2003) and Selman & Melnick (2013). Value of γ is consistent with the values derived by these authors. Computed value of a is consistent with the estimated value by Selman & Melnick (2013).

7. Discussion and conclusion

In this study we presented photometric analysis of the core of R136 using the VLT/SPHERE instrument in the near-IR. The high quality and resolution of these data open a new perspective on our understandings on R136. For the first time, more than thousand sources have been detected in K and J-band data in the small FoV of IRDIS ($10.9'' \times 12.3''$) covering almost $2.7 \times 3.1 pc$ of R136's core. HST WFPC2 and WFC3 data, due to a lower resolution and pixel sampling, did not detect such a number of

Table 4. Estimation of central density of R136 in three-dimension considering different $R_{cluster}$. First column gives the hypothetical radius of the cluster. The second column is the three-dimensional central mass density. Third and fourth columns are the fitting parameters, γ and a , in the Eq. 1. Finally the last column is the ratio of observed mass which is limited by $r < 1.4pc$, to the total mass estimated of the cluster, within a given radius. $M_{obs} = (1.06_{0.16}^{0.20}) \times 10^4 M_{\odot}$.

$R_{cluster}$ [pc]	$\log(\rho_0)$ [M_{\odot}/pc^3]	γ	a	M_{obs}/M_{total}
2	3.49 ± 0.10	1.72 ± 0.34	0.35 ± 0.08	0.91 ± 0.02
3	3.32 ± 0.10	1.97 ± 0.39	0.39 ± 0.09	0.84 ± 0.03
4	3.20 ± 0.10	2.07 ± 0.41	0.40 ± 0.09	0.81 ± 0.03
5	3.11 ± 0.10	2.13 ± 0.42	0.41 ± 0.09	0.79 ± 0.03
6	3.03 ± 0.10	2.17 ± 0.43	0.42 ± 0.10	0.78 ± 0.03

sources in the R136's core. For the ground-based telescopes, the best data comes from VLT/MAD, where the AO quality (Strehl ratios of 15-30% in Ks) is not as good as with SPHERE (Strehl ratios of 80% in Ks). So the confusion, especially in the core remains large enough for the sources being undetectable in its core.

In SPHERE/IRDIS data, more than 60% of stars have companions closer than $0.2''$ ($0.05pc$). 90% of the very massive bright stars which already have been studied spectroscopically by Crowther et al. (2016), have visual companions. The large error-bars on the spectroscopic parameters (T_{eff} and $\log L$) prevent us to estimate the age, extinction and stellar masses accurately. From our analysis, the most probable age of the core is $1.8_{-0.8}^{+1.2}$ Myr and the extinction in J and K are $A_J = (1.3 \pm 0.5) mag$ and $A_K = (0.4 \pm 0.5) mag$, respectively. Considering the photometric errors, the stellar masses are estimated at different ages with a broad extinction range. The MF slope for 2 Myr isochrone is $\Gamma_{2Myr} = -1.21 \pm 0.11$ for the mass range of (6 - 160) M_{\odot} . As the core gets better resolved, more stars are detected. The MF slope is consistent with Kroupa value ($\Gamma = -1.3$) and smaller than Salpeter value ($\Gamma = -1.35$). The derived MF is limited to the resolution of the instrument and also on the detection limit of the observation. Higher angular resolution data may resolve binaries and low-mass stars which affects the shape of MF. Figure 13 shows the density profile of the R136's core at 2 Myr. The lower limit of the central density of R136 is $\rho_0 = (1.15_{0.24}^{0.29}) \times 10^4 [M_{\odot}/pc^2]$ at 2 Myr which is about $\rho_0 = 288 [stars/pc^2]$. Observed total mass of R136 for $r < 1.4pc$ is $M_{obs} = (1.06_{0.16}^{0.20}) \times 10^4 M_{\odot}$. Considering R136 is a spherically symmetric cluster with Radius $R_{cluster}$ (Table 4), we estimated 3D density profile. The 3D central densities are smaller than the values estimated in previous studies. Computed values of γ and a (Eq. 1) are consistent in 2D and 3D considering different $R_{cluster}$. All density profiles are flatter than Plummer model ($\gamma = 4.0$).

Very massive stars in R136 have similar characteristics as the galactic WR stars in the core of NGC3603. NGC3603 is almost 8 times closer than R136. One can see the effect of confusion in Figure 14 in which we visualize NGC3603 at the distance of R136 (Figure 14 Middle). Using Starfinder we detected 408 and 288 stars in J and Ks images respectively (Khorrami et al. 2016). Using the same criteria for Starfinder, we only detect 109 and 52 sources in J and Ks images of NGC3603 at the distance of R136, which means that more than 70% of the stars cannot be detected. This implies that about 1000 detected stars in the R136's core ($r < 6''$) are possibly 30% of the real number. The average density in this region ($r < 6''$) would increase from 71 [star/pc²] to 230 [star/pc²]. The lack of resolution prevents us to accurately

estimate stellar masses, core density and density profile, whilst SBP turns out to be less affected. Figure 15 shows the SBP of NGC3603 both from IRDIS data in J and Ks band, directly and simulated as would be located at a distance of R136. The general trend is not affected.

Using SPHERE data, we have gone one step further and partially resolved and understood the core of R136 but this is certainly not the final step. R136 needs to be observed in the future with higher resolution (E-ELT) and/or a more stable PSF (JWST), therefore deeper field imaging. The cluster would then be better characterized for its age, individual and multiple stars and ultimately its kinematics on a long enough temporal baseline of observation.

Acknowledgements. Acknowledgements. ZK is supported by the Erasmus Mundus Joint Doctorate Program by Grant Number 2012-1710 from the EACEA of the European Commission and the University of Nice foundation. The authors are indebted to Dr. A. Stolte for her comments and suggestions for improving the original manuscript. SPHERE is an instrument designed and built by a consortium consisting of IPAG (Grenoble, France), MPIA (Heidelberg, Germany), LAM (Marseille, France), LESIA (Paris, France), Laboratoire Lagrange (Nice, France), INAF– Osservatorio di Padova (Italy), Observatoire de Genève (Switzerland), ETH Zurich (Switzerland), NOVA (Netherlands), ONERA (France) and ASTRON (Netherlands), in collaboration with ESO. SPHERE was funded by ESO, with additional contributions from CNRS (France), MPIA (Germany), INAF (Italy), FINES (Switzerland) and NOVA (Netherlands). SPHERE also received funding from the European Commission Sixth and Seventh Framework Programmes as part of the Optical Infrared Coordination Network for Astronomy (OPTICON) under grant number RII3-Ct-2004-001566 for FP6 (2004-2008), grant number 226604 for FP7 (2009-2012) and grant number 312430 for FP7 (2013-2016).

References

- Andersen, M., Zinnecker, H., Moneti, A. et al. 2009, ApJ 707, 1347
Banerjee, S., Kroupa, P., Oh, S. 2012, MNRAS 426, 1416
Beuzit, J.-L., Feldt, M., Dohlen, K., et al. 2008, SPIE, 7014, 701418
Bressan, A.; Marigo, P.; Girardi, L. et al., 2012, MNRAS, 427, 127
Campbell, B., Hunter, D. A., Holtzman, J. A., et al. 1992, AJ, 104, 1721
Campbell, M.A., Evans, C.J., Mackey, A.D., Gieles, M., Alves, J., Ascenso, J., Bastian, N., Longmore, A.J. 2010, MNRAS 405, 421
Cassinelli, J. P., Mathis, J. S., Savage, B. D., 1981, Sci, 212, 1497
Crowther, P. A., Schnurr, O., Hirschi, R., Yusof, N., Parker, R. J., Goodwin, S. P., Kassim, H.A. 2010, MNRAS, 408, 731
Crowther, P. A., Caballero-Nieves, S. M., Bostroem, K. A., et al. 2016, MNRAS, 458, 624
Diolaiti, E., Bendinelli, O., Bonaccini, D., Close, L., Currie, D., Parmeggiani, G. 2000, A&AS, 147, 335
Elson, R. A. W., Fall, S. M., & Freeman, K. C. 1987, ApJ, 323, 54
Feast, M.W., Thackeray, A.D., Wesselink, A.J., 1960, MNRAS 121, 337
Feitzinger, J.V., Schlosser, W., Schmidt-Kaler, T., Winkler, C., 1980, A&A 84, 50
Feitzinger, J.V., Hanuschik, R.W., Schmidt-Kaler, T. 1983, A&A 120, 269
Figer, D.F., 2005, Nat 434, 192

- Gibson, B. K. 2000, MemSAI, 71, 693
Hunter, D. A., Shaya, E. J., Holtzman, J. A. 1995, ApJ 448, 179
Khorrami, Z., Lanz, T., Vakili, F., et al. 2016, A&A, 588, L7
Kroupa, P., 2001, MNRAS, 322
Langlois, M., Vigan, A., Dohlen, K., et al. 2014, SPIE, 9147, 91479P
Mackey, A. D., & Gilmore, G. F. 2003, MNRAS, 338, 85
Massey, P., Hunter D. A., 1998, ApJ. 493, 180
Pugliese, G., Christou, J., Koehler, R., & Drummond, J. 2002, Bulletin of the American Astronomical Society, 34, 55.05
Savage, B. D., Fitzpatrick, E. L., Cassinelli, J. P., & Ebbets, D. C. 1983, APJ, 273, 597
Schnurr, O., Chené, A. -N., Casoli, J., Moffat, A. F. J., St-Louis, N. 2009, MNRAS, 397, 2049
Selman, F. J., & Melnick, J. 2013, A&A, 552, A94
Weigelt, G., Baier, G., 1985, A&A 150, L18

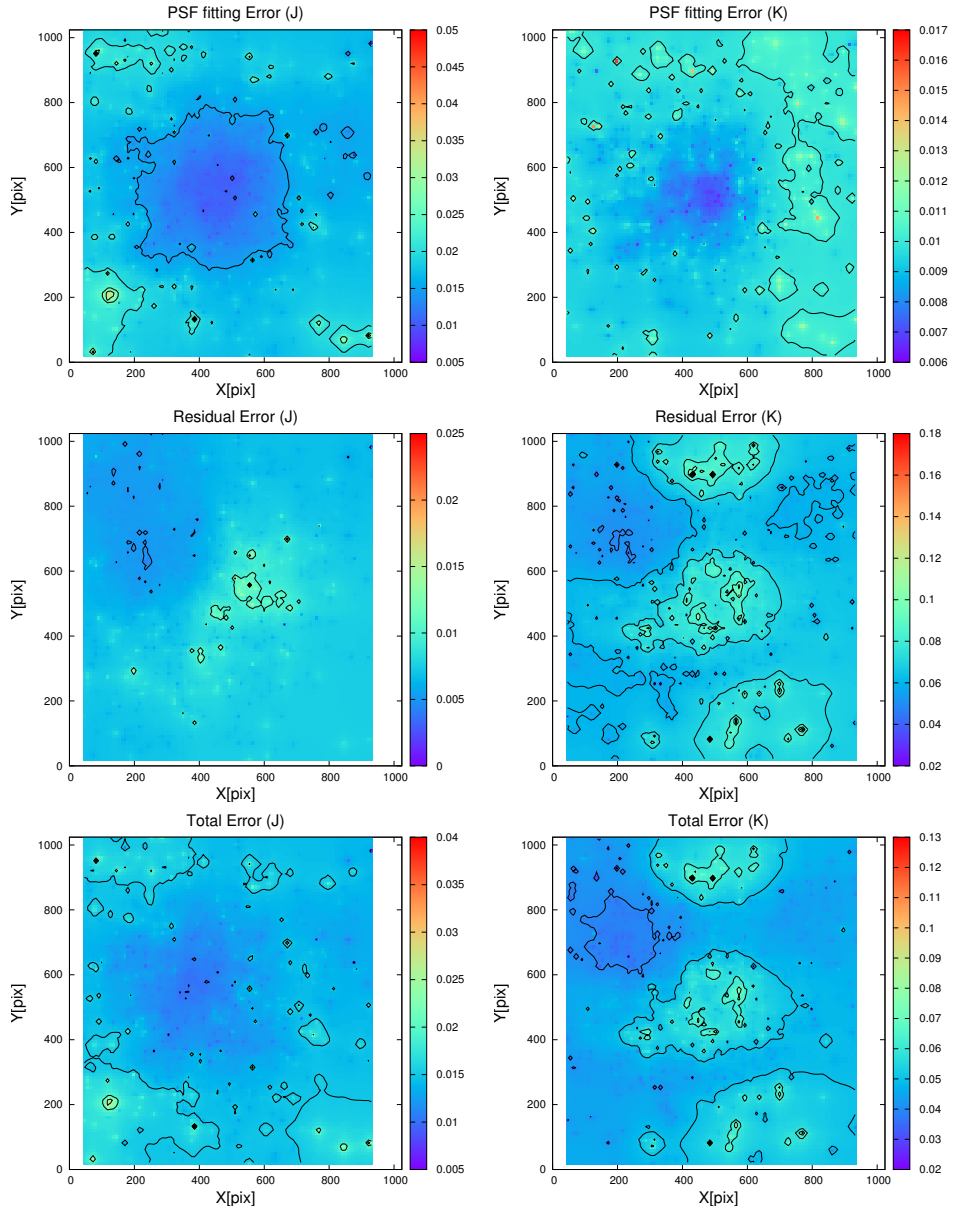


Fig. 5. Map of the photometric, residual and total error-bars. Top: map of the PSF fitting errors (outcome pf the Sairfinder photometry) along the IRDIS FoV. Middle: map of the residual errors, outcome of the background analysis after removing the stellar sources signals from the image. Bottom: map of the total error, combination of the PSF-fitting errors and the residuals background errors. Left images are in the J band. Right images are in the Ks band

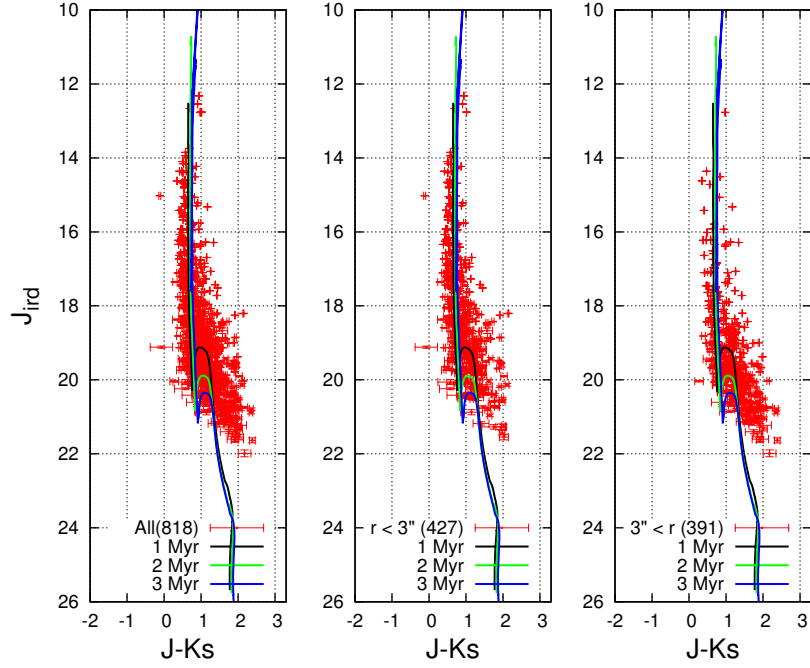


Fig. 6. CMD of 818 detected sources in J and Ks band images of SPHERE/IRDIS from the core of R136. Solid black, pink and blue lines show the PARSEC isochrones at the ages of 1, 2 and 3 Myr (corrected for distance modulus of 18.45 and central values of extinctions, $A_J = 1.3 \text{ mag}$ and $A_K = 0.4 \text{ mag}$). The CMD is plotted for the whole FoV (818 sources), in the very core of the cluster ($r < 3''$) and outside ($r > 3''$), from left to right respectively. The error-bars on each point is the combination of the PSF-fitting errors and the residual errors from the background image after removing the stellar sources signals from the images.

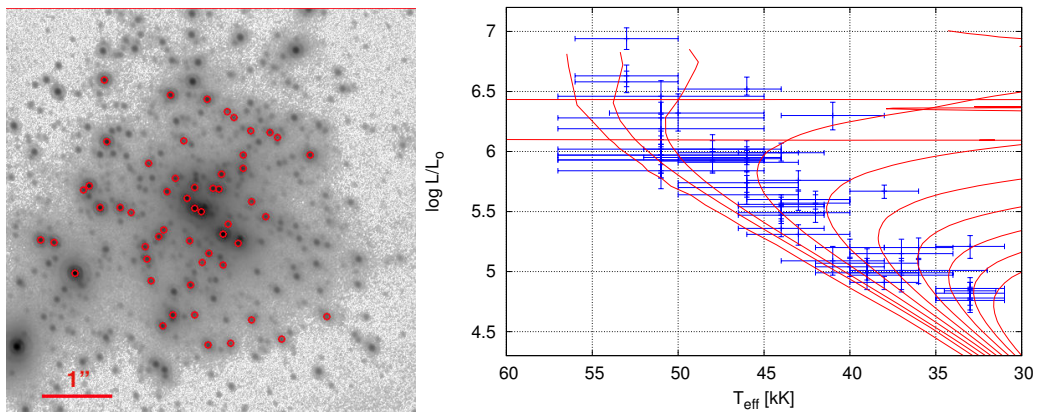


Fig. 7. The left image corresponds to the IRDIS/Ks (FoV $6'' \times 6''$) on which the 54 spectroscopically known stars from (Crowther et al. 2016) have been added as red circles. The right plot depicts the T_{eff} , $\log L/L_{\odot}$ and corresponding error-bars on these 54 sources taken from Crowther et al. 2016 in blue. The solid red lines indicate the PARSEC isochrones covering ages from 0.1 to 8 Myr.

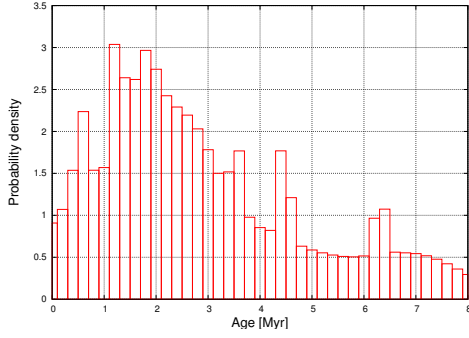


Fig. 8. Generalized histogram of the age of 54 known stars from Crowther et al. 2016. (shown in Figure 7). We used PARSEC isochrones at different ages to estimate the age-range for each spectroscopically known stars.

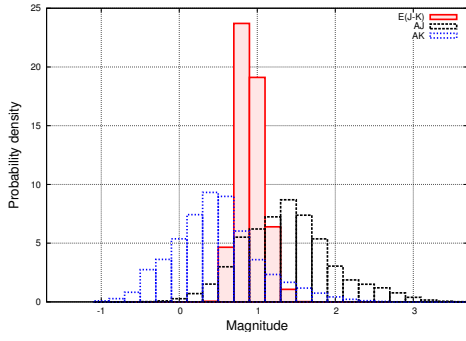


Fig. 9. Generalized histogram of the extinction of 54 spectroscopically known stars from Crowther et al. 2016. (shown in Figure 7). We used PARSEC models to estimate the extinction for each of these stars according to its age-range.

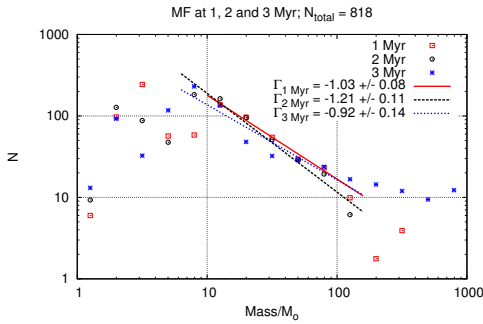


Fig. 10. Generalized histogram of the stellar masses (MF) at 1, 2 and 3 Myr. PARSEC models used to estimate the stellar-mass range for each source using extinction-range.

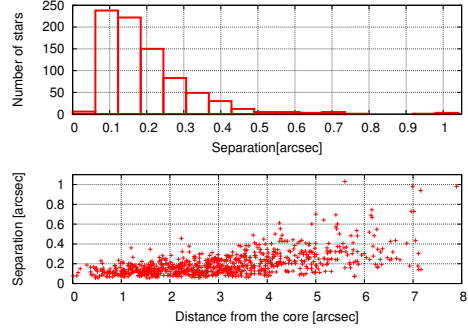


Fig. 11. Top: Histogram of the separation of the close detected sources. For each star which is detected in both J and K data, we determined a distance between the star and its closest neighbor. Bottom: Separation of the visual close detected sources versus their distance from the core of R136.

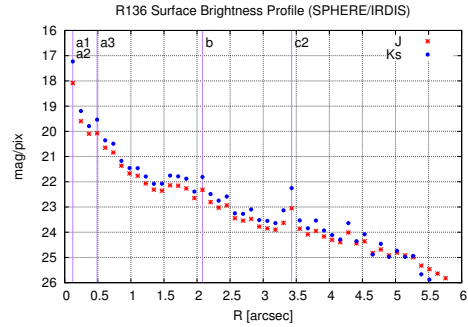


Fig. 12. SBP (mag/pixel) of R136 in IRDIS FoV in IRDIS FoV centered on R136a1. The radial position of the five WR stars are shown with the solid vertical purple lines.

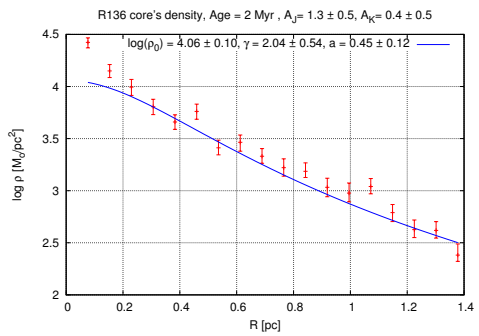


Fig. 13. Projected mass density [M_{\odot}/pc^2] profile of R136 in IRDIS FoV centered on R136a1. The stellar masses are estimated at the age of 2 Myr with extinction values of $A_J = (1.3 \pm 0.5) \text{ mag}$ and $A_K = (0.4 \pm 0.5) \text{ mag}$ in J and Ks band. Eq. 1 is used to fit the blue solid line to the data.

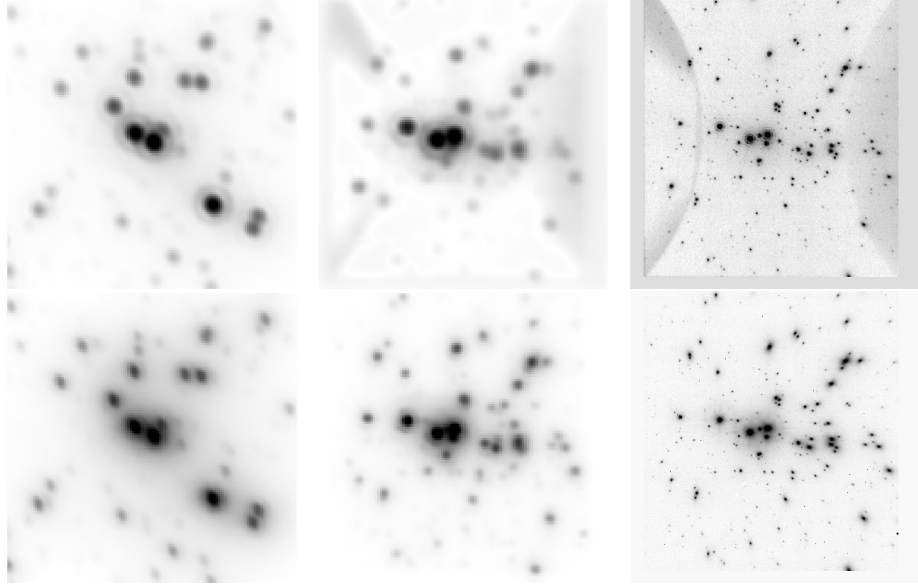


Fig. 14. Comparison of NGC3603 and R136 images from VLT/SPHERE. Left: Core of R136 ($1.56'' \times 1.56''$) at its real distance. Right: Core of NGC3603 ($12.5'' \times 12.5''$) at its real distance. Middle: NGC3603 as it would appear at the same distance as R136. Upper and bottom panels are in IRDIS Ks and J band bands images, respectively.

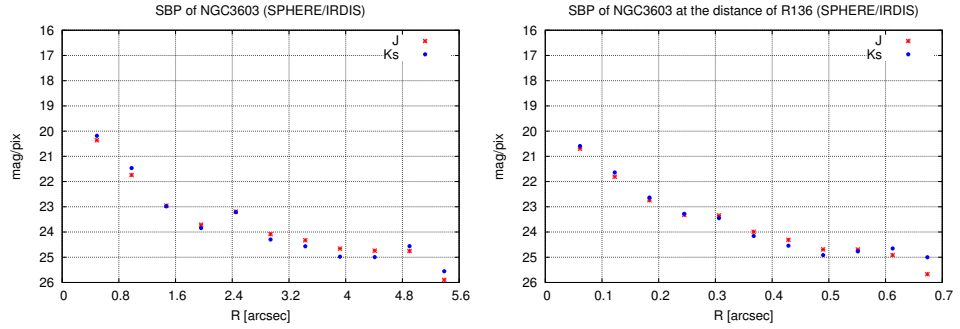


Fig. 15. SBP of NGC3603 in SPHERE/IRDIS J and Ks band data. Left: NGC3603 real images. Right: simulated NGC3603 at the distance of R136.

Bibliography

- [Aarseth et al. (1974)] S.J. Aarseth, M. Henon, R. Wielen, 1974, *A&A*, 37, 183-187
- [Aarseth et al. (2003)] Aarseth, S. J. 2003, *Gravitational N-Body Simulations* (Cambridge: Cambridge Univ. Press)
- [Ascenso et al. (2009)] Ascenso, J., Alves, J., & Lago, M. T. V. T. 2009, *AAP*, 495, 147
- [Bahcall et al. (1995)] Bahcall, J. N., Pinsonneault, M. H., Wasserburg, G. J. 1995, *Rev. Mod. Phys.*, 67(4), 781
- [Banerjee & Kroupa (2013)] Sambarab Banerjee and Pavel Kroupa, 2013, *ApJ*, 764:29
- [Bate (2009)] Bate, M. R. 2009, *MNRAS*, 392, 1363
- [Bate (2012)] Bate, M. R. 2012, *MNRAS*, 419, 3115
- [Bonnell & Davies (1998)] Bonnell, I. A., Davies, M. B. 1998, *MNRAS*, 295, 691
- [Bonnell et al. (2001)] Bonnell, I. A., Clarke, C. J., Bate, M. R., Pringle, J. E. 2001, *MNRAS*, 324, 573
- [Bonnell & Bate (2006)] Bonnell, I. A., Bate, M. R. 2006, *MNRAS*, 370, 488
- [Bosch et al. (2009)] Bosch, G., Terlevich, E., Terlevich, R. 2009, *AJ*, 137, 3437

- [Baumgardt & Klessen (2011)] Baumgardt, H.; Klessen, R. S., 2011, MNRAS, 413, 1810
- [Beuzit et al. (2008)] Beuzit, J.-L., Feldt, M., Dohlen, K., et al. 2008, SPIE, 7014, 701418
- [Bressan et al. (2012)] Bressan, A.; Marigo, P.; Girardi, L. et al., 2012, MNRAS, 427, 127
- [Bessel (1844)] Bessel, F. W. 1844, MNRAS, 6, 136
- [Bouret et al. (2003)] Bouret J.-C., Lanz T., Hillier D. J., Heap S. R., Hubeny I., Lennon D. J., Smith L. J., Evans C. J. 2003, ApJ, 595, 1182
- [Bouret et al. (2013)] Bouret J.-C., Lanz T., Martins F., Marcolino W. L. F., Hillier D. J., Depagne E., Hubeny I. 2013, A&A, 555, A1
- [Brandl et al. (1996)] Brandl, B., Sams, B. J., Bertoldi, F., Eckart, A., Genzel, R., Drapatz, S., Hofmann, R., Loewe, M., Quirrenbach, A. 1996, ApJ, 466, 254
- [Brandl et al. (1999)] Brandl B., Brandner W., Eisenhauer F., Moffat A. F. J., Palla F., Zinnecker H. 1999, A&A, 352, L69
- [Campbell et al. (2010)] Campbell, M. A., Evans, C. J., Mackey, A. D., et al. 2010, MNRAS, 405, 421
- [Cassinelli et al. (1981)] Cassinelli, J. P., Mathis, J. S., & Savage, B. D. 1981, Science, 212, 1497
- [Castelli et al. (1997)] Castelli, F.; Gratton, R. G.; Kurucz, R. L., 1997, A&A, 318, 841
- [Commerçon et al. (2011)] Commerçon, B., Hennebelle, P., & Henning, T. 2011, ApJ, 742, L9
- [Conti et al. (1995)] Conti, P. S., Hanson, M. M., Morris, P. W., et al. 1995, ApJ, 445, L35
- [Crowther et al. (2010)] Crowther, P. A., Schnurr, O., Hirschi, R., Yusof, N., Parker, R. J., Goodwin, S. P., Kassim, H.A. 2010, MNRAS, 408, 731

- [Crowther et al. (2016)] Crowther, P. A., Caballero-Nieves, S. M., Bostroem, K. A., et al. 2016, MNRAS, 458, 624
- [de Koter et al. (1997)] de Koter, A., Heap, S. R., Hubeny, I. 1997, ApJ, 477, 792
- [de Koter et al. (1998)] de Koter, A., Heap, S. R., Hubeny, I. 1998, ApJ, 509, 879
- [De Pree et al. (1999)] De Pree, C. G., Nysewander, M. C., Goss, W. M. 1999, AJ, 117, 2903
- [Diolaiti et al. (2000)] Diolaiti, E., Bendinelli, O., Bonaccini, D., Close, L., Currie, D., Parmegiani, G. 2000, A&AS, 147, 335
- [Drissen et al. (1995)] Drissen L., Moffat A. F. J., Walborn N. R., Shara M. M., 1995, AJ, 110, 2235
- [Eisenhauer et al. (1998)] Eisenhauer F., Quirrenbach A., Zinnecker H., Genzel R., 1998, ApJ, 498, 278
- [Elson et al. (1987)] Elson, R. A. W., Fall, S. M., & Freeman, K. C. 1987, ApJ, 323, 54
- [Feitzinger et al. (1980)] Feitzinger, J. V., Schlosser, W., Schmidt-Kaler, T., & Winkler, C. 1980, A&A, 84, 50
- [Figer et al. (1998)] Figer, D. F., Najarro, F., Morris, M., et al. 1998, ApJ, 506, 384
- [Figer (2005)] Figer, D. F. 2005, Nature 434, 192
- [Gieren et al. (1998)] Gieren, W. P., Fouqué, P., Gomez, M. 1998, ApJ 496, 17
- [Giersz & Heggie (1994)] Giersz, M., & Heggie, D. C. 1994, MNRAS, 268, 257
- [Girardi et al. (2002)] Girardi L., Bertelli G., Bressan A., Chiosi C., Groenewegen M. A. T., Marigo P., Salasnich B., Weiss A., 2002, A&A, 391, 195

- [Harayama et al. (2008)] Harayama Y., Eisenhauer F., Martins F. 2008, ApJ, 675, 1319
- [Henault-Brunet et al. (2012)] Henault-Brunet V., Evans C. J., Sana H., Gieles M., Bastian N., Maiz Apellaniz J., Markova N., Taylor W. D., Bressert E., Crowther P. A., van Loon J. T., 2012, A&A , 546, A73
- [Hennebelle et al. (2011)] Hennebelle, P., Commerçon, B., Joos, M., et al. 2011, A&A, 528, A72
- [Heydari-Malayeri et al. (1988)] Heydari-Malayeri, M., Remy, M., & Magain, P. 1988, A&A, 201, L41
- [Heydari-Malayeri & Hutsemekers (1991)] Heydari-Malayeri, M. & Hutsemekers, D. 1991, A&A, 243, 401
- [Hillier & Lanz (2001)] Hillier D. J., Lanz T. 2001, in The Challenge of high-resolution X-Ray through IR Spectroscopy, Ed. G. Ferland, ASP Conf. Ser., 247, 333.
- [Hillier & Miller (1998)] Hillier, D. J. & Miller, D. L. 1998, ApJ, 496, 407
- [Hubeny & Lanz (1995)] Hubeny I., Lanz T. 1995, ApJ, 439, 875
- [Hunter et al. (1995)] Hunter Deidre A., Shaya Edward J., Holtzman Jon A., Light Robert M., O'Neil Earl J. Jr., Lynds Roger, 1995, ApJ, 448, 179
- [Humphreys (1983)] Humphreys, R. M. 1983, ApJ, 269, 335
- [Hurley et al. (2000)] Hurley, J. R., Pols, O. R., Tout, C. A. 2000, MNRAS, 315, 543
- [Hurley et al. (2002)] Hurley, J. R., Tout, C. A., Pols, O. R. 2002, MNRAS, 329, 897
- [Hamann & Grafener (2004)] Hamann, W.-R. & Grafener, G. 2004, A&A, 427, 697
- [Huchra et al. (1983)] Huchra, J. P., Geller, M. J., Gallagher, J., et al. 1983, ApJ, 274, 125

- [Hunter et al. (1995)] Hunter D. A., Shaya E. J., Holtzman J. A., Light R. M., O'Neil E. J. Jr., Lynds R. 1995, ApJ, 448, 179
- [Hirschi (2015)] Hirschi, R. 2015, Very Massive Stars in the Local Universe, 412, 157
- [Johnston et al. (2014)] Johnston, K. G., Beuther, H., Linz, H., et al. 2014, aap, 568, A56
- [Kobulnicky& Fryer (2007)] /Kobulnicky H. A., Fryer C. L., 2007, ApJ, 670, 747
- [Kohler et al. (2015)] Kohler, K., Langer, N., de Koter, A., de Mink, S. E., Crowther, et al. 2015, A&A, 573, A71
- [Kennicutt (1984)] Kennicutt, R. C., Jr. 1984, ApJ, 287, 116
- [Kroupa (2001)] Kroupa P., 2001a, MNRAS, 322, 231
- [Kroupa (1995)] Kroupa P., 1995a, MNRAS, 277, 1491
- [Kroupa (2008)] Kroupa P., 2008, LNP, 760, 181
- [Kudritzki et al. (1989)] Kudritzki, R. P., Cabanne, M. L., Husfeld, D., et al. 1989, A&A, 226, 235
- [Kudryavtseva et al. (2012)] Kudryavtseva, N., Brandner, W., Gennaro, M., et al. 2012, ApJL, 750, L44
- [Kratte & Matzner (2008)] Kratter, Kaitlin M.; Matzner, Christopher D., 2006, MNRAS, 373, 1563
- [Kratte et al. (2008)] Kratter, Kaitlin M.; Matzner, Christopher D.; Krumholz, Mark R., 2008, The Astrophysical Journal, 681, 375
- [Kratte et al. (2010)] Kratter, Kaitlin M.; Matzner, Christopher D.; Krumholz, Mark R.; Klein, Richard I., 2010, The Astrophysical Journal, 708, 1585

- [Kratte & Matzner (2006)] Kratte, K. M., & Matzner, C. D. 2006, MNRAS, 373, 1563
- [Krumholz et al. (2007)] Krumholz, M. R., Klein, R. I., & McKee, C. F. 2007, ApJ, 656, 959
- [Krumholz et al. (2009)] Krumholz, M. R., Klein, R. I., McKee, C. F., Offner, S. S. R., & Cunningham, A. J. 2009, Science, 323, 754
- [Krumholz et al. (2010)] Krumholz, M. R., Cunningham, A. J., Klein, R. I., & McKee, C. F. 2010, ApJ, 713, 1120
- [Krumholz et al. (2011)] Krumholz, M. R., Klein, R. I., & McKee, C. F. 2011, ApJ, 740, 74
- [Krumholz et al. (2012)] Krumholz, Mark R.; Klein, Richard I.; McKee, Christopher F., 2012, The Astrophysical Journal, 754
- [Krumholz (2015)] Krumholz, Mark R., "The Formation of Very Massive Stars", 2015, SPRINGER, P43
- [Kupper et al. (2011)] Kupper, A. H. W., Maschberger, T., Baumgardt, H., Kroupa, P. 2011, MNRAS, 417, 2300
- [Lada & Lada (2003)] Lada, C. J. & Lada, E. A. ,2003, Annu. Rev. Astron. Astrophys. 41, 57-115.
- [Lamers & Cassinelli (1999)] Henny J. G. L. M. Lamers, Joseph P. Cassinelli, Cambridge University Press, Jun 17, 1999
- [Langlois et al. (2014)] Langlois, M., Vigan, A., Dohlen, K., et al. 2014, SPIE, 9147, 91479P
- [Lanz & Hubeny (2003)] Lanz T., Hubeny I., 2003, ApJS, 146, 417
- [Lanz & Hubeny (2007)] Lanz T., Hubeny I., 2007, ApJS, 169, 83
- [Lejeune & Schaerer (2001)] Lejeune T., Schaerer D. 2001, A&A, 366, 538

- [Melena et al. (2008)] Melena, N. W., Massey, P., Morrell, N. I., Zangari, A. M. 2008, AJ, 135, 878
- [Malumuth & Heap (1994)] Malumuth E.M., Heap S.R., 1994, AJ, 107, 1054
- [Martins et al. (2005)] Martins F., Schaerer D., Hillier D. J., 2005, A&A, 436, 1049
- [Martins (2015)] Martins, F. 2015, Very Massive Stars in the Local Universe, 412, 9
- [Mason et al. (1998)] Mason, B. D., Gies, D. R., Hartkopf, W. I., et al. 1998, AJ, 115, 821
- [Massey & Hunter (1998)] Massey P., Hunter D. A. 1998, ApJ, 493, 180
- [Massey (2003)] Massey P., 2003, ARA&A, 41, 15
- [Melnick (1982)] Melnick, J. 1982, Wolf-Rayet Stars: Observations, Physics, Evolution, 99, 545
- [Melnick (1983)] Melnick, J. 1983, The Messenger, 32, 11
- [Meynet & Maeder (2000)] Meynet, G., Maeder, A. 2000, A&A, 361, 101
- [Moeckel & Clarke (2011)] Moeckel, Nickolas; Clarke, Cathie J., 2011, MNRAS, 410, 2799
- [Moffat (1983)] Moffat, A. F. J. 1983, A&A, 124, 273
- [Moffat & Seggewiss (1983)] Moffat, A. F. J., & Seggewiss, W. 1983, A&A, 125, 83
- [Moffat et al. (1985)] Moffat, A. F. J., Seggewiss, W., & Shara, M. M. 1985, ApJ, 295, 109
- [Moffat et al. (2004)] Moffat, A. F. J., Poitras, V., Marchenko, S. V., et al. 2004, AJ, 128, 2854
- [Myers et al. (2013)] Myers, A. T., McKee, C. F., Cunningham, A. J., Klein, R. I., & Krumholz, M. R. 2013, ApJ, 766, 97

- [Najarro et al. (2009)] Najarro, F., Figuer, D. F., Hillier, D. J., Geballe, T. R., & Kudritzki, R. P. 2009, *ApJ*, 691, 1816
- [Neugent et al. (2015)] Neugent, K. F.; Massey, P.; Hillier, D. J.; Morrell, N. I., 2015, To be published by Universitätsverlag Potsdam as part of the International Workshop on Wolf-Rayet Stars conference proceedings
- [Offner et al. (2009)] Offner, S. S. R., Klein, R. I., McKee, C. F., & Krumholz, M. R. 2009, *ApJ*, 703, 131
- [Pang et al. (2013)] Pang X., Grebel E. K., Allison R. J., Goodwin S. P., Altmann M., Harbeck D., Moffat A. F. J., Drissen L., 2013, *ApJ*, 764, 73
- [Puls et al. (2005)] Puls, J., Urbaneja, M. A., Venero, R., et al. 2005, *A&A*, 435, 669
- [Pugliese et al. (2002)] Pugliese, G., Christou, J., Koehler, R., & Drummond, J. 2002, *Bulletin of the American Astronomical Society*, 34, 55.05
- [Portegies Zwart et al. (2010)] Portegies Zwart, S. F., McMillan, S. L. W., & Gieles, M. 2010, *ARA&A*, 48, 431
- [Rieke & Lebofsky (1985)] Rieke, G. H., & Lebofsky, M. J. 1985, *ApJ*, 288, 618
- [Rochau et al. (2010)] Rochau B., Brandner W., Stolte A., et al. 2010, *ApJ*, 716, L90
- [Schnurr et al. (2008)] Schnurr O., Casoli J., Chene A.-N. et al., 2008, *MNRAS*, 389, L38
- [Salpeter (1955)] Salpeter, E. E., 1955, *APJ*, 121
- [Sana & Evans (2011)] Sana H., Evans C. J., 2011, *IAUS*, 272, 474
- [Sana et al. (2013)] Sana, H., de Koter, A., de Mink, S. E., et al. 2013, *AAP*, 550, A107

- [Sagar et al. (2001)] Sagar, R., Munari, U., de Boer, K. S. 2001, MNRAS, 327, 23
- [Savage et al. (1983)] Savage, B. D., Fitzpatrick, E. L., Cassinelli, J. P., & Ebbets, D. C. 1983, ApJ, 273, 597
- [Selman et al.1999] Selman, F., Melnick, J., Bosch, G., Terlevich, R., 1999, A&A, 347, 532
- [Selman & Melnick (2013)] Selman, F. J., & Melnick, J. 2013, A&A, 552, A94
- [Simon-Diaz et al. (2014)] Simon-Diaz S., Herrero A., Sabin-Sanjulian C., Najarro F., Garcia M., et al. 2014, A&A, 570, L6
- [Spitzer (1987)] Spitzer, L. 1987, Princeton, NJ, Princeton University Press, 1987, 191 p.,
- [Stolte et al. (2004)] Stolte A., Brandner W., Brandl B., Zinnecker H., Grebel E. K., 2004, AJ, 128, 765
- [Stolte et al. (2006)] Stolte A., Brandner W., Brandl B., Zinnecker H., Grebel E. K. 2006, AJ, 132, 253
- [Soummer et al. (2009)] Remi Soummer, Anand Sivaramakrishnan, Ben R. Oppenheimer, Robin Roberts, Douglas Brenner, Alexis Carlotti, Laurent Pueyo, Bruce Macintosh, Brian Bauman, Les Saddlemyer, David Palmer, Darren Erickson, Christophe Dorrer, Kris Caputa, Christian Marois, Kent Wallace, Emily Griffiths, Jacob Mey, Proc. SPIE 7440, Techniques and Instrumentation for Detection of Exoplanets IV, 74400R (August 19, 2009)
- [Sung & Bessell (2004)] Sung H., Bessell M. S., 2004, AJ, 127, 1014
- [van den Bergh (1978)] van den Bergh, S. 1978, A&A, 63, 275
- [Vink (2015)] Vink, J. S. 2015, Very Massive Stars in the Local Universe, 412
- [Walborn (1973)] Walborn, N. R. 1973, ApJ, 182, L21

- [Walborn et al. (2002)] Walborn, N. R., Howarth, I. D., Lennon, D. J., et al. 2002, *AJ*, 123, 2754
- [Ward-Thompson & Whitworth (2011)] Ward-Thompson, D., & Whitworth, A. P. 2011, *An Introduction to Star Formation* by Derek Ward-Thompson and Anthony P. Whitworth. Cambridge University Press, 2011. ISBN: 9780521630306,
- [Weigelt, G. & Baie (1985)] Weigelt, G. & Baier, G. 1985, *A&A*, 150, L18
- [Weidner & Kroupa (2006)] Weidner, C., Kroupa, P. 2006, *MNRAS*, 365, 1333
- [Weidner et al. (2010)] Weidner, C., Kroupa, P., Bonnell, I. A. D., 2010 *MNRAS* 401, 275
- [Wolfire & Cassinelli (1987)] Wolfire, M. G., & Cassinelli, J. P. 1987, *ApJ*, 319, 850
- [Woosley & Heger (2015)] Woosley, S. E., & Heger, A. 2015, *Very Massive Stars in the Local Universe*, 412, 199
- [Yusof et al. (2013)] Yusof, N., Hirschi, R., Meynet, G., et al. 2013, *MNRAS*, 433, 1114
- [Zinnecker (2006)] Zinnecker, Hans, *The Scientific Requirements for Extremely Large Telescopes*, Proceedings of the 232nd Symposium of the International Astronomical Union, Held in Cape Town, South Africa, November 14-18, 2005, Edited by Patricia Ann Whitlock; Michel Dennefeld; Bruno Leibundgut. Cambridge: Cambridge University Press, 2006., pp.324-327
- [Zurlo et al. (2014)] A. Zurlo, A. Vigan, D. Mesa, R. Gratton, C. Moutou, M. Langlois, R. U. Claudi, L. Pueyo, A. Boccaletti, A. Baruffolo et al. (19 more), 2014, *A&A*, 572, A85